PIV Uncertainty Quantification and Beyond

Wieneke, Bernhard

DOI
10.4233/uuid:4ca8c0b8-0835-47c3-8523-12fc356768f3

Publication date
2017

Document Version
Final published version

PIV Uncertainty Quantification and Beyond

PIV Uncertainty Quantification and Beyond

Proefschrift

ter verkrijging van de graad van doctor
aan de Technische Universiteit Delft,
op gezag van de Rector Magnificus prof. ir. K.C.A.M. Luyben;
voorzitter van het College voor Promoties,
in het openbaar te verdedigen op
dinsdag 12 december 2017 om 12.30 uur

door

Bernhard Wieneke

Master of Science in Space Physics and Astronomy, Rice University,
United States of America
geboren te Köln, Duitsland

Dit proefschrift is geodgekeurd door de

Promotor: Prof. dr. F. Scarano
Copromotor: Dr. ir. A. Sciacchitano

Samenstelling promotiecommissie

Rector Magnificus,	voorzitter
Prof. dr. F. Scarano,	Technische Universiteit Delft, promotor
Dr. ir. A. Sciacchitano,	Technische Universiteit Delft, copromotor

Onafhankelijke leden:

Prof. dr. T. Astarita	University of Naples Frederico II
Prof. dr. Ch. Kähler	University of the Armed Forces, München
Prof. dr. B. Leclaire	ONERA, Meudon
Prof. dr. B. Smith	Utah State University
Prof. dr. J. Westerweel	Technische Universiteit Delft

Reserved
Prof. dr. L. Veldhuis Technische Universiteit Delft

This research was partly funded by LaVision GmbH, Göttingen.

Keywords: PIV uncertainty, anisotropic denoising, calibration correction, volumetric particle reconstruction.

Cover designed by: H.D. Wöhrle, Göttingen

Printed by: Rijna Repro Delft

ISBN: 978-94-92516-88-6

An electronic version of this dissertation is available at

http://repository.tudelft.nl

Summary

The fundamental properties of computed flow fields using particle imaging velocimetry (PIV) have been investigated, viewing PIV processing as a black box without going in detail into algorithmic details. PIV processing can be analyzed using a linear filter model, i.e. assuming that the computed displacement field is the result of some spatial filtering of the underlying true flow field given a particular shape of the filter function. From such a mathematical framework, relationships are derived between the underlying filter function, wavelength response function (MTF) and response to a step function, power spectral density, and spatial autocorrelation of filter function and noise.

A definition of a *spatial resolution* is provided independent of some arbitrary threshold e.g of the wavelength response function and provides the user with a single number to appropriately set the parameters of the PIV algorithm required for detecting small velocity fluctuations.

The most important error sources in PIV are discussed and an uncertainty quantification method based on correlation statistics is derived, which has been compared to other available UQ-methods in two recent publications (Sciacchitano et al. 2015; Boomsma et al. 2016) showing good sensitivity to a variety of error sources. Instantaneous local velocity uncertainties are propagated for derived instantaneous and statistical quantities like vorticity, averages, Reynolds stresses and others. For Stereo-PIV the uncertainties of the 2C-velocity fields of the two cameras are propagated into uncertainties of the computed final 3C-velocity field.

A new anisotropic denoising scheme as a post-processing step is presented which uses the uncertainties comparing to the local flow gradients in order to devise an optimal filter kernel for reducing the noise without suppressing true small-scale flow fluctuations.

For Stereo-PIV and volumetric PIV/PTV, an accurate perspective calibration is mandatory. A Stereo-PIV self-calibration technique is described to correct misalignment between the actual position of the light sheet and where it is supposed to be according to the initial calibration procedure. For volumetric PIV/PTV, a volumetric self-calibration (VSC) procedure is presented to correct local calibration errors everywhere in the measurement volume.

Finally, an iterative method for reconstructing particles (IPR) in a volume is developed, which is the basis for the recently introduced Shake-the-Box (STB) technique (Schanz et al. 2016).

Sammenvatting

De fundamentele eigenschappen van stromingsvelden berekend met particle imaging velocimetry (PIV) zijn onderzocht, waar de PIV-verwerking gezien is als een black box zonder in detail op algoritmische details in te gaan. PIV-verwerking kan geanalyseerd worden met een lineair model, d.i. aannemende dat het berekende verplaatsingsveld het resultaat is van enige ruimtelijke filtering van het onderliggende echte stromingsveld, gegeven een bepaalde vorm van de filterfunctie. Vanuit zo een wiskundig raamwerk zijn verbanden afgeleid tussen de onderliggende filterfunctie, de golflengte respons functie (MTF), en de respons op een stapfunctie, de spectrale vermogensdichtheid en de ruimtelijke autocorrelatie van de filterfunctie en de ruis.

Een definitie van *ruimtelijke resolutie* is gegeven, onafhankelijk van een arbitraire drempel van bijvoorbeeld de golflengte respons functie, wat de gebruiker een enkel getal geeft om op gepaste wijze de parameters van het PIV-algoritme in te stellen voor het detecteren van kleine snelheidsfluctuaties.

De belangrijke bronnen voor fouten in PIV zijn bediscussieerd en een onzekerheidskwantificatie (UQ) methode gebaseerd op correlatie statistieken is afgeleid, welke vergeleken is met andere beschikbare UQ-methoden in twee recente publicaties (Sciacchitano et al. 2015; Boomsma et al. 2016) en een goede gevoeligheid laat zien voor een variëteit aan foutbronnen. Instantane lokale onzekerheden in snelheid zijn gepropageerd voor afgeleide instantane en statistische grootheden als vorticiteit, gemiddelden, Reynolds spanningen en andere. Voor Stereo-PIV zijn de onzekerheden van de 2C-snelheidsvelden van de twee camera's gepropageerd in de onzekerheden van het uiteindelijke berekende 3C-snelheidsveld.

Een nieuw anisotroop ruis verminderingsschema als naverwerkingsstap is gepresenteerd, dat gebruik maakt van de onzekerheden vergeleken met de lokale snelheidsgradienten om een optimale filter kernel te creëren voor het verminderen van ruis zonder echte kleine-schaal snelheidsfluctuaties te onderdrukken.

Voor Stereo-PIV en volumetrische PIV/PTV is nauwkeurige perspectiefkalibratie een vereiste. Een Stereo-PIV zelf-kalibratie techniek om foutieve uitlijning te corrigeren tussen de echte positie van het lichtvlak en waar het zou moeten zijn volgens de initiële kalibratie procedure is beschreven. Voor volumetrische PIV/PTV is een volumetrische zelf-kalibratie (VSC) methode gepresenteerd om lokale kalibratie fouten overal in het meetvolume te corrigeren.

Tot slot is er een iteratieve methode voor deeltjes reconstructie (IPR) in een volume ontwikkeld die de basis vormt voor de recent geïntroduceerde Shake-the-Box (STB) techniek (Schanz et al. 2016).

Content

1

Introduction

Particle Image Velocimetry (PIV) is nowadays a wide-spread measurement technique of planar and recently volumetric flow fields. Advances in optics, cameras and laser performance together with available well-integrated commercial PIV systems have established PIV as the preferred technique for many flow measurement tasks. While point-wise measurement techniques like hot-wire anemometry and laser Doppler velocimetry often provide higher accuracy and temporal resolution ideal for the measurement of certain statistical quantities, instantaneous 2D- or 3D-flow fields from PIV enable direct insight into spatially coherent structures. Following flow patterns over time with high-speed cameras with up to 5-20 kHz frame rate in combination with powerful high-repetition rate lasers have opened the possibility of in-depth analysis of transient phenomena, fluid-structure interaction and turbulence analysis for fast water and air flows.

Applications range in size from a field-of-view of less than 1 mm in micro channels or blood vessels (μPIV) to meter scales even observing natural phenomena like river flows, ocean currents or cloud dynamics. Most experiments are conducted in the lab under controlled conditions with a field-of-view between 5 and 50 cm. Typically, small seeding particles are added to the fluid observing particle motion around objects, for example, in water channels, towing tanks, wind tunnels, inside pumps, turbine machinery, flames and other combustion environments, to name just a few of the many different application fields. About 70% of all PIV systems are used as a tool for fundamental and applied research at universities and research institutions, and 30% by industry, mainly by large energy, automotive, aerospace, chemical and medical companies with dedicated research departments.

1.1 History of PIV and particle / feature tracking

In PIV, the basic underlying image processing technology is the tracking of particles or group of particles, which is not a task unique to fluid dynamics research. In many scientific fields, there has been a need to track features in images recorded in time or e.g. matching features in images taken by two cameras from different perspectives for 3D vision. In the large field of computer vision, this is named *image registration*, i.e. finding the spatial correspondences of individual features or small image regions in at least two images. First applications included aerial photogrammetry (Webber 1973) on real photographs which have been scanned and digitally processed, measuring landscapes or, for example, changing tidal lands (Wrobel and Ehlers 1980; Ackermann 1984).

At about the same time, image registration has been applied to the field of fluid dynamics measuring planar flow fields using a laser light sheet and tracers in gases and liquids, at the beginning called *speckle velocimetry*, but soon after particle image velocimetry (PIV) (Meynart 1982; Pickering and Halliwell 1984; Adrian 1984). At the beginning, only film cameras were available with tedious scanning and time-consuming processing. The wide-spread use of PIV started in the 90's with the

availability of digital cameras capable of fast recording of two images together with inexpensive, but powerful personal computers for fast processing.

Similarly, in the experimental mechanics field, image registration has been used for measuring deformation of solid surfaces, named *digital image correlation* (DIC) (Peters and Ranson 1982; Sutton et al. 1983; Sutton et al. 1986), relating locally measured surface strain tensors to material properties like Young's module.

Interestingly, the development of image registration techniques proceeded quite independently in these three fields with different names for similar algorithms. Only recently there has been more exchange with special techniques or algorithms from one field applied to another.

Image registration of two images consists of finding a displacement field (*disparity map*) which provides for a point in image 1 the displacement vector to the same feature or local patch in image 2. Natural scenes are often dominated by features, i.e. points, edges or objects with specific shapes. Therefore, most work in computer vision has focused on detection and tracking of available features, but cross-correlation of image patches is well known, too, as *block matching*.

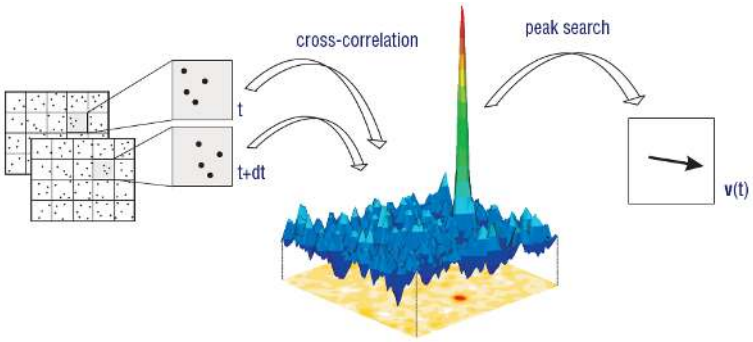

Figure 1.1. Block-matching cross-correlation technique typically used in PIV. The position of the highest peak in the correlation plane indicates the most likely displacement vector.

In fluid or solid mechanics (PIV and DIC), on the other hand, recorded images usually consist of random speckle pattern of solid particles, oil or water droplets, (helium-filled) air bubbles, fibers or granular materials in PIV, and fine spray paint blobs or natural features/scratches on solid surfaces in DIC. Observed displacement fields are mostly continuous with small displacements between recorded images usually in the range of at most 5-20 pixels. Tracking is typically done on local patches (named *subsets*, *interrogation windows*, or *blocks*) of the image containing sufficient number and contrast of speckle pattern elements or particles.

1.2 PIV development from light sheet to volume

The basic experimental setup for a 2D-PIV system consists of a laser formed into a thin light sheet, adding tracer particles to the fluid, which are small enough to faithfully follow the flow, and recording two images shortly after each other with a time separation Δt using a digital camera. The particles move by some distance, typically up to 5-10 pixels, and the local velocity is given by the measured distance divided by the time interval Δt.

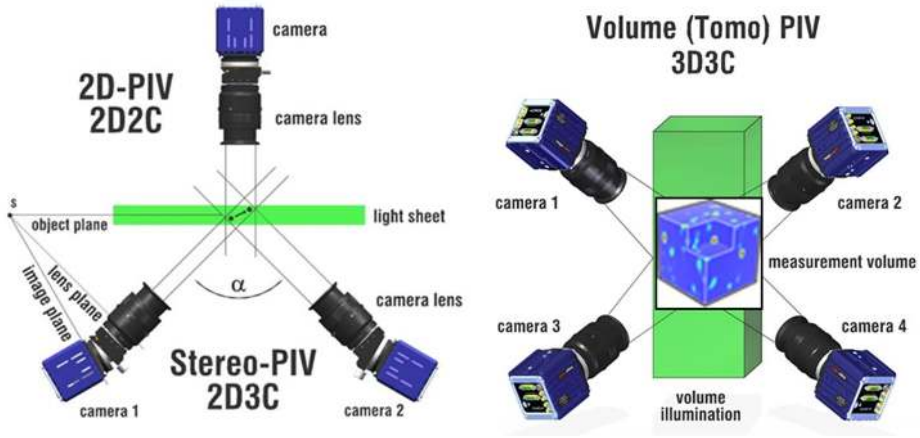

Figure 1.2. Experimental setup for single-camera 2D-PIV, dual-camera Stereo-PIV, and volumetric tomographic PIV.

Single-camera 2D-PIV is limited to the measurement of the two in-plane velocity components (2C). The natural extension into *Stereo-PIV* is facilitated by the addition of a second camera observing the true velocity vector from another viewing angle (Prasad and Adrian 1993; among others). The corresponding two 2C-displacement vectors from each camera are combined into the true 3C-velocities by a geometrical reconstruction step.

Another useful extension has been the introduction of *time-resolved PIV*, not just recording two images but continuously recording images at a sufficiently high frame rate to observe the dynamical evolution of the flow pattern. At the beginning, the best digital high-speed cameras could record e.g. 500 frames-per-second (fps) with 256x256 pixels mostly useful for water applications, while modern CMOS-cameras are now capable of frame rates above 20 kHz with a one megapixel sensor. Similarly, the power of high-repetition-rate lasers has significantly increased in the last decades enabling time-resolved PIV also in air flows.

Measurement in a full volume instead of just a light sheet has been done for a long time by tracking individual particles by photogrammetry (3D-particle tracking velocimetry (3D-PTV); Maas et al. 1993; among others). The principle is based on simultaneously recording the light scattered by illuminated particles from typically three to four cameras with different viewing directions. Particle image positions are

first obtained in the 2D image-plane, e.g. by a 2D-Gaussian intensity peak fit. A triangulation procedure matches the particle images from the different cameras onto possible 3D-particle locations. Finally, the 3D-locations are tracked in time and space computing particle velocities and Lagrangian trajectories. Problems with overlapping particles and ghost particles have limited the classical 3D-PTV approach to rather low seeding densities of 500 to 5000 particles per megapixel sensor (0.0005 to 0.005 particles per pixel (ppp)).

For acquiring dense volumetric flow fields on a regular grid, the *tomographic PIV* technique has been developed by Elsinga et al. (2006), enabling much higher seeding density by using an iterative reconstruction technique (MART; Herman and Lent 1976) to compute the intensities of all voxel in the measurement volume. This is followed by a 3D-cross-correlation procedure on local interrogation volumes to compute the 3D3C-flow field.

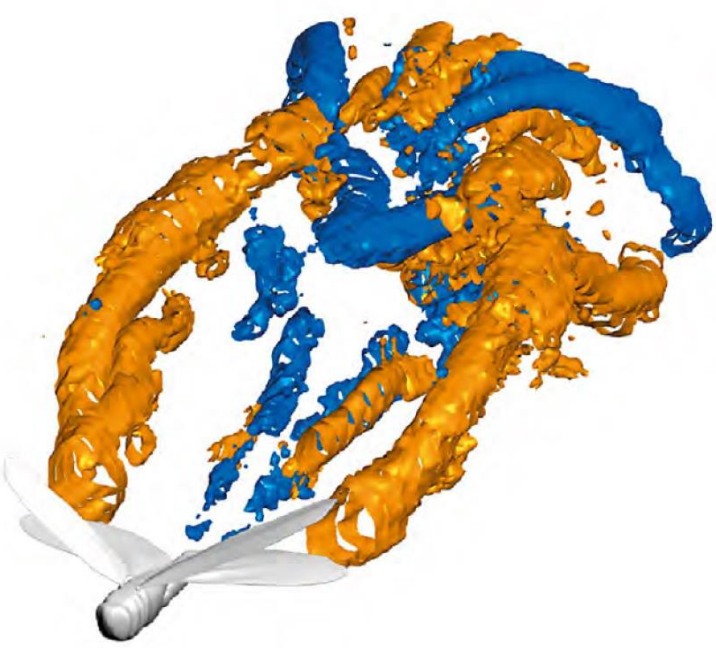

Figure 1.3. Instantaneous vortex pattern using time-resolved tomographic PIV behind a locust (from Bomphrey et al. 2012).

Many good reviews and books are available about image registration (e.g. Zitova and Flusser 2003), for DIC (Hild and Roux 2006; Sutton et al. 2009; Sutton and Hild 2015) and for PIV (Willert and Gharib 1991; Adrian 2005; Raffel et al. 2007; Schröder and Willert 2008; Adrian and Westerweel 2011; Scarano 2013) addressing many aspects of suitable experimental setups, processing steps and error sources.

1.3 Organization and Outline

Chapter 2 reviews the basic information content of planar PIV flow fields. PIV will be viewed from as a kind of black box without going into details of PIV processing schemes. Besides the actual velocity data, knowledge of the associated uncertainties and spatial resolution is relevant for a full understanding of the quality and accuracy of the flow field. PIV can be viewed as a linear spatial filter averaging the displacement content of the seeding particles inside some local interrogation window. A useful definition of the spatial resolution and its inverse, the corresponding filter length, is provided together different ways of measuring it from the wavelength response function of PIV, from the response to a step function in displacement, or from the spatial auto-correlation coefficients of the noise.

Despite the major progress in planar, volumetric and time-resolved PIV techniques, there has been a lack of specifying the uncertainties of the computed flow velocities in actual experiments. While substantial work has been done analyzing the error of synthetically generated images, only in recently uncertainty quantification (UQ) methods have been developed to quantify the uncertainty of each computed velocity vector. Chapter 3 reviews the major error sources in PIV and provides an UQ-method based on correlation statistics. Uncertainty propagation techniques are derived in chapter 4 attaching uncertainty bounds to derived statistical and instantaneous quantities like Reynolds stresses or vorticity. Chapter 5 presents an optimal spatial filter reducing the noise using the measured uncertainty values while preserving true small-scale flow fluctuations.

Chapter 6 reviews the errors of perspective calibration required for Stereo-PIV and volumetric PIV/PTV. For planar Stereo-PIV, possible misalignment of the actual light sheet position and where one assumes it to be according to the initial calibration are corrected by a self-calibration procedure using actual recordings (section 6.2). Similarly, remaining calibration errors for volumetric PIV/PTV can be corrected by a volumetric self-calibration procedure described in section 6.4**.**

Finally, chapter 7 presents the volumetric iterative particle reconstruction (IPR) method as an improvement to standard 3D-PTV enabling high seeding densities comparable to tomographic PIV. IPR is part of the recently developed time-resolved Shake-the-Box technique (Schanz et al. 2016), which performed extremely well in the most recent PIV Challenge (Kähler et al. 2016).

The work presented here is concluded with a summary and outlook of current developments in PIV/PTV, in particular incorporating data assimilation techniques and computation of instantaneous and averaged pressure fields from PIV/PTV-data.

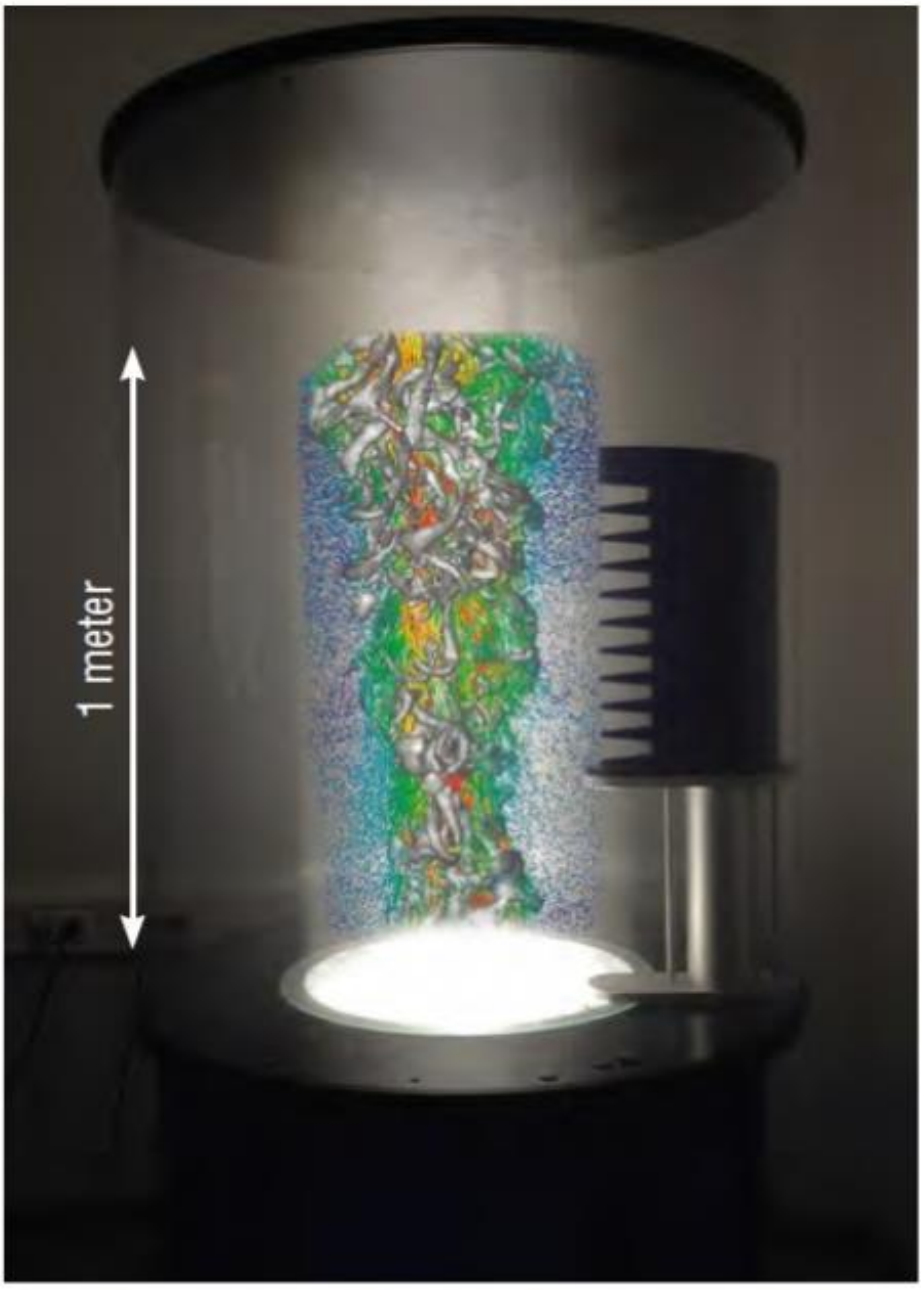

Figure 1.4. Large-Scale 4D-velocimetry in a convective air flow seeded with helium-filled soap bubbles processed by the Shake-the-Box (STB) particle tracking algorithm. Courtesy A. Schröder and D. Schanz, DLR Göttingen.

2

Fundamentals of PIV

2.1 Motivation

The processing scheme for PIV is in principle straightforward. Given various experimental parameters (timing, perspective calibration, geometrical setup ...), the recorded camera images are processed by the PIV algorithm with user supplied processing parameters computing the best-fit displacement field between the images, which, divided by the time separation between the images, yields the planar or volumetric velocity field (Figure 2.1).

In this chapter, PIV processing is viewed mostly as a black box without going into the details of the processing algorithm. The focus will be on quantifying the quality and intrinsic properties of the computed velocity field in a general way. The discussion is restricted here to planar 2D-PIV and Stereo-PIV, but can be easily extended to volumetric PIV/PTV.

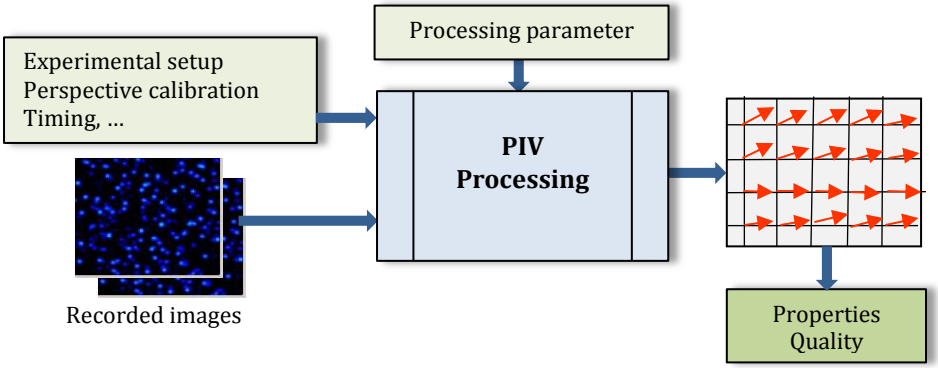

Figure 2.1. Flow chart of PIV processing.

The velocity field (u,v(,w)) of planar PIV is specified at spatial positions (x,y) inside a measurement field-of-view, which is usually defined as the z=0 plane. Traditionally, PIV computes a single displacement vector for each interrogation windows of e.g. 32x32 pixels, with an overlap between neighboring interrogation windows of 50 or 75%, thus providing velocity information on a regular grid with spacing of typically 8 to 16 pixels.

The simplest 2D2C-PIV (two-dimensional (i.e. planar), two-component) processing scheme would consist of a single pass computation of displacement vectors by cross-correlation (Figure 1.1). It has been improved considerable in the last decades to address issues of stability, precision and accuracy in conditions of low image quality, large displacements and strong gradients (see e.g. Adrian and Westerweel 2011; Raffel et al. 2007).

Nowadays, most state-of-the-art PIV processing schemes employ an iterative predictor-corrector method (Huang et al. 1993 (*Particle Image Distortion Technique* PID); Scarano and Riethmuller 1999, 2000; Astarita and Cardone 2005 (*Image Deformation Method* IDM), Astarita 2006, 2007, 2008; Schrijer and Scarano 2008).

Once an initial displacement field is calculated, subsequent iterations consist of dewarping the two images (usually symmetrically) using the calculated predictor displacement field (Figure 2.2). If the predictor field would be the perfect solution, the two dewarped images would perfectly overlap. A new (non-zero) corrector displacement field computed between the two dewarped images is then added to the predictor. Typically, some vector validation and predictor/corrector filter is included to remove erroneous vectors (*outliers*) and to ensure numerical stability field (Figure 2.3). Convergence is reached after a few (e.g. 3-5) passes with a sufficiently small remaining corrector field.

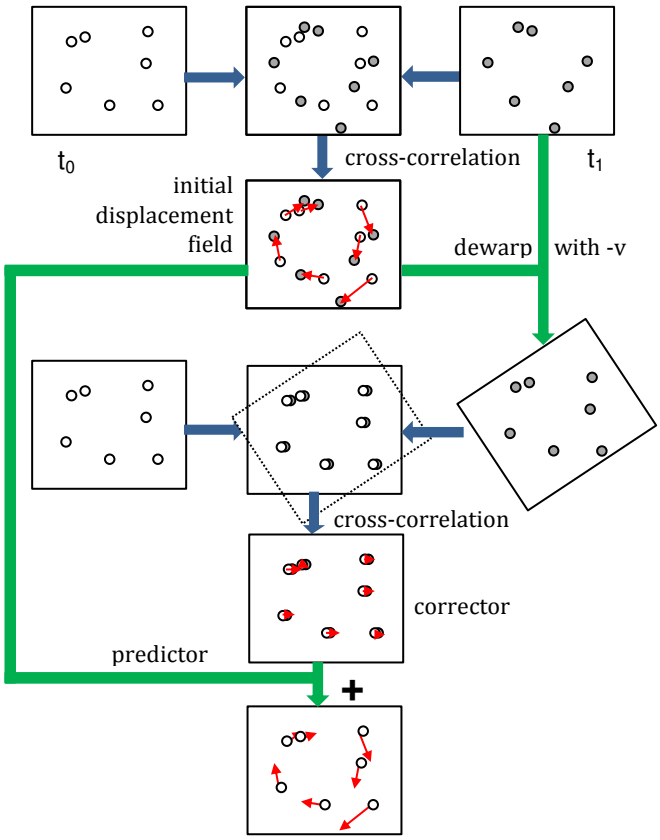

Figure 2.2. Simplified block diagram of the iterative predictor-corrector scheme.

Discrete versus continuous velocity field

Ideally the computed velocity field is provided in a *continuous* form, i.e. for all spatial locations, not just on grid points spaced apart e.g. by 4-32 pixels. in the predictor-corrector scheme, image dewarping uses the displacement field at every (sub-)pixel location, so whatever vector interpolation scheme is used here (usually

bilinear, bicubic, or B-splines) defines also the way, the final vectors on the grid locations should be interpolated to achieve a continuous velocity field.

Therefore, while most PIV processing schemes only compute displacement vectors on a regular grid, they (should) provide implicitly a *recipe* for computing a continuous velocity field if necessary. The difference between bilinear and bicubic interpolation becomes small for larger overlap factors. Some algorithms like FOLKI even compute vectors at every pixel locations (Champagnat et al. 2011).

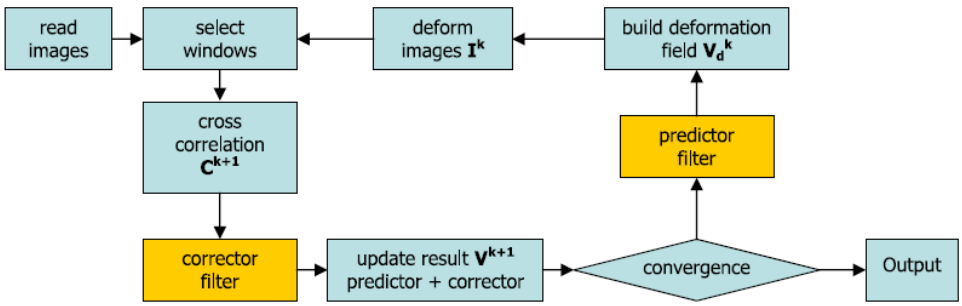

Figure 2.3. Adding predictor/corrector filter to the predictor-corrector scheme (from Schrijer and Scarano 2008).

Figure 2.4 shows a portion of a typical vector field with vectors computed on a regular grid. The associated u-component and vorticity field are shown here represented as one square per vector, with bilinear and with bicubic interpolation (from top to bottom). The smooth bicubic version is closest to what one would expect physically. Bilinear interpolation clearly shows visible artefacts.

In the following, especially for computing spatial correlation functions, always a continuous representation of the displacement field will be used. Computations are not restricted to vector locations on a grid.

Properties of a PIV flow field

Returning to the black box viewpoint, the PIV output information not only contains the (continuous) velocity field, but also some additional intrinsic properties, which are not readily visible. They are essential for a deeper understanding of the quality of PIV vector fields. Three main properties can be identified:

- Local uncertainty of the velocity field components
- Autocorrelation coefficients of noise: spatial, inter-component and temporal (for time-resolved PIV)
- Response function to velocity fluctuations of different spatial wavelengths (and temporal for time-resolved PIV)

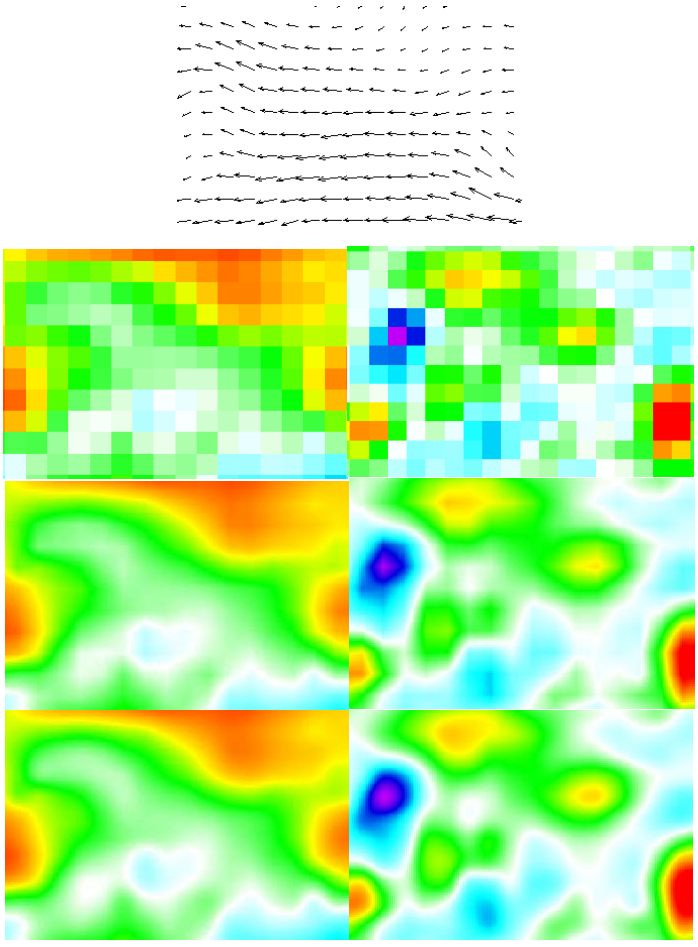

Figure 2.4. Vector field (top) below with u-component (left) and vorticity (right) and one square per vector, bilinear and bicubic interpolation (from top to bottom).

These points are relevant for uncertainty quantification (chapter 3) and propagation (chapter 4) and relate to the spatial resolution of a PIV measurement system as investigated further in this chapter.

For this purpose, PIV will be analyzed using a *linear filter model*, i.e. assuming that the computed displacement field is the result of some spatial filtering of the underlying true flow field using a particular shape of the filter function. The validity of the linear filter model is accessed and a general definition of a single-number *spatial resolution* is provided.

2.2 Linear Filter Model of PIV

PIV cross-correlation is a statistical process of averaging the displacement information inside an interrogation window. This can be approximated quite well by a linear filter function as noticed among others by Scarano and Riethmuller (2000). PIV can then be viewed as averaging the local displacement information u(x,y) over some local neighborhood IW ('interrogation window') into an averaged filtered displacement $u_F(x,y)$ using a 2D filter function with weighting coefficients F(x,y):

$$u_F(x_0, y_0) = \frac{\sum_{x,y \in IW} F(x,y)\, u(x_0 + x, y_0 + y)}{\sum_{x,y \in IW} F(x,y)} \tag{2.1}$$

For simplicity, the following equations are reduced to the 1D-case (x-direction), and sometimes provided in a more elegant integral notation. The transition to 2D and 3D is straightforward. Here, the filter function F is always normalized by:

$$\sum_{x,y=-\infty}^{+\infty} F(x,y) = 1 \tag{2.2}$$

It is also assumed that the 2D filter function is separable in x and y, i.e. $F(x,y) = F_x(x)\, F_y(y)$, with the same function in x and y and symmetrical around the origin: $F_x(x) = F_x(-x)$.

The following quantities are associated with F and are derived in the following sections:

- Flow field u_F
- Autocorrelation $AF_F(\Delta x)$ of F
- Autocorrelation of the random noise $AF_{\delta u}(\Delta x)$
- Spatial resolution, respectively filter length L_{sr}
- Response to spatial wavelengths $R_A(\lambda)$ (or as a function of frequency $f=1/\lambda$)
- Power spectra density PSD(f)
- Response to step function in displacement

For illustration, three types of normalized filter functions are considered as reference for the comparison with actual PIV algorithms (Table 2.1 and Figure 2.5):

- Top-hat function of width L_{TH} corresponding to single-pass PIV processing with a square interrogation window
- Gauss curve with standard deviation σ_G
- Mixture between Mexican-hat function (Marr-Hildreth, Laplacian-of-Gaussian) and Gauss ('MHG')

The MHG-function reduces to the Gaussian curve for b=0. A pure Mexican-hat function corresponds to b=1. Plotted in Figure 2.5 are sample curves for a 'filter length' L_{sr} of 22 pixel (‚sr' = spatial resolution). L_{sr} is defined later in section 2.3 as $1 / \int F(x)^2\, dx$.

Table 2.1. Typical filter functions.

Filter function	F(x)	Filter length L_{sr}
Top-Hat	$F_{TH}(x) = \begin{cases} 1/L_{TH} & \text{for } \lvert x \rvert \le L_{TH}/2 \\ 0 & \text{otherwise} \end{cases}$	$L_{sr} = L_{TH}$
Gauss	$F_G(x) = \frac{1}{\sigma_G\sqrt{2\pi}} e^{-\frac{x^2}{2\sigma_G^2}}$	$L_{sr} = \sigma_G\sqrt{4\pi}$
Mexican-Hat-Gauss (MHG)	$F_{MHG}(x) = \frac{\left(1 - b\frac{x^2}{\sigma_G^2}\right)}{(1-b)\sigma_G\sqrt{2\pi}} e^{-\frac{x^2}{2\sigma_G^2}}$	$L_{sr} = \sigma_G\sqrt{4\pi}\frac{(1-b)^2}{1-b+\frac{3}{4}b^2}$

The normalized autocorrelation of the filter function F is given by:

$$AF_F(\Delta x) = \frac{\sum_{x=-\infty}^{+\infty} F(x)\,F(x+\Delta x)}{\sum_{x=-\infty}^{+\infty} F(x)^2} \tag{2.3}$$

An important relationship is the fact that this AF_F-function is the same as the normalized autocorrelation $AF_{\delta u}(\Delta x)$ of the random noise δu of neighboring vectors separated by Δx (see proof in appendix A, δu here always in units of pixel):

$$AF_F(\Delta x) \equiv AF_{\delta u}(\Delta x) \tag{2.4}$$

with

$$AF_{\delta u}(\Delta x) = \frac{\sum_{x=-\infty}^{+\infty} \delta u(x)\,\delta u(x+\Delta x)}{\sum_{x=-\infty}^{+\infty} \delta u(x)\,\delta u(x)} \quad \text{or} \quad AF_{\delta u}(\Delta x) = \frac{\int \delta u(x)\,\delta u(x+\Delta x)\,dx}{\int \delta u(x)\,\delta u(x)\,dx} \tag{2.5}$$

Function $AF_{\delta u}(\Delta x)$ can be determined easily with synthetic images. This provides one possibility to deduce the underlying filter function F(x) as shown later.

2.3 PIV Spatial Resolution

The spatial resolution of PIV quantifies the ability to resolve small-scale velocity fluctuations. Historically, in optics, the spatial resolution has often been defined, for example, when two dark or bright lines are still distinguishable by some contrast level, specifying e.g. 50 lines-pairs per mm for the resolution of a photo-cathode tube or an image intensifier, where the two dark lines still have a contrast level of 10% or 20% relative to the bright intermediate line. This is a common specification, for example, by manufacturer of image intensifiers. Such tests are often performed using the USAF resolution test chart conforming to the MIL-STD-150A standard.

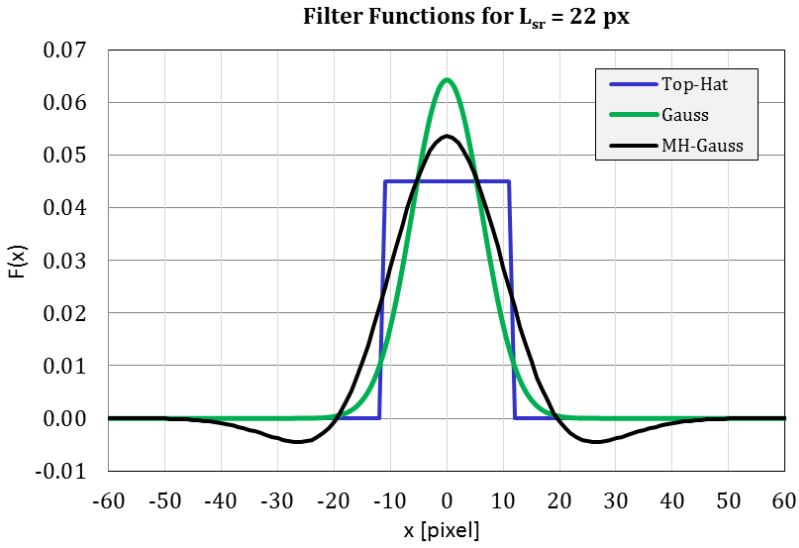

Figure 2.5. Filter functions with L_{TH} = 22 px, σ_G = 22 / sqrt(4π), σ_{MHG} = 12.4 px and b_{MHG} = 0.4.

Reference to some spatial resolution is often vague and unprecise. For example, a common quote in the PIV literature is 'with an interrogation window size of 32x32 pixel the spatial resolution of a PIV algorithm is 32 pixels'. First, the spatial resolution more accurately has the dimension of the *inverse* of the spatial dimension (1/pixel or 1/mm), and secondly, as we see later for state-of-the-art PIV algorithms, the actual spatial resolution may differ substantially from the interrogation window size. In any case, there is a need for a precise definition.

There are many possible definitions of such a spatial resolution. A common procedure is to use the cutoff-frequency in the frequency response curve ('MTF', see section 2.5) at some – rather arbitrary – threshold like 50%, 71% (-3dB) or 80/90% (3rd PIV Challenge, Stanislas et al. 2005). Another option is the width of the response to a step function in velocity (Elsinga and Westerweel 2011; *step response width*: Kähler et al. 2012).

In the following, we will not specify values for the spatial resolution itself, but for its inverse 'filter length' L_{sr} in the context of a linear filter model of PIV. A higher/lower spatial resolution will then correspond to a smaller/larger value of L_{sr}.

In a linear filter model, the complete performance of PIV processing is determined by the width and shape of the filter function. Reducing this functional form to a single number 'spatial resolution' will always disregard the complete, possibly non-linear, behavior of the PIV algorithm. But, as shown later, it serves as a good indicator for the wavelength response of PIV and can help to simplify, for example, the computation of PIV uncertainties allowing easy uncertainty propagation (see chapter 3 and 4).

A good choice is to base a definition of a spatial resolution directly on the filter function. The definition introduced first is more general based on the sum of the autocorrelation function of the error statistics without any reference to a filter function, but such a definition is easily linked to the filter function:

Definition: The (1D-)spatial resolution represented by its spatial length L_{sr} is given by the sum of the autocorrelation coefficients of the error between neighboring vectors:

$$L_{sr} = \int_{-\infty}^{+\infty} AF_{\delta x}(\Delta x)\ d(\Delta x) \tag{2.6}$$

Equivalent to: A PIV algorithm based on a linear spatial filter function F(x) has a spatial resolution with a filter length of:

$$L_{sr} = 1/\int_{-\infty}^{+\infty} F(x)^2\,dx = 1/\sum_i F(x_i)^2 \tag{2.7}$$

The proof is given in appendix B. Such a definition of the spatial resolution has some favorable properties:

First of all, as shown in Table 2.1, for a top-hat filter of length L, it can be easily verified that L_{sr} = L as one would expect. For a Gaussian curve, the equivalent filter length or filter kernel size is given by $L_{sr} = \sigma\sqrt{4\pi}$.

Secondly, such a definition describes the basic error propagation when averaging the displacement information within an interrogation window:

Property: A PIV algorithm based on a linear spatial filter has a 2D spatial resolution of L_{sr} x L_{sr} if it reduces the random noise of pixel-wise contribution of displacement information by a factor of L_{sr}.

The proof is given in appendix C. The random noise σ of noisy values u_i, i=1-n, is in the following always defined as the standard deviation $\sigma = (\Sigma(u_i-u_{i\_true})^2/n)^{1/2}$.

Such a definition of a spatial resolution in eqn. (2.7) has been used before to enable a fair comparison between different interrogation window sizes and

weighting functions (e.g. square or Gaussian shaped, see also Nogueira et al. 1999, 2001) by Astarita (2007, eqn. 7) named *equivalent noise bandwidth*, "the spatial frequency bandwidth of a rectangle filter with the same peak power gain that would accumulate the same noise power" (Harris 1978). As shown later, the actual *effective* filter function of some PIV processing scheme may deviate substantially from the weighting function of the interrogation window used for cross-correlation.

For uncertainty propagation involving spatial neighborhood functions – e.g. vorticity or divergence – it is required to know the functional form of the autocorrelation function $AF_{\delta u}$ (see chapter 4). For vorticity, the knowledge of a few values of $AF_{\delta u}$ at discrete neighbor vector locations is sufficient. For more complicated uncertainty propagation, e.g. for spatial averaging, a full explicit derivation becomes unpractical and using a single-number spatial resolution enables the computation of uncertainties of derived quantities more easily and with sufficient accuracy.

The above definition of a spatial resolution is similar, apart from a factor of two, to the integral length scale and integral time scale (Hinze 1975, Swamy and Gowda 1979, O'Neill et al. 2004), which operate not on error fluctuations but on the flow field fluctuations itself. These quantities have been found useful for turbulent characterization, providing e.g. the time passing of the largest vortex.

When integrating the autocorrelation factors in eqn. (2.6), one needs to decide where to stop the integration, for example, at the first zero-crossing, which may cut-off longer range correlation fluctuations, or at the first minimum encountered. For unrestricted integration, the spatial resolution can become more noisy than necessary by collecting noisy correlation coefficients in the tail of the function. For the case considered here and for most PIV settings, the autocorrelation of the noise decays quite quickly and behaves well in comparison to turbulent flow fluctuations correlating over longer ranges, where it is not easy to decide the integration length (O'Neill et al. 2004). In the following, the integration is stopped at the first zero-crossing.

2.4 Spatial Resolution and Noise

The autocorrelation function $AF_{\delta u}(\Delta x)$ can be determined easily for any PIV processing scheme for a specific set of user selected processing parameters by generating synthetic images with a constant known displacement and analyzing the computed errors (Table 2.2). The PIV-software Davis 8 (LaVision GmbH) is used in the following for processing. As shown in Figure 2.6 the error map for IW=32x32 px processing has larger spatial wavelengths than for 16x16 processing, and lower absolute errors as expected. Systematic errors are below 0.002 pixel.

From the combination of u/v-component in x/y-direction, four values of L_{sr} could be computed. Here L_{sr} is computed from the error of the u-component in x- and y-direction and then averaged. The autocorrelation function of the u-error computed from the entire error field is shown in Figure 2.7 for 32x32 and 75% overlap together with a MHG-function of the same filter length with best-fit parameter

b=0.31 accommodating the undershoots at about ±35 pixel. Clearly, a triangle-shaped autocorrelation function of a top-hat filter or a Gaussian function would not fit as well.

Table 2.2: Random error levels and the derived spatial resolution (eqn. (2.6)) as the sum of the normalized spatial autocorrelation $AF_{\delta u}(\Delta x)$. 4 passes, Gaussian weighted IWs.

PIV parameter		Random noise σ [px]	Spatial resolution L_{sr} [px]	Product σ x L_{sr}
IW-size	Overlap			
16x16	75%	0.146	15.8	2.30
24x24	75%	0.098	22.9	2.25
32x32	0%	0.050	47.1	2.35
	25%	0.052	41.6	2.16
	50%	0.060	38.4	2.30
	75%	0.076	29.7	2.26
	87%	0.084	25.8	2.17
48x48	75%	0.050	42.6	2.13
64x64	75%	0.038	57.3	2.18

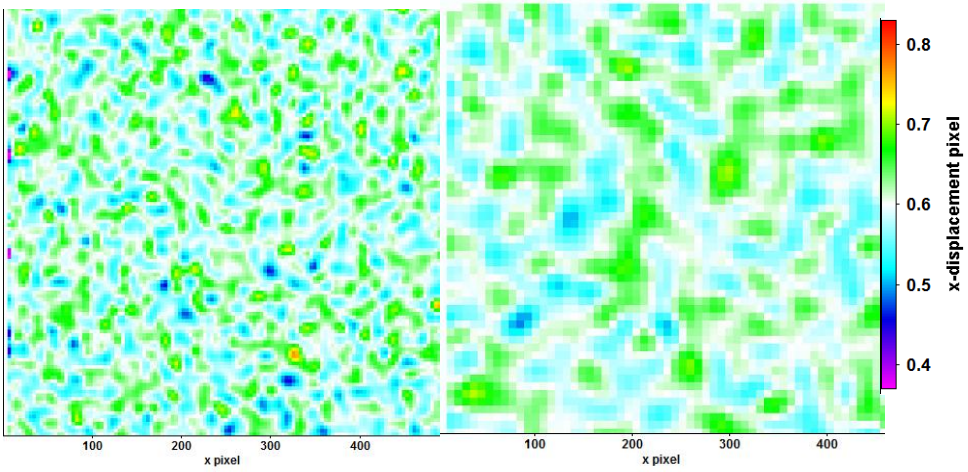

Figure 2.6. Synthetic image with constant (u,v) = (0.6,0.3) px, 10% out-of-plane motion, N_{ppp} = 0.1, d_p = 2.5 px, no extra noise added, Gaussian weighted windows, 4 passes, 75% overlap, showing u-displacement for IW=16x16 px (left) and 32x32 (right).

There is some variation in the functional form of the 2D-autocorrelation function, for example, as a function of fractional displacement as shown in Figure 2.8 as little squares for discrete neighbor vector locations with a grid spacing of 8 pixels. Derived spatial resolutions may vary by 1-2 pixels, but overall the functional form

with undershoots remains. Note that small correlation values further out have little impact on the accuracy of uncertainty quantification and propagation.

As shown in Table 2.2 and Figure 2.9, the product of the random noise and filter length remains almost constant for all interrogation window sizes and overlaps.

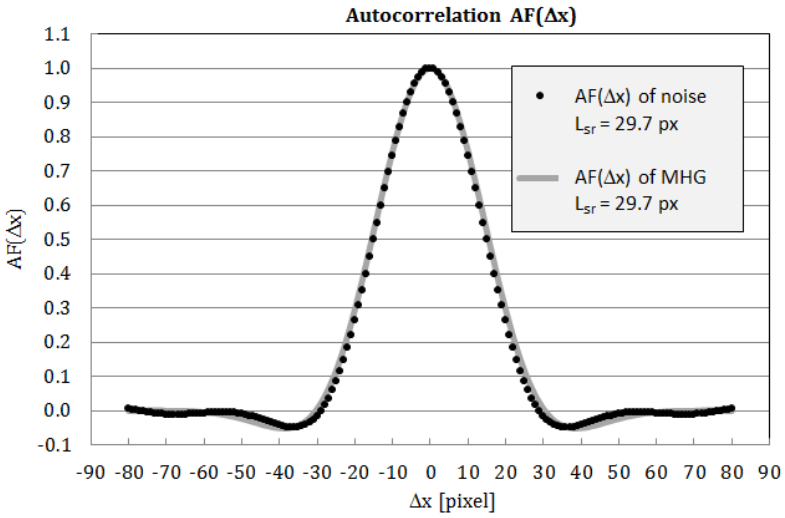

Figure 2.7. Spatial autocorrelation function of random noise δu for IW=32x32, 75% overlap, 4 passes, averaged in x- and y-direction and compared to AF_F from Mexican-Hat-Gauss-function (σ_G=12.4, b=0.31) with same spatial resolution.

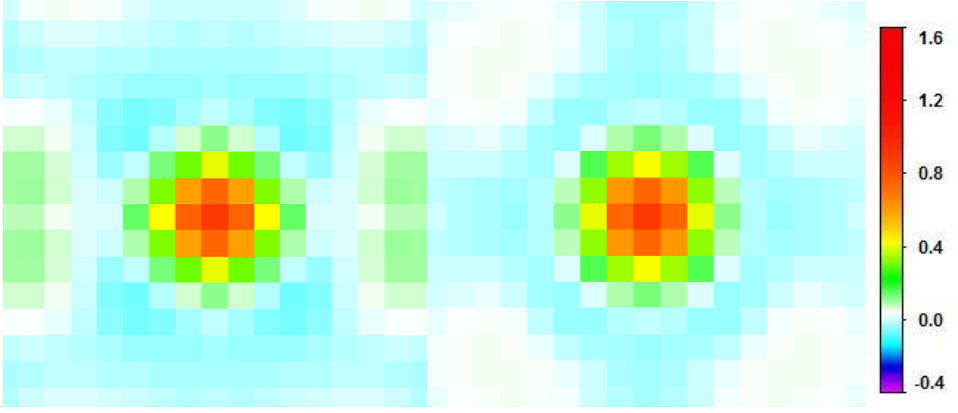

Figure 2.8. 2D-AF with (u,v)=(0.2,0.8) px (left) and (u,v)=(0.2,1.0) px (right).

Universal rule: On a specific data set, varying PIV processing parameters, the product of PIV filter length as computed from $AF_{\delta u}(\Delta x)$ and random noise σ stays constant:

$$L_{sr}(\delta u) \bullet \sigma \sim \text{const} \qquad (2.8)$$

Obviously, this is because e.g. doubling the interrogation window size with 4x more pixel and information content reduces the random noise by $\sqrt{4}=2$. The same argument applies to spatial smoothing of vector fields. Applying a smoothing filter, which doubles the filter length in both directions, reduces the random noise by a factor of 2. On the other hand, systematic errors due to amplitude reduction of small-scale flow fluctuations (*truncation errors*) may increase.

PIV is always a compromise between resolving small-scale flow structures requiring small interrogation windows and reducing the random noise using large interrogation windows. In chapter 5 a non-isotropic adaptive filtering technique is presented which locally optimizes the filter kernel size and shape according to the local noise (uncertainty) taking local flow gradients into account.

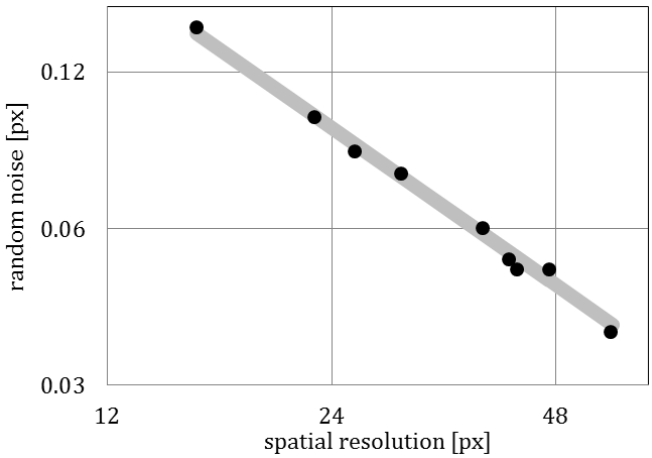

Figure 2.9. Double logarithmic plot of random noise versus spatial resolution from Table 2.2 with a fitted grey line of slope -1.

In Davis, an extensive table of spatial autocorrelation coefficients of the noise has been stored for all combinations of PIV parameters. Some simplifications have been made, e.g. assuming that the PIV algorithm has sufficiently converged, i.e. not taking single-pass processing into account. This internal table consists of autocorrelation coefficient for the close vector neighborhood together with the parameters of an approximated functional form (usually Gaussian or MHG) and the reduction to a single-number spatial resolution (filter length). This is needed for proper uncertainty propagation as described in chapter 4.

2.5 Spectral Response (MTF)

2.5.1 Response to displacement sine waves

Extensive work has been done to evaluate the response and stability of PIV algorithms to different spatial displacement wavelengths (Nogueira et al. 1999, 2001, 2005a, 2005b; Lecordier and Trinité 2003; Scarano 2004a; Astarita 2006; Schrijer and Scarano 2008; among others).

Almost in every PIV Challenge (Stanislas et al. 2003, 2005, 2008; Kähler et al. 2016) synthetic images have been provided with sine-waves of different amplitude and wavelengths or images with a particular spectral content. In all cases, the goal has been to verify the ability to resolve small-scale fluctuations relative to the size of the interrogation window – i.e. the effective spatial resolution – in conjunction with error estimates and stability. Advanced iterative predictor-corrector schemes may become unstable e.g. for wavelengths equal to 2/3rd of the interrogation window size (e.g. Nogueira et al. 1999; Scarano 2004a).

State-of-the art PIV algorithms use special weighting functions (e.g. Nogueira et al. 1999, 2001) or appropriate vector field filtering of the predictor/corrector field in iterative multi-pass processing (e.g. Astarita 2007; Schrijer and Scarano 2008) to suppress instabilities while ideally resolving as much as possible small-scale features equal or smaller than the interrogation window size. At the same time the random error should be minimized, too, according to the general linear relationship between spatial resolution and precision.

In the following, the response to sine-waves of different wavelengths either as shear $v(x)=A_0\sin(2\pi x/\lambda)$ or compression $u(x)=A_0\sin(2\pi x/\lambda)$ is investigated by generating synthetic images with small amplitude A_0 of e.g. 1 pixel. Measured is the amplitude reduction $R_A(\lambda)$ as a function of wavelength (or frequency $f=1/\lambda$):

$$R_A(\lambda) = \frac{A_{meas}}{A_0} \tag{2.9}$$

Assuming that PIV is a linear spatial filter according to eqn. (2.1), the amplitude reduction $R_A(\lambda)$ is, of course, given by the Fourier transform of filter function F:

$$R_A(f) = \int_{-\infty}^{+\infty} F(x) e^{-i2\pi fx} dx = \int_{-\infty}^{+\infty} F(x)\cos(2\pi fx) dx \tag{2.10}$$

Since all functions are real and even, the Fourier transform reduces to the discrete cosine transform (DCT).

Another useful quantity is the *power spectral density*, which is defined by

$$PSD(f) = R_A^2(f) \tag{2.11}$$

The loop between $F(x)\rightarrow AF_F(\Delta x)$ and $F(x)\rightarrow R_A(\lambda)\rightarrow PSD(f)$ (see Figure 2.10) can be closed by invoking the Wiener–Khinchin theorem (Wiener 1930; Khinchin 1934), which states that the power spectral density is the Fourier transform of the *unnormalized* autocorrelation function:

$$\mathrm{FFT}\left(\mathrm{AF}(\Delta x)\right) = \mathrm{PSD}(f) \tag{2.12}$$

A simplified proof is given in appendix D.

2.5.2 Response to displacement step function

Finally, the response of the PIV algorithm to a step function in the displacement is investigated, along the lines of Elsinga and Westerweel (2011) and Kähler et al. (2012).

Let's denote u(x) as the displacement response. According to the basic filter eqn. (2.1), the response u(x) is given by:

$$u(x) = \int_{-\infty}^{x} F(x')dx' \tag{2.13}$$

equivalent to

$$\frac{\partial u(x)}{\partial x} = F(x) - F(-\infty) = F(x) \tag{2.14}$$

Therefore the derivative of u(x) provides directly the filter function F(x) (named *point-spread-function* (PSF) by Elsinga and Westerweel 2011), requiring accurate data with sufficient noise suppression.

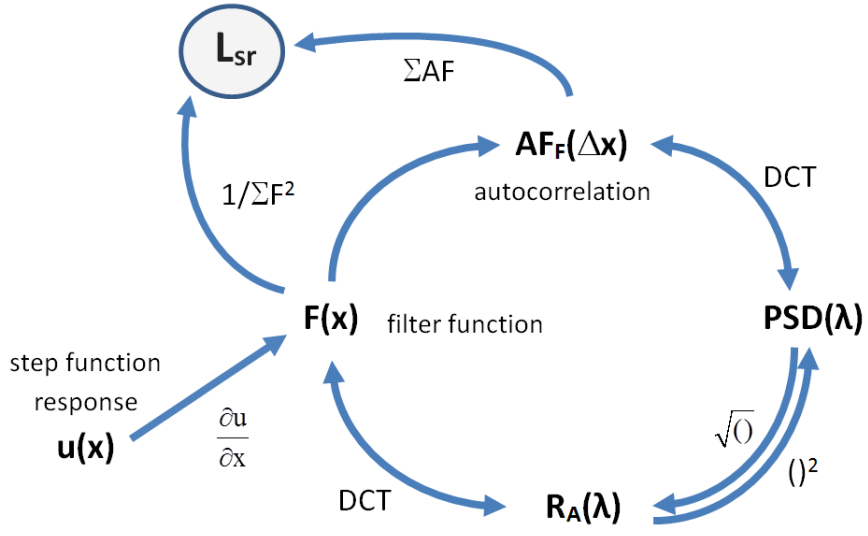

Figure 2.10. Relationship between filter function, spatial resolution, autocorrelation and response functions.

The complete picture is shown in Figure 2.10 pointing to different ways of calculating the underlying filter function F(x) and a corresponding single-number spatial resolution or filter length.

2.6 Results

The above derivations have been tested using Davis 8 PIV software. First, using synthetic images with sine-waves the wavelength response function $R_A(\lambda)$ and autocorrelation function $AF_{\delta u}(\Delta x)$ has been determined, from which the filter function F(x) is calculated. Finally, the response to a step function in displacement is investigated.

2.6.1 Response to displacement sine waves

For determining the wavelength response function $R_A(\lambda)$, synthetic images with a shear flow $u = \sin(2\pi y / \lambda)$ have been generated (seeding density 0.2 ppp, particle diameter 2.5 px, intensity 200 counts, sine wave amplitude 1.0 px) for wavelengths up to 200 px in increments of 1.37 px to avoid aliasing effects.

To start with, the simplest kind of PIV processing has been tested with a single-pass and square interrogation window of 32x32 pixel and 75% overlap (e.g. Figure 2.11 with λ=64 px).

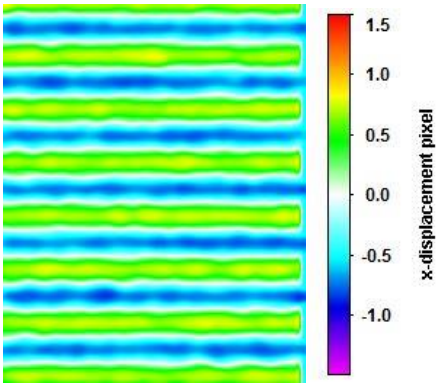

Figure 2.11. Example of measured shear flow for u = sin(2πy/64).

The measured sine wave amplitude ratio $R_A(\lambda) = A_{meas}$ / 1px (Figure 2.12 top) shows the typical form of a sinc-function as the Fourier transform of a top-hat filter function. The negative response at about 2/3rd of the IW-size has been noticed before (Nogueira et al. 1999, Scarano 2004a) together with remedies how to avoid numerical instabilities in multi-pass PIV processing (e.g. Schrijer and Scarano 2008). One should note that even at λ=200 px the amplitude is still reduced by 10%.

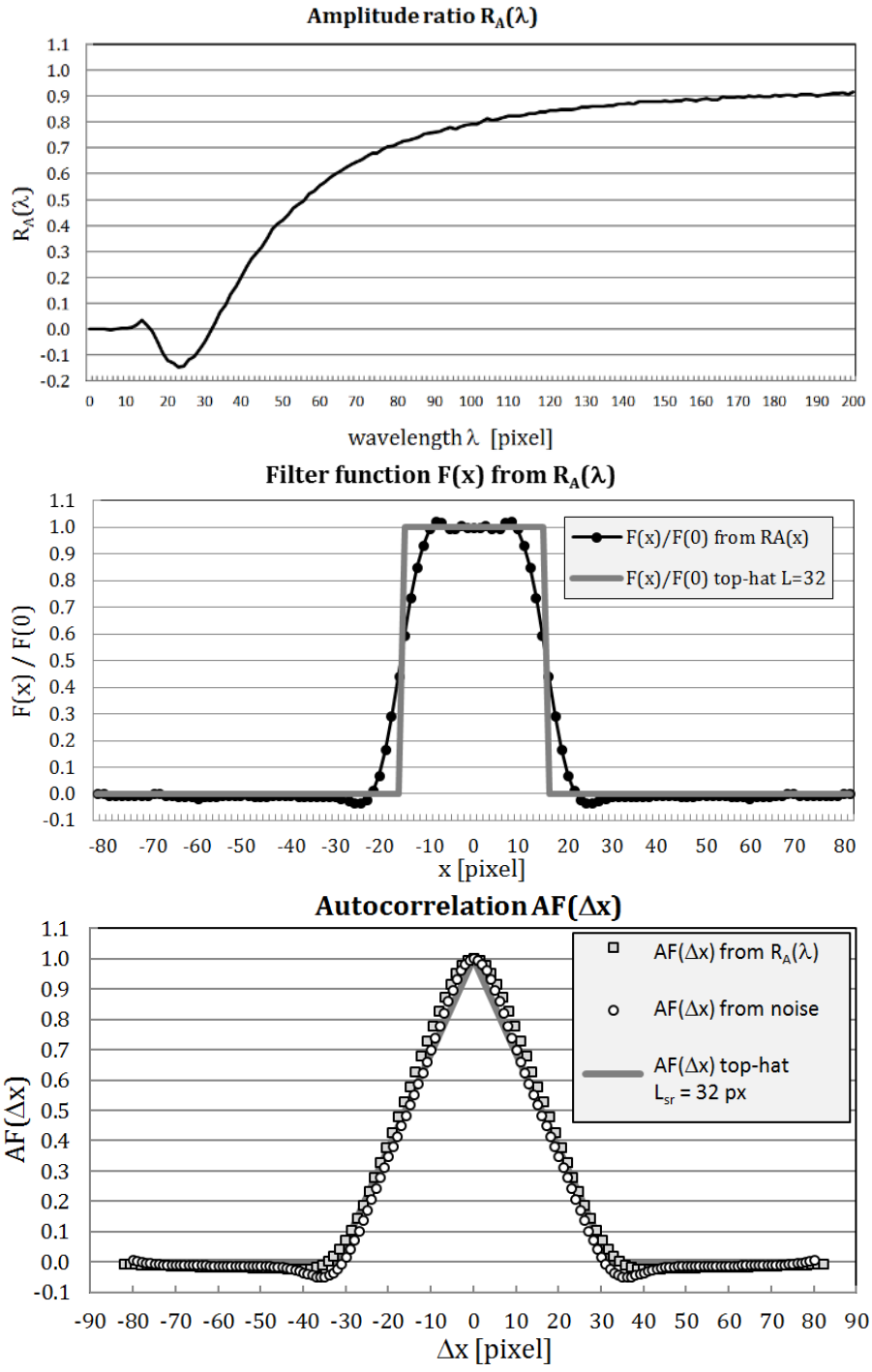

Figure 2.12. Amplitude ratio, derived filter function, and autocorrelation function as a function of displacement wavelengths. Result from single-pass square IW.

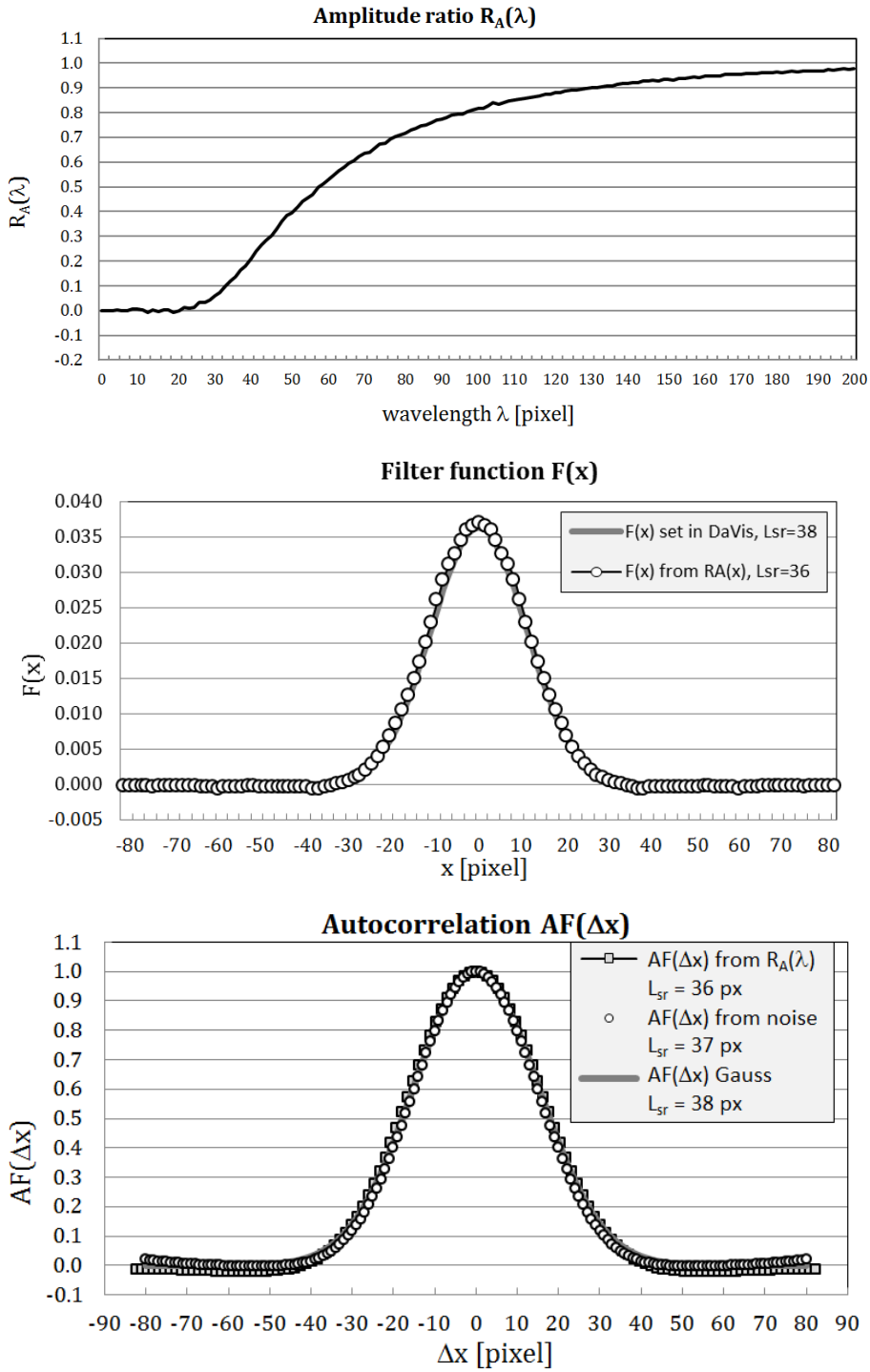

Figure 2.13. Same as Figure 2.12 for single-pass Gaussian IW.

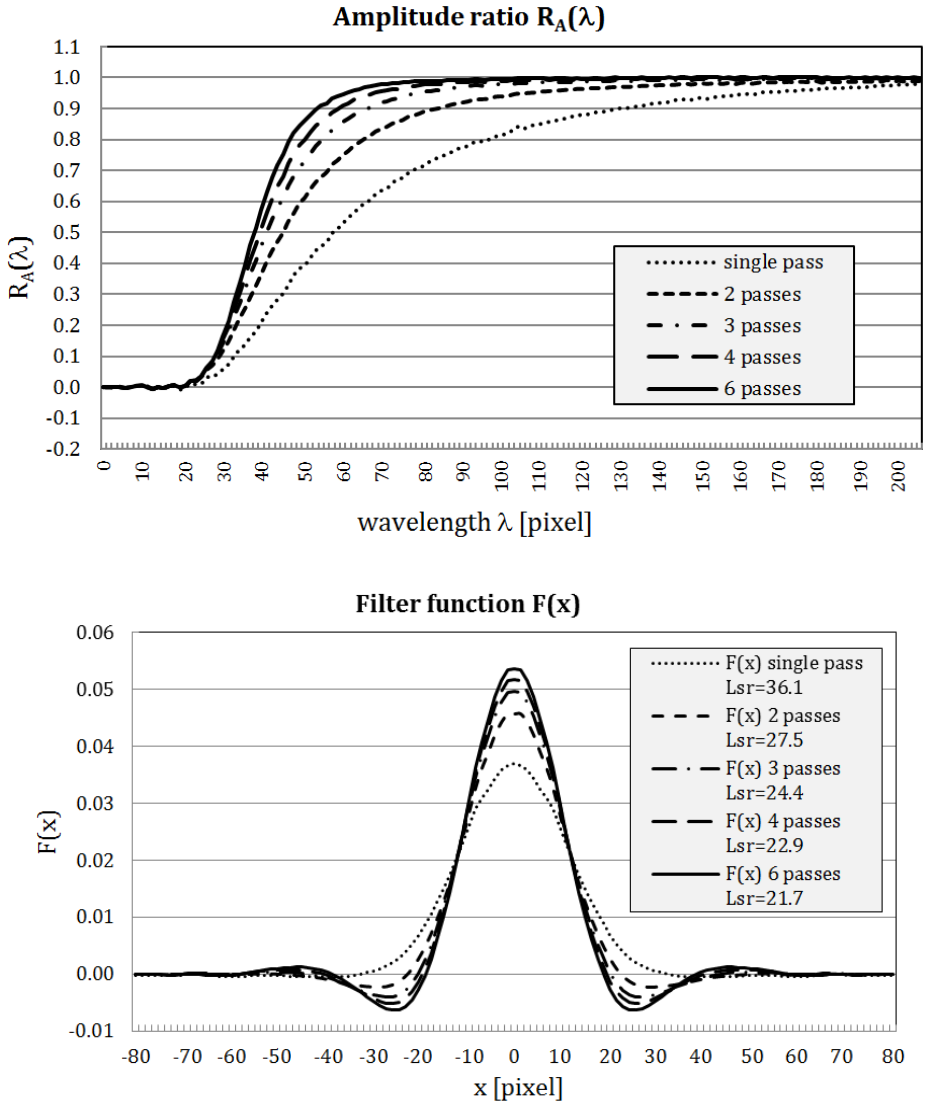

Figure 2.14. Wavelength response functions for 1-6 passes (top) and corresponding filter functions (bottom) using Gaussian IW.

Transforming $R_A(\lambda)$ back to F(x) yields roughly the initial top-hat function (square interrogation window) slightly smoothed by border effects and extended particle image sizes (Figure 2.12 middle). At the bottom of Figure 2.12 is shown the autocorrelation function as computed from $R_A(\lambda)$ via PSD(λ) together with the auto-correlation function of the noise (eqn. (2.5)). Both functions agree quite well and with a triangle-shaped autocorrelation function of a top-hat filter with L=32 px.

Next, a single-pass PIV processing has been done with a Gaussian weighted window (Figure 2.13). Internally in Davis, the interrogation windows are weighted with a Gaussian function equivalent to a filter length of 38 pixel (for historical reasons to make it similar to square IWs in multi-pass processing). The deduced filter function is close to a Gaussian function with L_{sr}=36 px. The noise autocorrelation function is also Gaussian shaped with a derived filter length of 37 px.

The situation becomes more complicated for iterative multi-pass processing. The wavelength response function gets steeper adjusting better to smaller wavelengths with correspondingly higher spatial resolution (Figure 2.14 top).

The corresponding filter function evolves into a mixture of Gaussian and Mexican-hat function with L_{sr} decreasing from 36 for single-pass to 22 pixel for 6 passes (Figure 2.14 bottom). Actually, for an infinite steep R_A-curve, the filter function would not be exactly a Mexican-hat function, but would exhibit multiple ringing of a sinc-function which is the Fourier transform of a step function. Nevertheless, the approximation as a MHG-function captures the functional shape of the filter function for our cases very well.

Increasing the number of iterations, the spatial resolution as computed from the noise autocorrelation is decreasing from 37 pixel to only 30 pixel and then deviates from the spatial resolution derived from R_A (Table 2.3**).** While the product of noise and L_{sr} derived from noise δu stays constant at about 2.1-2.2, the product of noise and L_{sr} derived from R_A decreases down to 1.7, which is an improvement of 20%. Through multi-pass processing, the PIV algorithm is able to resolve smaller scales while keeping the noise level lower than expected from the increase in spatial resolution.

Table 2.3. Noise and spatial resolution for 1-6 passes.

PIV parameter		Random Noise	Noise δu spatial resolution	Product	R_A-spatial resolution	Product
IW-size Overlap	Passes	σ [px]	L_{sr} [px]	σ x L_{sr} (δu)	L_{sr} [px]	σ x L_{sr} (R_A)
32x32 75%	1	0.057	37.0	2.10	36.1	2.06
	2	0.064	32.2	2.06	27.5	1.76
	3	0.070	30.7	2.15	24.2	1.69
	4	0.076	29.7	2.26	22.9	1.74
	6	0.077	29.5	2.27	21.7	1.67

Unfortunately, PIV processing in Davis can no longer be quantified by a single filter function, but needs two functions, one for the spatial autocorrelation of the noise between neighboring vectors (needed for uncertainty propagation), and one for the wavelength response. Both functions are of MHG-type with around b=0.3-0.4 (30-40%) Mexican-hat contribution. Table 2-4 shows all values for 4-pass PIV for a

range of interrogation window sizes and overlap. Clearly, 0% or 25% overlap is not recommended as the spatial resolution from R_A is worse, not being able to sample small-scale fluctuations sufficiently. In general, 3-4 passes, 75% overlap and Gaussian weighted windows provide an optimum between processing time and achievable spatial resolution while keeping the random noise floor low.

Table 2.4. Table 2.2 complete with added columns for the spatial resolution derived from RA and the product with the noise.

PIV parameter 4 passes		Random noise	Noise δu spatial resolution	Product	R_A-spatial resolution	Product
IW-size	Overlap	σ [px]	L_{sr} [px]	σ x L_{sr} (δu)	L_{sr} [px]	σ x L_{sr} (R_A)
16x16	75%	0.146	15.8	2.30	12.2	1.78
24x24	75%	0.098	22.9	2.25	17.5	1.67
32x32	0%	0.050	47.1	2.35	59.3	2.97
	25%	0.052	41.6	2.16	44.5	2.31
	50%	0.060	38.4	2.30	29.8	1.76
	75%	0.076	29.7	2.26	22.9	1.74
	87%	0.084	25.8	2.17	20.8	1.75
48x48	75%	0.050	42.6	2.13	33.9	1.65
64x64	75%	0.038	57.3	2.18	44.6	1.69

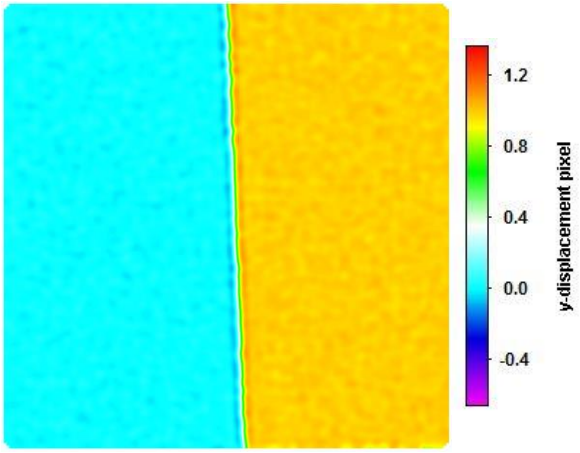

Figure 2.15. Slightly oblique step function in v-component, v=0 (left) and v=1 px (right).

2.6.2 Response to displacement step function

A single synthetic image has been generated with v=0 pixel on the left, and 1 pixel on the right (Figure 2.15). It is slightly tilted to avoid aliasing effects, i.e. one is measuring the displacements for all positions of the edge within the interrogation window. In a similar way, Elsinga and Westerweel (2011) used a series of synthetic images with the step position shifted in x-position and then adding the displacement profiles of all images. Processing is done in the following way:

1. Extract v-component as a scalar field, same size as original image (with bicubic interpolation between vector positions)
2. Rotate the scalar field back so that the edge is vertical again
3. Take a vertically-averaged x-profile of v
4. Compute filter function as the derivative of the displacement function

This is shown in Figure 2.16 together with the derived filter function in Figure 2.17. For comparison, the displacement function from a top-hat, Gaussian and MHG-function of the same spatial resolution is displayed as well. The MHG-curve fits best with the same spatial resolution of about 22.7 px as in the previous section using R_A.

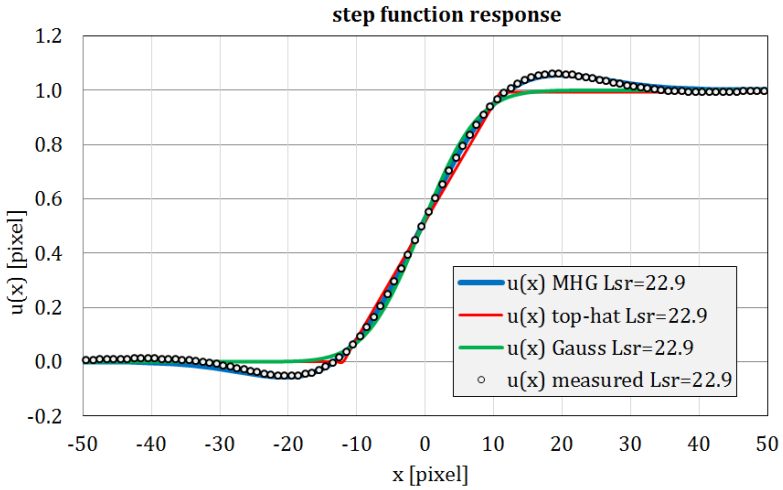

Figure 2.16. Step function response, measured displacement function together with top-hat, Gaussian and MHG-function (b=0.385) of same spatial resolution. MHG follows closely the measured data.

The under- and overshoots in the displacement curve has also been noticed by Elsinga and Westerweel using a different PIV software from TU-Delft. The authors propose a definition of a spatial resolution when two features are no longer separable, in this context by two step functions. They conclude that the spatial resolution defined this way is the same as the interrogation window size plus 1 pixel, probably owing to the particular processing details of their predictor-corrector

scheme and using square interrogation windows. With Gaussian weighted windows such a condition of features being separable is not so clear, rather a smooth transition of detectability is expected, again with the question where to set a rather arbitrary threshold.

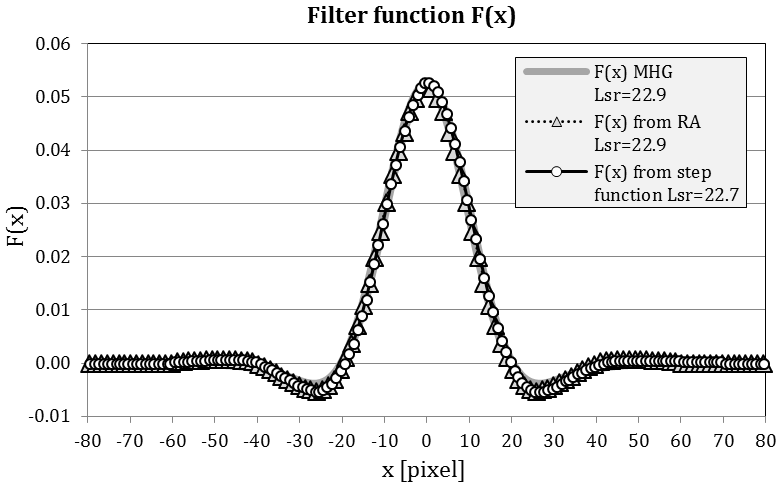

Figure 2.17. Corresponding filter function together with filter function derived from R_A and MHG-function (b=0.385) of same spatial resolution.

Kähler et al. (2012) did not observe overshoots, only a straight line in the displacement, probably using only a single pass correlation with square interrogation windows as is visible in the filter function ('velocity gradient') in their Figure 4 bottom. They define a step response width (SRW) as the width needed for the displacement to go from one displacement level to the other.

This agrees with our definition of L_{sr} when using top-hat filter functions, but, again, becomes fuzzy when quantifying smoother curves. They also observe the rounding-off of the top-hat filter function, respectively step function response for single-pixel ensemble correlation, due to the finite particle image size (our Figure 2.12 middle).

2.7 Summary

PIV processing is viewed as a black box without going into the details of processing parameters and algorithms. The input is given by the experimental setup, a wide range of error sources as discussed in the next chapter, PIV processing parameter and the actual recorded images. The PIV processing scheme produces an output vector field with some intrinsic properties. In most cases, it can be viewed as a continuous smooth velocity field with an appropriate recipe for vector interpolation, in case the data is given as discrete vectors on a regular grid.

Together with the actual velocity data, the vector field has some important associated properties, which are not readily visible:

- Local uncertainty of the velocity field components
- Autocorrelation coefficients of noise: spatial, inter-component and temporal (for time-resolved PIV)
- Response function to velocity fluctuations of different spatial wavelengths (and temporal for time-resolved PIV)

The first two points are relevant for PIV uncertainty quantification (chapter 3) and uncertainty propagation (chapter 4).

The performance of most PIV algorithms can be closely approximated by a linear spatial filtering model. The shape and width of the spatial filter function determines the wavelength response function and the response to a step function in displacement. The corresponding mathematical relationships are derived and a statistically motivated definition of a *spatial resolution* is provided which can easily be derived using synthetic images. The filter function itself can be deduced as well. It is shown that state-of-the-art PIV algorithms like Davis behave closely according to a Gaussian filter function with some Mexican-hat contributions, one function for the noise autocorrelation and another one with higher spatial resolution for the wavelength response function.

For a given PIV interrogation window size, shape and overlap, the resulting functional shape of the filter function or wavelength response function can vary significantly depending on algorithmic details, number of iterations and convergence behavior. For PIV publications, it is recommended to quote the (possible locally varying) effective spatial resolution together with the uncertainty bands of velocity and derived quantities.

3

PIV Uncertainty Quantification

Section 3.3 has been published in Wieneke (2015) PIV uncertainty quantification from correlation statistics, Meas Sci Technol 26(7).

PIV as a measurement technique has been used for more than 30 years and extensive work has been undertaken to quantify different error sources. A large part of the attention has been given to the basic cross-correlation algorithm itself to extract the displacement information in a most accurate and precise way. For this purpose, often synthetic images have been generated simulating known error sources. The known ground truth is then compared to the computed displacement field. Unfortunately, such studies usually underestimate the error level present in real experiments. Another possibility is the comparison of experimental PIV data with velocity data from another measurement system like hot-wire or LDA hopefully closer to ground truth, as recently done, for example, by Neal et al. (2015) in the context of validating uncertainty quantification methods.

Previously, it has been stated that for typical experimental conditions the displacement errors are about 0.05 to 0.2 pixel, recent effort in the last three years has been undertaken to specify the uncertainty of each computed displacement vector in a more quantitative way. Such uncertainties may vary locally depending on seeding density, out-of-plane motion, flow gradients and other factors.

Section 3.1 covers briefly the main error sources of PIV with the focus on how to avoid them experimentally and on the possibility to quantify them by some uncertainty quantification (UQ) method. In section 3.2, some simple, but quite useful, practical ways of estimating PIV errors are described together with more advanced methods quantifying errors under special conditions, methods to optimize experimental and processing parameters and, finally, full UQ-methods trying to quantify the uncertainty of every computed vector. An uncertainty quantification (UQ) method based on correlation statistics is described in section 3.3. Meanwhile, two studies exist comparing some of the available uncertainty methods (Sciacchitano et al. 2015; Boomsma et al. 2016).

3.1 PIV Error Sources

There is a wide range of possible error sources in PIV measurements (see Figure 3.1) as investigated by many researchers together with recommendations for optimal experimental setups (e.g. Adrian and Westerweel 2011; Raffel et al. 2007; among others). Avoiding errors in the first place should be the primary goal for any experimenter.

A selection of error sources is investigated here divided into two groups based on the possibility of quantifying the error by some UQ-method. While all error sources are somehow encoded in the recorded images as erroneous particle positions, optical distortions and other types of image noise, some mostly systematic errors like timing and synchronization offsets and jitters of the involved hardware components (cameras, laser, etc.) are hidden and can not be extracted and quantified by analyzing the recorded images. Here it is even more important to check and optimize the experimental setup and conditions beforehand.

Other error sources are factors visible in the recorded images like particle image size, seeding density, camera noise, laser speckle effects together with

properties of the computed velocity field, which, ideally, can be quantified by UQ-methods.

Accurate perspective calibration is an essential prerequisite for Stereo-PIV and incorporates a few distinct possible error sources. The misalignment between actual light sheet plane and the supposed position of the light sheet as deduced from the initial calibration can be corrected by a method termed 'Stereo-PIV Self-Calibration' (section 6.2), while, for example, inaccurately manufactured calibration plates and unaccounted-for optical distortions remain invisible in the images, introducing mostly systematic bias errors.

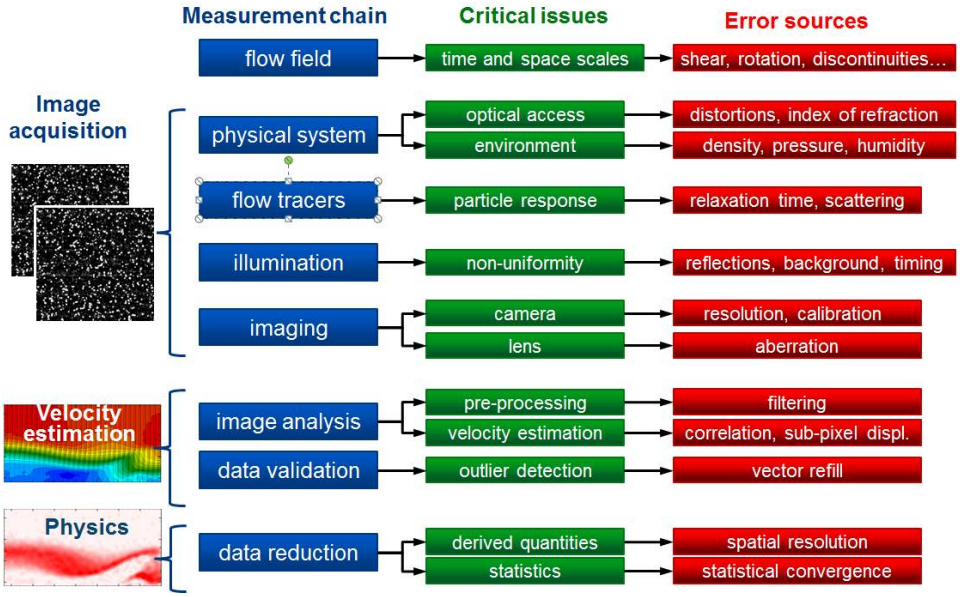

Figure 3.1. Overwiew of PIV error sources (courtesy of A. Sciacchitano, TU-Delft).

Errors are split into random (precision) and systematic bias (accuracy) parts, where systematic errors are usually harder to quantify. Following the suggestion of Coleman and Steele (2009), known systematic errors should be corrected right away as an integral part of the processing scheme and not unnecessarily be kept and propagated into uncertainty estimations. Therefore, in general, UQ-methods mostly quantify the random error components.

There are even systematic error sources with *unknown bias* for a particular experiment, but *known standard deviation* of the bias magnitude. For example, it may be known that the calibration plates provided by the manufacturer have a certain tolerance of global magnification scale (average distance between marks) leading to an unknown systematic scaling error in a particular experiment. In principle, such errors can be propagated by appropriate, quite complicated, UQ-procedures (Wilson and Smith 2013a, 2013b). Instead, if possible, it is recommended to increase the accuracy on the experimental side and to verify that

the remaining systematic (and random) errors are insignificant compared to typical levels from other PIV error sources.

The following list shows some important sources of PIV errors for planar 2D-PIV and Stereo-PIV with suggestions for optimization and reduction of error levels. Hidden factors not readily visible in the images are listed first:

- Timing and synchronization errors
- 2D-PIV perspective errors
- Stereo-PIV:
    - Inaccurate calibration targets
    - Insufficient calibration model
    - Errors due to right/left camera viewing different interrogation volumes
    - Llight sheet misalignment
- Particle response and lag

Some error sources can ideally be estimated from the recorded images and used in UQ-methods:

- Particle image size and shape, laser speckle effects
- Camera noise
- Seeding density and inhomogeneity
- Illumination intensity variations
- Spatial velocity gradients
- Brownian particle motion
- Particle out-of-plane motion
- PIV processing scheme

3.1.1 Timing and synchronization errors

Typically, synchronization electronics used for PIV experiments has very low jitter and offset of the order of less than 1 ns, small in comparison to typical time delays between two light pulses. Note also, that the shortest laser pulses of Nd:YAG-lasers have durations of 5-10 ns. For the most demanding double-pulse experiments with e.g. 100-300 ns between laser pulses (either in µPIV or for supersonic flows) the expected error is still less than 1% and less than typical other PIV errors in such experiments.

More critical is the time delay between the trigger to the laser and the time of the actual light output. Especially for long-pulse (100-300 ns) high-repetition-rate Nd:YLF-lasers, there can be quite some variation in the delay of up to 0.5 to 1 µs depending on repetition rate and power setting (Bardet et al. 2013). For double-pulse single- or double-cavity lasers, this problem can be solved by continuously measuring the time of the light output with a photodiode for both light pulses and delaying the trigger signal of one laser electronically for the next pulses (Bardet et al. 2013).

Camera electronics is usually quite reliable and predictable. Activating the exposure of the camera(s) can be done beforehand. Critical is only the time instant and duration of switching between the first and second exposure in the double-frame mode of PIV cameras to make sure that the first and second light pulses are recorded in the first and second exposure. There is some small jitter and duration in this transition of 0.1 to 4 µs depending on the camera model, which limits the shortest possible time between the laser pulses. Activating only one laser pulse, it can be checked easily if the recorded light is fully in the correct frame or e.g. visible partly of fully in the wrong one, requiring some timing adjustments.

3.1.2 2D-PIV perspective errors

When viewing a planar light sheet with a single camera, the 2C- displacement components are always measured perpendicular to the viewing direction possibly deviating substantially from the true in-plane components toward the corners of the field-of-view. A larger working distance or using (expensive) telecentric lenses helps. In general, if this poses a problem, it is recommended to apply Stereo-PIV using a second camera with the added advantage of measuring the out-of-plane component as well.

For lenses with strong optical distortions, e.g. fish-eye lenses, xy-positions for the computed vectors can be corrected by a calibration with a single view of a flat calibration plate with known marker positions at the position of the light sheet.

3.1.3 Stereo-PIV errors

As mentioned before, manufacturing tolerances of the calibration plate can lead to deviations in the magnification scale or coordinate system twisting. Given e.g. 10 µm tolerance relative to a plate size of 100 mm leads to an insignificant error in the in-plane scale. But for the out-of-plane scale and using a two-level plate with 10 µm tolerance relative to e.g. 3 mm, this amounts to 0.3% (0.03 px for 10 px out-of-plane motion) already close but in most cases still smaller than other error sources. The remedy is higher manufacturing quality or measuring actual marker position accurately in 3D beforehand and feeding this information into the calibration procedure. Another possibility is using a full camera pinhole calibration with a single-level plate and multiple (5-10) views at shifted and rotated position – the common procedure in computer vision – instead of a more convenient single-view calibration with a two-level plate, which is typically used together with polynomial calibration function.

Another aspect is whether the chosen calibration model (e.g. polynomial, pinhole, with/without Scheimpflug correction, …) is able to account for all optical distortions. For most experiments even a simple pinhole model with e.g. 6-10 parameters per camera is usually sufficient, as small deviations (e.g. <1-3 pixel) in the vector positions in one camera relative to the supposedly same position in the second camera lead only to small errors in the 3C-reconstruction of the final (u,v,w)-vector. But larger deviations e.g. due to misalignment of light sheet and calibration plane become relevant (Giordano and Astarita 2009).

When viewing through multiple possibly curved interfaces (air – glass – water), even a multi-level polynomial model with dozens of parameters per camera may reach its limit, warranting even higher-order, e.g. piece-wise spline models. See also the extensive work by Belden (2013) incorporating a physical model for the case of changing index of refraction.

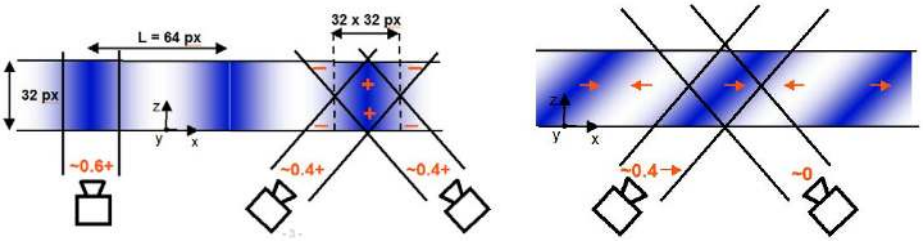

Figure 3.2. Flow with gradient of v in x-direction (left), flow with gradient of u in xz-direction (right). Stereo-PIV: measured non-zero u_1 and $u_2 \approx 0$ leads to small amplitude u- and erroneous w-components (from Wieneke and Taylor 2006).

One rarely mentioned error source in Stereo-PIV is due to both cameras not viewing the same interrogation volume due to the finite thickness of the light sheet (Wieneke and Taylor 2006). Any out-of-plane gradient of the in-plane or out-of-plane velocity components leads to possibly substantial systematic errors in the computed 3C-velocity components, which remain unnoticed in the recorded images (Figure 3.2). One can try to reduce the light sheet thickness in case the out-of-plane velocity component is small enough, or use Tomographic PIV with a slightly thicker light sheet with the added advantage of measuring the full 3x3 strain tensor derived from at least two planes of velocity fields.

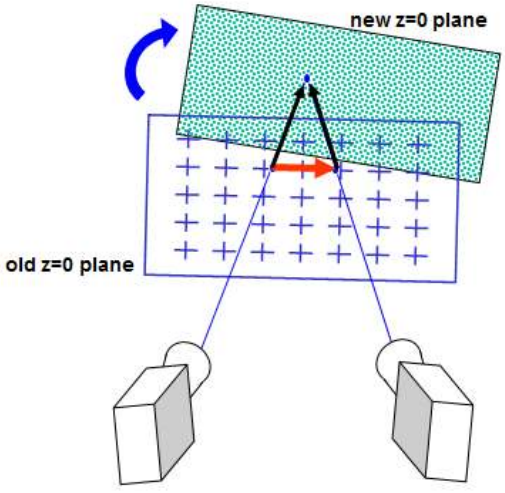

Figure 3.3. Stereo-PIV self-calibration procedure correcting misalignment of laser sheet.

As mentioned before, misalignment of actual light sheet position and where the initial calibration locates the light sheet, leads to deviations in the vector positions in one camera relative to the supposedly same position in the second camera. Thus systematic errors occur when the two 2C-displacements are combined into a 3C-vector (*3C-reconstruction*). Giordano and Astarita (2009) report possible significantly dephased and modulated wavelengths.

An efficient procedure to correct such a misalignment (Figure 3.3) is described in section 6.2**.** It is recommended for every Stereo-PIV measurement, at least to check for any misalignment. Standard UQ-methods usually assume that a misalignment has been corrected without the need of uncertainty propagation of possible (unknown and difficult to estimate) calibration errors. The assessment of errors in calibration mapping functions remains an open question so far.

3.1.4 Particle response and lag

Seeding particles should follow faithfully the flow and fluid element acceleration. For air flow with solid or liquid seeding particles heavier than air, seeding particles must be small enough with a short response time, requiring e.g. diameters of less than 1 µm for high accelerations like shock fronts (see e.g. Melling 1997). The scattering intensity reduces about quadratically with the particle size, so one needs to find some optimal size as large as possible, but small enough for the expected accelerations.

Recently, generators for sub-millimeter-sized Helium-filled soap bubbles (HFSB) have been developed in particular for large-scale volumetric PIV in closed compartments (Kühn et al. 2011) and wind tunnels (Scarano et al. 2015). These neutrally buoyant bubbles follow the flow accurately and scatter orders-of-magnitude more light than micrometer oil droplets. Another problem of vortex cores being devoid of oil droplets due to centrifugal forces can also be avoided with HFSBs with bubbles slightly lighter than air.

For water and other liquids a wide range of neutrally buoyant (plastic) seeding particles with similar density are available.

In general, the topic of appropriate seeding particles should be addressed experimentally, not related to any special issue of PIV processing or uncertainty quantification. Heavy particles may not follow the flow accurately when subjected to strong accelerations, but it is not recommended to try to correct particle paths a-posteriori given the complexity and limitations, in particular, when the particles are not mono-dispersive.

3.1.5 Particle image size and shape, laser speckle effects

In most experiments the particle image size as visible in the recorded images is diffraction limited largely independent of the real particle size, with a size of about two times the F-stop number in µm ($d=2.44\lambda F\#(1+m)$, see e.g. Raffel et al. 2007).

The optimal particle image size is about 2 pixel as noticed by many researchers utilizing synthetic image data (e.g. Prasad et al. 1992, Adrian and Westerweel 2011). Larger particle image sizes lead to additional random errors, while smaller particle image sizes lead to strong systematic bias errors ('peak locking') favoring integer pixel displacements as well as strong random errors. For 2D-PIV this is easily visible in the histogram of the displacements, while for Stereo-PIV or Tomographic PIV it is more hidden. It will show up as aliasing bands when averaging almost laminar and slowly varying flow fields with a turbulence level below about 0.3 pixel.

Errors associated with peak-locking adversely affect the estimation of turbulent statistics (Christensen 2004) and have therefore motivated a number of investigations. Some methods for reducing these effects a posteriori through data processing algorithms have been proposed. These methods include the use of a correlation mapping method (Chen and Katz 2005), alternative sub-pixel displacement algorithms (Roesgen 2003; Roth and Katz 2001), modifications to the particle displacement histogram (Roth and Katz 2001; Hearst and Ganapathisubramani 2015), spectral domain image shifting techniques (Liao and Cowen 2005), the use of simplified (1-D) modeling and correction (Cholemari 2007) and processing using phase correlations (Eckstein et al. 2008). Most approaches reduce the bias error but not the equally strong random errors.

It is recommended to experimentally avoid such a condition beforehand by, as one option, closing the aperture with the disadvantage of less light. This approach is not practical for high-speed cameras with large pixels of ≥20 µm. Rather, it is recommended to either manually defocus the lens slightly (Overmars et al. 2010) with possible difficulties achieving equal defocusing everywhere in the image for Scheimpflug-mounted objectives, or to mount extra diffusor(s) between camera and lens with just the right defocusing (Michaelis et al. 2016). One should note, that defocussing does not work for volumes (Tomo-PIV), since it only shifts the focused plane.

The theoretical Airy particle shape function can usually be approximated quite well by a circular Gaussian function. In case of astigmatism, it will change into ellipses, equivalent to larger particle image size in some direction. This or any other deformed particle image shape from other optical effects will not add to the error in any special way – in particular for correlation-based PIV – because the particle shape at the second time instance will look the same. In general, extended particle shapes lower the contrast and increase the random error.

Worse are e.g. potato-shaped tumbling seeding particles changing intensity rapidly (blinking), leading to strong random errors as described below for the effect of out-of-plane motion. Laser speckle also adds to the random noise but is difficult to quantify. Improvement in image quality would be possible with incoherent light sources (e.g. LEDs) but they are difficult to form into a thin light sheet of sufficient intensity. For large-scale volumetric PIV the use of mono-disperse helium-filled-soap bubbles illuminated by an array of strong LEDs offers the potential of excellent image quality (e.g. Scarano et al. 2015).

3.1.6 Camera noise

Cameras have mainly three types of noise sources. First the average background dark image has a characteristic *fixed pattern* which tends to bias the correlation toward the (0,0)-peak location. Especially for CMOS-cameras with stronger fixed pattern it is recommended to subtract a pixel-wise average or minimum of all recorded images before processing. This also removes constant background illumination (e.g. reflections).

Secondly, each pixel exhibits a characteristic random *dark noise* in the order of typically 3-20 e- (photo-electrons). High-speed CMOS-cameras are noisier (>15 e-) while sensitive (cooled) CCD-cameras can have noise levels below 5 e-. Recently a major breakthrough has been achieved with *scientific CMOS* sensors (sCMOS) developed together by Fairchild, PCO and Andor with noise levels below 1-3 e-, high full-well capacity and relatively fast 50-100 Hz frame rate. Sony recently introduced global shutter CMOS-chips with similar specifications and will actually discontinue its line of CCD chips in a few years, because the newly CMOS-sensors are better in almost all specification: dark noise, full-well capacity and speed. Unfortunately, the Sony chips do not support the fast-shutter double-frame mode.

Finally, given any illumination of a pixel with some number of photo-electrons N, the unavoidable Poisson-distributed random *photon shot noise* is simply the square-root of N. As soon as the illumination increases above some rather low level, the photon shot noise will be the dominant source of camera noise. A high full-well capacity helps to increase the image contrast provided enough light is available.

3.1.7 Particle out-of-plane motion

Particles change intensity when moving through the light sheet with, for example, a Gaussian intensity profile. Unmatched particles leaving or entering the light sheet will add to the general noise background in the correlation maps. Even more critical are two partially overlapping particles at different z-position being brighter-darker at the first laser pulse, changing to darker-brighter at a later time instance due to the out-of-plane motion. The result is a significant asymmetry of the correlation peak leading to strong virtual displacements of up to half the particle image size. For typical out-of-plane motions the averaged random error can reach 0.1 px quite independent of the seeding density (Nobach and Bodenschatz 2009, Nobach 2011). This is often the dominant error source in PIV. For a more top-hat shaped intensity profile the effect may be slightly smaller, but a combination of bright-bright to bright-gone has the same effect.

A thicker light sheet helps with the previously mentioned advantages and disadvantages, but a significant improvement is only possible with volumetric measurement techniques, for example, processing a slightly thicker light sheet with Tomographic PIV using at least 3 cameras.

3.1.8 Illumination intensity variations

Slowly varying in-plane light sheet intensity variations or difference in global intensity from first to second laser pulse do not add any special systematic or random error component, as cross-correlation is insensitive to absolute intensity variations. Common practice is to subtract the local mean intensity of the interrogation window before correlation leading to noise reduction. Again, the random noise is always proportional to the particle intensity and contrast, in general to the available information content.

More critical is the case of the two laser pulses not being perfectly aligned or with different intensity profiles. This has the same effect as particle out-of-plane motion. Grayson et al. (2016) propose to use an extra camera for measuring the laser profile. A simple check of laser misalignment consists of setting the time between the two laser pulses as short as possible. The PIV cross-correlation coefficient should then be close to 1. A value of 0.5 would indicate only 50% overlap between the two lasers.

Laser adjustments, good light sheet forming optics and appropriate checks before recording the actual data are part of the experimental expertise recommended for successful PIV experiments.

3.1.9 Spatial velocity gradients

A mostly unrecognized source of error is related to out-of-plane velocity gradients. Particles within the light sheet will have different depth positions not averaging out to zero due to the random positions. A standard deviation σ of the random position of n particles leads to a mean z-position with a standard deviation $\sigma/\sqrt{n}$ and subsequently to an averaged velocity different than the velocity at the center of the light sheet due to the out-of-plane gradient of the velocity.

For example, let's assume a light sheet with 10 pixel standard deviation ('width' of 20 pixel) in the Gaussian intensity profile. An ensemble of 20 particles within the interrogation window/volume has a standard deviation in the center-of-mass z-position of $10/\sqrt{20}=2.2$ pixel. Together with a possible out-of-plane gradient of typically up to 5-10% (i.e. 5-10 px change in displacement over a distance of 100 px), this can lead to a random error of up to 0.11 to 0.22 px, which is significant compared to the other error sources.

A synthetic image has been generated with some camera noise, seeding density of 0.02 ppp (20 per 32x32 IW), and constant (u,v)-velocity with a z-gradient simulated by half the particles at v=+0.25 pixel, and half with -0.25 pixel (equivalent to 2.5% gradient in a light sheet of 20 pixel width). This yields 0.078 px random error in the v-component (0.010 px without z-gradient), compared to the theoretical $0.25/\sqrt{20}=0.056$ px. The measured error is probably slightly larger due to overlapping particles of different velocities disturbing the correlation peak and increasing the random error.

For 2D-PIV only the out-of-plane gradients of the *in-plane* velocity components are relevant, while for Stereo-PIV also the *out-of-plane* component will contribute to the error magnitude. In principle, one can reduce the effect by decreasing the time between laser pulses or by reducing the light sheet thickness. But in the presence of out-of-plane gradients one also expects significant out-of-plane velocity itself requiring thicker light sheets to prevent too large fractions of unmatched particles. Again, some improvement can be expected from Tomographic PIV or 3D-PTV/STB.

Random motion of particles also leads to a broader and less well-defined correlation peak and thus to even more random errors. The particle disparity UQ-method (Sciacchitano et al. 2013) and the correlation statistics UQ-method (section 3.3) are well suited to quantify the estimated error level.

This effect needs to be distinguished from *in-plane gradients* together with random particle positions which lead to an average in-plane particle ensemble position not at the middle of the interrogation window. Some *vector relocation* scheme has been proposed to correct for it (Lindken et al. 2003). For state-of-the-art PIV algorithms, this is no longer necessary, since the predictor-corrector scheme iteratively adjusts to in-plane gradients independently of the exact location of the seeding particles. Seeding inhomogeneity determines the amount of information and thus indirectly the random error level, but introduces per se no systematic shift in mean vector position.

As mentioned in the previous chapter, small wavelengths will be truncated (*truncation errors*) due to the limited spatial resolution of any PIV algorithm. This is visible again – just like for the out-of-plane gradient case – as random motion of the particles within the interrogation window – systematic on smaller scales than the interrogation window size – and should be again detectable by sensitive UQ-methods.

A similar random particle motion occurs directly on micro-scales due to Brownian particle motion. It becomes visible in high-magnification μPIV as a random in-plane jitter of particle positions as a function of temperature. The random particle motions never cancel out completely to zero.

3.1.10 PIV processing scheme

Finally, any PIV algorithm has its strength and weaknesses. While state-of-the-art PIV processing schemes are already highly optimized, they never extract 100% of the available information in an optimal way. For example, ongoing research tries to optimize processing parameters to locally changing image conditions (*adaptive PIV*, see chapter 5).

PIV processing may also lead to false vectors (*outliers*) far off the true value due e.g. to random correlation peaks. A good algorithm should recognize during processing or as a post-processing step if a computed vector is valid or should be disregarded due to insufficient local information content or incompatibility to the neighborhood (e.g. Westerweel and Scarano 2005). An unrecognized outlier can spoil statistical quantities significantly further down the processing chain.

Without going into the details of possible error sources related to imperfect processing schemes, it should be noted that UQ-methods partly require knowledge of some processing details. The *image matching/particle disparity* method (Sciacchitano et al. 2013) and the *correlation statistics* method (section 3.3) need the effective spatial resolution of the PIV algorithm and the shape of the filter function (in most cases assuming a Gaussian function is sufficient) but otherwise would work with any PIV algorithm. The *uncertainty surface* method (Timmins et al. 2012), the *peak ratio* method (Charonko and Vlachos 2013) and the similar *mutual information* method (Xue et al. 2014; Boomsma et al. 2016) require previous calibration of the actual PIV software under various image conditions.

To summarize, from a pure image processing point of view, the accuracy of PIV is determined first of all by the total amount of information content (seeding density, number of matched particles, image contrast, light intensity, etc.) and additional random error sources visible in the image and potentially quantifiable by UQ-methods. They can be combined into three categories:

- Random pixel noise due to:
  - Camera background noise, evenly distributed
  - Camera photon shot noise, highest at particle positions
- Jitter in particle position due to:
  - Out-of-plane gradient of in-plane particle motion (Stereo-PIV: also out-of-plane motion)
  - Unresolved in-plane particle motion for small wavelengths
  - Brownian motion for tiny particles in µPIV
- Changing intensity pattern for overlapping particles due to:
  - Out-of-plane motion together with changing light intensity (e.g. Gaussian laser profile)
  - Misalignment of lasers or differently shaped light sheet profiles
  - Temporally changing light sheet profile for a single-cavity laser in time-resolved PIV
  - Tumbling motion of non-spherical particles

The sensitivity of any UQ-method should be validated regarding these categories of image noise. For example, the particle disparity method (Sciacchitano et al. 2013) partly neglects the (usually smaller) contribution of random pixel noise, while it is unclear how the correlation peak ratio method (Charonko and Vlachos 2013) can be sensitive to errors due to overlapping particles, where the second random correlation peak might be effected in the same way as the highest true correlation peak.

3.2 Ways to estimate PIV Uncertainties

A few easy indicators of PIV uncertainties are widely used. First of all, often in some part of the flow field the flow is rather constant and the visible fluctuations are most likely due to the random noise. When decreasing the size of the interrogation

window, the random fluctuations will increase proportionally. This is, of course, very rough and constitutes only a lower bound as the error increases, for example, in regions of larger flow gradients.

For time-resolved PIV, one can compare instantaneous flow fields with time-filtered ones (e.g. with a polynomial regression of second- or third-order over some kernel length) or processed by advanced multi-frame correlation techniques (Hain and Kähler 2007; Sciacchitano et al. 2012; among others) requiring that the length of the temporal filter kernel is short enough not to smooth over temporal fluctuations but long enough to decrease the noise sufficiently. When viewing unsmoothed TR-PIV data as a movie, the noise is easily visible as a flickering from vector field to vector field.

For Stereo-PIV the 3C-reconstruction of the two vectors (u_1,v_1) and (u_2,v_2) into a (u,v,w)-vector provides a residual related to the error of the two vectors in the direction perpendicular to the epipolar line. For example, for both cameras aligned along the x-axis, any vector error in u_1 and u_2 are swallowed up by the computed u and w-component, but comparing v_1,v_2 to the average $v=(v_1+v_2)/2$ provides an estimate of the uncertainty of v, which using isotropy and the angle between the two cameras can be extended to u- and w-uncertainties. So, on average for many vectors or vector fields, one can derive uncertainties but not an uncertainty for every vector as done by the full UQ-methods described below.

Some methods are tailored toward quantifying specific error sources. As mentioned before, one can record a few images with a very short Δt between laser pulses to measure the overlap between the two laser sheets. A normalized cross-correlation coefficient of 0.5 indicates, for example, a 50% overlap between the two pulses.

Recording a few data sets with different Δts (*multiple-Δt strategy*) can be used to increase the dynamic range of the PIV algorithm but also quantifying the peak-locking bias and random error and camera noise as well as potentially correcting for them (Legrand et al. 2012, Persoons 2014).

There are other parameters that can be extracted to assess at least qualitatively the PIV accuracy and to provide a guideline for the user to improve experimental and processing parameters. A higher cross-correlation peak height or ratio to the second random correlation peak indicates higher matching accuracy and in most cases higher accuracy. A quantitative deduction is more complicated as done for the peak-ratio UQ-method by Charonko and Vlachos (2013) (see below).

Comparing the volume of the autocorrelation peak with the volume of the cross-correlation peak (Scharnowski and Kähler 2016a) or the height of the two correlation peaks (Scharnowski and Kähler 2016b) provides a useful indicator for the out-of-plane motion and image noise together with a good definition of a signal-to-noise (SNR) ratio.

Recently, full UQ-methods have been developed with the intention of accurately quantifying the uncertainty of every computed PIV vector (Figure 3.4).

In the *uncertainty surface* (US) method developed by Timmins et al. (2012) recorded images are analyzed for parameters that influence the error. Presently, four parameters are examined: particle image size, particle density, displacements and shear. Initially, the PIV algorithm has to be tested with synthetic images varying these parameters, i.e. generating an uncertainty surface for a particular algorithm and selected processing options. By comparison with the measured parameters (particle size, etc.) inside each interrogation window, an uncertainty measure can be assigned to each vector.

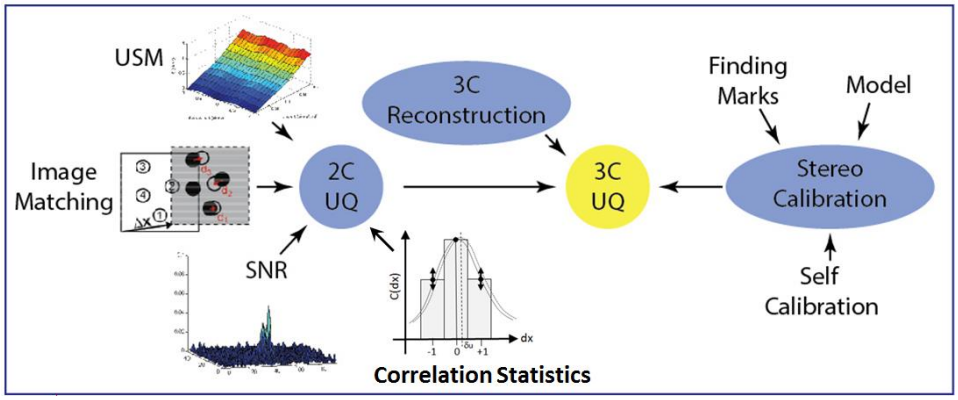

Figure 3.4. Overview uncertainty quantification methods for 2D2C- and 2D3C-PIV.

The *peak ratio* (PR) method (Charonko and Vlachos 2013) assumes that the ratio between the highest correlation peak and the second highest correlation peak is a good measure of the uncertainty. An empirical relationship has been derived between the peak ratio and the most likely uncertainty of the displacement. As a drawback, only a single uncertainty value or band is available for all velocity components.

The peak ratio has also been used by Persoons (2014) in conjunction with local displacement fluctuations over a spatial 5x5 and temporal 9-point kernel in time-resolved PIV. These fluctuations are a combination of physical turbulent fluctuations and measurement uncertainty and were shown to successfully guide the settings and processing of a variable pulse separation scheme in order to enhance the dynamic range of the PIV measurement. In the same way, advanced multi-pulse or multi-frame techniques (see e.g. PIV Challenge 2015, Kähler et al. 2016) would benefit from accurate uncertainty estimation for guiding the filter kernel size and other processing parameters.

In the *image matching / particle disparity* (PD) method (Sciacchitano et al. 2013), the measured displacement field is used to dewarp back the second image (or both by half) to overlay on the first one. The position of the particles for both frames is computed in each interrogation window and the residual disparity in the position of matching particles leads to an estimate of the uncertainty of the displacement vector components.

The *correlation statistics* (CS) method is described in the next section. It is similar to the IM-method, but uses the information of all pixels, not just particles, affecting the shape and possible asymmetry of the correlation peak from which the uncertainty for all velocity components is derived.

Recently the *mutual information* (MI) method (Xue et al. 2014; Boomsma et al. 2016) has been introduced, which is an extension of the PR-method.

PD, CS, US, and PR-methods have been compared by Sciacchitano et al. (2015) using dedicated experimental data (Neal et al. 2015) with two PIV systems, a measurement PIV system and a high-dynamic-range PIV system with less errors closer to the ground truth.

CS and slightly less PD performed quite well with high sensitivity to changing experimental conditions (e.g. seeding density, velocity gradients, out-of-plane motion), while PR and US showed less sensitivity to some conditions. For example, US could not account for out-of-plane motion, simply because this has not yet been one of the parameters of the initial training of US. Of course, this information is also difficult to extract from local image data. It is only possible for Stereo-PIV knowledge the w-component, but in addition also the exact shape of the laser profiles is required.

PD, CS, PR, and MI have been compared in a similar way by Boomsma et al. (2016), showing also higher sensitivity for the CS-method, but also an underestimation of the true error by 20-30%.

3.3 PIV uncertainty quantification using correlation statistics

3.3.1 Introduction

In general, planar PIV relies on matching two images and to compute a displacement field dx(x,y) as the best fit between the intensities in images I_1(x,y) and I_2 (x+dx(x,y),y+dy(x,y)) = I_2^* (x,y). Usually this involves maximizing the correlation given by the sum of ($I_1 I_2^*$). Alternatively, one can minimize the sum of the L_2-norm or mean squared error $(I_1 - I_2^*)^2$, sometimes called minimum quadratic difference (MQD), least squares matching (LSM) or sum of squared differences method (SSD). It can be shown that the two methods are mathematically identical provided the intensity I is normalized by $(I - I_{avg})/(\Sigma(I - I_{avg})^2)^{1/2}$ (Medan et al. 1991).

These image matching algorithms can be further differentiated into local or global regularization schemes. Global methods like different types of optical flow (Horn and Schunck 1981; Lukas and Kanade 1981) iteratively optimize the whole displacement field at once while local methods more common in PIV select a small interrogation window to be matched to the corresponding window in the second image and repeating the procedure for all windows in the image. Typically, an iterative multi-pass predictor-corrector scheme is used (e.g. Schrijer and Scarano

2008). Due to the intermediate vector field regularization including outlier removal, this can then be considered an intermediate local-global approach.

The focus here is not on a particular PIV algorithm, but to provide a generic uncertainty estimation method for any algorithm as a post-processing step once the displacement field has been calculated. It is an extension of the particle disparity method (Sciacchitano et al. 2013) but instead of taking individual particle displacements it analyzes individual pixel contributions to the correlation peak.

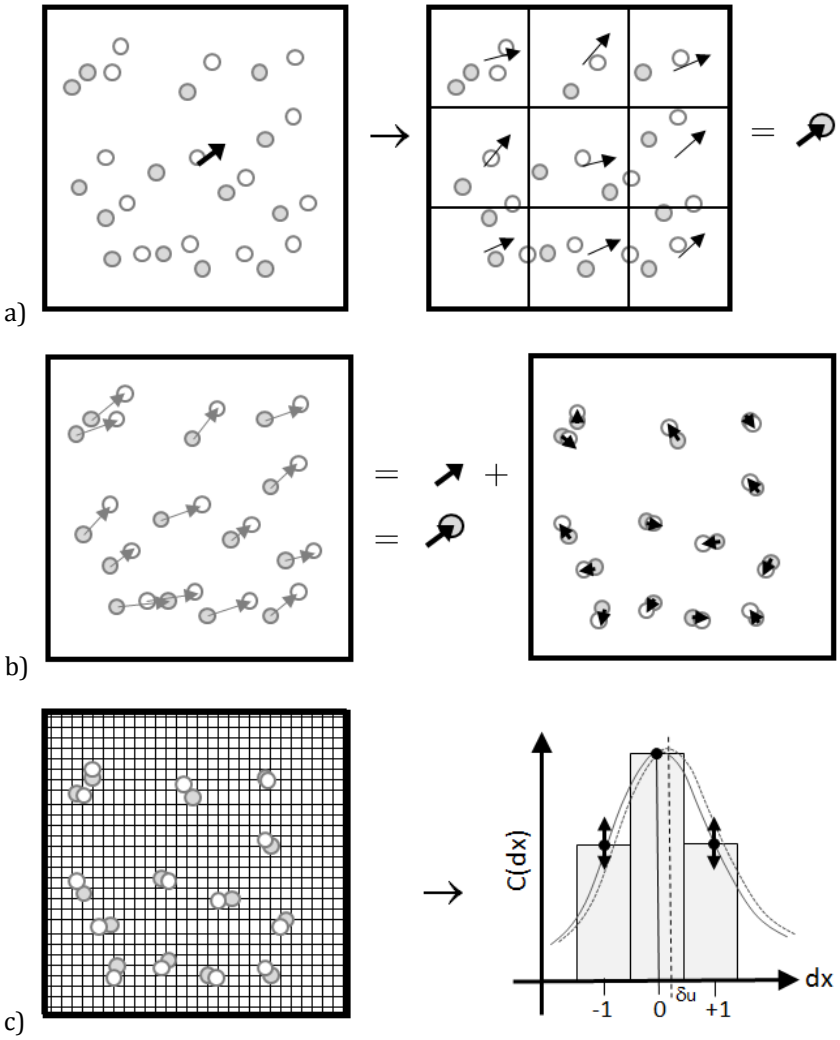

Figure 3.5. Principle of uncertainty estimation by a) splitting into sub-windows, b) particle disparity and c) correlation statistics method.

3.3.2 Uncertainty estimation from correlation statistics

The general concept is presented in Figure 3.5 . For computing the uncertainty of a single vector inside an interrogation window one could in principle divide the interrogation window into smaller parts (Figure 3.5a) where each sub-window corresponds to a displacement vector with higher noise level due to fewer pixels and fewer particles. So the standard deviation of these *n*x*n* vectors divided by sqrt(*n*x*n*) is a rough estimate of the uncertainty of the vector computed from the complete interrogation window, given idealized circumstances with no outliers, no small-scale flow gradients, etc.

The particle disparity method goes to smaller scales analyzing individual particles and their spread in displacements (Figure 3.5b) and provides better statistics for the uncertainty estimation. The correlation statistics method presented here zooms in even further to individual pixels and their fluctuating contributions to the shape of the correlation peak from which an uncertainty estimate is derived (Figure 3.5c). As shown later, despite analyzing single pixels and their neighbours, the effective local spatial scale is determined by the width of a spatial covariance matrix, which is again related to the average particle image size.

The correlation statistics method takes as input the two images to be matched and the displacement field computed by PIV. First image 2 is dewarped back onto image 1 using the displacement field $u(x)$, i.e.

$$I_2^*(x) = I_2(x + u) \tag{3.1}$$

requiring a sufficiently accurate high-order sub-pixel interpolation scheme (see Astarita and Cardone 2005; Astarita 2006). For simplifying the following equations, this asymmetric dewarping scheme is used here keeping I_1 constant. This is sometimes used for time-resolved PIV processing with subsequent Lagrangian analysis of fluid element trajectories. For standard double-frame PIV the symmetric dewarping of both frames with $\pm u/2$ is preferred, applied here to process the data in section 3.3.3**.** Both methods have been implemented in the DaVis-software and no difference in performance has been detected.

The following equations are given only for the u-component in x-direction, but apply equally to the v-component. The sums are evaluated over all $N = n^2$ pixels of an interrogation window of linear dimension n, in general over a region related to the effective spatial resolution L_{sr}. This needs to be determined for every PIV algorithm and set of parameters, discussed in section 3.2. Depending on window overlap factor and details of the multi-pass scheme with intermediate vector regression filter, the effective spatial resolution can be quite different from n.

Instead of a square window the sums can be evaluated over a somewhat larger Gaussian weighted interrogation window, where the diameter of the 2D-Gaussian weighted curve is close to L_{sr}. In general, computing the uncertainty one should use the same square, round or elliptical interrogation window, weighting function and sub-pixel interpolation function as in the underlying PIV algorithm.

It is assumed that the PIV algorithm has converged sufficiently such that for the computed displacement u the correlation function

$$C(u) = \sum(I_1(x,y)I_2(x+u,y)) = \sum(I_1(x,y)I_2^*(x,y)) \tag{3.2}$$

is at a maximum with zero slope dC/du. A small distance $\pm\Delta x$ away from u the correlation function $C_+ = C(u+\Delta x)$ should therefore be equal to $C_- = C(u-\Delta x)$:

$$\Delta C = C_+ - C_- = \sum\left(I_1(x,y)I_2^*(x+\Delta x,y) - I_1(x,y)I_2^*(x-\Delta x,y)\right) \cong 0. \tag{3.3}$$

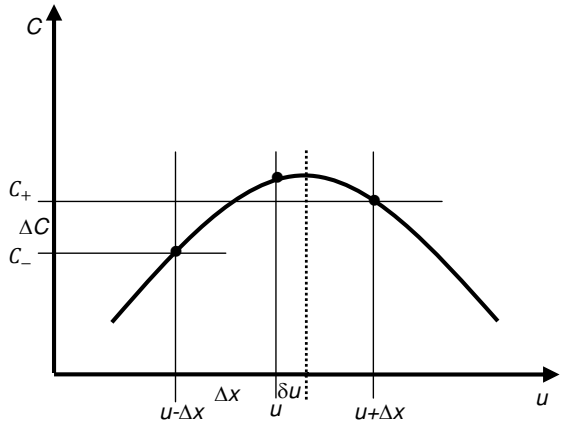

Figure 3.6. Correlation function $C(u)$.

Typically Δx will be 1 pixel as discussed later. Non-zero ΔC indicates that the algorithm has not yet converged or was not able to converge due to some reason, and taking the three points $C_0 = C(u)$, C_- and C_+ one could calculate an improved optimal displacement u+δu which would be equivalent to an extra iteration step of the PIV algorithm. Note that in the usual predictor-corrector scheme with filtering of the predictor, there is always some correction in each iteration. As shown in Figure 3.6, for non-zero ΔC fitting a Gaussian curve through the 3 points leads to the residual displacement δu given by:

$$\delta u = \frac{\Delta x}{2}\frac{\log(C_+)-\log(C_-)}{2\log(C_0)-\log(C_+)-\log(C_-)}$$

$$= f(C_0,\ C_-,\ C_+) = f(C_0,\ C_\pm - \Delta C/2,\ C_\pm + \Delta C/2) \tag{3.4}$$

with $C_\pm = (C_+ + C_-)/2$.

Eqn. (3.3) can be rewritten as:

$$\Delta C = \sum \Delta C_i = \sum\left(I_1(x,y)I_2^*(x+\Delta x,y) - I_1(x+\Delta x,y)I_2^*(x,y)\right) \tag{3.5}$$

ignoring small differences at the window border when shifting the second term by Δx. Now every term ΔC_i represents the elemental contribution to the total correlation difference ΔC. It is evident that all terms ΔC_i (and the sum ΔC) would be

zero for perfect image matching, i.e. if $I_1 = \text{const} \cdot I_2^*$. All pixel-wise contributions to the side lobes of the correlation peak are equal (Figure 3.7 left).

Due to various error sources I_1 and I_2^* will not match perfectly even for the true displacement u_{true}. Assuming one would dewarp I_2 by the true displacement u_{true}, the pixel-wise contributions to the side lobes of the correlation peak are unequal and the individual ΔC_i add up in a random walk fashion to a non-zero ΔC (Figure 3.7 middle). This difference will be optimized away by the PIV predictor-corrector scheme such that ΔC is zero again, leading to an erroneous measured displacement $u_{meas} = u_{true} + \delta u$ (Figure 3.7 right). Thus from the given known variability in ΔC_i an estimate of the standard deviation $\sigma_{\Delta C}$ of ΔC can be derived (as described below) which is then propagated by eqn. (3.4) to an uncertainty estimate of the displacement field.

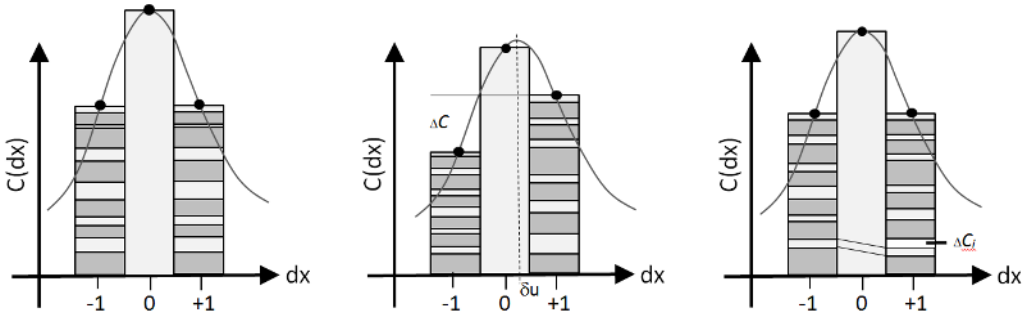

Figure 3.7. Correlation function between I_1 and I_2^* for ideal noise-free image (left). With added noise this would lead to correlation peak asymmetry (middle). PIV predictor-corrector scheme is shifting the correlation peak back to 0 thus introducing a measurement error (right).

In general, the standard deviation of $\Delta C = \sum \Delta C_i$ is related to the sum of the covariance matrix of ΔC_i:

$$\sigma_{\Delta C}^2 \equiv \text{var}\left(\sum_{i=1}^{N} \Delta C_i\right) \equiv \text{var}\left(\sum_{x,y=1}^{n} \Delta C_{xy}\right)$$

$$= \sum_{i,j=1}^{N} \text{cov}(\Delta C_i, \Delta C_j) = \sum_{x_1,y_1,x_2,y_2=1}^{n} \text{cov}(\Delta C_{x_1,y_1}, \Delta C_{x_2,y_2}) \qquad (3.6)$$

with the requirement that the ΔC_i have a zero mean ($\sum \Delta C_i = 0$). The auto-covariance terms are non-zero inside a neighborhood (x_1, y_1 close to x_2, y_2) given by the particle image diameter. Outside the pixel intensities become uncorrelated and the auto-correlation drops to zero. Thus, the right-hand side with a 4D-sum can be rewritten as a 2D-sum over distances Δx, Δy:

$$\sigma_{\Delta C}^2 = n^2 \sum_{\Delta x,\Delta y} \mathrm{cov}\left(\Delta C_{x,y}, \Delta C_{x+\Delta x,y+\Delta y}\right)$$

$$= \sum_{\Delta x,\Delta y} \sum_{x,y=1}^{n} \left(\Delta C_{x,y} \cdot \Delta C_{x+\Delta x,y+\Delta y}\right) = \sum_{\Delta x,\Delta y} S_{\Delta x,\Delta y} \,. \tag{3.7}$$

In case of complete independence between ΔC_i and ΔC_j – i.e. with only a single non-zero covariance term $S_{0,0}$ for $\Delta x = \Delta y = 0$ – this reduces to the random walk eqn.:

$$\sigma_{\Delta C}^2 = N\sigma_{\Delta C_i}^2 = \sum \Delta C_i{}^2 \,. \tag{3.8}$$

Unfortunately, ΔC_i and ΔC_j are not completely uncorrelated for $i \neq j$. So the covariance sums $S_{\Delta x,\Delta y}$ need to be evaluated over a sufficiently large neighborhood $\pm\Delta x, \pm\Delta y$ given roughly by the particle image size.

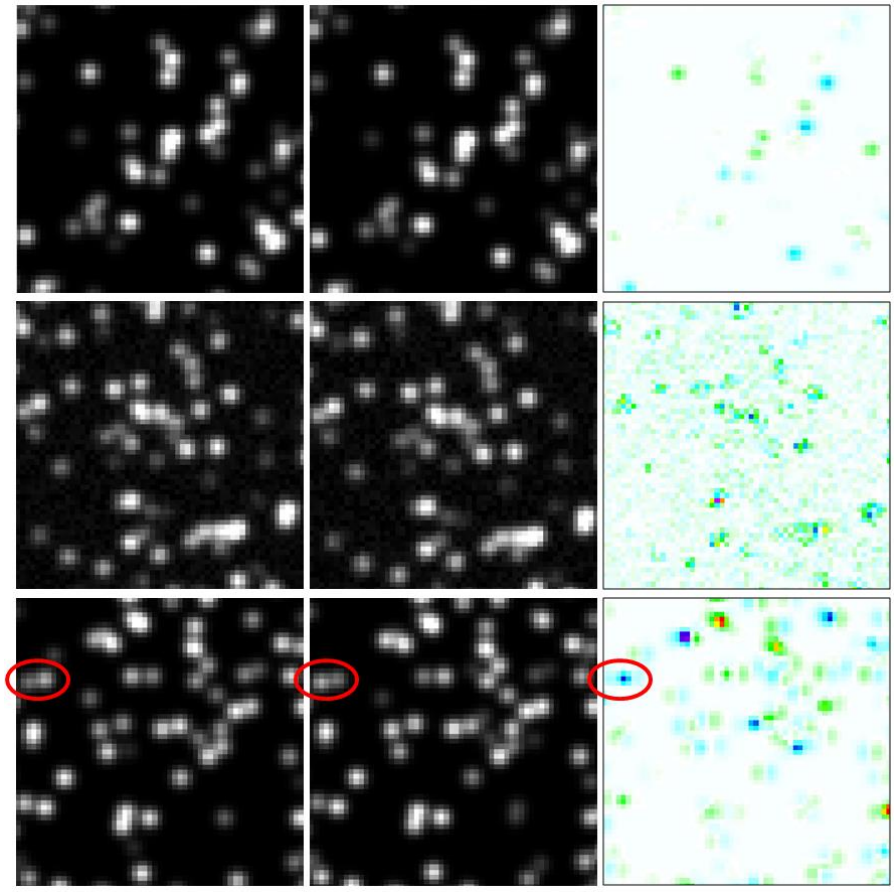

Figure 3.8. First and second image frame (left and middle) and correlation difference ΔC_i (right) for Brownian type of particle jitter (top), camera pixel noise (middle) and out-of-plane motion (bottom). Bluish color indicates negative values, green to red positive values of ΔC_i.

Finally, using eqn. (3.4) the uncertainty estimation of the displacement field can be computed by:

$$\sigma_u = f(C_0,\ C_{\pm} - \sigma_{\Delta C}/2\ ,\ C_{\pm} + \sigma_{\Delta C}/2) \tag{3.9}$$

since the right-hand-side is first-order linear in $\sigma_{\Delta C}/\ C_{-}$ provided $\sigma_{\Delta C}$ is sufficiently smaller than $C_0 - \ C_{\pm}$, i.e. it is accurate for $\sigma_u \lesssim 0.3$ px. This has been validated by Monte-Carlo simulations.

For illustration, the field of ΔC_i has been plotted in Figure 3.8 for different types of noise. At the top, the particles have a positional jitter, similar to Brownian motion in µPIV, of up to 0.1 px which is barely visible. The correlation differences ΔC_i in x-direction clearly show positive and negative shifts at the particle locations. This is also the basis for the particle disparity method of Sciacchitano et al. (2013). In the middle, only camera pixel noise has been added, a background level of noise together with photon shot noise proportional to the sqrt of the intensities. The correlation difference field has a grainy appearance with higher noise at the particle positions.

Finally, at the bottom the particles have a 10% out-of-plane motion within a light sheet with Gaussian intensity profile. Where particles overlap the change of a combination of weak and bright particle to bright and weak due to movement within the light sheet introduces a strong error, e.g. clearly visible in the circled area with a virtual displacement in negative x-direction. Weaker pattern of horizontally aligned blue-green or green-blue stripes indicate single particles changing in intensity, but the overall noise is dominated by overlapping particles.

3.3.2.1 Implementation details

First of all, the choice of Δx in eqn. (3.5) and following is guided by the requirement that it should capture well the form of the correlation function to be maximized, where the width is related to the particle image size. Therefore Δx must be smaller than the particle image size, but well larger than the computed σ_u. So a natural choice is Δx = 1 pixel which also requires only a single dewarped function I_2^*(x) instead of three in eqn. (3.5) and following.

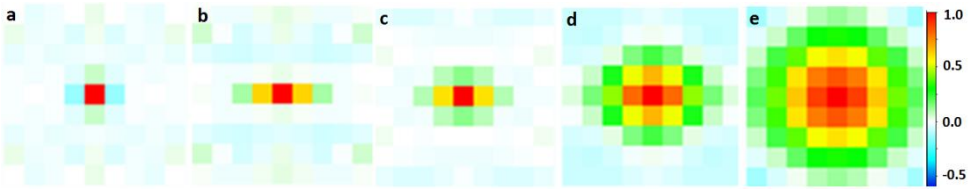

Figure 3.9. Typical auto-correlation matrix $S_{\Delta x,\Delta y}$ / $S_{0,0}$ for pure pixel noise and particle image size of 2.5 px without (a) and with (b) smoothing of ΔC_i, and for size of 1.0 (c), 2.5 (d) and 4.0 px (e) with out-of-plane motion of 5% and with ΔC_i smoothed.

For very large particle image sizes it might be advantageous to use larger Δx (e.g. 2) – also for the PIV algorithm itself for a more accurate 3-point Gaussian fit of the correlation peak – but this has not been investigated.

For particle related error sources – in particular for out-of-plane motion or random particle motion due to e.g. Brownian motion in μPIV – the auto-covariance matrix $S_{\Delta x,\Delta y}$ is about a positive 2D-Gaussian curve with a diameter roughly given by the average particle image size as shown in Figure 3.9c-e. Here $S_{\Delta x,\Delta y}$ is first evaluated for all Δx, Δy < 5 px, but only the inner values are summed up until $S/S_{0,0}$ drops below 0.05 to avoid adding outer random and possibly negative covariance terms.

In the case of pure camera noise independent for each pixel, due to the inverse coupling between I(x) and I(x + 1) in eqn. (3.5), the covariance for $\Delta x = \pm 1, \Delta y = 0$ is negative but relevant (similar for the y-component in y-direction) as shown in Figure 3.9a, which makes it difficult to find a suitable criterion for limiting the summing of S. To simplify processing, first all ΔC_i are smoothed in x-direction by a simple filter $\Delta C_i'(x) = (\Delta C_i(x-1) + 2\Delta C_i(x) + \Delta C_i(x+1))/4$ (same in y-direction for the y-component) which eliminates the negative covariance terms (Figure 3.9b). This does not change any other property of the statistical analysis. For particle related noise, it only makes the S-matrix slightly wider in one direction.

The relevant values of C_0, C_+, C_-, and $S_{\Delta x,\Delta y}$ (Δx, Δy = 0-4) need to be evaluated as sums over the interrogation window, in the case of Gaussian weighted windows as weighted sums over an area at least twice as large as the nominal interrogation window size. In particular, for 75% overlap this can lead to processing times equivalent to 2-3 PIV iterations. A faster implementation consists of computing the Cs and $S_{\Delta x,\Delta y}$ first as fields of the whole image for each pixel. These fields are spatially smoothed – equivalent to the weighted summing process – by a fast recursive 2D-Gaussian filter (Lukin 2007) with a filter length equal to the effective interrogation window size followed by multiplication with the filter length squared (difference between smoothing and summing). Then at each vector location the local values of C_0, C_+, C_-, and $S_{\Delta x,\Delta y}$ are taken to compute σ_u. This reduces the processing time to less than one PIV iteration. Further implementation on a GPU has reduced the processing time another order of magnitude. This scheme has also been successfully tested for PIV processing with square non-weighted windows, where due to the multi-pass PIV predictor-corrector scheme the effective filter shape is also closer to a Gaussian curve than to a top-hat function (see chapter 2).

The above one-dimensional derivation is done independently for the *x*- and *y*-component of the displacement field. Dependencies between x- and y-directions have not been observed yet for real PIV data, although e.g. for strong astigmatism in oblique directions one could expect some cross-terms. The discussion here is restricted to 2D displacements under various error sources.

3.3.3 Synthetic data

The procedure has been tested with synthetically generated images varying parameters such as noise level, particle image size, seeding density and out-of-plane motion. The image size is 1kx1k pixel. Default settings are particle image size of 2.5 px, seeding density of 0.1 particles per pixel (ppp), peak particle intensity of 1000 counts, particles distributed in a Gaussian laser intensity profile, and a constant displacement of 0.6 pixel in x, 0.3 pixel in y-direction and no out-of-plane motion. The particle image size is defined as 2σ with an intensity profile proportional to $\exp(-(x^2+y^2)/2\sigma^2)$.

Processing is done with LaVision DaVis 8.2 using 4-passes, 75% overlap, interrogation windows with a Gaussian weighting function and nominal window sizes of 16x16 up to 64x64 pixel. Due to the intermediate vector regularization adjusting to shorter displacement wavelengths, for 32x32 windows the effective window size is e.g. 32/28/22 pixel for an overlap of 0/50/75%. The method used here to measure the effective spatial resolution is similar to Elsinga and Westerweel (2011).

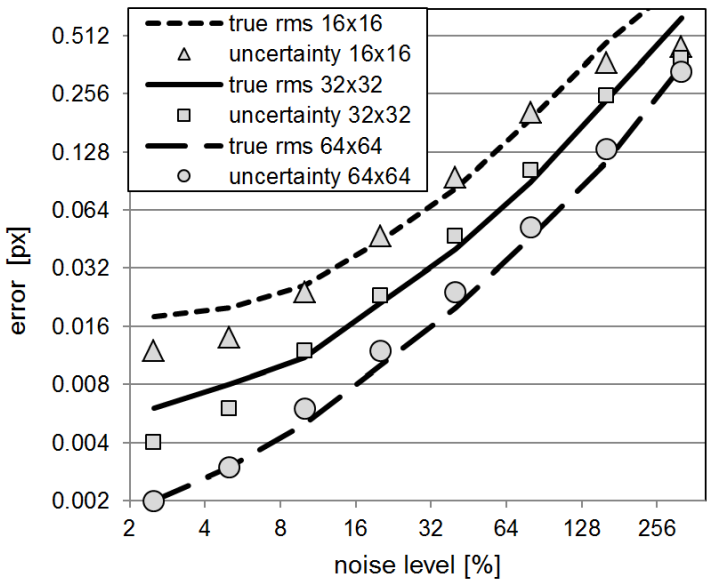

Figure 3.10. Error as a function of Gaussian pixel noise.

Assuming a typical camera with a conversion rate of 4 e-/count, Gaussian background pixel noise of 16e- (sigma of ±4 counts and adding 12 counts offset to keep intensities positive) has been added to the images. In addition, there is photon shot noise proportional to the sqrt of the number of photo-electrons leading to up to e.g. 16 counts noise for pixels with 1000 counts intensity.

In the following figures, the total uncertainty $\sigma = \sqrt{\sigma_u^2 + \sigma_v^2}$ is combined to an average value by computing the root-mean-square of the uncertainties of all vectors (see appendix in Sciacchitano et al. 2015). The total true error is computed as the rms of the differences of all vectors relative to the known displacement. It is usually dominated by the random part, significant bias is only encountered for small particle image sizes ≤ 1 px ('peak locking'). For the range of tested parameter no outliers have been observed and no post-processing has been done.

First, varying only the background pixel noise, it is shown that the uncertainty can be accurately estimated for window sizes of 16x16 to 64x64 for a wide range of noise levels given in percent relative to the particle peak intensity of 1000 counts (Figure 3.10). Only for very large noise amplitudes the uncertainties level off at about 0.3-0.4 px as expected from the limitation of eqn. (3.9). The relevant error levels in PIV to be considered are typically 0.02 px to 0.2-0.3 px, rarely less due to all error sources combined and, if larger, the correlation peak is less well defined with possibly many outliers and one should consider improving the experimental setup or using larger interrogation windows.

The results for varying the out-of-plane motion from 0 to 30% of the light sheet thickness are shown in Figure 3.11 for particle image sizes of 1.5 px (top) and 2.5 px (bottom). The uncertainties are correctly calculated for window sizes of 32x32 and 64x64, but again slightly underestimated for 24x24 and by 20% for 16x16 windows for a particle size of 2.5 px.

The error in case of out-of-plane motion is dominated by (possibly very few) overlapping particles which change their intensity from e.g. bright-weak to weak-bright as they move together through the light sheet as mentioned before. Thus a strong virtual in-plane displacement is introduced. The error is smaller for a particle size of 1.5 px because the probability of overlapping particles is significantly smaller.

As noted by Nobach and Bodenschatz (2009) this error level is quite independent of the seeding density. For low seeding densities there are fewer particles overlapping, but they contribute significantly to the error level since there are few particles in total. Conversely, for high seeding densities, almost all particles overlap and produce errors, but the information content is much higher which reduces the error correspondingly.

This is confirmed in Figure 3.12 for an out-of-plane motion of 10%, where the seeding density is varied from very low to very dense with almost constant error level. The uncertainty quantification works reasonably well with slight overestimation for 64x64 windows and underestimation for 16x16.

In general, out-of-plane motion is often the dominant error source in PIV processing (Nobach and Bodenschatz 2009). The same effect is also introduced by a misalignment of the profile of the first and second laser pulse or unstable laser intensity profiles from shot to shot.

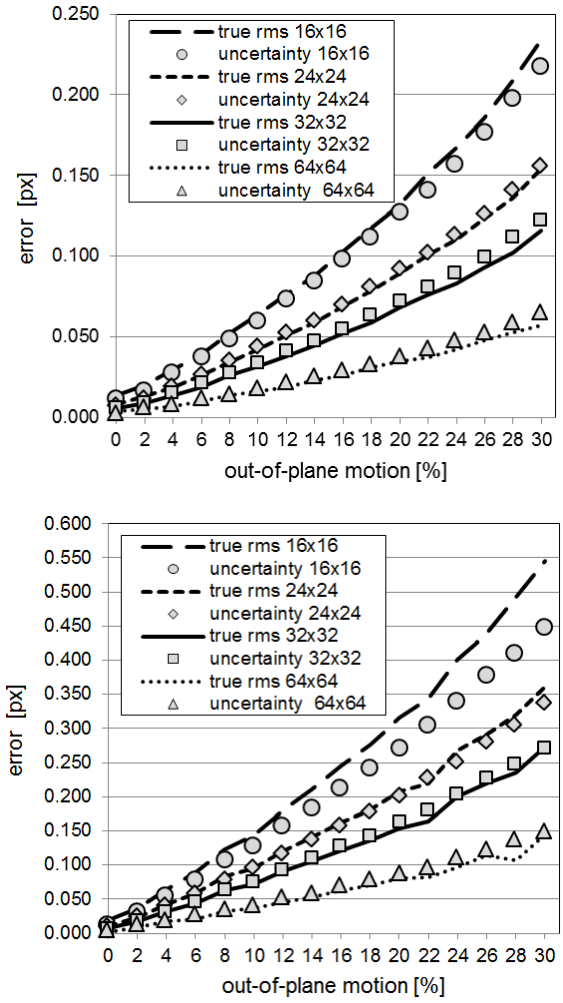

Figure 3.11. Error as a function of out-of-plane motion, left: particle image size = 1.5 px, right: 2.5 px.

Another particle size related error source is given by e.g. the random Brownian motion of each particle in μPIV. Here the error and estimated uncertainty becomes lower with higher seeding density due to the averaging effect of more particles (Figure 3.13). Again, the agreement between true error and uncertainty is good except for 16x16 windows, where the uncertainty is about 20-30% too low.

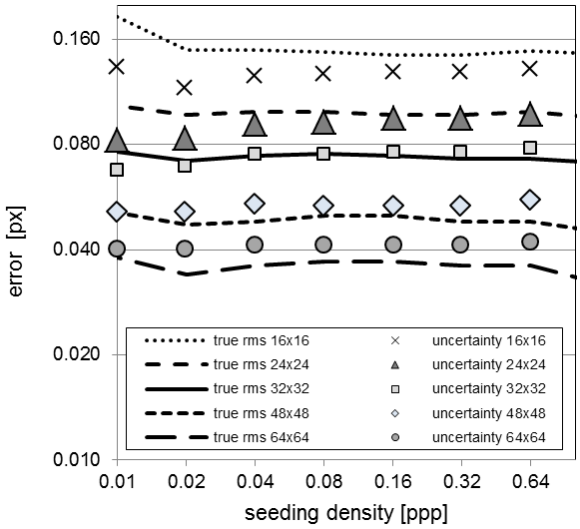

Figure 3.12. Error as a function of seeding density for out-of-plane motion.

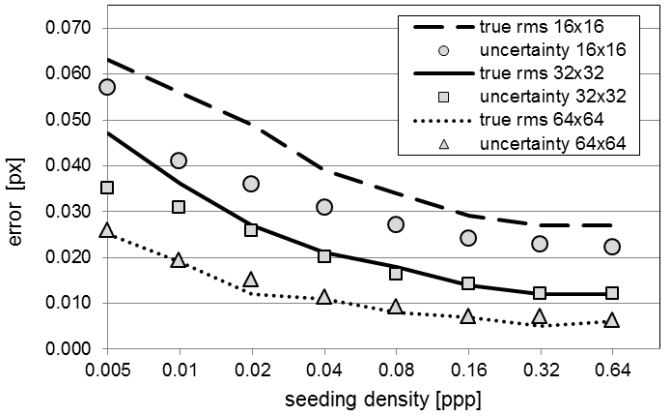

Figure 3.13. Error as a function of seeding density for random Brownian particle motion of ±0.1px.

Varying the particle image size for constant out-of-plane motion of 10% shows again a reasonable agreement between the average true error and the uncertainty (Figure 3.14). For sizes of <1 pixel the random and bias errors increase drastically ('pixel or peak locking') due to unrecoverable loss of information. Closer inspection reveals that the error by the uncertainty quantification for sizes of <1 pixel is close to the expected random part of the error, while the systematic peak locking bias remains undetected. Errors for larger particles are slightly underestimated especially for 16x16 windows.

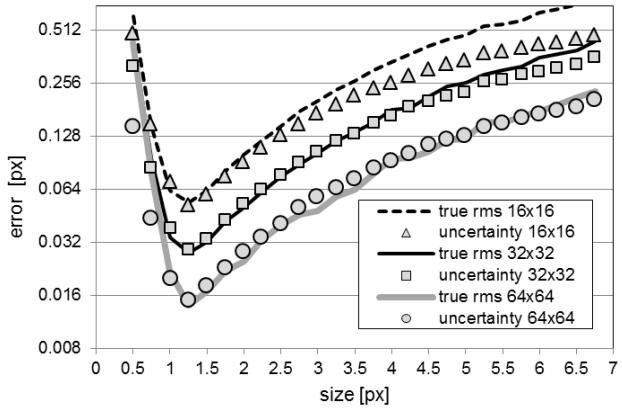

Figure 3.14. Error as a function of particle image size for out-of-plane motion of 10%.

Finally, the effect of in-plane gradients is investigated generating synthetic images with a width of 400 and height of 1000 pixel and varying the in-plane shear from 0 to 30%, i.e. up to -60/+60 px displacement in y on the left and right of the image, respectively. This amounts to up to 10 px change inside a 32x32 interrogation window which can only be handled by PIV algorithms using image deformation techniques. As shown in Figure 3.15, the true error for a particle image size of 2 px and no out-of-plane motion stays below 0.01 px, which validates the accuracy of the synthetic image generator, the PIV algorithm and the dewarping function under such extreme conditions. Even an inaccuracy in a vector position by only 0.1 px would lead to a bias error of already 0.03 px.

The computed uncertainty is overestimated as 0.03 px for 30% shear, even more for a particle image size of 4 px. This is probably due to image dewarping shearing round particles into ellipses rotated in different directions in the first and second frame. While the PIV algorithm correlating two rotated ellipses still computes an accurate mean displacement, the uncertainty method assumes that these intensity differences lead to additional noise, not knowing that in the end the symmetrical contributions still cancel out to an accurate displacement vector.

Often such strong velocity gradients are accompanied by additional larger error sources like out-of-plane motion as shown in Figure 3.15 for 10% out-of-plane motion. Again, a good agreement between true error and uncertainties is achieved.

More complicated is the subject of second-order gradients, i.e. velocity fluctuations of small-scale wavelengths, where the amplitude is reduced by the PIV algorithm due to the finite spatial resolution (e.g. Schrijer and Scarano 2008). A detailed analysis of the response function of the PIV algorithm and the computed uncertainties is beyond the scope of this work, including the basic question if such truncation errors should be really considered 'errors' with the – unrealistic – expectation that uncertainty quantification methods should be able to estimate them, or if the uncertainty should rather be quoted relative to the known spatial and temporal response function of the PIV measurement system.

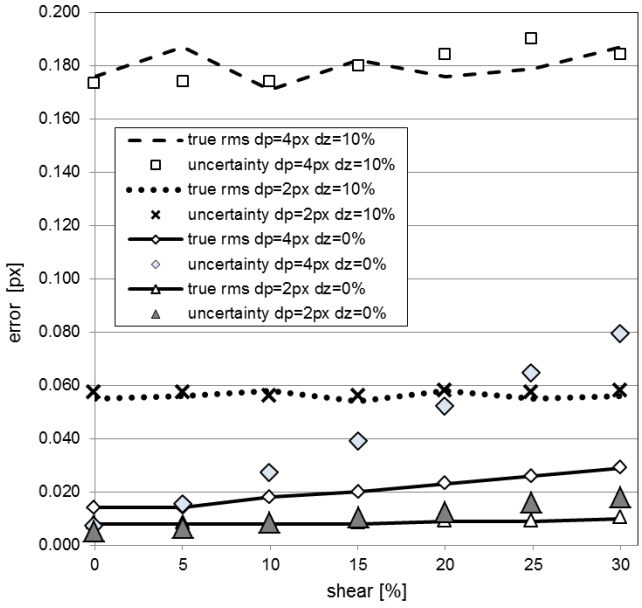

Figure 3.15. Error as a function of shear rate for different particle image size and out-of-plane motion, window size of 32x32.

3.3.3.1 Limitation of the uncertainty quantification

First of all, it should be noted that this uncertainty quantification method is not able to detect outliers. It is always assumed that outliers have been removed beforehand by some e.g. median filter and that the investigated correlation peak is the true one. The uncertainty method has no indication if the correlation peak found by the PIV processing routine is the correct one. In general, outliers will have larger uncertainties. This can help to detect them e.g. by a weighted median filter with a weight inversely proportional to the uncertainty.

It is also important to notice that the uncertainty estimation field will show quite some variability in the order of e.g. 5 to 25% even with perfect synthetic data with constant displacement field and same parameters everywhere as shown in Figure 3.16. This is partly due to the variability of the random pattern with more or less particles or overlapping particles in each interrogation window. But additionally, there is the intrinsic random character of the uncertainty estimation due to the random walk process (eqn. (3.6)-(3.8)). This standard deviation of the standard deviation ('SoS') has a relative variability of about $\pm 1/\sqrt{2N}$ given N independent events, which is e.g. for 10 particles per interrogation window already ±22%.

Another limitation of the above uncertainty quantification method is the case of insufficient independent events contributing to the statistical analysis, for example, in case of too few or too large particles in 16x16 windows. So far correction terms have not yet been calculated for such small-number statistics. It

may require again counting particles as in the 'image matching' method (Sciacchitano et al. 2013), but it is difficult counting e.g. overlapping particles as it would be required for errors dominated by out-of-plane motion.

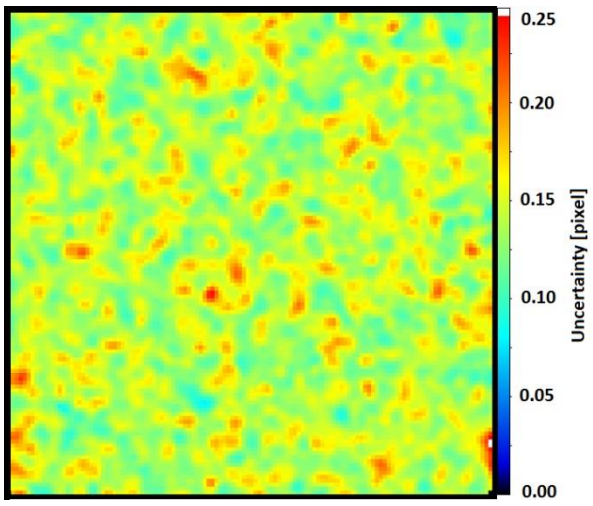

Figure 3.16. Typical uncertainty field with an average of 0.142 px and stdev of 0.018 px.

Finally, the method mainly estimates the random part of the uncertainty. Bias errors can in principle be quantified by eqn. (3.4), but it is assumed that the PIV algorithm is converged sufficiently so that the correlation peak is symmetrical and there should be no bias per se. Unknown biases as in strong peak locking stay undetected and may be better quantified by the uncertainty surface method (Timmins et al. 2012). The magnitude of the bias error is usually smaller than the random error/uncertainty even for strong peak locking, but may become dominant in derived statistical quantities.

3.3.3.2 Preparation for uncertainty propagation

Subsequent uncertainty propagation into derived quantities like vorticity, divergence, turbulent kinetic energy or Reynolds-stresses requires the knowledge of the spatial and/or temporal auto-correlation coefficients of the true errors as well as the correlation between u and v error terms, and w for Stereo-PIV (see chapter 4). These terms are stored in Davis together with the velocity and uncertainty components.

For the synthetic data used in section 3.3.3, there has been no significant coupling observed between the true errors δu and δv, $|C(\delta u, \delta v)| \leq 0.05$. The exception are data points with almost ideal image quality and errors below 0.01 px (e.g. Figure 3.10, low noise), where correlation values of the order of -0.1 to -0.3 have been measured. Since such low errors are typically not encountered in real

experiments, this has not been investigated further. It may relate to some floor noise level of the PIV algorithm together with intricacies in the processing scheme.

For Stereo-PIV, on the other hand, due to the 3C-reconstruction of (u,v,w) from (u_1,v_1,u_2,v_2) there is always a coupling in particular between u and w when e.g. the cameras are aligned along the x-axis, since both u and w depend on u_1 and u_2. These coupling terms, which can be calculated directly from the calibration function or measured using synthetic data, need to be taken into account in particular for the Reynolds stress R_{uw} and other quantities (see section 4.5).

3.3.4 Summary

The local measurement uncertainty of a PIV displacement field is estimated based on a post-processing of the differences between the two images to be matched. The standard deviation of the pixel-wise contributions of intensity differences to the shape of the correlation function is computed in a statistical way. This is then related to the random uncertainty of the displacement vectors.

This uncertainty quantification method has been tested with synthetic data varying e.g. random Gaussian noise, particle image size and density, in-plane and out-of-plane motion, and shows good agreement with the true random error in most cases, slightly underestimating the true error for 16x16 window sizes. The method is not able to estimate bias errors e.g. from peak-locking or other systematic error source.

The accuracy of this approach is furthermore investigated in designated experiments discussed elsewhere (Neal et al. 2015, Sciacchitano et al. 2015) as part of an international collaborative effort that includes comparisons to other PIV uncertainty quantification methods. It confirms the validity of the uncertainty method presented here.

4

PIV Uncertainty Propagation

Most of this chapter is a collaborative work with Andrea Sciacchitano, TU-Delft, published in Sciacchitano and Wieneke (2016) PIV uncertainty propagation, Meas Sci Technol 27(8).

4.1 Introduction

Several a-posteriori PIV uncertainty quantification methods have been recently proposed (see section 3.2) to estimate the unknown error for every velocity vector in the flow field. All these methods allow the a-posteriori quantification of the instantaneous measurement uncertainty. A thorough comparison of their performances in different imaging and flow conditions is reported in Sciacchitano et al. (2015), where the dedicated experimental data from Neal et al. (2015) has been used.

In many applications, PIV measurements are conducted to investigate flow properties derived from the velocity field, which can be instantaneous (e.g. vorticity, velocity divergence, acceleration, turbulence dissipation rate, pressure) or statistical quantities (e.g. time average and Reynolds stresses). Therefore, once the uncertainties of the instantaneous velocity components are estimated, they need to be propagated into the derived quantities of interest. The quantification of the uncertainty of derived quantities relies upon the following considerations:

i. the uncertainty of the velocity components propagates to that of the derived quantity of interest;
ii. the correlation (in space, time and/or inter-component) of velocity components affects the uncertainty of derived quantities;
iii. for statistical quantities, additional uncertainty is due to the finite number of samples N, which yields lack of statistical convergence.

The works of Wilson and Smith (2013a, 2013b) provide upper and lower uncertainty bounds for a number of statistical quantities, such as average, variance and covariance. In their analysis, the authors considered the contributions of random errors, mainly due to the finite sample size, and unknown time-dependent systematic errors. For velocity variance and covariance, the lower uncertainty bound was found to be larger than the upper uncertainty bound because spurious fluctuations tend to elevate the time-averaged measured fluctuations, yielding an error in the negative direction.

Recently, uncertainty estimation has been done for the dissipation rate (Charonko and Prestridge 2016), which is difficult to measure accurately since the available spatial resolution of PIV is not sufficient to resolve important small-scale fluctuations. Tokgoz et al. (2012) report that at least a spatial resolution better than twice the Kolmogorov-scale is required for accurate dissipation rates measured with Tomographic PIV.

In the work presented here, uncertainty quantification is provided for many commonly used derived quantities in PIV processing, both statistical and instantaneous. Following Coleman and Steele (2009), we assume that each systematic error whose sign and magnitude are known has been removed by appropriate correction. Thus this work focuses on random errors and uncertainties. The work discusses the basic concepts of uncertainty propagation and its applications for flow properties of interest in typical PIV measurements, such as

vorticity, mean velocity and Reynolds stresses. A correction of the Reynolds stresses based on the magnitude of the noisy fluctuations is proposed. Finally, the uncertainty propagation for Stereo-PIV 3C-reconstruction is provided.

4.2 Uncertainty propagation methodology

4.2.1 Basic concepts

Let us consider a derived quantity of interest y, which is a general function F of N measured variables x_i, with i = 1, 2, …, N.

$$y = F\left(x_1, x_2, \ldots, x_N\right) \tag{4.1}$$

Assuming that each variable x_i has a standard deviation σ_{x_i}, and given sufficient linearity of F, the variance of y can be approximated by the variance-covariance matrix of F (Bendat and Piersol 2010):

$$\begin{aligned} \mathrm{var}\left(y\right) &= \sum_{i=1}^{N}\sum_{j=1}^{N}\frac{\partial F}{\partial x_i}\frac{\partial F}{\partial x_j}\mathrm{cov}\left(x_i, x_j\right) \\ &= \sum_{i=1}^{N}\left(\frac{\partial F}{\partial x_i}\right)^2 \mathrm{var}\left(x_i\right) + 2\sum_{i=1}^{N-1}\sum_{j=i+1}^{N}\frac{\partial F}{\partial x_i}\frac{\partial F}{\partial x_j}\mathrm{cov}\left(x_i, x_j\right) \end{aligned} \tag{4.2}$$

or in another notation:

$$\begin{aligned} \sigma_y^2 &= \sum_{i=1}^{N}\sum_{j=1}^{N}\frac{\partial F}{\partial x_i}\frac{\partial F}{\partial x_j}\rho\left(x_i, x_j\right)\sigma_{x_i}\sigma_{x_j} \\ &= \sum_{i=1}^{N}\left(\frac{\partial F}{\partial x_i}\right)^2 \sigma_{x_i}^2 + 2\sum_{i=1}^{N-1}\sum_{j=i+1}^{N}\frac{\partial F}{\partial x_i}\frac{\partial F}{\partial x_j}\rho\left(x_i, x_j\right)\sigma_{x_i}\sigma_{x_j} \end{aligned} \tag{4.3}$$

where $\rho(x_i, x_j)$ is the cross-correlation coefficient between x_i and x_j, defined by:

$$\rho\left(x_i, x_j\right) = \mathrm{cov}\left(x_i, x_j\right) / \sigma_{x_i}\sigma_{x_j} \tag{4.4}$$

Notice that when x_i and x_j are independent, then $\rho(x_i, x_j) = 0$ and eqn. (4.3) reduces to:

$$\sigma_y^2 = \sum_{i=1}^{N}\left(\frac{\partial F}{\partial x_i}\right)^2 \sigma_{x_i}^2 \tag{4.5}$$

Eqn. (4.3) can be interpreted in two ways. First, assuming that the set of input variables x_i is measured many times, each time yielding an output variable y_j, the standard deviation σ_y provides a measure of the fluctuation of the derived y_j's. Secondly, σ_y provides a measure of the uncertainty U_y of y for a single measurement

given the standard uncertainties U_{x_i} of each input variable x_i (Coleman and Steele 2009):

$$U_y^2 = \sum_{i=1}^{N}\left(\frac{\partial F}{\partial x_i}\right)^2 U_{x_i}^2 + 2\sum_{i=1}^{N-1}\sum_{j=i+1}^{N}\frac{\partial F}{\partial x_i}\frac{\partial F}{\partial x_j}\rho\left(\delta x_i, \delta x_j\right)U_{x_i}U_{x_j} \tag{4.6}$$

where $\rho(\delta x_i, \delta x_j)$ is now the cross-correlation coefficient between the *errors* of x_i and x_j, which are indicated with δx_i and δx_j, respectively. This eqn. will be used extensively in the following.

In the present work, the uncertainty of instantaneous velocity components is quantified with the correlation statistics method (section 3.3). Eqn. (4.6) shows that the evaluation of the uncertainty of y requires the knowledge of the cross-correlation between velocity vectors separated in time or space or inter-component. Most PIV-UQ methods are unable to compute such values from single interrogation windows. The values of ρ are usually determined beforehand for a particular set of PIV processing parameter e.g. by Monte-Carlo simulation with synthetic data, similar to the uncertainty surface method by Timmins et al. (2013), which analyses the local imaging and flow conditions and looks up the corresponding potentially skewed and biased error distribution. Further details on the computation of the error spatial/temporal correlation are given in next sections.

4.2.2 Time-averaged statistical quantities

Given a set of samples $x = \{x_1, x_2, \ldots, x_N\}$ recorded over time, the temporal mean value, standard deviation and variance of x are defined as, respectively:

$$\bar{x} = \frac{1}{N}\sum_{i=1}^{N} x_i \tag{4.7}$$

$$\sigma_x = \sqrt{\frac{1}{N-1}\sum_{i=1}^{N}\left(x_i - \bar{x}\right)^2} \tag{4.8}$$

$$\sigma_x^2 = \frac{1}{N-1}\sum_{i=1}^{N}\left(x_i - \bar{x}\right)^2 \tag{4.9}$$

Given two sets of samples x and y, the covariance $\mathrm{cov}(x,y)$ or σ_{xy}^2 between them is defined as:

$$\sigma_{xy}^2 = \frac{1}{N-1}\sum_{i=1}^{N}\left(x_i - \bar{x}\right)\left(y_i - \bar{y}\right) \tag{4.10}$$

Notice that eqns. (4.7) to (4.10) provide the mean, standard deviation and variance for the *sample population*. These values are estimates of the corresponding values for the *parent population*, which comprises the totality of all samples (not only those acquired during the measurement). The accuracy of the estimate increases for increasing N; the estimates are exact for $N \to \infty$.

Assuming that the samples are independent and follow a normal distribution of standard deviation σ_x, the standard uncertainty of the above quantities is (Benedict and Gould 1996):

Uncertainty of mean:
$$U_{\bar{x}} = \frac{\sigma_x}{\sqrt{N}} \tag{4.11}$$

Uncertainty of standard deviation:
$$U_{\sigma_x} = \frac{\sigma_x}{\sqrt{2(N-1)}} \tag{4.12}$$

Uncertainty of variance:
$$U_{\sigma_x^2} = \sigma_x^2 \sqrt{\frac{2}{N-1}} \tag{4.13}$$

Finally, the uncertainty of the covariance is (Bendat and Piersol 2010):
$$U_{\sigma_{xy}^2} = \sigma_x \sigma_y \sqrt{\frac{1+\rho_{xy}^2}{N-1}} \tag{4.14}$$

where ρ_{xy} is the cross-correlation coefficient between x and y.

These equations are valid for sufficiently large N. Ahn and Fessler (2003) report that for $N \geq 30$ these formulae are accurate within 1%. For a smaller number of samples, the formulae typically underestimate the actual standard uncertainty by up to 10%, and correction factors should be used for the mean, standard deviation and variance to make them unbiased (Coleman and Steele 2009). The results of eqns. (4.11) to (4.14) will be used in the following for determining the uncertainty of statistical quantities of interest in turbulent flows.

4.2.2.1 Uncertainty of the mean velocity

Consider the generic velocity component u. Based on eqns. (4.7) and (4.11), the uncertainty of the mean velocity $\overline{u}$ is:

$$U_{\bar{u}} = \frac{\sigma_u}{\sqrt{N}} \tag{4.15}$$

Analogous equations are obtained for the v and w velocity components. In eqn. (4.15), systematic uncertainties due to spatial modulation errors or peak locking are not taken into account. The standard deviation σ_u contains both the true velocity fluctuations ($\sigma_{u,\,fluct}$) and the measurement errors ($\sigma_{u,\,err}$):

$$\sigma_u^2 = \sigma_{u,\,fluct}^2 + \sigma_{u,\,err}^2 \approx \sigma_{u,\,fluct}^2 + \overline{U_u^2} \tag{4.16}$$

where U_u is the uncertainty of the instantaneous velocity component and $\overline{U_u^2}$ is the mean-square of U_u. The right-hand-side of eqn. (4.16) is obtained by considering that the error variance $\sigma_{u,err}^2$ is approximately equal to the uncertainty mean-square

$\overline{U_u^2}$ for accurate uncertainty quantification methods (see appendix of Sciacchitano et al. 2015).

When the samples are not independent, the parameter N of eqn. (4.15) must be substituted with the effective number of independent samples N_{eff}, as discussed below.

4.2.2.2 Uncertainty of Reynolds stress

The Reynolds stress plays a crucial role in turbulent flows because it represents the rate of mean momentum transfer by turbulent fluctuations. In this section, the expression of the uncertainty is derived for the Reynolds normal stress and for the Reynolds shear stress.

Reynolds normal stress

The Reynolds normal stress for the x-velocity component u is defined as the variance of u:

$$R_{uu} = \overline{u'^2} = \sigma_u^2 = \frac{1}{N-1}\sum_{i=1}^{N}\left(u_i - \bar{u}\right)^2 \tag{4.17}$$

where u' is the fluctuating part of u: $u' = u - \bar{u}$. Due to its definition, the uncertainty of R_{uu} is computed with eqn. (4.13):

$$U_{R_{uu}} = \sigma_u^2\sqrt{\frac{2}{N-1}} \cong \sigma_u^2\sqrt{\frac{2}{N}} = R_{uu}\sqrt{\frac{2}{N}} \tag{4.18}$$

It is assumed that the samples are statistically independent. If not, N must again be substituted with the effective number of independent samples N_{eff} (section 4.2.2.3). As discussed in section 4.2.2.1, σ_u contains both the effects of true velocity fluctuations and spurious fluctuations due to noise. The latter yield an over-estimate for R_{uu} with respect to the true value $R_{uu,\,true}$:

$$R_{uu} = R_{uu,true} + \sigma_{u,err}^2 = R_{uu,true} + \overline{U_u^2} \tag{4.19}$$

When the uncertainty of the measured velocity is known, a corrected (more accurate) estimate of R_{uu} can be retrieved by subtracting the spurious fluctuations mean square $\overline{U_u^2}$ from the measured Reynolds stress:

$$R_{uu,corr} = R_{uu} - \overline{U_u^2} \tag{4.20}$$

Thus, according to eqn. (4.6), the uncertainty of the corrected normal Reynolds stress estimate $R_{uu,\,corr}$, indicated with $U_{R_{uu,corr}}$, is given by:

$$U_{R_{uu,corr}} = \sqrt{U_{R_{uu}}^2 + U_{\overline{U_u^2}}^2} \tag{4.21}$$

The latter is composed by two components: a) the uncertainty of the measured Reynolds stress, which is given by eqn. (4.18); b) the uncertainty of the spurious fluctuations mean square $\overline{U_u^2}$. Notice that U_u^2 can only assume positive values, therefore its distribution is better approximated by a log-normal distribution rather than by a Gaussian distribution. At least when approximating the distribution with a Gaussian distribution with positive mean, an analytical expression of the uncertainty of $\overline{U_u^2}$ can be derived using eqn. (4.6):

$$U_{\overline{U_u^2}} = \frac{2}{\sqrt{N}} \sigma_{U_u} \overline{U_u} \cdot \sqrt{1 + \frac{\sigma_{U_u}^2}{2\overline{U_u}^2}} \tag{4.22}$$

The accuracy of eqn. (4.22) is assessed in section 4.3.1. Combining both eqns. (4.18) and (4.22), the uncertainty of $R_{uu,\,corr}$ is:

$$U_{R_{uu,corr}} = \sqrt{R_{uu}^2 + \left(\sqrt{2}\, \sigma_{U_u} \overline{U_u} \cdot \sqrt{1 + \frac{\sigma_{U_u}^2}{2\overline{U_u}^2}} \right)^2} \cdot \sqrt{\frac{2}{N}} \tag{4.23}$$

In many applications, the measurement error is small with respect to the actual velocity fluctuations, therefore the term within brackets is negligible and eqn. (4.23) reduces to:

$$U_{R_{uu,corr}} = R_{uu} \cdot \sqrt{\frac{2}{N}} \tag{4.24}$$

In practice, the uncertainty of the Reynolds normal stress according to (4.23) and (4.24) is often strongly underestimated for two reasons. First, the subtraction of eqn. (4.20) is subject to the accuracy of the uncertainty quantification method itself. As shown by Sciacchitano et al. (2015), the uncertainty estimations of state-of-the-art UQ methods may deviate from the true errors by as much as a factor two for different flow and imaging conditions. Secondly, the finite spatial resolution of the PIV processing algorithm does not allow resolving fluctuations of length scale smaller than about the interrogation window. This may lead to a substantial underestimation of R_{uu} depending on Reynolds number, turbulent level and imaging magnification.

It is important to remark here that the computation of the uncertainty of R_{uu} according to eqn. (4.18) does not require the knowledge of the uncertainty of the instantaneous velocity. On the other hand, in order to compute the corrected value $R_{uu,\,corr}$, the uncertainty of the instantaneous velocity must be known.

Turbulent kinetic energy

The turbulent kinetic energy *TKE* is defined as half of the sum of the Reynolds normal stresses:

$$TKE = \frac{1}{2}\overline{u_i{}' u_i{}'} = \frac{1}{2}\left(R_{uu} + R_{vv} + R_{ww}\right) \tag{4.25}$$

Based on the error propagation formula (4.6), the uncertainty of the *TKE* is equal to:

$$U_{TKE} = \frac{1}{2}\sqrt{U_{R_{uu}}^2 + U_{R_{vv}}^2 + U_{R_{ww}}^2} \tag{4.26}$$

Assuming N>>1 and that the instantaneous measurement uncertainty is negligible with respect to the velocity fluctuations, the result of eqn. (4.24) can be used and the expression of U_{TKE} reduces to:

$$U_{TKE} = \sqrt{R_{uu}^2 + R_{vv}^2 + R_{ww}^2} \cdot \sqrt{\frac{1}{2N}} \tag{4.27}$$

When R_{ww} is unknown (e.g. in planar 2D2C-PIV, which only provides two velocity components), its value can be estimated as $R_{ww} = \left(R_{uu} + R_{vv}\right)/2$ under the assumption of isotropic turbulence.

Reynolds shear stress

The Reynolds shear stress R_{uv} is defined as the covariance of the u and v velocity components:

$$R_{uv} = \overline{u'v'} = \frac{1}{N-1}\sum_{i=1}^{N} u_i{}' v_i{}' = \frac{1}{N-1}\sum_{i=1}^{N}\left(u_i - \bar{u}\right)\left(v_i - \bar{v}\right) = \rho_{uv}\sigma_u\sigma_v \tag{4.28}$$

The quantity ρ_{uv} is the cross-correlation coefficient between the velocity components u and v. Assuming that the velocity fluctuations are affected by error δu and δv, respectively, and that the error of the time-averaged velocity is negligible, eqn. (4.28) becomes:

$$\begin{aligned} R_{uv} &= \frac{1}{N-1}\sum_{i=1}^{N}\left(u'_{i,true} + \delta u\right)\left(v'_{i,true} + \delta v\right) \\ &= \frac{1}{N-1}\sum_{i=1}^{N}\left(u'_{i,true}\, v'_{i,true} + u'_{i,true}\,\delta v + v'_{i,true}\,\delta u + \delta u\delta v\right) \\ &= \frac{1}{N-1}\sum_{i=1}^{N}\left(u'_{i,true}\, v'_{i,true} + \delta u\delta v\right) \\ &= R_{uv,true} + \rho_{\delta u\delta v}\sigma_{\delta u}\sigma_{\delta v} \cong R_{uv,true} + \rho_{\delta u\delta v}\sqrt{\overline{U_u^2}\,\overline{U_v^2}} \end{aligned} \tag{4.29}$$

In eqn. (4.29), $\rho_{\delta u\delta v}$ is the cross-correlation coefficient between the errors of the two velocity components. The true velocity fluctuations are assumed to be independent of the measurement errors, thus cancelling the cross-terms $\sum_{i=1}^{N}\left(u'_{i,true}\,\delta v\right)$ and $\sum_{i=1}^{N}\left(v'_{i,true}\,\delta u\right)$. As a consequence, the Reynolds shear stress R_{uv}

exhibits a systematic error (equal to $\rho_{\delta u \delta v}\sqrt{\overline{U_u^2}\,\overline{U_v^2}}$) only if δu and δv are correlated ($\rho_{\delta u \delta v} \neq 0$); however, this is typically not the case for planar 2C-PIV. Conversely, for stereo-PIV there may be non-zero inter-component correlations dependent on the experimental setup of the two cameras relative to the *x*- and *y*-axis.

The uncertainty of R_{uv} is obtained by applying the covariance uncertainty eqn. (4.14):

$$U_{R_{uv}} = \sigma_u \sigma_v \cdot \sqrt{\frac{1+\rho_{uv}^2}{N-1}} \tag{4.30}$$

The uncertainty of the Reynolds shear stress has a minimum value of $\sigma_u \sigma_v / \sqrt{N-1}$ when u and v are uncorrelated and increases with higher correlation between the two velocity components.

4.2.2.3 Effective number of independent samples

Consider a generic statistical quantity, as the mean $\bar{x}$. In this section we will show that if the N samples from which $\bar{x}$ is computed are not independent, a larger uncertainty of $\bar{x}$ is expected. In fact, from eqn. (4.6) it is obtained:

$$U_{\bar{x}}^2 = \sum_{i=1}^{N}\sum_{j=1}^{N}\frac{1}{N^2}\rho\left(x_i, x_j\right)\sigma_x^2 \tag{4.31}$$

having assumed a constant underlying fluctuation distribution $\sigma_{xi} = \sigma_{xj} = \sigma_x$. The auto-correlation coefficient $\rho(x_i, x_j)$ can be written as:

$$\rho\left(x_i, x_j\right) = \rho\left(x_i, x_{i+n}\right) = \rho\left(n\Delta t\right) \tag{4.32}$$

with Δt the inverse of the sampling frequency. The auto-correlation coefficient ρ is a function of the time separation $n\Delta t$ between samples x_i and $x_j = x_{i+n}$. As a result, eqn. (4.31) can be written as:

$$U_{\bar{x}}^2 = \frac{\sigma_x^2}{N^2}\sum_{i=1}^{N}\sum_{n=1-i}^{N-i}\rho\left(x_i, x_{i+n}\right) = \frac{\sigma_x^2}{N^2}\sum_{i=1}^{N}\sum_{n=1-i}^{N-i}\rho\left(n\Delta t\right) \tag{4.33}$$

The quantity $\rho(n\Delta t)$ is equal to one for $n = 0$ and decays to zero for increasing n. Furthermore, $\rho(n\Delta t)$ is an even function: $\rho(n\Delta t) = \rho(-n\Delta t)$. Assuming $N \to \infty$ and neglecting the edge effects in the summation, eqn. (4.33) becomes:

$$U_{\bar{x}}^2 = \frac{\sigma_x^2}{N^2}\sum_{i=1}^{N}\sum_{n=-\infty}^{+\infty}\rho\left(n\Delta t\right) = \frac{\sigma_x^2}{N^2}N\sum_{n=-\infty}^{+\infty}\rho\left(n\Delta t\right) = \sigma_x^2\frac{\sum_{n=-\infty}^{+\infty}\rho\left(n\Delta t\right)}{N} \tag{4.34}$$

Defining the effective number of independent samples as:

$$N_{eff} = \frac{N}{\sum_{n=-\infty}^{+\infty} \rho(n\Delta t)} \tag{4.35}$$

leads to:

$$U_{\bar{x}}^2 = \frac{\sigma_x^2}{N_{eff}} \quad \text{or} \quad U_{\bar{x}} = \frac{\sigma_x}{\sqrt{N_{eff}}} \tag{4.36}$$

Typically, the summation of eqn. (4.35) is stopped when the correlation value reaches zero for the first time. Notice that when the samples are uncorrelated, then $\rho(n\Delta t)$ is 1 for $n = 0$ and zero otherwise, so in this case $N_{eff} = N$. Conversely, when the samples are correlated then $\sum_{n=-\infty}^{+\infty} \rho(n\Delta t) > 1$; therefore, N_{eff} is smaller than N, thus the uncertainty of the mean value is larger.

The integral time scale T_{int} is defined as the integral of the auto-correlation function $\rho(t)$ of the time series $x(t)$ (George et al. 1978):

$$T_{int} = \int_0^{\infty} \rho(t)\, dt \tag{4.37}$$

T_{int} is a measure of the time interval over which $x(t)$ is dependent on itself. For time intervals large compared to T_{int}, $x(t)$ becomes statistically independent of itself. Then, the effective number of independent samples can be written as a function of the observation time T and the integral time scale T_{int}:

$$\begin{aligned} N_{eff} &= \frac{N}{\sum_{n=-\infty}^{+\infty} \rho(n\Delta t)} = \frac{N \cdot \Delta t}{\sum_{n=-\infty}^{+\infty} \rho(n\Delta t) \cdot \Delta t} \\ &\approx \frac{T}{\int_{-\infty}^{+\infty} \rho(dt)\, dt} = \frac{T}{2\int_0^{+\infty} \rho(dt)\, dt} = \frac{T}{2T_{int}} \end{aligned} \tag{4.38}$$

The relevance of eqns. (4.36) and (4.38) for experimental measurements in turbulent flows is discussed by Tennekes and Lumley (1972) among others. The equations illustrate the fact that, when $\Delta t < T_{\text{int}}$ and the total observation time T is fixed, increasing the sampling frequency and therefore the number of samples does not improve the accuracy of the derived statistical quantities (Taylor 1997), because the effective number of independent samples stays constant. Instead, it is advantageous to limit the sampling frequency to $1/(2T_{\text{int}})$ and increase the recording time T.

4.2.3 Instantaneous quantities

4.2.3.1 Uncertainty of vorticity

Let us consider a planar-PIV measurement where the velocity components (u, v) are measured in a 2D domain. The out-of-plane vorticity component is defined as:

$$\omega_z = \frac{\partial v}{\partial x} - \frac{\partial u}{\partial y} \tag{4.39}$$

For sake of brevity, we will drop the subscript z in the reminder and we will indicate the out-of-pane vorticity component simply with ω. The velocity components u and v are discrete functions, defined at grid points with uniform spacing d (both in x- and y-direction). As an example, the vorticity can be computed by the central-difference scheme by:

$$\omega(x,y) = \frac{1}{2d}\left[v(x+d,y) - v(x-d,y) - u(x,y+d) + u(x,y-d)\right] \tag{4.40}$$

Other methods using larger kernel sizes are available at the expense of lower spatial resolution of the vorticity field. Using the error propagation eqn. (4.6), the uncertainty of the vorticity at grid point (x,y) is (apart from truncation errors):

$$\begin{aligned} U_\omega^2 &= \left(\frac{1}{2d}\right)^2 \left[U_v^2 + U_v^2 + U_u^2 + U_u^2 - 2\rho(2d)U_v^2 - 2\rho(2d)U_u^2\right] = \\ &= 2\left(\frac{1}{2d}\right)^2 \left[1-\rho(2d)\right]\left(U_u^2 + U_v^2\right) \end{aligned} \tag{4.41}$$

where the following assumptions have been made:

i. The errors of u and v at the same or neighboring spatial locations are uncorrelated (2C-PIV).

ii. The errors of $u(x,y+d)$ and $u(x,y-d)$ are spatially correlated (and similarly the errors of $v(x+d,y)$ and $v(x-d,y)$). The corresponding cross-correlation coefficient, indicated with $\rho(2d)$, is assumed to be the same for the two velocity components. It represents the normalized cross-correlation of the measurement error at two grid points at spatial separation $2d$.

iii. The uncertainty of $u(x,y+d)$ is assumed to be equal to the uncertainty of $u(x,y-d)$ and is indicated with U_u. Likewise, the uncertainty of $v(x+d,y)$ is assumed to be equal to the uncertainty of $v(x-d,y)$ and is indicated with U_v. In practice, an appropriate local average of uncertainties can be taken.

If we further assume that the two velocity components have the same uncertainty ($U_u = U_v = U$), the expression of the uncertainty of the vorticity simplifies to:

$$U_\omega = \frac{U}{d}\sqrt{1-\rho(2d)} \tag{4.42}$$

Eqn. (4.42) shows the proportionality between the uncertainties of vorticity and velocity. The grid spacing d has a twofold effect on U_ω: on the one hand, U_ω is inversely proportional to d, which would cause a reduction of U_ω when d is increased. On the other hand, increasing d yields a reduction of the spatial cross-correlation coefficient and in turn an increase of the square-root term. When the interrogation window overlap is increased, d tends to zero faster than $\sqrt{1-\rho(2d)}$: as a consequence, the uncertainty of the vorticity increases (see figure 4.1). However, two things should be kept in mind: a) eqn. (4.42) accounts only for the random errors of the vorticity and not for the truncation errors, which are systematic and decrease when increasing the interrogation window overlap; b) the uncertainty of the vorticity can be reduced by computing the spatial derivatives using a larger spacing in the finite differences (e.g. using $\left[v(x+2d,y)-v(x-2d,y)\right]/4d$ instead of $\left[v(x+d,y)-v(x-d,y)\right]/2d$).

For noisy data, Vollmers (2001) reports that lower uncertainty can be achieved by computing the vorticity from the flow circulation, rather than via eqns. (4.39) and (4.40). Linear error propagation can be used to evaluate the uncertainty of the vorticity calculated with advanced algorithms; the determination and analysis of that uncertainty goes beyond the scope of the present chapter.

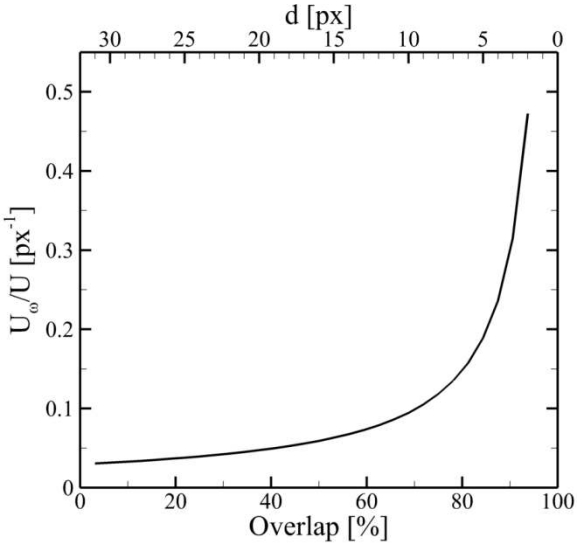

Figure 4.1. Uncertainty of the vorticity as a function of the interrogation window overlap. Results for interrogation window of size 32×32 px².

It can be shown that eqn. (4.42) also corresponds to the uncertainty of the 2D divergence of the velocity. Conversely, for 3D divergence in tomographic PIV, the following expression of the uncertainty is derived:

$$U_{div} = \frac{U}{d}\sqrt{\frac{3}{2}\left[1-\rho\left(2d\right)\right]} \tag{4.43}$$

The above derivations can be modified accordingly when the central-difference scheme is replaced by more elaborate functions, e.g. fitting flow derivatives by a Levenberg-Marquardt algorithm on a 3×3 or 5×5 vector kernel size. For stereo-PIV with non-zero correlations between *u* and *v*, additional terms must be taken into account in the above equations. Stereo-PIV requires the uncertainty propagation of the two 2D2C-vector components into the 2D3C-vector which is covered in section 4.5.

4.2.4 Spatially averaged quantities

When a velocity component is spatially averaged over a profile, region or volume, the uncertainty of the average could be computed either by eqn. (4.11) using the fluctuations of the velocity vectors, or, alternatively, by considering the mean as a simple function and propagating the individual velocity uncertainties according to eqn. (4.6). Usually, the second option is preferred, since the mean should be considered here as an instantaneous quantity and not as a statistically converged value. Most often, the underlying mean and standard deviation will be anyway different at different spatial locations. Only in the case of averaging over isotropic homogeneous turbulence with sufficient data points one could try to measure turbulent statistical values; even in this case, it would be more accurate to record a large number of images over time for unbiased statistics.

The derivation of the uncertainty of the mean is done in the same way as in eqn. (4.31) to (4.36), replacing standard deviations with uncertainties, and replacing temporal correlation of velocity components with the spatial correlation of the velocity errors, which are closely related to the spatial resolution of the PIV processing scheme.

Consider the 1D-case with *N* values of the *u* velocity component averaged along a profile in *x*-direction:

$$\overline{u} = \frac{1}{N}\sum_{i=1}^{N} u_i \tag{4.44}$$

According to eqn. (4.6), the uncertainty of the mean is:

$$U_{\overline{u}}^2 = \sum_{i=1}^{N}\sum_{j=1}^{N}\frac{1}{N^2}\rho\left(\delta u_i,\delta u_j\right)U_{u_i}U_{u_j} \approx \sum_{i=1}^{N}\sum_{j=1}^{N}\frac{1}{N^2}\rho\left(\delta u_i,\delta u_j\right)\overline{U_u^2} \tag{4.45}$$

where, for simplification, the product of individual uncertainties $U_{u_i}U_{u_j}$ is substituted by the mean square uncertainty $\overline{U_u^2}$. The spatial auto-correlation coefficients $\rho(\delta u_i, \delta u_j)$ can be written as a function of the vector grid spacing *d*:

$$\rho\left(\delta u_i, \delta u_j\right) = \rho\left(|j-i|d\right) = \rho\left(nd\right) \tag{4.46}$$

where *n* is the number of grid points between locations *i* and *j*. Neglecting edge effects, i.e. requiring large *N*, eqn. (4.45) leads to:

$$U_{\bar{u}}^2 = \frac{\overline{U_u^2}}{N^2}\sum_{i=1}^{N}\sum_{n=-\infty}^{+\infty}\rho\left(nd\right) = \frac{\overline{U_u^2}}{N^2}N\sum_{n=-\infty}^{+\infty}\rho\left(nd\right) = \frac{\overline{U_u^2}}{N}\sum_{n=-\infty}^{+\infty}\rho\left(nd\right) \tag{4.47}$$

Again, an effective number of independent samples can be defined as:

$$N_{eff} = \frac{N}{\sum_{n=-\infty}^{+\infty}\rho\left(nd\right)} \tag{4.48}$$

thus:

$$U_{\bar{u}} = \frac{U_u^{rms}}{\sqrt{N_{eff}}} \tag{4.49}$$

having defined the root-mean-square averaged uncertainty $U_u^{rms} = \sqrt{\overline{U_u^2}}$.

The integral of the auto-correlation coefficients can be defined as the spatial resolution L_{sr} of the PIV algorithm (see chapter 2), which in pixel units is:

$$L_{sr} = \int_{-\infty}^{+\infty}\rho\left(x\right)dx \tag{4.50}$$

The spatial resolution can also be written relative to the vector spacing *d*:

$$L_{sr}^* = \frac{\int_{-\infty}^{+\infty}\rho\left(x\right)dx}{d} \approx \sum_{n=-\infty}^{+\infty}\rho\left(nd\right) \tag{4.51}$$

In the 2D-case, when the average is conducted over a region of $N_x \times N_y$ vectors, eqn. (4.48) becomes:

$$N_{eff} = \frac{N_x N_y}{L_{sr}^{*2}} \tag{4.52}$$

with L_{sr}^* again in units of vector spacing and assuming the same spatial resolution in *x* and *y*. This is, for example, not the case for advanced locally adaptive PIV schemes with elongated windows e.g. adjusting to boundaries. For a single-pass PIV

processing scheme with a square interrogation window of $n_{pix} \times n_{pix}$ pixel, the correlation function $\rho(x)$ is the triangle function $\left(1-\frac{|x|}{n_{pix}}\right)$ for $|x| \leq n_{pix}$, and 0 otherwise. Hence, the spatial resolution is simply $L_{sr} = n_{pix}$. For a Gaussian weighted interrogation window with a standard deviation of σ, it can be shown that the spatial resolution is equal to $L_{sr} = \sqrt{4\pi}\sigma$. For state-of-the-art PIV algorithms using multi-pass window deformation (like DaVis 8), it has been found that the correlation function – when approximating the PIV algorithm as a linear spatial filter function – is Gaussian with some Mexican-hat contribution leading to slight overshooting for steep velocity step functions as observed by Elsinga and Westerweel (2011). More details are provided in chapter 2.

In practice, the correlation coefficients and spatial resolution need to be specified for a particular set of PIV processing parameters. When the averaging process is conducted with a small number of vectors over a region comparable to the spatial resolution, the simplifying assumptions that led to eqn. (4.49) are not valid anymore. In this case, the uncertainty of the spatial mean must be computed via eqn. (4.6), where all individual correlation coefficients must be taken into account.

4.2.4.1 Spatial correlation of the measurement error

The errors of neighboring vectors are spatially correlated due to the interrogation window overlap. To investigate the spatial correlation of the error, a Monte Carlo simulation is conducted considering a null displacement field. The images have a resolution of 5,000×400 pixels, with a seeding concentration of 0.05 ppp. The particle images have a Gaussian intensity profile with peak intensity of 1024 counts; their diameter is set to 2 pixels. Noise is added to the recordings (white background noise with 5 counts standard deviation and photon shot noise, assuming a conversion factor of 4 electrons per count) to cause errors in the measured velocity. The images are processed with the commercial software DaVis 8.2 from LaVision. The auto-correlation function ρ of the measurement error is computed to investigate the spatial correlation among

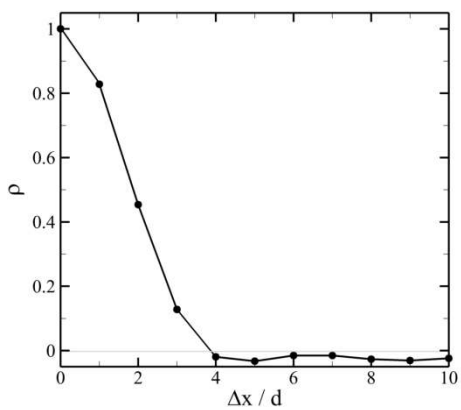

Figure 4.2. Spatial auto-correlation of the measurement error for interrogation window of 32×32 pixels and 75% overlap (see also Figure 2.7, Figure 2.12, and Figure 2.13).

neighboring vectors. The results of figure 4.2, which refer to the case of Gaussian-weighted interrogation window size of 32×32 pixels with 75% overlap, show that a significant correlation is present up to sample spacing of $3d$. Notice that in this case $\rho(2d) \cong 0.45$; hence, the spatial correlation of the error is relevant and cannot be neglected for the computation of the uncertainty of the vorticity via eqn. (4.42). Note that the above mentioned mixture of Gaussian and Mexican-hat filter function of PIV leads here to the slight undershooting of the correlation values below zero.

4.3 Numerical assessment via Monte Carlo simulations

4.3.1 Uncertainty of statistical quantities

The uncertainty of mean, standard deviation, variance and mean square is verified by Monte Carlo simulations. For each sample size N, normally distributed random data are generated with $\bar{x} = 1$ and $\sigma_x = 0.3$, and the statistical quantities of interest are computed. The procedure is repeated 1,000 times to evaluate the standard deviation of the mean, standard deviation, variance and mean square. The results of the Monte Carlo simulations are compared with the theoretical predictions of eqns. (4.11), (4.12), (4.13) and (4.22). Figure 4.3-left shows the uncertainty as a function of the sample size N: as predicted by the theoretical uncertainty propagation equations, the uncertainty decreases with $1/\sqrt{N}$. The agreement between theoretical values and Monte Carlo simulation is excellent.

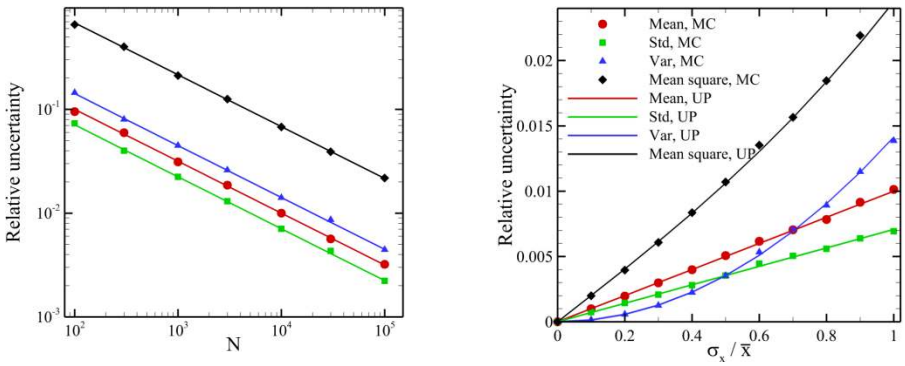

Figure 4.3. Comparison between the results of Monte Carlo simulations (MC) and uncertainty propagation (UP) for the uncertainty of mean, standard deviation (Std), variance (Var) and mean square. Left: uncertainty as a function of the sample size. Right: uncertainty as a function of the sample standard deviation. For mean and standard deviation, the relative uncertainty is computed dividing the absolute uncertainty by σ_x; for variance and mean square, it is computed dividing the absolute uncertainty by σ_x^2. The symbol keys apply to both plots.

The simulation is repeated with constant sample size $N = 10{,}000$ and varying the sample standard deviation σ_x (figure 4.3-right). The uncertainty of mean,

standard deviation and mean square increases linearly with $\sigma_x/\overline{x}$ in the range [0, 1]. Conversely, the uncertainty of the variance features a quadratic increase according to eqn. (4.13).

4.3.2 Uncertainty of vorticity

A Monte Carlo simulation using synthetic vector fields is conducted to assess the accuracy of the uncertainty estimate given by eqn. (4.42). A null velocity field (u = 0, v = 0) is considered on a two-dimensional domain composed by 1,000×100 grid points, yielding a null exact vorticity field ω = 0; thus any measured vorticity directly provides the true error. The grid spacing is set to d = 8 px, which is the typical value obtained with 32×32 px interrogation windows with 75% overlap. Gaussian noise is added to the velocity field to simulate the error encountered in PIV measurements. The noise is spatially correlated to simulate the effect of interrogation window overlap in PIV. The standard deviation of the noise, which coincides with the measurement uncertainty U, is varied between 0.02 px and 0.3 px. Three values of the cross-correlation coefficient $\rho(2d)$ are considered, namely 0, 0.11, 0.45. These values are representative of the cross-correlation coefficient encountered in PIV for overlap factors of 0%, 50% and 75%. The results are averaged (via root-mean-square) in the entire measurement domain and for a total number of 1,000 velocity fields for each value of ρ. An example of instantaneous horizontal velocity field and vorticity field is shown in figure 4.4.

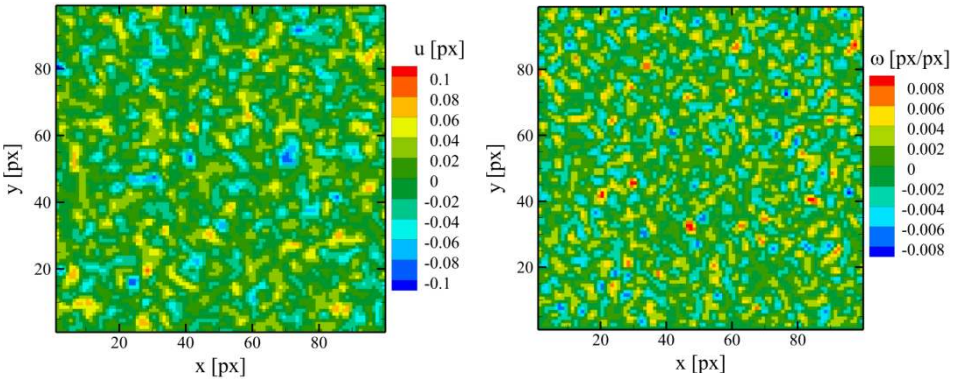

Figure 4.4. Instantaneous horizontal velocity (left) and vorticity fields (right) for the case U = 0.1 px and ρ = 0.45.

The results of figure 4.5 show the excellent agreement between the uncertainty obtained with Monte Carlo simulations and with the theoretical uncertainty propagation (eqn. (4.42)). As predicted, the uncertainty of the vorticity increases linearly with the uncertainty of the velocity. It is also noticed that the spatial correlation of the measurement error (ρ = 0.45) yields a reduction by factor 5 of U_ω with respect to the case where the error is uncorrelated (ρ = 0).

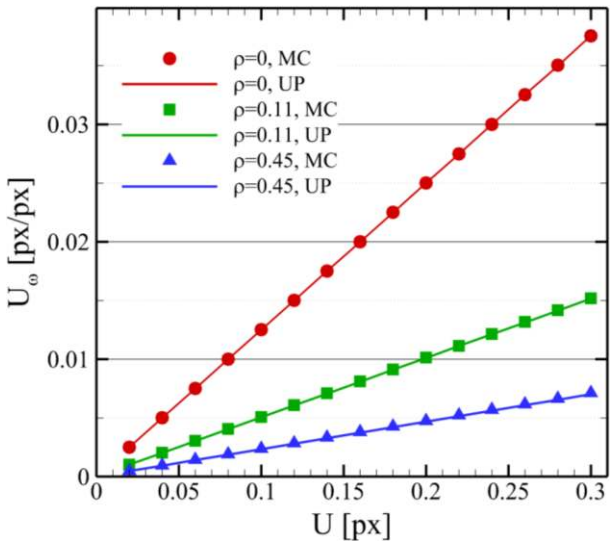

Figure 4.5. Uncertainty of the vorticity as a function of the uncertainty of the velocity. Comparison between Monte Carlo simulation results (MC) and uncertainty propagation (UP).

4.3.3 Effective number of independent samples

The influence of the effective number of independent samples on the accuracy of the statistical results in investigated by Monte Carlo simulations. Three signals are considered, each composed by N = 10,000 samples and having actual mean and standard deviation equal to 1.0 and 0.3, respectively. Signal x_1 is composed by statistically independent samples, whereas the samples of signals x_2 and x_3 are statistically dependent. The integral time scale of the signals is evaluated from the auto-correlation function (ρ_1, ρ_2 and ρ_3, respectively) via eqn. (4.37) (see Figure 4.6). The effective number of independent samples is then computed via eqn. (4.38) and reported in table 4.1.

Table 4.1. Integral time scale and effective number of independent samples for the three signals.

Signal	Total number of samples N	Integral time scale T_{int}	Effective number of samples N_{eff}
x_1	10,000	0.50	10,000
x_2	10,000	1.69	2950
x_3	10,000	6.74	742

For each signal, the mean value is computed. The simulation is repeated 1,000 times to compute the standard deviation of the estimated mean. The latter is compared with the theoretical prediction of eqn. (4.15). The results of Figure 4.7

show the excellent agreement between Monte Carlo simulation and theoretical prediction: the uncertainty of the mean decreases with $1/\sqrt{N_{eff}}$, even if the total number of samples N is the same for the three signals.

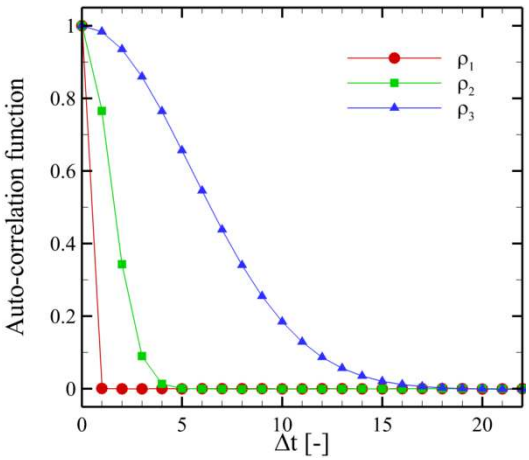

Figure 4.6. Auto-correlation functions of the three signals. Mean values out of 1,000 simulations.

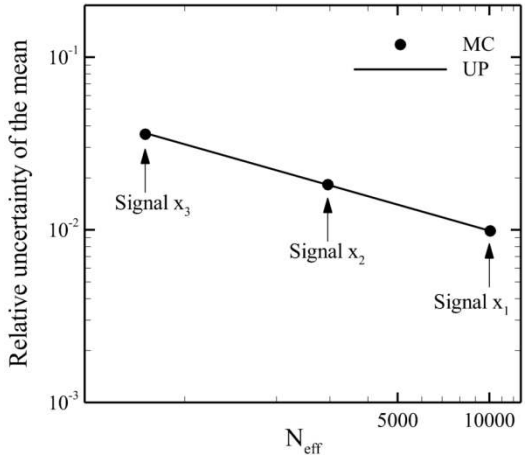

Figure 4.7. Uncertainty of the mean value (relative to the standard deviation) as a function of the effective number of samples N_{eff}. Comparison between Monte Carlo simulation results (MC) and theoretical uncertainty propagation (UP).

4.4 Experimental assessment

4.4.1 Turntable experiment

The first experimental validation has been conducted using a turntable with a diameter of 30 cm rotating at constant speed. A printed pattern with small particles (size of about 200 μm) is applied onto the turn table to simulate flow tracer particles. Images were acquired with a PCO Dimax S4 camera (CMOS sensor, 2016×2016 pixel resolution, 11 μm pixel pitch, 12 bit, maximum 1279 frames per second at full resolution), see figure 4.8-a. The camera mounted a Nikkor lens with 28 mm focal length and the f-number was set to 4.0. The camera was placed at about 1 m distance from the turntable, resulting in a magnification factor of 0.027. A diffusor was mounted between camera and lens to blur the image in order to suppress peak locking errors (Michaelis et al. 2016). The acquisition frequency is 1 kHz with an area of interest of 980×1080 pixels. The illumination was provided by an LED light source. The rotational speed of the turntable was set to 37 rpm (0.61 Hz), yielding a uniform vorticity ω_0 = 0.00758 px/px. Since the exact vorticity is known, the difference between measured and exact value yields the error of the vorticity. The latter quantity is compared with the uncertainty estimated by the linear propagation (eqn. (4.42)).

The images were processed with the LaVision DaVis 8.2 software, using 32×32 pixels interrogation window and 75% overlap factor. An instantaneous vorticity field with the velocity vectors is shown in figure 4.8-b. The root-mean-square of the error of the *x*-displacement and the standard deviation of the error of the vorticity are shown in figure 4.8-c and -e, respectively: both errors are lower in the bottom part of the field of view and increase in the top part due to a reduction of the illumination intensity. The uncertainty of the measured displacement was quantified via the correlation statistics approach (section 3.3). It is verified that the uncertainty U_v of the vertical displacement component (not shown here) is comparable with U_u. The uncertainty of the vorticity is retrieved from the displacement uncertainty via eqn. (4.42), using $U = (U_u + U_v)/2$ and $\rho(2d) = 0.45$ Figure 4.8-d and -f show the root-mean-square of the uncertainty of displacement and vorticity, respectively: both results agree very well with the statistical true error (figure 4.8-c and -e) and reproduce the increase of uncertainty from bottom to top of the field of view.

The measurements were repeated for different overlap factors (0%, 25%, 50% and 75%) and interrogation window sizes of 16×16 and 32×32 px. The uncertainty of the vorticity computed via eqn. (4.42) was averaged in space and time over the entire set of 200 fields and compared with the root-mean-square of the vorticity error. The results of the comparison are illustrated in figure 4.9. The agreement between uncertainty propagation from eqn. (4.42) and true uncertainty (stemming from the actual error of the vorticity) is very good.

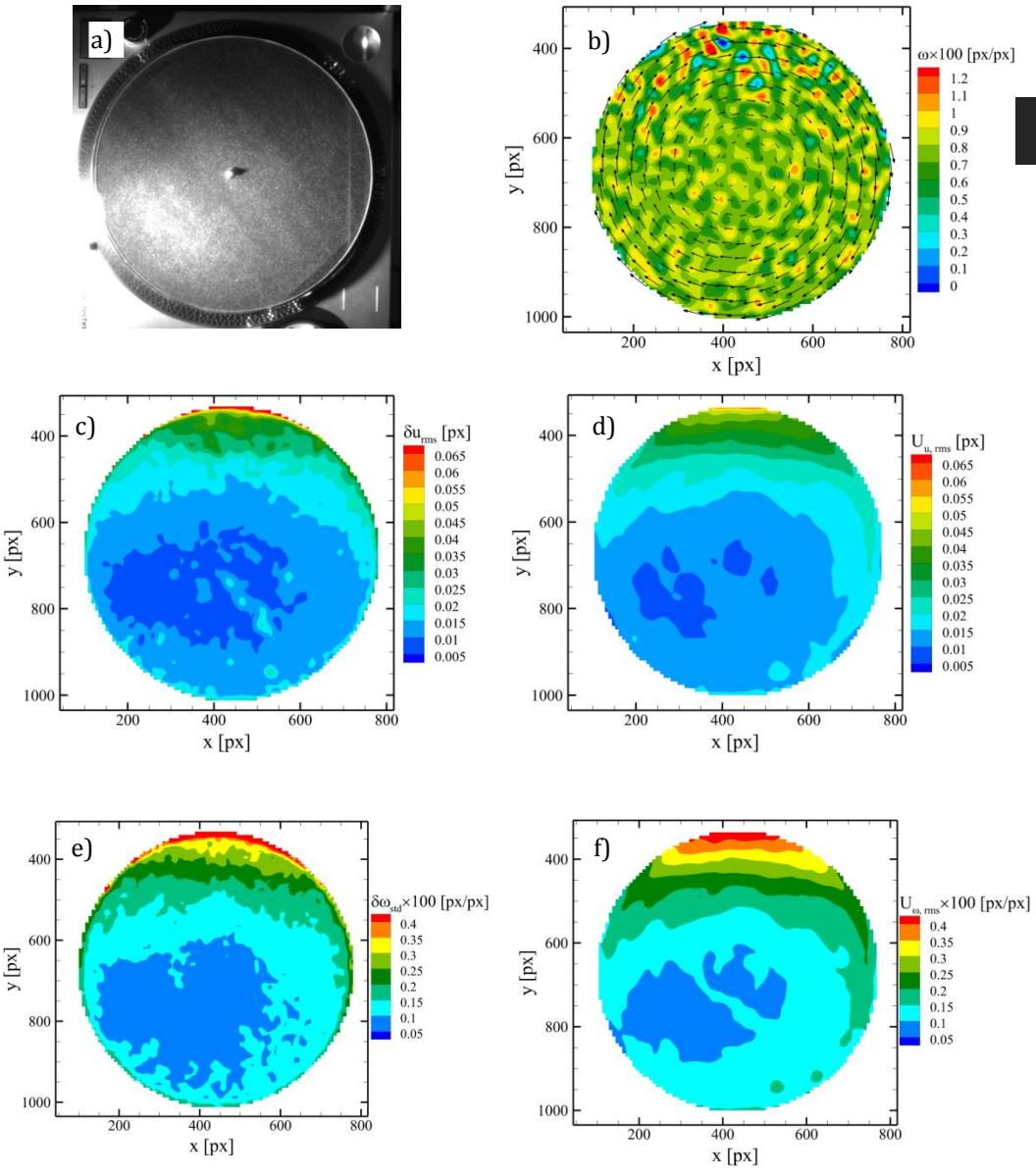

Figure 4.8. a) Raw image of the turntable; b) Measured instantaneous vorticity field with velocity vectors. For sake of clarity, one of 4 vectors is displayed both in x- and y-direction; c) Root-mean-square of the actual error of the x-displacement; d) Root-mean-square of the uncertainty of the x-displacement computed with the correlation statistics method; e) Standard deviation of the actual error of the vorticity; f) Root-mean-square of the uncertainty of the vorticity, estimated with eqn. (4.42).

Figure 4.9 shows that the uncertainty of the vorticity increases with reducing the interrogation window size, because less information carriers are contained in a

smaller window. Furthermore, the uncertainty increases with the overlap factor, because a smaller grid spacing d results in larger uncertainty of the vorticity according to eqn. (4.42). However, it is important to notice that high overlap factors lead to higher spatial resolution of the vorticity field (smaller d), thus in general to less truncation errors and higher peak vorticity levels at the expense of higher noise.

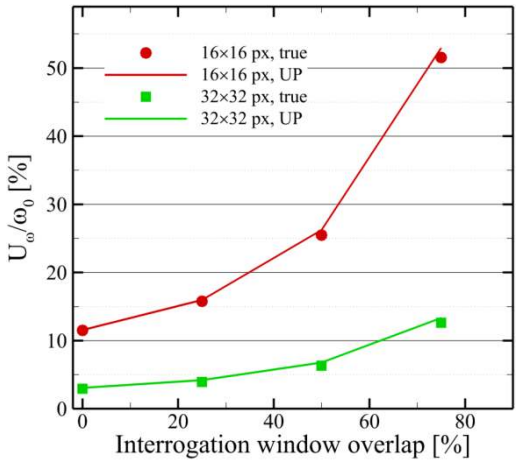

Figure 4.9. Comparison between true vorticity error and uncertainty propagation (UP) result. Root-mean-square in time over 200 velocity fields and space in the rectangular region x∈[291; 594] px, y∈[732; 941] px.

4.4.2 Turbulent flow

The uncertainty propagation methodology is applied to two PIV measurements of a turbulent flow. The first one is the rectangular jet flow described in Neal et al. (2015). The peculiarity of the database is that two PIV measurement systems were used, namely the *measurement system* (MS) and the *high-dynamic range* system (HDR). The latter is composed by two cameras in stereoscopic configuration and features a magnification factor larger by factor 3. Via comparison with hot-wire measurements, Neal et al. (2015) showed that the HDR system yields more accurate results by about factor 4 with respect to the measurement system. As a consequence, the HDR velocity can be used as a reference to retrieve the error of the MS data. The parameters of the experiment are reported in table 4.2. The measurements were conducted at x/h = 20, being x the streamwise direction and h the jet height, where the turbulent flow is in the turbulent regime.

The MS images were processed with LaVision DaVis 8.2 with 16×16 pixels interrogation window with Gaussian window weighting and 75% overlap factor. For the HDR images, 48×48 pixels interrogation windows with Gaussian weighting and 75% overlap factor were selected. Notice that, due to the difference in optical magnification factor, the different interrogation windows yielded approximately the same spatial resolution for the two systems. The HDR velocity fields were finally

mapped onto the MS coordinate system. The time-average velocity field and the turbulence intensity, defined as $TI = \sqrt{\left(\sigma_u^2 + \sigma_v^2\right)/2}$, are shown in figure 4.10: the turbulence intensity is about 12% of the time-average velocity.

Table 4.2. Parameters of the rectangular jet experiment.

Seeding	Glycol-water droplets, 1 μm diameter
Illumination	Photonics Industries DM40-527 laser
Recording device	MS: LaVision HighSpeedStar 5 CMOS camera HDR: 2× LaVision HighSpeedStar 6 CMOS camera
Imaging	MS: Nikon objective, f = 105 mm, f# = 4 HDR: Nikon objectives, f = 105 mm, f# = 5.6
Field of view	MS: 69.3×69.3 mm^2 HDR: 22.8×22.8 mm^2
Acquisition frequency	10,000 Hz
Magnification factor	MS: 0.126; HDR: 0.449
Number of images	MS: 8,000; HDR: 20,000

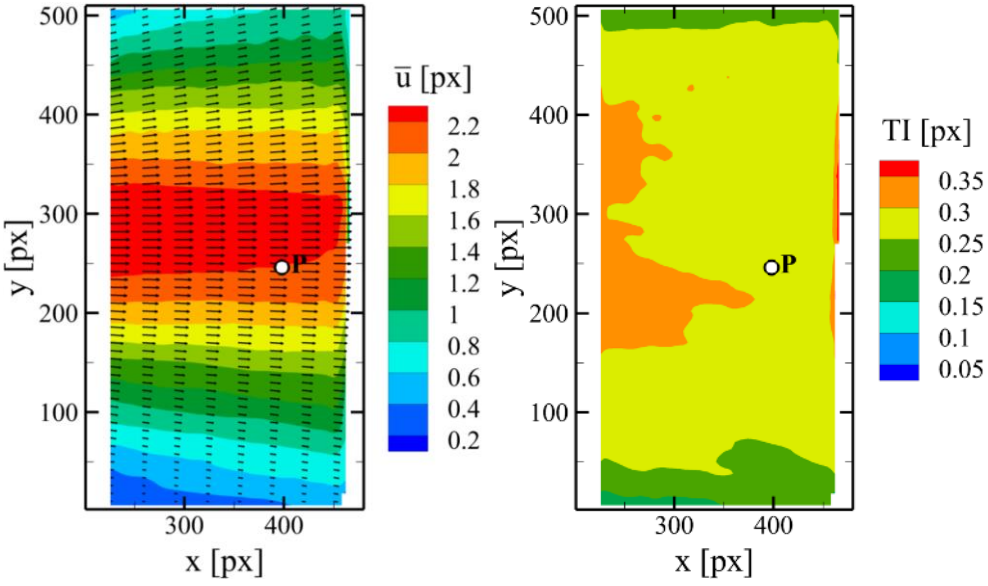

Figure 4.10. Left: time-average velocity field. For sake of clarity, one every eight vectors is shown in the horizontal direction, one every two in the vertical direction. Right: turbulence intensity.

The second experiment is a PIV measurement over a cavity flow. The experiment is conducted in the M-tunnel, a low-speed open-jet open-return wind tunnel of the Aerodynamics Laboratories of TU Delft. The wind tunnel has a squared test section of 40×40 cm^2. The cavity model is made out of wood and has height H = 2 cm and spanwise dimension W = 40 cm. The length of the cavity is L = 24 cm. The free-stream velocity is set to 5 m/s, yielding a Reynolds number Re_H = 6,500 based on the cavity height. A series of 2,000 uncorrelated image pairs are acquired at acquisition frequency f_{acq} = 8.3 Hz. The field of view, which is 70×55 mm^2, is positioned 3H downstream of the beginning of the cavity. The resulting magnification factor is 0.093. The parameters of the cavity flow experiment are reported in table 4.3. A sketch of the cavity flow experiment is shown in figure 4.11. Further details of the experiment are reported in Iannetta et al. (2016).

Table 4.3. Parameters of the cavity flow experiment.

Seeding	Glycol-water droplets, 1 μm diameter
Illumination	Quantel Evergreen Nd:YAG Laser (200 mJ @ 15Hz)
Recording device	LaVision Imager LX 2MPx
Imaging	f = 75 mm, f# = 3.9
Field of view	70×55 mm^2
Acquisition frequency	8.33 Hz
Magnification factor	0.093
Number of images	2,000

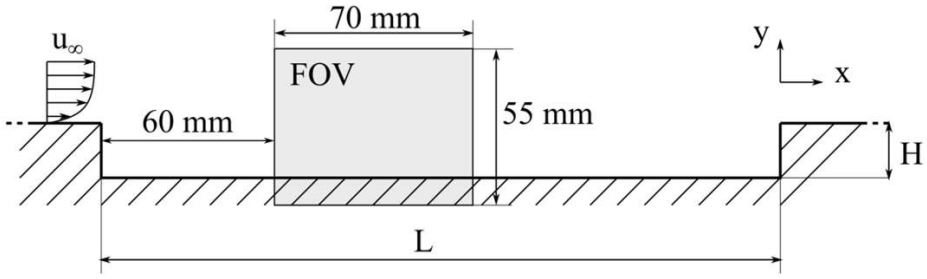

Figure 4.11. Sketch of the cavity flow experiment.

Uncertainty of the vorticity

To assess the uncertainty of the vorticity, the rectangular jet data are used. The velocity time series is extracted at a point P = (398, 246) as shown in Figure 4.12. Figure 4.13 shows a portion of the vorticity time series for a time interval of 10 ms.

The comparison between MS and HDR data on the entire time series yields the error for the MS reported in table 4.4. It is noticed that: a) the two error components δu and δv have comparable magnitude; b) the random component of the error (error standard deviation) is significantly larger than the mean bias component.

Table 4.4. Actual error and estimated uncertainty at P.

	Mean error	Error standard deviation	Error root-mean-square (rms)	Uncertainty rms
u-component [px]	–0.005	0.060	0.060	0.063
v-component [px]	–0.021	0.060	0.063	0.064
vorticity [px/px]	0.0008	0.0104	0.0104	0.0116

The vorticity is computed with the central-difference scheme of eqn. (4.40), with grid spacing d = 4 px. The vorticity time series for the first 10 ms is shown in figure 4.13. Both HDR and MS yield the same peak vorticity (ω_{max} = – 0.15 px/px at t = 2.2 ms), which confirms that the two systems have the same spatial resolution. The vorticity error $\delta\omega$ is computed as the difference between MS and HDR vorticity. The results of table 4.4 show that the random error dominates over the mean bias error.

The uncertainty at P is again evaluated with the correlation statistics method. Uncertainty propagation is done according to eqn. (4.42) using d = 4 px, $U = (U_u + U_v)/2$ and $\rho(2d)$ = 0.45. The root-mean-square of the uncertainty is equal to $U_{u,rms}$ = 0.063 px and $U_{v,rms}$ = 0.064 px, which agrees very well with the error root-mean-square of 0.060 and 0.063, respectively. The calculation is repeated in the entire measurement domain in common between HDR and MS. The contours of figure 4.14 illustrate the comparison between the rms of the error and the uncertainty of the vorticity. Both uncertainty and error exhibit small variations within the considered domain, with values between 0.010 and 0.016 px/px. Again, the agreement between estimated uncertainty and error is very good.

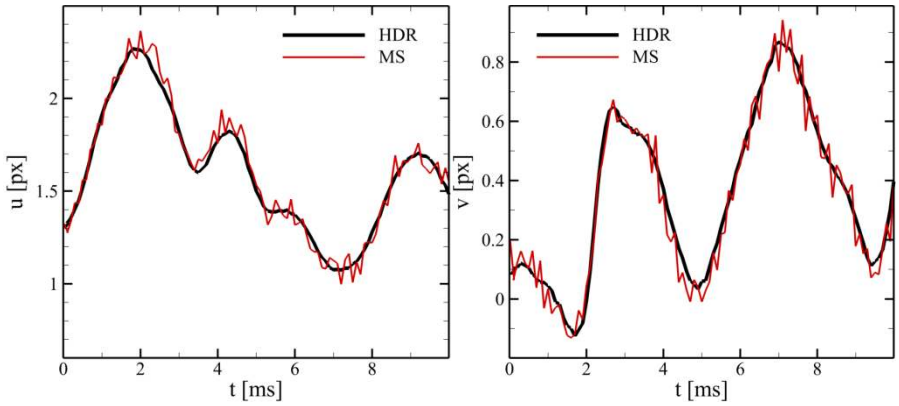

Figure 4.12. Longitudinal (left) and transverse (right) velocity time series at point P.

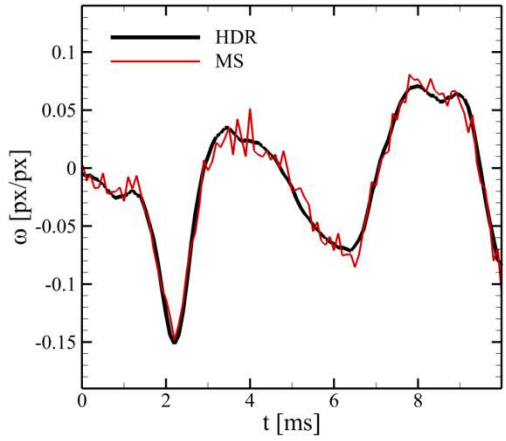

Figure 4.13. Comparison between MS and HDR vorticity time series at P.

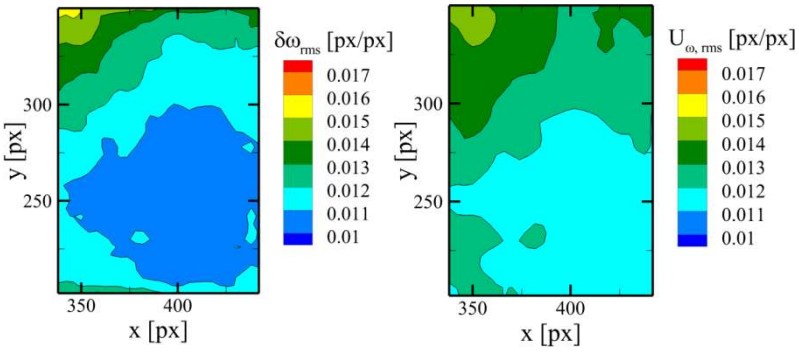

Figure 4.14. Comparison between root-mean-square of the vorticity error (left) and root-mean-square of the estimated vorticity uncertainty (right).

4.4.2.1 Uncertainty of statistical quantities

The time-resolved jet data are not suited for statistical analysis because the low effective number of independent samples (N_{eff} =243, despite the total number of samples is N = 8,000) does not guarantee the statistical convergence of the results. Hence, to assess the uncertainty of statistical flow properties, the cavity flow data are used, where 2,000 statistically independent velocity field are available.

Velocity data are extracted at a point P located close to the reattachment point; the turbulence intensity in P is equal to 22.0% of the free-stream velocity. The entire set of 2,000 samples is divided into 100 independent subsets composed by 20 samples each. The statistical flow properties, namely time averages and Reynolds stresses, are computed from the subsets and compared with the value obtained with the entire set. Figure 4.15-left shows the comparison between the time-averaged vertical velocity computed with the subsets of 20 samples and that evaluated from the entire set of 2,000 samples. The uncertainty bars are evaluated with eqn. (4.15) and correspond to a theoretical confidence level of 68%. In most of the cases the results agree within the uncertainty of the measured mean velocity. To assess the accuracy of the uncertainty propagation formulae, the uncertainty coverage for different statistical quantities is computed and displayed in figure 4.15-right. The uncertainty coverage is defined as the number of samples for which the error is smaller than or equal to the estimated uncertainty.

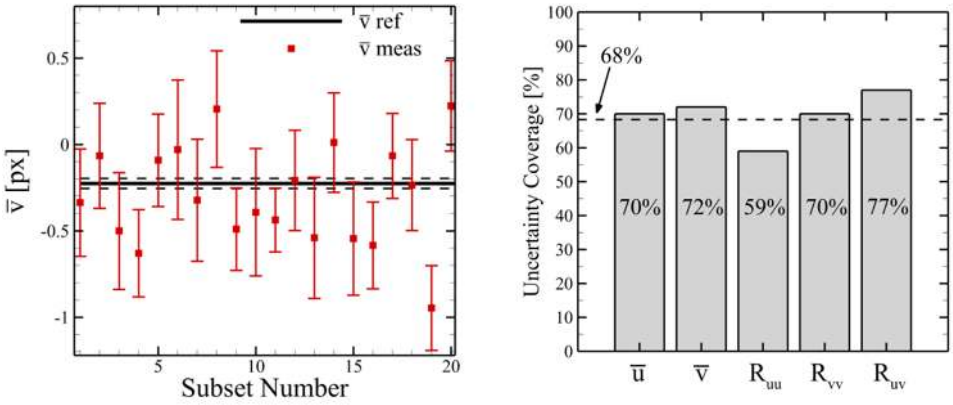

Figure 4.15. Left: comparison between time-averaged vertical velocity obtained with the subsets of 20 samples and that computed with the entire set of 2,000 samples. For sake of clarity, only the first 20 subsets (out of 100) are shown. The uncertainty bars are evaluated at 68% confidence level with the corresponding uncertainty propagation formula. The uncertainty of the reference value is displayed with a dashed black line. Right: uncertainty coverage for different statistical quantities. The theoretical uncertainty coverage for Gaussian error distribution is 68%.

In case of Gaussian error distribution, the theoretical uncertainty coverage is about 68%. The results of figure 4.15-right show the accuracy of the uncertainty propagation methodology: the uncertainty of the time-averaged quantities ($\overline{u}$ and

$\bar{v}$) is accurate within 5%, whereas that of the Reynolds stresses is accurate within 10%.

The effect of the number of samples on the accuracy of the statistical results is shown in Figure 4.16. It is evident that the random uncertainty of the mean (Figure 4.16-a) is initially large and decreases with increasing sample size. In the entire range of sample sizes considered, the reference mean velocity is within the uncertainty bounds estimated with eqn. (4.15). Similarly, the normal Reynolds stress R_{vv} converges to the reference value with rate $1/\sqrt{N}$ (Figure 4.16-b). For low sample size (N < 250), the measured R_{vv} overestimates the reference value due to the effect of spurious fluctuations by about 10%.

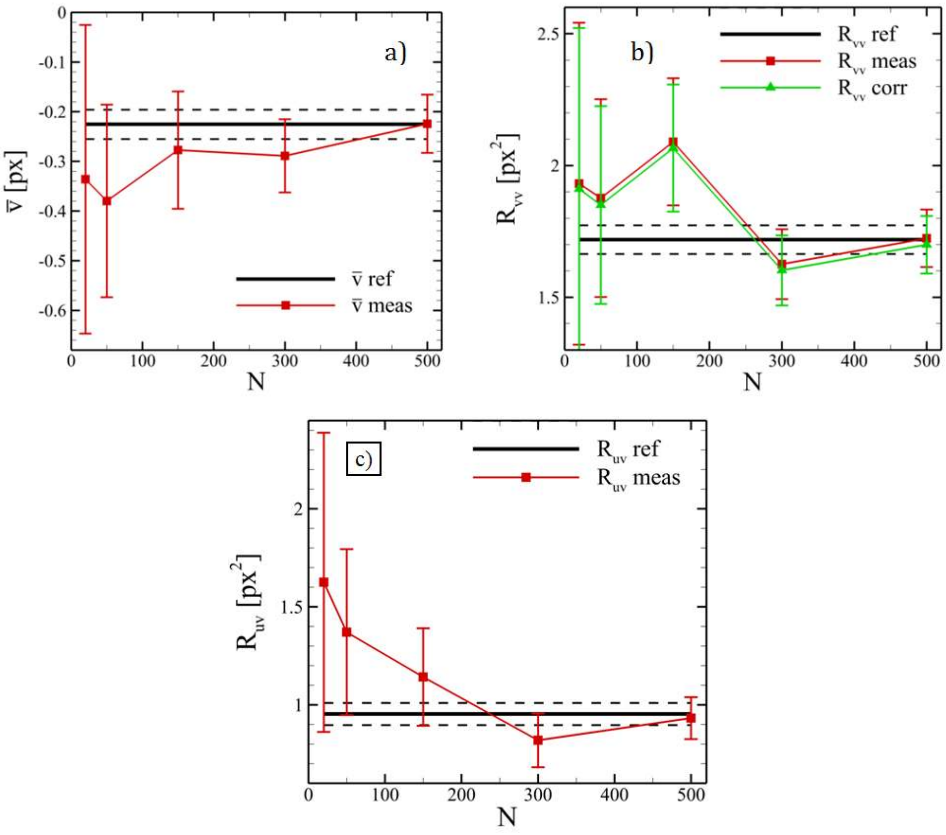

Figure 4.16. a) Convergence of the mean vertical velocity as a function of the sample size. b) Convergence of the Reynolds normal stress as a function of the sample size. c) Convergence of the Reynolds shear stress as a function of the sample size. In all plots, the uncertainty bars are evaluated at 68% confidence level with the corresponding uncertainty propagation formula. The uncertainty of the reference value is displayed with a dashed black line.

A corrected value of R_{vv} is computed by subtracting the mean-square fluctuation: $R_{vv,\,corr} = R_{vv} - U_{rms}^2$. The uncertainty of uncorrected and corrected R_{vv} is computed via eqn. (4.18) and (4.23), respectively. The two uncertainties are the same within 1%, meaning that the uncertainty of R_{vv} is mainly due to statistical convergence rather than to the measurement uncertainty of u and v. For a correction of less than 1%, one would need at least 20,000 independent samples according to eqn. (24) before the uncertainty of the Reynolds stress decreases to the same level as the correction term U_{rms}^2. Generally, a correction remains useful for low levels of Reynolds stress comparable to the uncertainties.

The Reynolds shear stress R_{uv} is illustrated in Figure 4.16-c. To compute the uncertainty U_{Ruv}, the cross-correlation coefficient between u and v is calculated: ρ_{uv} =0.41. The measured R_{uv} converges to the reference value with rate $1/\sqrt{N}$. As the estimated uncertainty, also the measurement error (difference between measured and reference value) decreases with increasing the sample size.

4.5 Stereo-PIV Uncertainty

The main task is to propagate the uncertainties of the two 2C-vectors computed from the two cameras into the final 3C-vector. Let's assume that, like in Davis, the 2C-vectors (u_1,v_1) and (u_2,v_2) for the two cameras are already computed in the dewarped images at the same correct (X,Y,Z=0)-position. They are converted by the 3C-reconstruction step into world displacements (u,v,w) by some reconstruction function F, typically implemented by the 'normal' equation (see also Arroyo and Greated 1991; Prasad and Adrian 1993; Willert 1997; Soloff et al. 1997; Prasad 2000; Giordano and Astarita 2009):

$$\begin{pmatrix} u \\ v \\ w \end{pmatrix} = \begin{pmatrix} F_u\left(u_1, v_1, u_2, v_2, M\right) \\ F_v\left(u_1, v_1, u_2, v_2, M\right) \\ F_w\left(u_1, v_1, u_2, v_2, M\right) \end{pmatrix} \tag{4.53}$$

where M stands for the set of mapping function parameters. By uncertainty propagation, the uncertainties U_{u1}, etc. determine the uncertainties of (u,v,w), e.g. here shown for u:

$$U_u^2 = \left(\frac{\partial F_u}{\partial u_1}\right)^2 U_{u_1}^2 + \left(\frac{\partial F_u}{\partial v_1}\right)^2 U_{v_1}^2 + \left(\frac{\partial F_u}{\partial u_2}\right)^2 U_{u_2}^2 + \left(\frac{\partial F_u}{\partial v_2}\right)^2 U_{v_2}^2 \tag{4.54}$$

assuming that the error of components (u_1,v_1,u_2,v_2) are independent with zero covariance terms and ignoring any systematic and random uncertainties of the calibration mapping function.

The function derivatives are easily computed by numerical differentiation, e.g.:

$$\frac{\partial F_u\left(u_1,v_1,u_2,v_2,M\right)}{\partial u_1}=\frac{F_u\left(u_1+\Delta u_1,v_1,u_2,v_2,M\right)-F_u\left(u_1,v_1,u_2,v_2,M\right)}{\Delta u_1} \tag{4.55}$$

Calibration errors are difficult to quantify. They are mostly systematic in nature but of unknown magnitude. In this respect, some work has been done by Bhattacharya et al. (2016) analyzing the effect of calibration misalignments which, hopefully, can be fully corrected by the Stereo-PIV self-calibration procedure (see section 6.2).

Finally, one needs to compute the inter-component correlation coefficients:

$$\begin{aligned}\rho\left(\delta u,\delta v\right)&=\frac{\mathrm{cov}\left(\delta u,\delta v\right)}{U_u U_v}\\&=\frac{\frac{\partial F_u}{\partial u_1}\frac{\partial F_v}{\partial u_1}U_{u_1}^2+\frac{\partial F_u}{\partial v_1}\frac{\partial F_v}{\partial v_1}U_{v_1}^2+\frac{\partial F_u}{\partial u_2}\frac{\partial F_v}{\partial u_2}U_{u_2}^2+\frac{\partial F_u}{\partial v_2}\frac{\partial F_v}{\partial v_2}U_{v_2}^2}{U_u U_v}\end{aligned} \tag{4.56}$$

again, using the independence of the errors of (u_1,v_1,u_2,v_2). This is in the same way computed for ρ(δu,δw) and ρ(δv,δw). Unfortunately, these correlation coefficients are in general non-zero and locally changing, adding an extra level of complexity and storage requirement in the PIV software for subsequent uncertainty propagation.

Let's look at two simplified cases (Figure 4.17) of camera setup to investigate the magnitude and significance of these inter-component correlation coefficients.

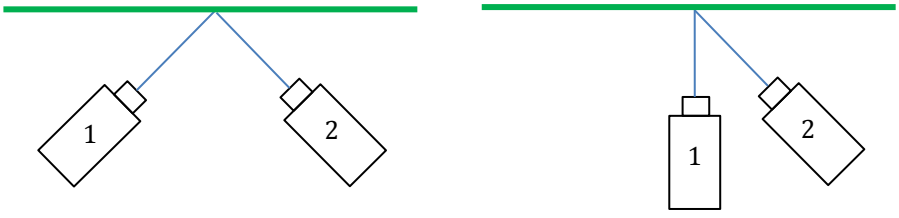

Figure 4.17. Case A (left) and case B (right) setup.

Case A: Typical setup: cameras aligned along the x-axis at ±45 degree viewing angle

At least in the middle of the image, 3C-reconstruction function F (standard 'normal eqn.') is given by:

$$u=\left(u_1+u_2\right)/2,\quad v=\left(v_1+v_2\right)/2,\quad w=\left(u_1-u_2\right)/2 \tag{4.57}$$

with correlation coefficients:

$$\rho(\delta u,\delta w)=\frac{U_{u_1}^2-U_{u_2}^2}{U_{u_1}^2+U_{u_2}^2},\quad \rho(\delta u,\delta v)=\rho(\delta v,\delta w)=0 \tag{4.58}$$

Usually, the uncertainties U_{u1} and U_{u2} are similar in magnitude leading to small correlation values between the coupled u and w-component. Thus, derived statistical quantities like Reynolds shear stress (see eqn. (4.29)), where this correlation enters as an average, will be very little influenced.

Case B: Asymmetric setup: camera 1 looking perpendicular, camera 2 at +45 degrees

Function F is given by:

$$u=u_1,\quad v=(v_1+v_2)/2,\quad w=u_1-u_2 \tag{4.59}$$

with correlation coefficients:

$$\rho(\delta u,\delta w)=\frac{U_{u_1}}{\sqrt{U_{u_1}^2+U_{u_2}^2}},\quad \rho(\delta u,\delta v)=\rho(\delta v,\delta w)=0 \tag{4.60}$$

Clearly, the uw-correlation is non-zero. Since camera 2 is viewing the light sheet from 45° angle, it has $\sqrt{2}$ less pixels of the original image available for each interrogation window compared to camera 1. On average, one expects therefore $U_{u_2}\approx\sqrt[4]{2}U_{u_1}$ and an average $\rho(\delta u,\delta w)\approx 0.64$ with an elevated R_{uw} in eqn. (4.29).

In Davis, the locally changing non-zero inter-component correlation coefficients are stored together with each velocity vector. For correct uncertainty propagation, modifications to a number of derived instantaneous (e.g. vorticity) or statistical quantities have been made.

4.6 Summary

The present study proposes a mathematical framework for the propagation of the instantaneous measurement uncertainty to derived quantities of interest, either instantaneous (e.g. velocity derivatives, vorticity, divergence) or statistical (mean, Reynolds stresses, turbulent kinetic energy). The framework relies upon the use of linear error propagation.

For statistical quantities, the uncertainty is typically dominated by random errors due to the finite sample size. The uncertainty decreases with $1/\sqrt{N_{eff}}$, being N_{eff} the effective number of independent samples. It is noticed that, in many time-resolved PIV experiments, N_{eff} may be significantly lower than the total number of samples N, thus yielding an uncertainty of statistical quantities larger than that obtained when the samples are statistically independent. The quantification of the uncertainty of statistical quantities does not require the knowledge of the uncertainty of the instantaneous velocity fields. Nevertheless, the instantaneous

uncertainty allows correcting the normal Reynolds stress for the spurious fluctuations due to random errors. In fact, in absence of systematic errors due to peak locking or spatial modulation, the random errors have the effect to increase the measured normal Reynolds stress with respect to the actual one. The uncertainty of velocity spatial derivatives (e.g. vorticity and divergence) depends upon the spatial correlation of the measurement error along *x*- and *y*-directions. The latter is related to the measurement spatial resolution, which can be evaluated from the sum of the error spatial auto-correlation values. Although the error correlation is typically unknown in an experiment, it can be estimated a-priori by Monte Carlo simulations for a given set of PIV processing parameters.

The proposed uncertainty propagation methodology is assessed via both Monte Carlo simulations and experiments. The Monte Carlo simulations showed the accuracy of the estimated uncertainty for varying testing conditions (sample size, signal variance, error correlation) under the assumption of Gaussian error distribution of the velocity. In the experimental assessment, the reference velocity is either known (turntable experiment) or estimated with an auxiliary PIV system featuring a higher dynamic range (turbulent flow experiment), as done in Neal et al. (2015), or evaluated with a much larger sample size for statistical convergence. From the experimental assessment, three main conclusions can be drawn:

i. When the spatial correlation of the error is correctly taken into account, the uncertainty of the vorticity is estimated typically within 5-10% accuracy.
ii. When the actual flow fluctuations are larger than the instantaneous uncertainties, the uncertainty of statistical quantities is dominated by the finite sample size rather than the random instantaneous uncertainties.
iii. the uncertainty of the time-averaged quantities ($\overline{u}$ and $\overline{v}$) is accurate within 5%, whereas that of the Reynolds stresses is accurate within 10%.

PIV uncertainty quantification for derived flow quantities is an ongoing subject of research assessing currently available derivations and to identify possible improvements.

5

PIV anisotropic denoising using uncertainty quantification

This chapter has been published in Wieneke (2017) PIV anisotropic denoising using uncertainty quantification, Exp in Fluids, 58:94.

5.1 Introduction

The fundamental challenge to any PIV processing scheme is to select the optimal spatial resolution - mainly determined by interrogation window size and overlap factor - for a given image quality and information density or signal-to-noise ratio. In many cases this is not uniform across the image or varying from image to image. Typically, one tries to find some compromise in interrogation window size and other processing parameters which work reasonably well everywhere. Instead, it would be advantageous to locally adapt the spatial resolution.

For this purpose, several adaptive PIV techniques have been developed taking into consideration local seeding densities, flow gradients or physical constraints like walls, locally adjusting the interrogation window position, size and shape (Scarano 2004b; Theunissen et al. 2007, 2008, 2010; Wieneke and Pfeiffer 2010; Astarita 2009). These techniques have shown to reduce the systematic and random noise level significantly, in particular close to object surfaces.

For time-resolved PIV (TR-PIV), one can (additionally) use the temporal information for noise reduction applying various multi-frame correlation techniques (Hain and Kähler 2007; Sciacchitano et al. 2012; Jeon et al. 2014; see also recent PIV Challenge: Kähler et al. 2016).

Once a velocity field has been obtained, various post-processing noise-reduction schemes can be applied, among them standard spatial top-hat or Gaussian smoothing filters, polynomial regression fits or POD analysis (Raiola et al. 2014). For TR-PIV, more options are available since the noise is usually less correlated in time than in space. For example, Oxlade et al. (2012) apply a spectral white noise subtraction recovering the true velocity spectra. Vétel et al. (2011) use an optimal temporal Wiener filter with better results than convolution- or wavelet-based filters.

Other denoising approaches utilize physical constraints. In particular, for volumetric data and divergence-free incompressible flows one can use the criterion of non-zero divergence for uncertainty quantification (Sciacchitano and Lynch 2015) as well as reducing the noise by making the flow field divergence-free (de Silva et al. 2013; Schiavazzi et al. 2014; Azijli and Dwight 2015; Wang et al. 2016). Atkinson et al. (2014) estimate the noise of volumetric velocity data directly from the velocity fields and apply an appropriate spatial filter to achieve more accurate turbulent power spectra. For time-resolved volumetric data one can apply Navier-Stokes or some simplified version as a regularizer. For example, Schneiders et al. (2015) apply a time-marching vortex-in-cell procedure to average multiple flow fields with more accurate results than retrieved with spatial/temporal moving average and polynomial regression filters.

The main issue for any denoising scheme is to select the appropriate spatial or temporal filter kernel size, which should be as large as possible to average out the random noise and short enough not to reduce the amplitude of true flow fluctuations (truncation errors). With recent work on PIV uncertainty quantification

(Charonko and Vlachos 2013; Timmins et al. 2012; Sciacchitano et al. 2013; Wieneke 2015; Sciacchitano and Lynch 2015) it is now possible to estimate the uncertainty of each computed vector. This can help to guide any denoising scheme for optimal noise reduction while preserving the true flow fluctuations.

The anisotropic denoising filter described here is based on local polynomial approximation (LPA) with locally adaptive kernel size well known in the digital signal processing community (e.g. Katkovnik 2005; Browne et al. 2007) for 1D- and 2D-data (images). While adaptive LPA estimates the local noise level from the residual between the fitted and the original data, direct knowledge of the PIV uncertainties is employed here to guide the size and shape of the final 2D filter kernel size. This anisotropic denoising scheme is finally validated using synthetic and experimental vector field data.

5.2 Method

The denoising scheme described here is restricted to planar velocity fields with u, v, and possibly w-components together with uncertainty values U_u, U_v, U_w on a 1-sigma-level, i.e. the true velocity value u_{true} is expected to lie within $u \pm U_u$ with a probability of 68%. Denoising is done independently for each vector of the flow field.

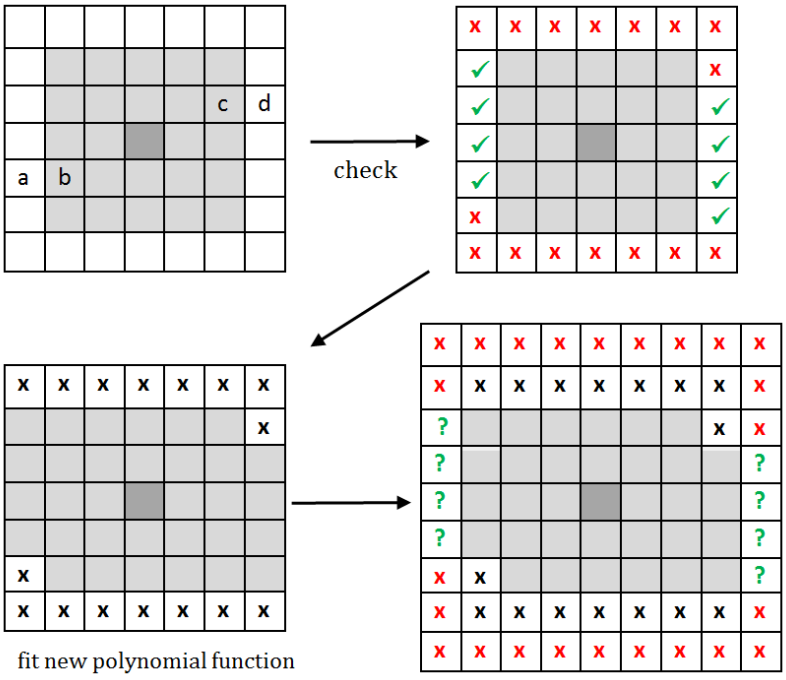

Figure 5.1. Adding a new shell to the filter kernel.

At the beginning, for each vector component (u,v,w) a second-order 2D-polynomial function is fitted to a 5x5 vector neighborhood around the center vector. The uncertainty of the vectors in the 5x5 neighborhood is averaged and taken as a reference in the following. Vectors just outside the center 5x5 region (white squares in Figure 5.1) are tested if they should be added to the filter kernel. Vector a and at the same time vector d on the opposite will be added if both adjacent inner vectors b and c are part of the filter kernel, and if all components (u,v,w) of vectors a and d are within an uncertainty band around the fitted polynomial function as shown in Figure 5.2.

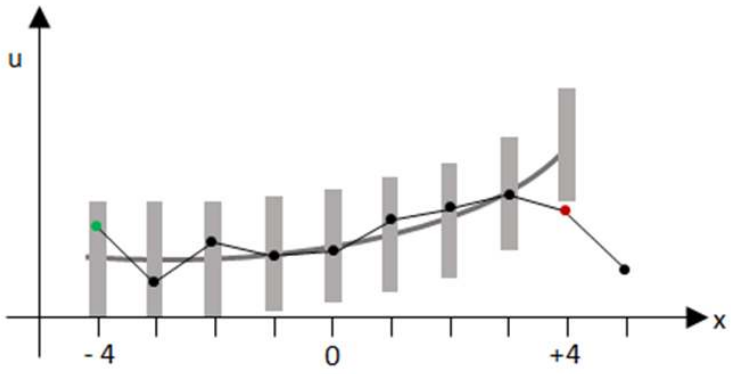

Figure 5.2. Polynomial function computed around the center vector at x=0 with data between -3 and +3 and extrapolated to ±4. Red vector at +4 is rejected since it lies outside the grey uncertainty band.

If any of the conditions fails, then both vectors, a and d, will be discarded, and subsequently all vectors further out in this direction are prevented to become part of the smoothing kernel. With such a symmetrical vector addition, the center of mass of the filter kernel remains at the center vector location for all kernel shapes. The resulting 2D-array of valid vectors is then made more compact and regular by deleting vectors if they have ≤ 2 neighbors and adding vectors if they have ≥ 5 neighbors, even if they would be rejected otherwise.

The uncertainty band (Figure 5.2) is given by $\pm$ S times the uncertainty (provided on a 1-sigma level), where S is a user-selected filter strength, as shown later typically set to around 2.5 - 3.5. A narrow band of $\pm$ 1-sigma would be too tight, since with a probability of 32% a vector falls outside this range preventing the growth of the filter kernel. The procedure stops when no more vectors are added or when a user-selected maximum kernel size is reached. At the end, the often quite irregular shape of the filter kernel is converted to a closest ellipse (Figure 5.3). The difference in performance with and without ellipse fitting is only minor.

Then LPA is executed on the vector field inside the filter kernel, and the center vector is replaced by the value of the polynomial function at the center location. Since the spatial derivatives of the flow field are readily available from the fitted

polynomial function, they are stored, e.g. for subsequent vorticity or divergence computation.

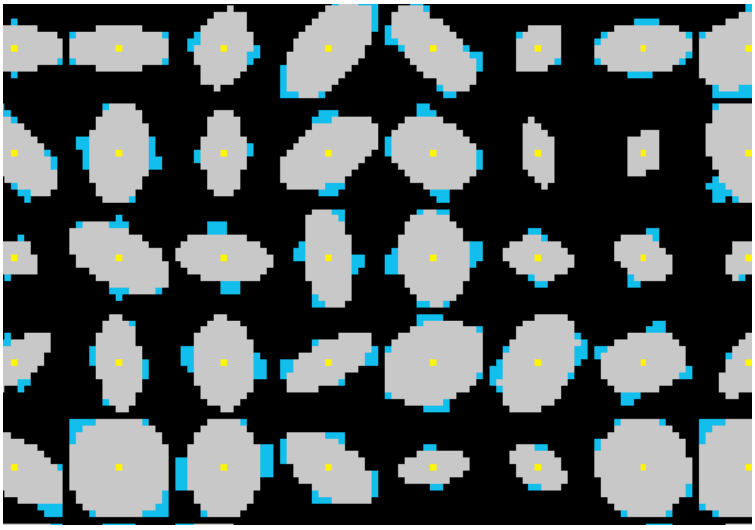

Figure 5.3. Final filter kernel (blue) is converted to an ellipse (gray) shown for every 13th vector.

Finally, the procedure computes a new uncertainty for each vector component using the uncertainty propagation rules outlined in Sciacchitano and Wieneke (2016). A simplified version is used here by taking the reference uncertainty divided by sqrt(N_{eff} - 6), where N_{eff} is the number of independent vectors in the final filter kernel and 6 is the number of parameters (degrees of freedom) of the second-order 2D-polynomial function. Roughly, N_{eff} is the total number of vectors in the filter kernel divided by the number of vectors within the size of the interrogation window (more details in chapter 2). For example, with an interrogation window size of 32x32 pixel and 75% overlap, there will be 16 vectors within the window. If one would smooth over these 16 vectors, there will be effectively very little reduction of the uncertainty and noise, since the errors of all vectors are closely correlated.

It is also necessary to update the spatial resolution of the vector field, which is related to the spatial auto-correlation coefficients between neighboring vectors. Due to variable filter size and shape, this is different for each vector in magnitude and direction, similar to the adaptive PIV techniques with varying interrogation window sizes and shapes. A fully correct treatment is complicated and would require the storage of many additional correlation values for each vector for subsequent uncertainty propagation. Again, a simplified version is adopted here setting the spatial resolution to the average linear dimension of the filter kernel. It needs to be shown, if this is sufficient for accurate uncertainty quantification when the directional dependency of the effective spatial resolution becomes important, e.g. for the vorticity field.

The proposed denoising scheme takes typically a few seconds of processing time on a standard PC. It can easily be extended to volumetric data and to the time domain.

5.3 Synthetic data validation

The denoising scheme is first tested on a synthetic vector field with a wide range of spatial wavelengths L and signal-to-noise ratios (velocity dynamic range). The vector field contains 200 x 75 vectors with a grid spacing d of 4 pixel. The (true) flow field contains vortices of various sizes with spatial wavelengths of 512 pixel on the left and 32 pixel on the right of the image with a constant (true) amplitude of 1 pixel (Figure 5.4 top). Vortices constitute a more challenging case than simple shear flows, where the filter kernel shape can be strongly elongated along the shear.

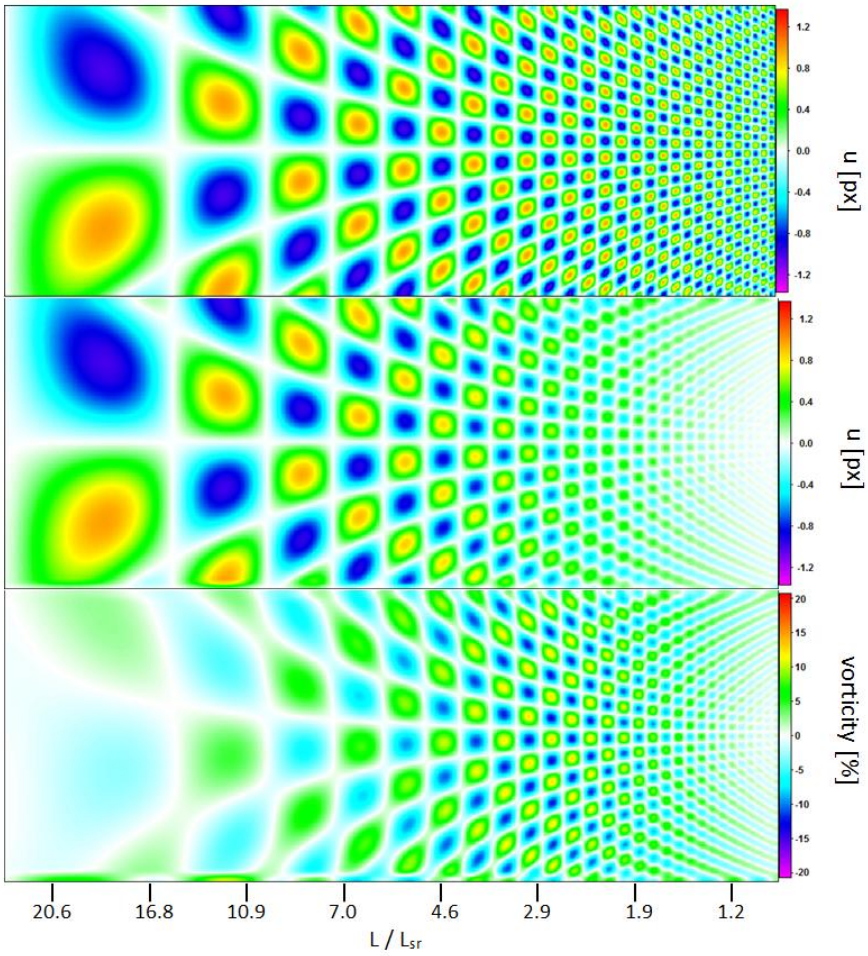

Figure 5.4. Synthetic vector field with constant fluctuation amplitude (top) and after taking the finite spatial resolution of a PIV algorithm into account showing u-component (middle) and vorticity (bottom).

Any PIV algorithm has a finite spatial resolution equivalent to a characteristic filter length L_{sr} reducing small-scale fluctuations. Here it is assumed that L_{sr} is 16 pixel, equivalent to 4 vectors, which is similar to using 16x16 pixel interrogation windows with 75% overlap. The filter length L_{sr} as the inverse of the spatial resolution is defined here as the sum of the auto-correlation coefficients between the errors of neighboring vectors (section 2.3). If PIV would be a simple single-pass linear top-hat filter averaging the displacement information within an interrogation window of L x L pixel, then L_{sr} would be equal to L, as can be easily verified. The vector field is filtered here with a Gaussian filter function ($\propto \exp(-x^2/2\sigma^2)$) of equivalent filter length $L_{sr} = \sigma \, \mathrm{sqrt}(4\pi)$. This leads to a significant reduction in amplitude for small wavelengths, e.g. about 50% for $L/L_{sr} = 2$ (Figure 5.4 middle and bottom). The exact spatial frequency response depends on details of e.g. the predictor-corrector scheme of a multi-pass PIV algorithm. This smoothing is included to put the noise level and its reduction by the anisotropic denoising scheme in perspective to the unavoidable amplitude reduction of small wavelengths due to the limited spatial resolution of the PIV algorithm itself.

Noise levels of 0 to 100% are added to each vector component, again subject to the PIV spatial filtering, which leads to locally correlated noise components between neighboring vectors. This becomes important when applying locally confined averaging, where the noise is very little reduced since it is locally correlated. Viewed another way, local averaging/denoising must be done over a kernel size larger than L_{sr} to become effective. The maximum filter kernel size is set to 41x41 vectors. Final computed kernel sizes are typically in the range of 5-15 vectors in each direction.

Figure 5.5 shows the u-component with increasing noise level from top to bottom of the original vector field and after denoising with strength S of 1, 2, 2.5, 3, and 4 (from left to right). For zero noise level (top) the denoising scheme does not change the vector field apart of slightly decreasing the spatial resolution, i.e. increasing L_{sr} from 16 to 19, due to the initial 5x5 polynomial regression, which is always done. This is barely visible on the top right, where the amplitude of small-scale fluctuations is decreased slightly.

For low noise levels, the procedure accurately recovers the round shape of vortices for almost all wavelengths. Large-scale vortices with larger possible kernel sizes are recovered even at 100% noise level. For smaller wavelengths further to the right the denoising procedure is able to reduce the noise as long as the true fluctuations are larger than the errors. Beyond that, the algorithm cannot distinguish between true and noisy fluctuations anymore. Here, given a strong enough filter, the vector field is simply averaged over large regions. The algorithm assumes that everything is noise (see bottom right of the noise plot in Figure 5.6). The optimal filter strength seems to be between 2.5 and 3.0, strong enough to eliminate noise over potentially large regions for larger wavelength while not smoothing over true fluctuations.

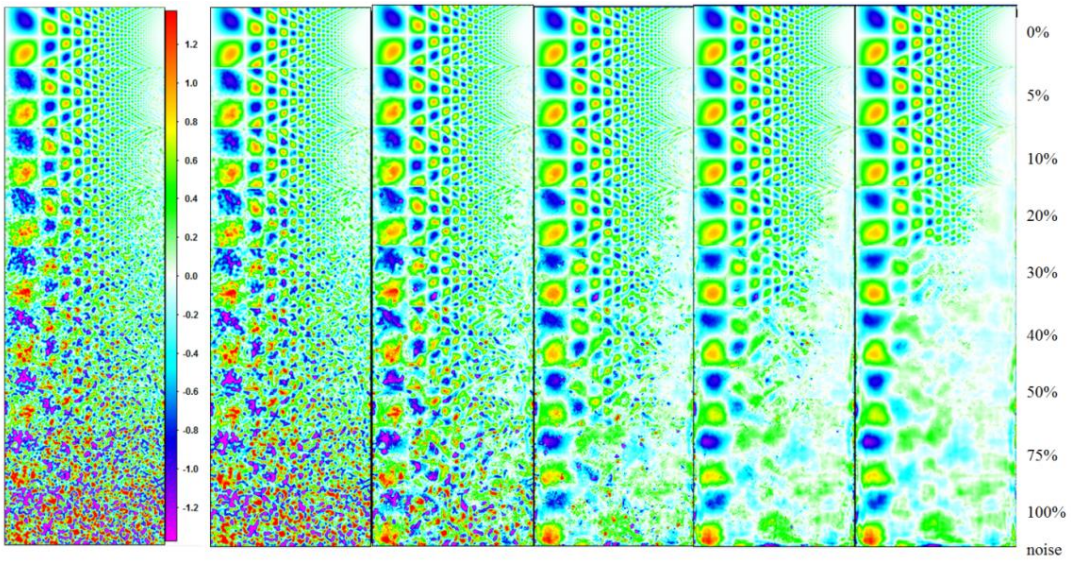

Figure 5.5. Original vector field and after denoising with strength S = 1, 2, 2.5, 3, and 4 from left to right. Noise level 0-100% from top to bottom. Color = u-component.

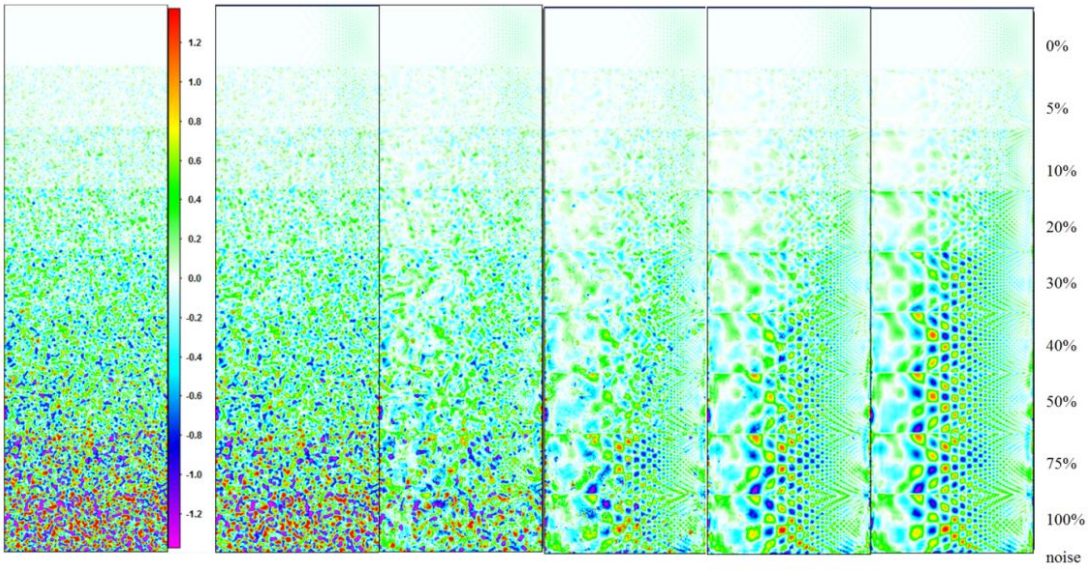

Figure 5.6. Original noise and after denoising (equal to Figure 5.5 minus Figure 5.4 middle) with strength S = 1, 2, 2.5, 3, and 4 from left to right. Noise level 0-100% from top to bottom. Color = u-component of noise.

The performance of the denoising scheme is quantified in Figure 5.7 plotting the local rms of the noise for a filter strength of S=3 as a function of wavelength for the different noise levels of 0-100% (0-1 px). For larger wavelength $L/L_{sr} > 10$ the noise is reduced by a factor of 2, up to a factor of 4 in some cases and larger wavelengths. For large noise levels >50% only wavelengths $L/L_{sr} > 15$ are recovered, which is not surprising, since even visually it is difficult to detect smaller vortices in the noisy vector field. Smaller wavelengths are simply smoothed-over as the algorithm is unable to distinguish between true vortices and noise. The overall noise level is decreased but hidden flow structures are also removed.

For the noise-free vector field the error increases for small wavelengths (L/L_{sr} = 1-3) by about 5% of the true amplitude due to the 5x5 polynomial regression, which, as mentioned before, leads to 15% lower spatial resolution. Still, one has to keep in mind that for these wavelengths the amplitude reduction due to the spatial filtering effect of PIV (truncation error) is anyway above 50%.

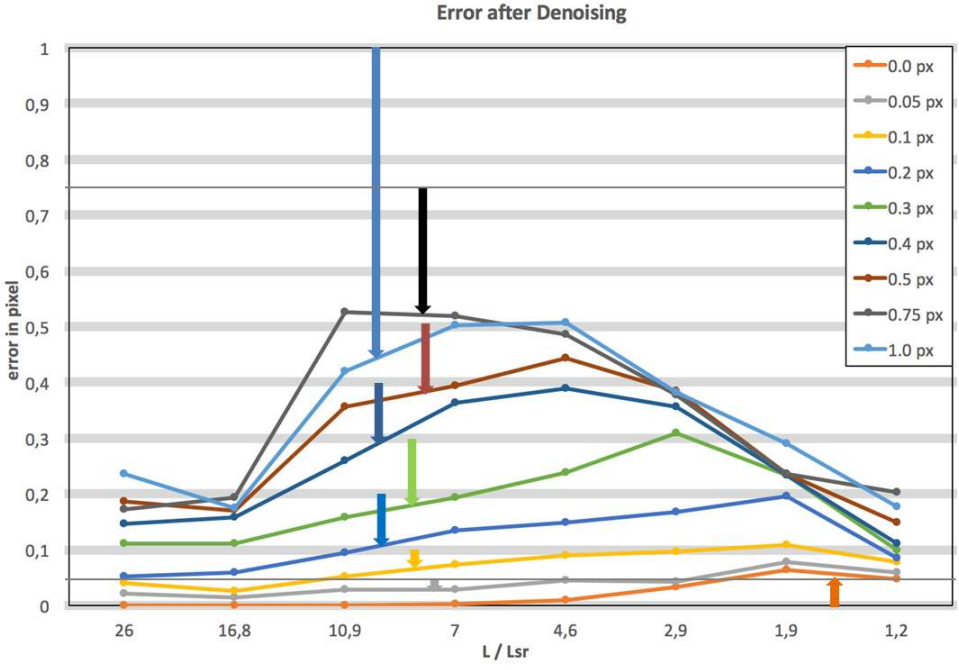

Figure 5.7. Remaining noise level after denoising as a function of spatial wavelengths for different original noise levels of 0-1 px.

The denoising scheme has been compared to a standard 2nd-order polynomial regression filter with a fixed kernel size of 5x5 to 11x11 vectors and a top-hat smoothing filter over 9x9 vectors for the case of 20% (0.2 px) noise level (Figure 5.8). For large wavelengths, the polynomial regression filter reduces the noise level with successively larger filter kernels. The top-hat 9x9 filter performs better than polynomial fit of 11x11, since it is roughly equivalent to a polynomial filter of 20x20

vectors. For the intermediate range of L/Lsr between 2 and 7, the polynomial regression filter even increases the noise level, since the reduction of random noise is less than the extra noise added due to increased truncation errors, i.e. smoothing the true flow fluctuations. Clearly, the anisotropic denoising filter outperforms all other schemes due to locally adapting the kernel size to the wavelength of the true flow fluctuations.

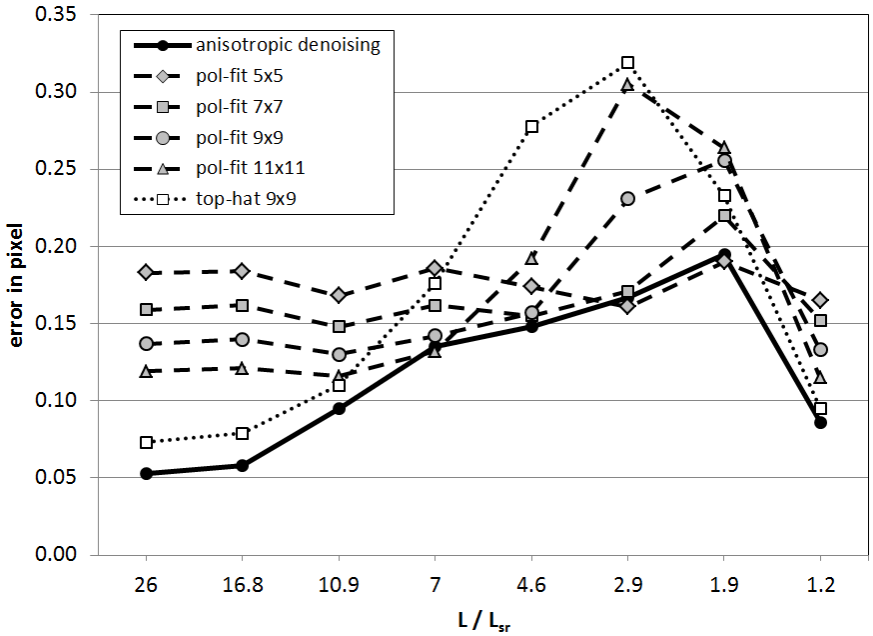

Figure 5.8. Comparison of anisottropic denoising with 2nd-order polynomial regression filter with 5x5 to 11x11 vector kernel and 9x9 top-hat smoothing filter. Original noise level = 0.2 pixel.

5.4 Experimental verification

The denoising scheme is first tested on image 50 of PIV challenge 2003 case A (Stanislas et al. 2005). Standard PIV processing with 16x16 px window size reveals small-scale vortices inside the jet with a few remaining outliers even after vector validation and leaves a high noise level outside the jet (Figure 5.9). It is not clear if some of the small-scale vortices are actually real or noise. Increasing the interrogation window size reduces the noise level but at the same time smears out small-scale vortices leading to lower peak vorticity levels. The user has to choose some compromise, e.g. selecting 24x24 or 32x32 pixel windows.

Figure 5.10 shows the result of the denoising scheme with a filter strength S of 3.5 and a maximum kernel size of 15x15 vectors. Compared to 32x32 windows without denoising, when using 24x24 with denoising one arrives at higher peak

vorticity levels and smaller resolved flow features. At the same time, the noise levels in regions of low flow gradients outside the jet are strongly reduced, which would be otherwise only achievable with e.g. 48x48 or larger windows.

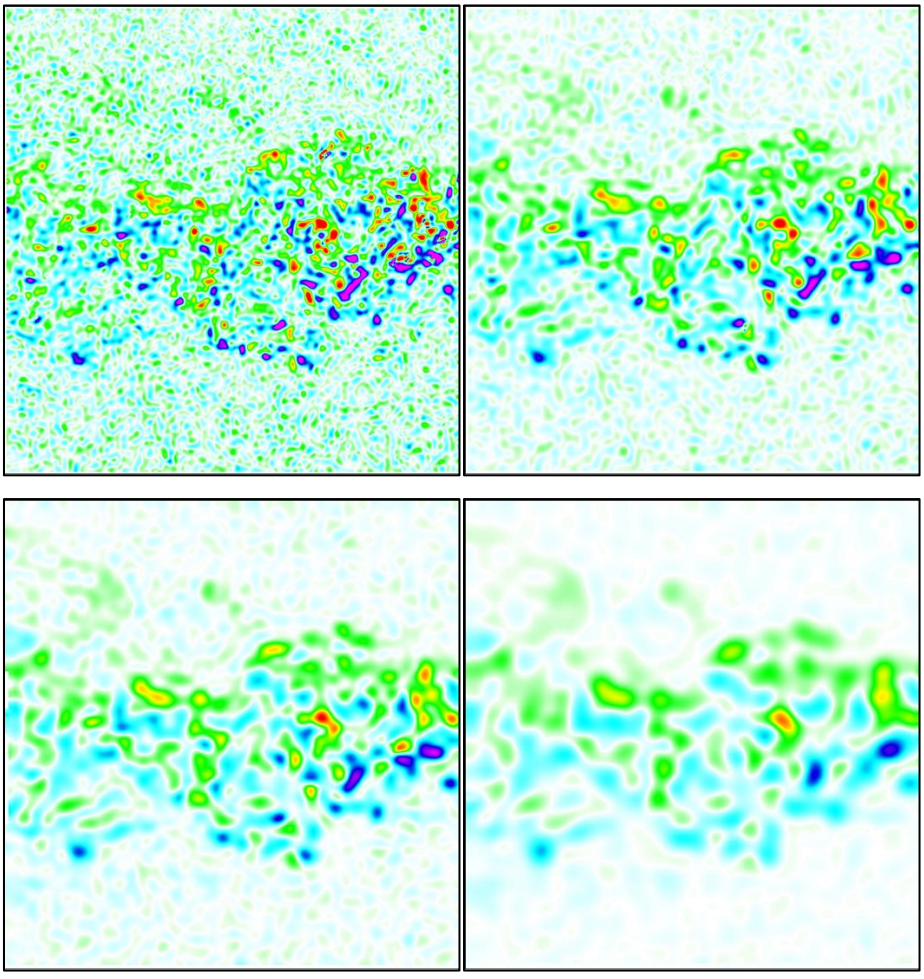

Figure 5.9. PIV Challenge 2003, case A, image 50 processed with interrogation window sizes of 16x16, 24x24, 32x32, and 48x48 pixel (from top-left to bottom-right) with 75% overlap. Color = vorticity (a.u.).

Another experimental example is a cut through a ring vortex in air (Figure 5.11) with 24x24 interrogation windows and 75% overlap. Since the jet is mostly laminar, the small-scale granular structure of the vorticity pattern is purely noise related. Denoising clearly reduces the noise level while preserving and highlighting the true flow structures.

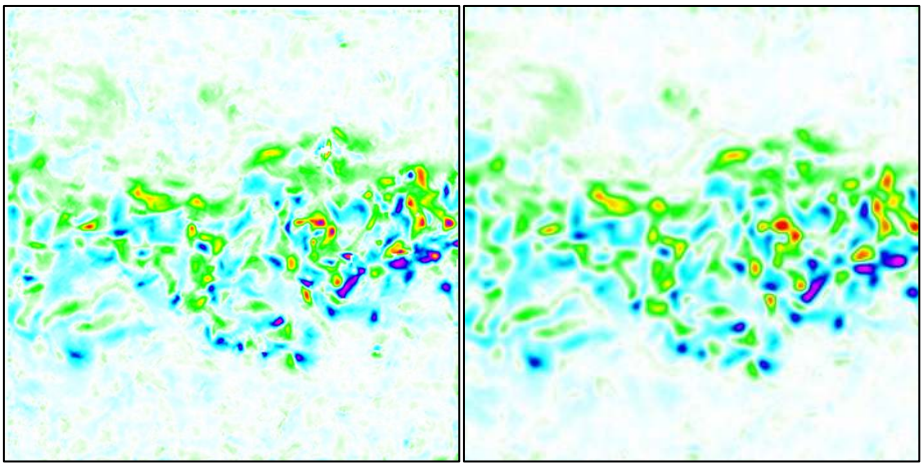

Figure 5.10. Denoising applied on vector fields with IW=16x16 (left) and 24x24 (right). S=3.5.

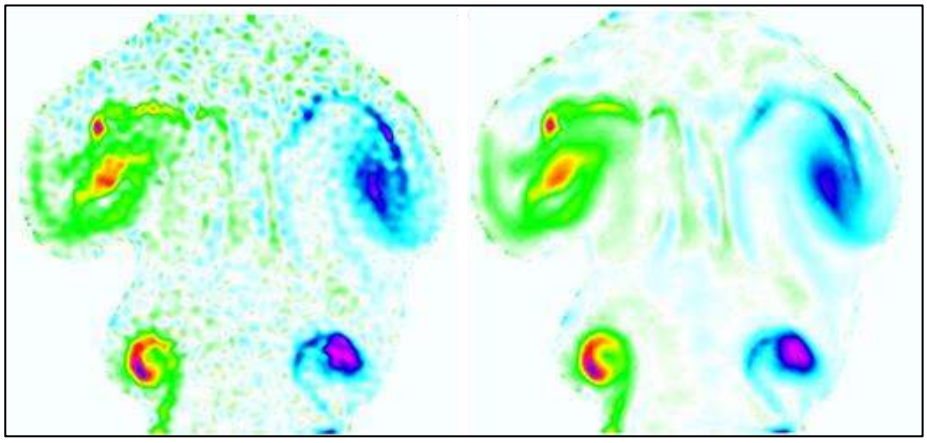

Figure 5.11. Ring vortex processed with 24x24 windows and 75% overlap without (left) and with denoising (right, S=3.5). Seeding and PIV processing is only applied inside the vortex. Color = vorticity (a.u.).

Finally, time-resolved PIV data from a turbulent pipe flow (van Doorne and Westerweel 2007) is analyzed using the new spatial denoising technique and/or applying at each location a temporal polynomial regression filter of second order over 11 time steps. As shown in Figure 5.12 and better visible in the associated movie (https://youtu.be/ZckKc1I-tfQ), with an interrogation window size of 32x32 pixel the vector fields at each time step (top-left) are clearly quite noisy in space and flickering also over time. This qualitative judgement is based on the knowledge that here small-scale spatial variations lack physical justification. Within the 2 ms between time-steps and corresponding 3-5 pixel displacement of particles the temporal flickering is mostly due to noise.

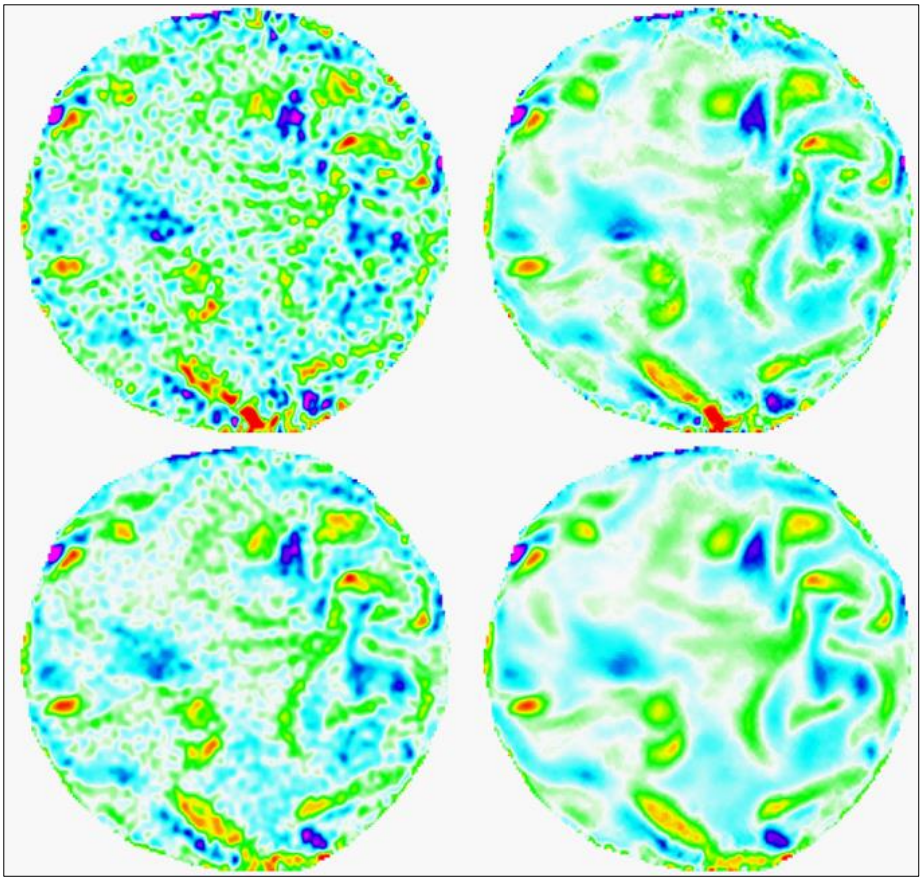

Figure 5.12. Turbulent pipe flow (van Doorne and Westerweel 2007), raw vector field (top-left) after anisotropic denoising (top-right, S=3.5), and for both with polynomial regression filter of 2nd-order over 11 time steps (bottom). Color = vorticity (a.u.). See movie in supplementary data (https://youtu.be/ZckKc1I-tfQ).

After applying the anisotropic denoising scheme the flow field is much smoother spatially (top-right), but still flickering significantly over time. When applying the temporal filter on the raw vector fields, the result is now temporally smooth over time at each spatial location, but still spatially noisy (bottom-left). Applying both schemes (here first spatial denoising, then temporal filter, bottom-right), the result is finally spatially and temporally smooth with only small reduction in spatial and temporal resolution compared to the raw vector fields. This indicates a significant reduction of the noise level, about equally by the temporal and spatial denoising scheme.

5.5 Summary

A rather simple denoising scheme is presented as a post-processing step on vector fields using the uncertainty value for each vector as a reference. Vectors will

be progressively added in all directions to the filter kernel if the velocity value is inside the uncertainty band around the locally fitted function. This is repeated until the true flow field can no longer be approximated by the second-order polynomial function. The final shape and size of the filter kernel automatically adjusts to local flow gradients in an optimal way preserving true velocity fluctuations above the noise level.

This anisotropic denoising scheme is validated on synthetic vector fields with varying spatial wavelengths and noise levels showing a significant increase of the velocity dynamic range for wavelengths about 4 times larger than the spatial resolution. For noise levels above 50%, the procedure is no longer able to distinguish between true flow fluctuations and noise except for large wavelengths of $L/L_{sr} > 10$. The procedure has been shown to work well for typical experimental flow fields. It can be easily extended to volumetric data and to the time domain.

6

PIV Calibration Error Estimation and Correction

Section 6.2 has been published in Wieneke (2005) Stereo-PIV using self-calibration on particle images. Exp Fluids 39:267

Section 6.4 has been published in Wieneke (2008) Volume self-calibration for 3D particle image velocimetry. Exp Fluids 45:549

6.1 Introduction

For multi-camera Stereo-PIV and volumetric PIV/PTV an accurate perspective calibration between cameras and measurement volume is an important prerequisite for further processing. The calibration procedure computes mapping functions between world points (X,Y,Z) and camera pixel locations (x_1,y_1), (x_2,y_2), … . Many functional forms for the mapping function have been proposed, including polynomials (Soloff et al. 1997; Prasad 2000), DLT and full camera pinhole with distortion parameter (Tsai 1987; Zhang 2000; Willert 2006), with Scheimpflug corrections (Fournel et al. 2004; Louhichi et al. 2007; Astarita 2012; Cornic et al. 2016) or accounting for multi-media models with changing index of refraction (Belden 2013) among others. All mapping functions are equally valid as long as they accurately accommodate the optical setup including all optical distortions.

Error sources include manufacturing accuracy of the calibration plate, inaccurate calibration procedure e.g. during translation of the calibration plate, measurement errors in the position of the detected calibration marks, or inadequate functional form of the mapping function with e.g. insufficient number of free parameters.

The reader is referred to the PIV books of Raffel et al. (2007) and Adrian and Westerweel (2011) for more information on PIV calibration. The focus here is on quantifying the accuracy of the calibration mapping function together with correction techniques.

For Stereo-PIV, besides accurate mapping functions, the relative position of the calibration plate (reference Z=0-plane) with respect to the light sheet is very important. During the initial calibration, one usually tries to place the (first view of the) calibration plate exactly at the location of the light sheet. Misalignments are unavoidable and can be corrected by a *Stereo-PIV self-calibration* technique (SPIV-SC) as discribed in section 6.2, motivated by earlier work by Willert (1997) and Coudert and Schon (2001). The term *self-calibration* is known from computer vision for perspective calibration of cameras based on detecting corresponding features in the two images. It has been used here to emphasize that the technique works on recordings with the actual tracer particle images.

Initial misalignments are often of the order of 5-20 pixel and remaining disparities after self-calibration are typically below 1-3 pixels. For some special procedures with e.g. initial calibration outside in air and then self-calibration into a water channel it can be initially up to 200 pixel. In comparison to the spatial resolution of PIV (related to the size of an interrogation window, see section 2.5) of e.g. 15-30 pixels, small remaining disparities below e.g. 3-5 pixel still ensure that both cameras use almost the same vector locations for 3C-reconstruction. It should be noted that the intrinsic limitation of Stereo-PIV due to both cameras viewing different interrogation volumes of the light sheet (Wieneke and Taylor 2006) leads to much higher differences in overlap of up to 10-30%.

SPIV-SC measures the disparity by cross-correlation between the two cameras, usually summing many images or correlation maps and correcting the initial calibration function with an appropriate coordinate translation and rotation.

Table 6.1. Comparison of Stereo-PIV self-calibration and volume self-calibration.

	Stereo-PIV self-calibration	**Volume self-calibration**
Purpose	correction of laser sheet misalignment relative to z=0 calibration plane	correction of (small) calibration errors and optical distortions
Basic method	correlation between images of the two cameras	particle detection and disparity computation
Typ. number of cameras	2	3+
Measurement volume	planar sheet / thin volume	volume
Useful for	Stereo-PIV and thin volume PIV/PTV	volumetric PIV/PTV
Correction of laser sheet misalignment	yes initial misalignment up to ≈200 pixel remaining misalignment ≤ 1-5 pixel	no, only visual indication of illuminated volume
Correction of calibration errors/ optical distortions	partially: (rough) 2D-refit of mapping function based on remaining disparities perpendicular to epipolar line	yes works for initial errors ≤ 20 pixel remaining errors ≤ 0.1-0.3 pixel
Correction of single-image vibrations	___	yes, ≤ 5-10 pixels, one global translational correction
Transformation	3D-translation and rotation of coordinate system	local correction of mapping function

Apart from laser sheet misalignment, the main source of error is the accuracy of the mapping function itself. Even if the initial calibration is ok, at the time of image recording cameras might have sagged due to weak mounting or somebody has hit the mechanical setup, or, even worse, the recording is subject to vibration of cameras, light source, wind tunnel, ground floor or all together.

The volume self-calibration (VSC) as a correction technique for inaccurate mapping functions, described in section 6.4, was motivated by the advent of Tomographic PIV, where an accuracy of the mapping function of less than 0.3 pixel everywhere in the volume is required for accurate (S)MART reconstruction (Elsinga et al. 2006).

VSC works by finding possible 3D particle positions in the measurement volume by triangulation from 2D particle positions in the recorded images. Back-projection of the 3D-particle position might deviate from the original 2D-position (*disparity*) which can be used to correct the calibration mapping function.

VSC is needed for iterative particle reconstruction (IPR, chapter 7) which is the basis for the newly developed Shake-the-Box method (Schanz et al. 2016).

SPIV-SC and VSC are complementary techniques. For thin-volume Tomographic-PIV an initial misalignment correction can be useful to align the measurement volume with the z-axis by simultaneous coordinate transformation and rotation of the mapping function of all cameras. The two techniques are compared in Table 6.1.

6.2 Stereo-PIV Self-Calibration

6.2.1 Introduction

For Stereo-PIV a correct calibration is an essential prerequisite for measuring accurately the three velocity components. Most often an empirical approach is used by placing a planar calibration target with a regularly spaced grid of marks at exactly the position of the light sheet and moving the target by a specified amount in the out-of-plane direction to two or more z-positions (Soloff et al. 1997). At each Z-position (light sheet plane defined by Z = 0) a calibration function with sufficient degrees of freedom maps the world xy-plane to the camera planes, while the difference between Z-planes provides the Z-derivatives of the mapping function necessary for reconstructing the three velocity components. This empirical approach has the advantage that all image distortions arising from imperfect lenses or light path irregularities (e.g. from air/glass/water interfaces) are compensated automatically in one step.

Alternatively, one can use a 3D calibration plate with marks on two z-levels avoiding the need for rigid mechanical setups with accurate translation stages. Different mapping functions have been used from a second-order or third-order polynomial in X, Y, and Z (Soloff et al. 1997) to functions derived from the perspective equations (camera pinhole model) (Willert 1997). A major drawback of this empirical method is the need to position the calibration plate exactly at the same position as the light sheet which is oftentimes very difficult to accomplish. A correction scheme based on a cross-correlation between the image of camera 1 and 2 has been proposed (Willert 1997, Coudert and Schon 2001) which is also the basis for the calibration correction method proposed in this section.

In parallel, especially with the advent of inexpensive digital cameras extensive work has been done in the field of computer vision and photogrammetry to compute accurate camera calibrations. While only a 2D mapping function with additional z-derivatives is required for Stereo-PIV with thin light sheets, computer vision, in general, requires a volume mapping function to map all XYZ-world-points to the recorded xy-pixel-locations on one or more cameras. Usually this is done with a camera pinhole model with added parameters for lens distortions (Tsai 1986).

There are 6 external projective parameters mapping the calibration plate by a rotation and translation to the world camera plane perpendicular to the optical axis and internal camera parameters like the focal length, the principal point which is the foot point of the optical axis onto the CCD, the pixel size and radial lens distortion terms. The optical axis is defined as the line perpendicular to the CCD-chip passing through the pinhole.

A variety of 2D and 3D calibration targets have been used successfully. A common calibration method consists of recording a known planar calibration target at a few (4-8) shifted and rotated positions. This is either done by moving a single camera or a stereo-rig setup with two cameras around a fixed target (‚walk-around problem'), or having the cameras fixed and moving the target. All fixed parameters (internal camera parameters and the relative position and orientation of the two cameras) together with all parameters unique for the particular view are fitted by a non-linear least-square fit (bundle adjustment). Due to a very sparsely populated Hessian matrix, since the external parameters unique for each view are independent of each other, special provisions are incorporated in the fit algorithm for better numerical convergence, less computing time and higher accuracy. A good overview of self-calibration methods and bundle adjustment fits is given by Hartley and Zissermann (2000).

In the present work a Stereo-PIV calibration method has been implemented and tested using the camera pinhole model. Instead of requiring a perfect alignment between the calibration plate and the light sheet, a correction scheme has been developed which provides accurate mapping functions even when the calibration plate is quite far away or tilted relative to the light sheet. This makes the Stereo-PIV calibration easier and more accurate. Similar work has been done before on a setup with telecentric lenses (Fournel et al. 2003) and with standard lenses and Scheimpflug adapter (Fournel et al. 2004).

An important application of self-calibration is the case where it is difficult or even impossible to place a calibration plate inside a closed measurement volume. In these cases one would ideally like to calibrate the cameras outside the flow aparatus and self-calibrate onto the light sheet inside. For these cases, different strategies are presented in section 6.2.4 with experimental validation.

6.2.2 Self-calibration method

6.2.2.1 Camera pinhole model

For Stereo-PIV two mapping functions need to be determined, $\mathbf{M_1}$ for camera 1 and $\mathbf{M_2}$ for camera 2 relating a world coordinate $\mathbf{X_w} = (X_w,Y_w,Z_w)$ to pixel locations $\mathbf{x_1} = (x_1,y_1)$ and $\mathbf{x_2} = (x_2,y_2)$ in the recorded images of camera 1 and 2 (Figure 6.1):

$$\mathbf{x_1} = \mathbf{M_1}(\mathbf{X_w}) \text{ and } \mathbf{x_2} = \mathbf{M_2}(\mathbf{X_w}) \tag{6.1}$$

In the empirical approach with a calibration plate at 2 or more Z-positions (Soloff et.al. 1997) it is sufficient to know $\mathbf{M}(X_w,Y_w,Z_w=0)$ and the z-derivatives $\partial x_i / \partial Z_w$ and $\partial y_i / \partial Z_w$, i=1,2 of the mapping function at $(X_w,Y_w,Z_w=0)$ which do not change significantly across the thickness of the light sheet.

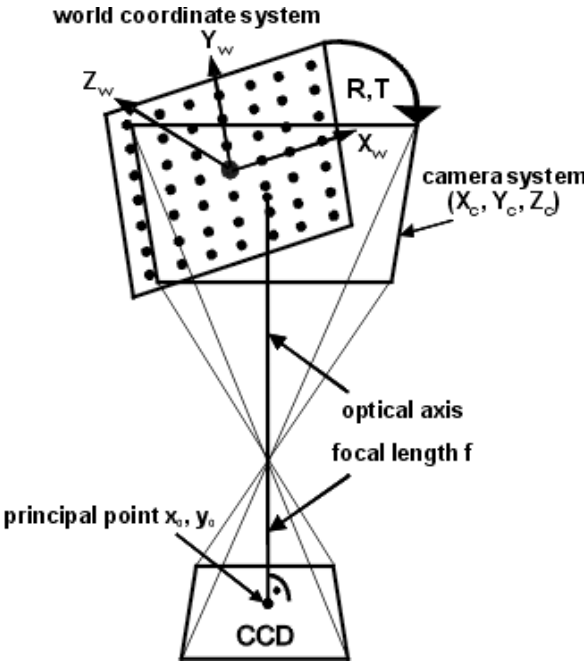

Figure 6.1. Camera pinhole model.

In contrast the camera pinhole model provides a complete mapping of the volume as given by eqn. 6.1. The camera pinhole model used here is based on Tsai's 11 parameter model (Tsai 1986). The 6 external camera parameters are given by the rotation $\mathbf{R}$ and translation $\mathbf{T}$ of the world coordinates $\mathbf{X_w}$ to the camera coordinates $\mathbf{X_c} = (X_c,Y_c,Z_c)$:

$$X_c = R \bullet X_w + T \tag{6.2}$$

The undistorted and distorted camera position $\mathbf{x_u} = (x_u,y_u)$ and $\mathbf{x_d} = (x_d,y_d)$ are computed by:

$$x_u = f \cdot X_c / Z_c \quad \text{and} \quad y_u = f \cdot Y_c / Z_c \tag{6.3}$$

with

$$x_d = x_u \cdot (1 + k_1 \cdot r + k_2 \cdot r^2) \quad \text{and} \quad y_d = y_u \cdot (1 + k_1 \cdot r + k_2 \cdot r^2) \tag{6.4}$$

and

$$r^2 = x_d \cdot x_d + y_d \cdot y_d. \tag{6.5}$$

where k_1 and k_2 are the first and second order radial distortion term. Usually for good quality lenses k_1 is sufficient, for wide-angle lenses or consumer cameras additional radial terms and even tangential distortion terms may be required. f is the distance between the principal point and the camera pinhole. This is close to but not exactly the focal length of the lens f_{lens}. Provided that the calibration plate is in-focus at distance T_z, f is theoretically related to f_{lens} by:

$$f = f_{lens} \cdot (1 + f_{lens} / (T_z + f_{lens})) \tag{6.6}$$

but, in practice, lenses specified with a fixed focal length do not obey exactly this equation. For good lenses the deviations are in the order of 2-5%. Finally the true pixel location $\mathbf{x} = (x,y)$ on the CCD-chip is given by:

$$x = S_x * x_d / S_{pixel} + x_0 \quad \text{and} \quad y = y_d / S_{pixel} + y_0 \tag{6.7}$$

S_x is an optional skew factor, which is 1 for square pixel. Otherwise S_x can be used as an additional distortion term. S_{pixel} is the (known) pixel size. Only the ratio of f / S_{pixel} is relevant. (x_0,y_0) is the principal point, which is usually close to the middle of the CCD-chip unless a Scheimpflug adapter is used. The set of parameters (f,S_x,k_1,x_0,y_0) constitute the 5 internal camera parameter of the Tsai-model.

While a possible Scheimpflug angle is included in the pinhole model, it might lead to radial distortion parameter which are no longer rotationally symmetric since the optical axis of the pinhole model does not coincide anymore with the optical axis of the camera lens. Fournel et al. (2004) therefore proposed a special Scheimpflug rotation into the pinhole model.

The world coordinates $\mathbf{X_w}$ are given in some physical units (e.g. mm). For dewarping images and the actual Stereo-PIV computation it is necessary to convert the world coordinates to pixel units. This can be done in an arbitrary way. In the following, computations of the conversion scale of mm to pixel is set in such a way that in both directions the size of a dewarped pixel is equal or smaller than in the raw image in order not to lose any information by pixel binning. The size of the dewarped image is chosen such that it corresponds to the part of the field-of-view visible by both cameras. The coordinate origin is initially defined by the position of one of the marks on the calibration plate.

For two cameras about 22 parameters are needed to specify the pinhole model. This compares to 80 parameters for the 3rd-order 2D polynomial defined on two z-

planes. With only a few correction terms the pinhole function has proven to be highly accurate in the field of computer vision. Therefore it is obvious that not all 80 parameters of the 3rd-order polynom are statistically significant. In general it is better to start with an appropriate physical model and then add a few significant correction terms. Otherwise one might fit noise e.g. in the detected position of the marks on the calibration plate. The 3rd-order polynomial is more appropriate in cases of strong non-perspective global or local distortions (e.g. viewing through cylinders where it is more difficult to design appropriate correction terms for the pinhole model).

6.2.2.2 Correction of mapping function

Whether or not the alignment of laser sheet and calibration plate is perfect can be checked by dewarping the camera images with $\mathbf{M}^{-1}$ at $Z_w = 0$ and comparing the two images. Ideally the two images should match perfectly. Any deviation d (Figure 6.2) ('disparity map') is an indication of some misalignment leading to different error sources. If the calibration plate has a z-offset relative to the measurement plane, the reconstruction of the three-component(3C)-vector (u,v,w) from the two two-component(2C)-vectors (u_i,v_i) uses vectors computed at different locations in the measurement plane. For example, an offset of 20 pixels and a velocity gradient of 5% (in units of pixel displacement per pixel distance) the displacement would change by 1 pixel over a distance of 20 pixel, which leads to considerable errors in the reconstructed 3C-vector. Also slightly wrong derivatives of the mapping functions would be used. Finally, the coordinate system itself remains warped. That is, a tilt of the calibration plate by 1 degree means that the calculated 3C-vectors are rotated by 1 degree.

This disparity map has been used by Willert (1997) for correcting the position at which the corresponding 2C-vectors are calculated for camera 1 and 2. A more advanced approach has been done for the case of telecentric lenses recomputing a new mapping function from the disparity map (Fournel et al. 2003) and more recently for normal lenses with Scheimpflug adapters (Fournel et al. 2004). A similar general approach is done here in a series of different steps.

First, the computation of the disparity vector map of the two dewarped images is computed by a standard cross-correlation PIV-technique. The particle pattern inside an interrogation window looks quite different when viewed from the two camera viewpoints since the particles are dispersed throughout the light sheet. Therefore, it is usually insufficient to simply correlate a single image pair. Instead an ensemble averaging algorithm is used by summing the correlation planes of many image pairs (Meinhart et al. 1999). Depending on the particle density and the thickness of the light sheet about 5 to 50 images are needed typically to compute an accurate disparity map from a well-shaped correlation peak. For large fields of view (e.g. in wind tunnels) a single view might be sufficient which offers the potential to correct vibrational displacements of the laser sheet or the cameras (Willert 1997). Multi-pass algorithms with deformed interrogation windows can be applied to further enhance the accuracy of the vector map. This means that all n images are

processed first to arrive at an initial guess of the disparity vector map, which is then used as a reference vector field to shift and deform the interrogation windows in the next pass and so on.

Willert (1997) is using these disparity vectors to correct the position where the vectors are computed. For small misalignments, this effectively removes the main error source of computing the vectors of camera 1 and 2 at different positions. In case of larger misalignments between plate and light sheet a more advanced volume correction scheme must be used to compute a correct coordinate system of the light sheet plane with accurate spatial derivatives of the mapping function as explained below.

Once the disparity map has been computed, a corresponding world point in the measurement plane is computed by a standard triangulation method for each vector (Figure 6.2). Errors in the disparity vectors means that the two reprojected lines from each camera do not exactly intersect in a single world point. It is optimal to find a point in space whose projections onto the two camera images is closest to the measured positions (Hartley and Sturm 1994). These criteria can be used to eliminate false disparity vectors using a sensible threshold (e.g. 0.5 pixel). Instead of working with dewarped images one can also compute the disparities between the original images and use them in the triangulation step to arrive at the same world points. The advantage of using dewarped images is that the PIV user can check for remaining disparities (non-zero vectors) more easily. Triangulation is only possible when one has a volume mapping function, but it must not necessarily be a pinhole mapping function. It can also be an accurate empirical 3rd-order 2D-polynomial function calculated for a number of parallel z-planes which cover enough of the volume to incorporate the laser light sheet to be fitted.

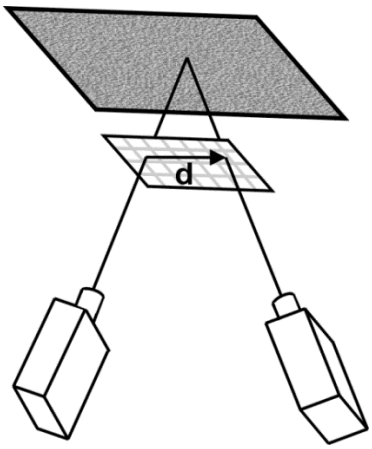

Figure 6.2. The world points of the light sheet can be computed by triangulation using the disparity vectors.

A plane is then fitted through the world points in 3D-space and the mapping functions of camera 1 and 2 are corrected by a corresponding transformation such that the fitted measurement plane becomes the z=0 plane. This is done by replacing in eqn. (6.2) R by R*dR and T by T + R*dT, where dR is the rotation of the fitted plane relative to the calibration plate and dT is the distance of the plane to the calibration plate. The freedom of choosing the new coordinate system due to in-plane rotation and choice of origin is reduced by setting the new origin as the point projected from the previous origin in camera 1 onto the measurement plane and the previous x-axis of camera 1 coincides with the x-axis of the measurement plane. This can be changed later by the user to set a new origin and x- or y-axis in a dewarped particle image. The complete correction scheme is shown in Figure 6.3.

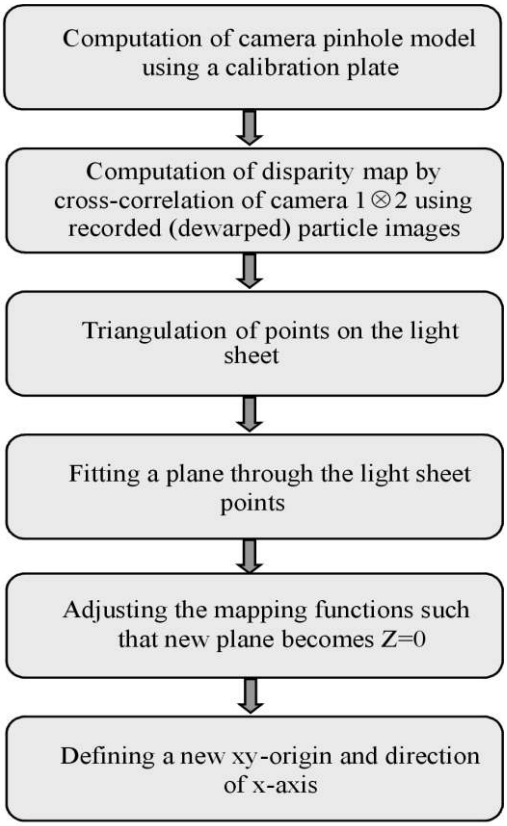

Figure 6.3. Flow chart of self-calibration procedure.

The whole procedure can be repeated again to arrive at better fits. Usually the process has converged and the disparity map does not get smaller after two or three passes. Good results have been achieved by using only a single-pass cross-correlation and repeating the complete correction process two or three times.

The triangulation error and the error fitting a plane through the world points provide information about the quality of the fit. Both errors are affected by inaccuracies in the disparity vectors, which are mostly random errors due to insufficient number of particles and the well-known bias errors of the correlation function, together with systematic calibration errors in case the computed mapping function becomes inaccurate when projected in space toward the light sheet plane. Calibration errors often lead to high triangulation errors, while the plane fit error might remain small. As shown later with a good setup it is possible to compute the position of the light sheet within 0.1 pixel of the center of the sheet with a thickness of typically 10-20 pixels, something hardly possible by simple visual inspection and manual placement of the plate.

The correction scheme above assumes that the internal camera parameters as well as the position and orientation of camera 2 relative to camera 1 do not change. In the 22 parameters of the stereo Tsai model one can substitute the external parameter $\mathbf{R_2}$ and $\mathbf{T_2}$ of camera 2 by the relative transformation $\mathbf{R_{12}}$ and $\mathbf{T_{12}}$ of camera 2 relative to camera 1. Then the self-calibration procedure above is equivalent of newly fitting $\mathbf{R_1}$ and $\mathbf{T_1}$ while keeping $\mathbf{R_{12}}$ and $\mathbf{T_{12}}$ fixed. Since the coordinate origin and the x-axis are free to choose, this leaves three parameters of $\mathbf{R_1}$ and $\mathbf{T_1}$ to be fitted, which are the three parameters of the position and orientation of a plane in space. Therefore, the procedure of triangulation, plane fit and transformation can be replaced by a single non-linear fit of the three free parameter of $\mathbf{R_1}$ and $\mathbf{T_1}$ using the relationship between the disparity and the mapping function parameter given by the well known fundamental equation (Hartley and Zissermann 2000):

$$\mathbf{x_1} \cdot \mathbf{F} \cdot \mathbf{x_2} = 0 \tag{6.8}$$

where $\mathbf{F}$ is the fundamental 3x3 matrix of rank 2 with 8 degrees of freedom and $\mathbf{x_1} = (x_1,y_1,1)$ and $\mathbf{x_2} = (x_2,y_2,1)$ are the camera coordinates. It is nevertheless quite instructive to perform the three steps separately to identify the different error sources and to check the flatness of the light sheet.

Advanced self-calibration methods can be devised to fit more than the three plane parameters since the fundamental equation has 8 degrees of freedom. One might fit user-adjusted focal lengths or Scheimpflug positions or even the relative position between camera 1 and 2 with some restrictions. This is subject of further research.

6.2.2.3 Stereo-PIV processing and 3C-reconstruction

Different approaches for stereo vector computation have been proposed as summarised e.g. by Prasad (2000) or Calluaud and David (2004). In all cases a 2D2C-vector field is computed for each camera from which by stereoscopic reconstruction a 2D3C-vector field is computed.

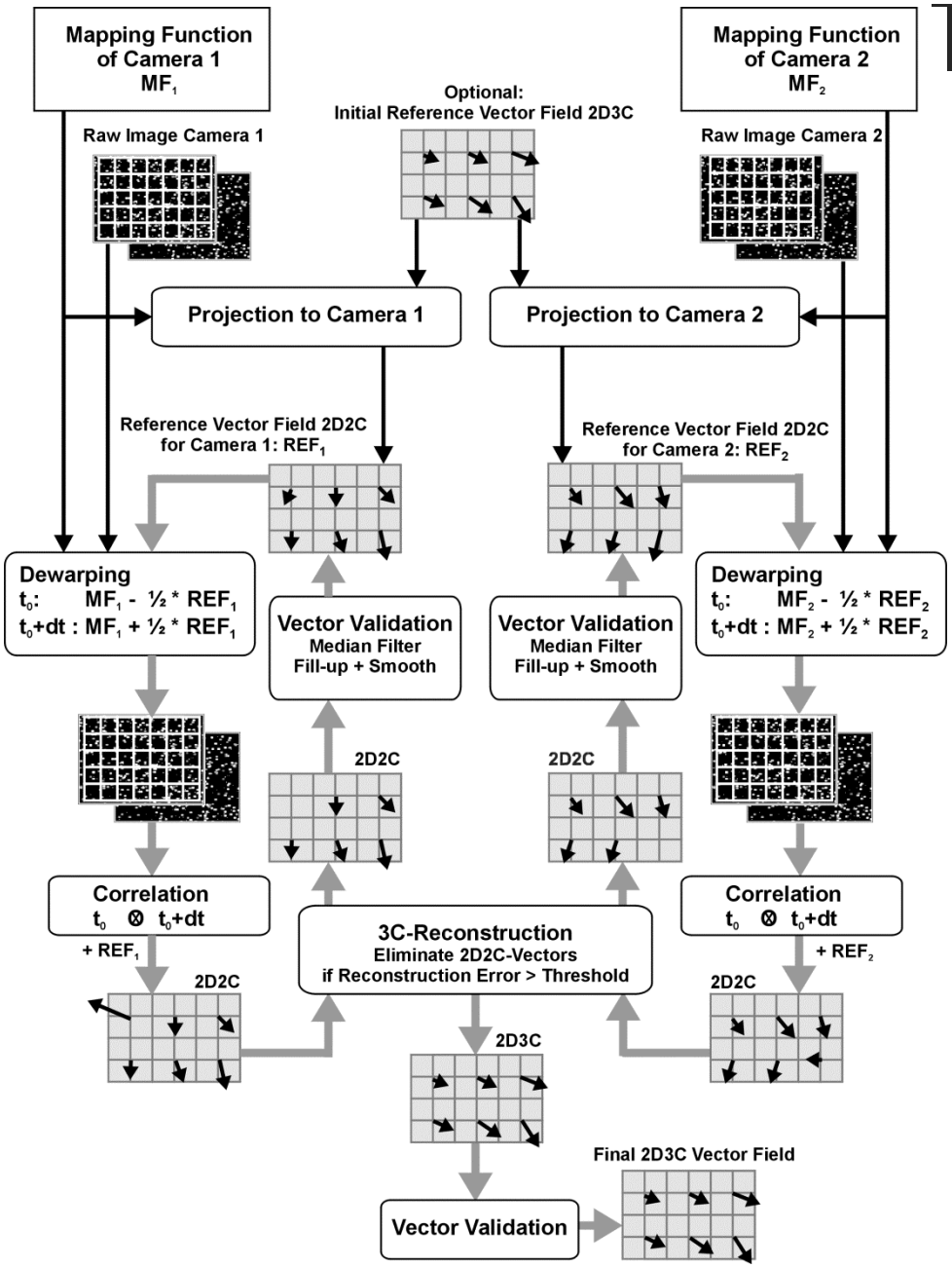

Figure 6.4. Flow chart of Stereo-PIV vector field computation.

One has the choice of:

1. computing the 2D2C-field on a regular grid in the raw images and using the two interpolated vectors to compute a 3C-vector at regular world grid positions,
2. computing the 2D2C-vectors in the raw image at a position corresponding to the correct world position or
3. dewarping the images first and computing the 2D2C-vectors at the correct world grid position.

Method 1 has the disadvantage that the vectors are not computed at the correct world position and due to vector interpolation false or inaccurate vectors affect four final 3C-vectors. Method 2 has the disadvantage that the size and shape of the interrogation windows differ between the two cameras due to the perspective viewing. For method 3 the computed 2D2C-vectors are already computed at the world correct position and originate from the same interrogation window of equal size and shape, but a sub-pixel interpolation is required during the dewarping, which together with the sub-pixel interpolation necessary for the multi-pass window deformation scheme leads to added image degradation. Therefore a modified method 3 approach is used here where the dewarping and image deformation is done at once before each step in the multi-pass iterative scheme.

For the first computational pass the two frames (t_0, t_0+dt) of each camera are dewarped and evaluated. This already provides vectors at the correct position in the world coordinate system. Also the size and shape of the interrogation windows for both cameras are the same, which means that the correlation is done on the same particles apart from effects due to the non-zero thickness of the light sheet. Then a preliminary 3C-reconstruction is done to remove corresponding vectors in the 2C-vector fields for which the reconstruction error is too large (e.g. larger than 0.5 or 1 pixel). This method very effectively removes spurious vectors since two false vectors with random directions are rarely correlated. At the end of the first pass missing vectors are interpolated and the vector field is smoothed slightly for numerical stability.

The resulting vector field is used as a reference for deforming the interrogation windows in the next pass. Actually, not each interrogation window is deformed individually, but the complete image is deformed at once with half the displacement in backward direction assigned to the first image at t_0 and the other half in a forward direction to the second image at t_0+dt. Image deformation requires less floating point operations, since e.g. for an overlap of 75% the same region would be deformed 16 times using window deformation. Image deformation is combined with the dewarping of the original image in one step. Usually after 3 or 4 passes at the final interrogation window size the 2D2C-vector fields have converged sufficiently. Then the 3C-reconstruction is done which consists of solving a system of 4 linear equations with three unknowns (u,v,w). This is done by using the normal equation which distributes the error evenly over all three components. Computing from (u,v,w) again (u_1,v_1)- and (u_2,v_2)-components the deviation from the measured

(u_1,v_1) and (u_2,v_2) can be calculated ('reconstruction error'). Usually with a good calibration and 2C-vector errors of less than 0.1 pixel, the reconstruction error is well below 0.5 pixel. This can be used as an efficient rejection of false random vectors which usually produce large reconstruction errors. The complete flow chart is shown in Figure 6.4. The 2D2C-vector fields are separately computed for camera 1 and 2. A typical multi-pass scheme consists, for example, of one or two passes with interrogation window size of 64x64 pixel and 50% overlap followed by 4 passes with 32x32 and 75% overlap. After each pass a 2D3C-reconstruction is done for the purpose of eliminating 2D2C-vectors with reconstruction errors above some threshold (e.g. 1 pixel), but the 2D3C-vector field is not used further. Only at the end the reconstructed 2D3C field is taken and validated e.g. by a median filter.

6.2.3 Experiments

In section 6.2.3.1 16 different calibrations have been taken and self-calibrated on a recording of a flat random pattern plate. A bundle adjustment of the closest 8 calibrations serves as a reference. The corrected calibrations are compared in different ways to assess the different residual errors after self-calibration. In section 6.2.3.2 a flat random pattern plate has been moved by a translation stage and the measured Stereo-PIV displacements are compared to the true displacement. This is for calibration and self-calibration done in air as well as in water to verify the accuracy of the pinhole model when used with intermediate index of refraction changes. In section 6.2.3.3 a real experiment in air has been performed and the vector fields before and after correction are computed and analysed.

6.2.3.1 Experimental results with synthetic images

16 views of a 3D calibration plate with a size of about 100 x 100 mm are recorded at different positions and orientations. The image size is 1280 x 1024 pixel, and a small aperture with an f-stop of 20 has been used to ensure a large depth-of-focus. From each view a camera pinhole mapping function is calculated with fixed s_x = 1 and k_2 = 0. Table 6.2 shows some of the pinhole parameters for camera 1.

A flat plate with a random dot pattern is recorded defining a light sheet position. This image is used later for self-calibration. A reference mapping function is computed by a bundle adjustment of the 8 calibration views closest to the random pattern plate. Note that the parameter for calibration 1 are almost the same as for the reference, since the first of the 8 views for the bundle adjustment is taken as the reference coordinate system z=0.

Table 6.2 shows the average length of the disparity vectors computed by cross-correlation between the random dot image of camera 1 and camera 2 for all calibrations. Even extreme disparities of up to 500 pixel are present, which means that only half the calibration plate was visible to both cameras simultaneously.

The self-calibration procedure of section 6.2.2. has been applied to the reference mapping function. In the following, the other mapping functions are compared to the corrected reference function in different ways.

Table 6.2. Mapping function parameter before correction.

Calibration	f_1 [mm]	T_{z1} [mm]	R_{x1} [°]	R_{y1} [°]	R_{z1} [°]	Disparity [px]	Synthetic image Error in V [px]	False vectors
Reference	60.66	449.4	6.2	29.2	13.5	1.0	0.07	0.0 %
1	60.03	444.8	6.0	29.8	13.4	1.0	0.07	0.0 %
2	60.29	443.4	2.1	29.6	6.2	8.2	0.39	6.7 %
3	60.36	442.9	1.2	29.7	4.2	9.0	0.44	7.1 %
4	61.23	447.3	2.7	33.6	-0.6	38	2.2	60 %
5	61.23	446.8	2.1	32.1	-0.6	41	2.2	70 %
6	60.89	446.6	5.7	29.7	-0.3	49	2.8	74 %
7	61.57	451.3	4.5	30.5	-0.5	87	3.4	95 %
8	60.32	435.4	-1,2	30.2	0.0	126	-	100 %
9	60.88	448.9	21.7	46.2	-1.9	144	-	100 %
10	60.28	456.3	25.9	32.4	7.8	166	-	100 %
11	61.44	458.3	16.3	34.7	6.9	178	-	100 %
12	62.68	465.2	12.6	8.6	0.1	182	-	100 %
13	61.23	433.0	3.8	33.9	-8.2	263	-	100 %
14	62.82	447.9	-13.6	30.6	-1.6	298	-	100 %
15	63.51	444.6	3.0	32.3	-13.6	351	-	100 %
16	62.11	482.1	7.6	26.0	-2.8	502	-	100 %

A synthetic double-frame random pattern image has been generated based on a 2D2C-velocity field of regular vortices with an average gradient of about 10% and ±5 pixel displacement. Seeding density is high, particle diameter around 2 pixels, and no noise is included. The two frames are warped to z=0 using the corrected reference mapping function, leading to a 4-frame reference Stereo-PIV image, two frames warped with camera 1 mapping function, two with camera 2 function. Since all particles are located at z=0, errors due to particles spaced throughout a light sheet are avoided. Evaluating this image with the Stereo-PIV procedure using the corrected reference mapping function gives back the original 2D3C-vector field with a zero out-of-plane w-component.

The still uncorrected 16 mapping functions are used to compute a Stereo-PIV 2D3C-vector field from the synthetic 4-frame image in the usual way including final vector validation. Final interrogation window size is 32x32 pixels with an overlap of 75%. For a disparity of only a few pixels the errors are still quite small and only few false vectors occur. Calibration 3 with 9 pixel disparity shows an error of 0.44 pixel which is roughly expected from disparity times the velocity gradient. For all larger disparities, a meaningful velocity field can not be calculated any more. All vectors are eliminated either by the reconstruction error filter, which throws out all vectors

with a reconstruction error above 1 pixel, or by the final vector validation using a regional median filter.

Table 6.3. Errors after self-calibration.

Calibration	Residual disparity [px]	Position error [px]	Synthetic image error in V [px]	Synthetic image reconstr. error [px]
Reference	0.004	0	0.023	0.008
1	0.040	0.073	0.024	0.008
2	0.017	0.076	0.023	0.008
3	0.036	0.107	0.024	0.008
4	0.050	0.181	0.025	0.008
5	0.048	0.153	0.024	0.008
6	0.043	0.024	0.027	0.008
7	0.047	0.195	0.026	0.008
8	0.055	0.406	0.035	0.008
9	0.074	0.312	0.030	0.009
10	0.095	0.189	0.031	0.010
11	0.051	0.544	0.046	0.008
12	0.101	0.561	0.030	0.010
13	0.038	1.335	0.087	0.008
14	0.286	3.275	0.212	0.018
15	0.103	1.480	0.100	0.010
16	0.073	0.771	0.052	0.009

In the next step, the mapping functions 1 to 16 are corrected using the self-calibration procedure on the recorded random pattern image. For the corrected mapping functions the average residual disparity is computed again (Table 6.3). It is usually well below 0.1 pixel even for very high initial misalignments. Most of the remaining errors are due to standard correlation errors. Only calibrations 10, 12, 14, and 15 have a higher residual misalignment relative to the reference calibration.

The corrected mapping functions are compared to the corrected reference mapping function first with a direct comparison of the functional form of the mapping functions. Using a grid of 10 x 10 image points in the z=0 plane the values of the mapping functions are computed and compared to the values of the corrected reference mapping function after equalizing the still different coordinate origins, in-plane rotations and conversion scales from mm to pixel. This positional deviation to the reference mapping function is shown in the third column of Table 6.3. For higher initial disparities, the final positional errors are also larger, but in most cases still acceptable. While the disparity tells if the vectors for camera 1 and camera 2 are computed at the same position, which is most important for the errors of the final velocity field in regions of strong gradients, the positional errors relate to general residual warping of the coordinate system. The vectors are then computed at wrong

x/y-position (typ. < 2 pixel) and with wrong spatial derivatives (typ. < 1-3%). Given a typical distance between vectors of 8 to 16 pixel a sub-pixel positional error in the coordinate system is still acceptable.

Finally using the corrected mapping functions the 2D3C-Stereo-PIV vector fields are computed and compared to the true displacement field. Table 6.3 shows the deviation from the true result as well as the average reconstruction error. The reconstruction error originates partly from normal correlation errors, secondly due to vectors from camera 1 and 2 computed at different positions and lastly due to slightly wrong spatial derivatives of the mapping function, as might be the case for calibration 14.

For most cases the reconstruction error is well below 0.02 pixel. The differences relative to the true velocity field are therefore mainly due to a residual disparity and warping of the in-plane x-y-world coordinate system. The results for calibrations 13, 14, and 15 show the limit of the self-calibration procedure for large disparities (1/3 of image size). Interestingly calibration 16 is more accurate again. Looking at the projection angles it might be due to the fact that this view is far off but still almost parallel to the light sheet, while calibrations 13-15 are more tilted and covering more depth in the observation volume.

For all other calibrations, the errors in V are less than 0.04 pixel, usually much smaller than what can be expected for real experiments with all other known error sources. The value of 0.023 pixel for the reference calibration is mostly due to the effect of image degradation due to warping and dewarping of the original synthetic particle image. At the same time the results validate the accuracy of the basic Stereo-PIV correlation and reconstruction algorithms. The multi-pass algorithm with simultaneously dewarped and deformed interrogation windows proves to be highly accurate.

The results show the potential of the self-calibration procedure to correct even large misalignments between calibration plate and light sheet. A small aperture has been used for a large depth-of-focus, and for the calibrations with the largest disparities some part of the images is already slightly out-of-focus. This suggests that the camera pinhole model is sufficiently accurate as long as images are recorded within the depth-of-focus.

6.2.3.2 Experimental results with translated plate

A flat target of size 5 x 7 cm with a random dot pattern has been translated in the z-direction using a translation stage with an accuracy of about 5 µm. The plate has been moved in z-direction by 1 - 5 mm. The calibration has been done using a 3D-calibration plate recorded at 8 views at arbitrary position which have been evaluated by bundle adjustment.

The experiment has been performed in air as well as in water where the z = 0 mm plane was about 45 mm deep in water behind a 3 mm glass plate. In Table 6.4 are shown the main camera pinhole parameter after self-calibration onto the random pattern target. In both air and water the small average residual disparity

after self-calibration is mainly due to uncertainties in the peak detection of the correlation peak. The angle between the cameras is about 45 degrees.

Table 6.4. Mapping function parameter for air and water, both with 8 views and bundle adjustment.

	initial / residual disparity [pixel]	x_0 / y_0 [pixel] cam 1 cam 2	s_x	f [mm]	T_x [mm]	T_y [mm]	T_z [mm]	R_x [°]	R_y [°]	R_z [°]
Air	65 / 0.07	586/552	0.998	60.8	16.1	1.3	411.7	1.4	20.3	2.7
		706/548	0.998	60.9	9.2	0.2	435.2	-0.2	-24.3	2.2
Water	7.9 / 0.16	-1882/560	0.957	81.0	113.9	-10.3	537.6	2.7	27.0	4.4
		4074/491	0.924	83.4	-162.0	-8.3	570.5	-1.7	-34.1	4.2

For water, the calculated pinhole parameters are quite different. The principal point lies way outside the chip and the skew-factor is much less than 1 as would be expected for square pixels. This is due to the distortions of the air-glass-water interface which can only be fitted by the camera pinhole model by unphysical values for s_x, f and the principal point. Nevertheless, the calibration as a whole seems to be very accurate which is indicated by the fact that for the bundle adjustment in water all calibration points in space were fitted with an accuracy better than 0.1 pixel.

Table 6.5. Comparison of measured displacements with true ones.

Translation stage moved by:	dz = 1 mm	dz = 2 mm	dz = 3 mm	dz = 4 mm	dz = 5 mm
Air triangulation	0.999 mm	2.002 mm	2.996 mm	4.002 mm	5.001 mm
Air Stereo-PIV	0.995 ± 0.001 mm 20.22 ± 0.03 pixel	1.992 ± 0.003 mm 40.46 ± 0.06 pixel	2.973 ± 0.003 mm 60.38 ± 0.05 pixel	3.962 ± 0.004 mm 80.47 ± 0.08 pixel	4.941 ± 0.006 mm 100.35 ± 0.12 pixel
Water triangulation	1.001 mm	2.005 mm	2.995 mm	3.998 mm	4.992 mm
Water Stereo-PIV	0.997 ± 0.004 mm 20.59 ± 0.06 pixel	1.995 ± 0.006 mm 41.18 ± 0.13 pixel	2.977 ± 0.007 mm 61.45 ± 0.15 pixel	3.969 ± 0.007 mm 81.92 ± 0.15 pixel	4.949 ± 0.009 mm 102.15 ± 0.19 pixel

In Table 6.5 are shown the results of the measured displacements. The second row shows for air the displacements using a triangulation and plane-fit method as in the standard self-calibration procedure. First the disparities of the images recorded at e.g. position z=1 mm are computed relative to the corrected mapping function at z=0, and using triangulation the position of points on the z=1 mm plane are determined, and a plane is fitted through those points. The measured position of the

z=1-5 mm planes agree with the translation stage movement within 4 μm which proves a high accuracy of the mapping function throughout the volume. This agrees well with the measurement errors of 2-4 μm reported by Fournel et.al. (2004) for the same type of experiment.

The next row shows the Stereo-PIV evaluation in air using the corrected 8-view bundle calibration. The vector computation was performed with multi-pass iterations and deformed interrogation windows of size 64x64 pixels. The measured displacements in air agree within the uncertainties of the translation stage for 1 and 2 mm displacements. For larger displacements, there seems to be a systematic bias. Given the good agreement of the triangulation and plane fit method using the same mapping function this error is probably due to the fact that the 3C-reconstruction uses mapping function derivatives calculated only at the z=0 plane. These derivatives change over the quite large distance of 5 mm (equal to 100 pixels). A better way would be to compute the 3C-reconstruction using the more accurate triangulation method. Further investigations are needed to look at this effect in detail. For practical purposes, a bias of 0.06 mm = 1.2 pixel at dz = 5 mm = 100 pixel would lead to a bias of 0.06 pixel for typical displacements of 5 pixel which is commonly less than due to all other error sources.

The rms in the other u- and v-components remain always around 0.03 pixel. While the average v-displacement is zero everywhere, the u-components show a bias of 0.36 pixel at dz = 1 mm, increasing linearly with larger displacements. Closer inspection revealed that the axis of the translation stage was not exactly perpendicular to the random pattern plate resulting in a slight x-movement.

The experiment has also been repeated with a translation in x-direction. Again, the measured displacements agree well with the settings from the translation stage within the uncertainties of the translation stage.

The results are similar in water. For up to 2 mm (40 pixel) the accuracy is high with some bias effect for larger displacements. The rms-values are larger than in air due to a residual incorrect warping of the coordinate system which e.g. for dz = 1mm shows up as a gradient across the image in the displacement of the order of 0.03 pixel. The triangulation and plane fit recovers accurately the movement of the plate by the translation stage. This proves that the camera pinhole model and the self-calibration method remains sufficiently accurate even with strong distortions from refractive index changes.

6.2.3.3 Experimental results with particle images

An experiment has been performed in air with water droplets of a few micron size. Two jets of air are passing upward with higher speed between two cylinders of 10 mm diameter generating high shear regions. The field-of-view is about 85 x 70 mm at a distance of 500 mm. The camera CCD array is 1280 x 1024 pixels. The angle between the cameras is about 50 degrees. Three calibrations 1-3 are taken using a 3D calibration plate. The average disparity relative to the recorded particle images is 44, 82, and 252 pixels, respectively. The disparity map for calibration 2 is shown

in Figure 6.5c which corresponds to a rotational misalignment around the y-axis of about 13 degrees together with a z-displacement of around 5 mm.

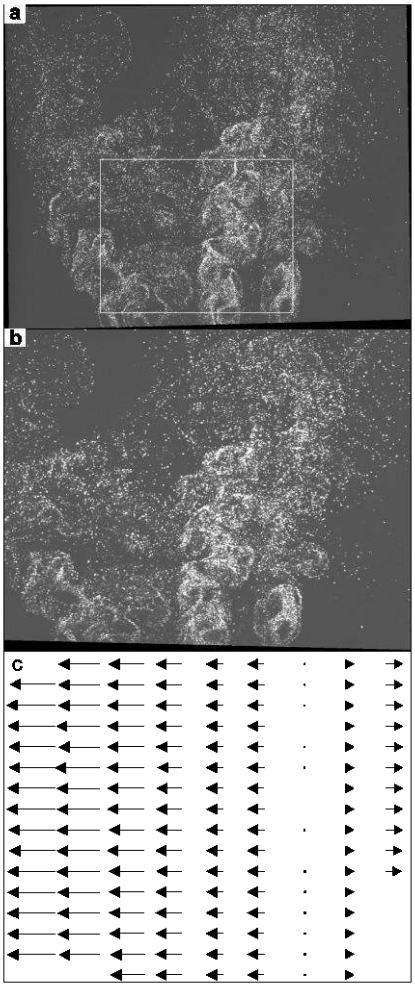

Figure 6.5. Particle image viewed by camera 1(a) and 2(b) dewarped with calibration 2. The white rectangle defines the high shear area evaluated. Bottom (c): corresponding disparity map typical of a rotation around the y-axis.

Vector fields are computed for the high shear region (Figure 6.5a). The final interrogation window size is 32x32 pixel with 75% overlap. The average velocity gradient is 3% with maximum values around 20% close to the jets. Without self-calibration correction, large displacement errors are visible and many vectors are removed due to reconstruction errors larger than 1 pixel as shown in Figure 6.6a for calibration 1. For calibration 2 and 3 no meaningful vector fields can be calculated.

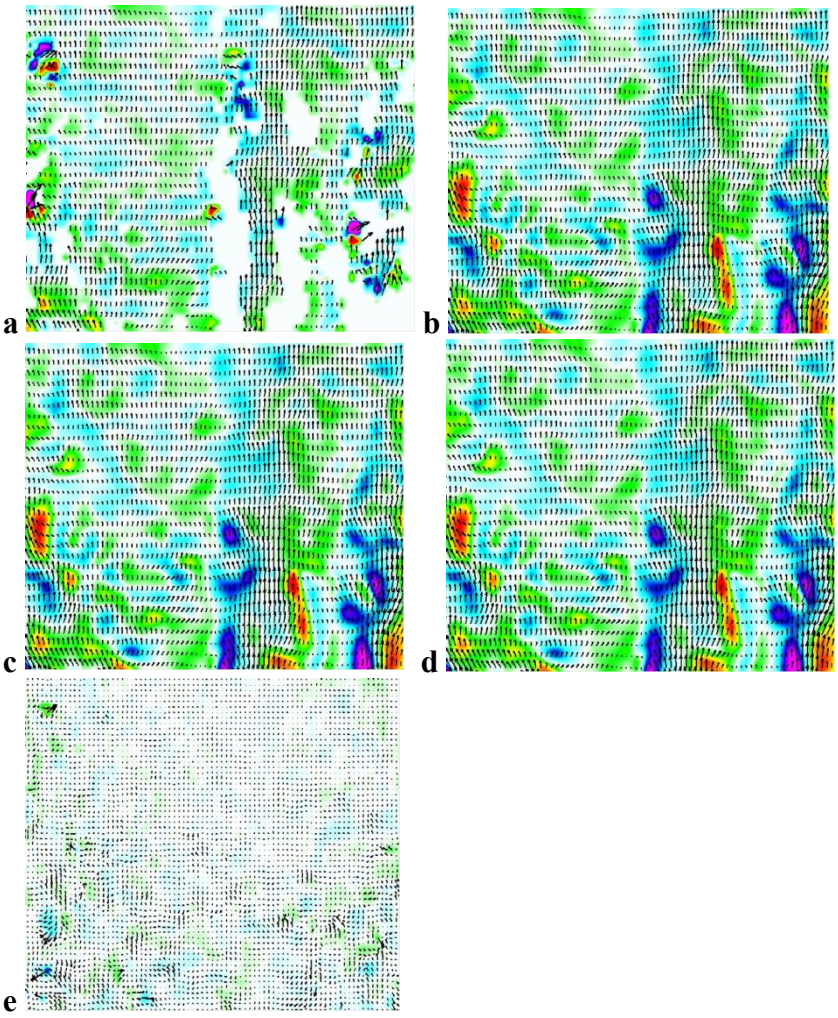

Figure 6.6. Vector field for uncorrected calibration (a), b-d: velocity fields after self-calibration for calibration 1 to 3. e: difference between vector field of calibration 1 and 3. The vectors in e are enlarged 50x. Field-of-view of about 600x500 pixel. Background color = vorticity.

Self-calibration has been performed using interrogation window sizes of 128 x 128 pixel with an overlap of 50% and a summation of 16 correlation maps, which provided correlation peak positions with an accuracy better than 0.1 pixel as can be deduced from the laser plane fit error which is less than 0.1 pixel for all three mapping functions. After equalizing the coordinate origin, the direction of the x-axis, and the global scale from pixel to mm between the three corrected mapping functions, the average difference in the mapped x/y-position between the three

corrected mappings is less than 0.4 pixel as calculated directly from the functional form of the mapping functions.

With self-calibration correction, the vector fields of the three calibrations are almost identical (Figure 6.6b-d with background color = vorticity). The rms vector difference between calibration 1 and 3 in the high shear region is only 0.055 pixel (Figure 6.6e). Note that the displayed vectors are enlarged by a factor of 50.

6.2.4 Self-calibration into closed measurement volumes

In many applications, it is difficult if not impossible to perform an accurate calibration inside the measurement volume. Here it is necessary to calibrate outside and somehow compute a corrected mapping function for the measurement plane inside the volume using the disparity map and an appropriate correction scheme. Different strategies are investigated in section 6.2.4.1 and 6.2.4.2 together with experimental verification.

6.2.4.1 Calibration outside with similar optical setup

It is shown in section 6.2.3.2 that the camera pinhole model without modifications can handle the refractive index change with sufficient accuracy. A straight forward strategy is then to perform the calibration outside under conditions as similar to the real measurement condition as possible. As shown in Figure 6.7 (left, middle) this can be done by first focussing the cameras onto the light sheet plane, then sufficiently retracting both cameras with a translation stage such that a small water basin can be placed in front of the water channel, and performing a calibration inside the water basin in the standard way with a single or multiple views of a 2D- or 3D-calibration plate. It is important that the distance between the cameras and the front side of the water basin is the same as it is relative to the front side of the water channel in the real measurement position (L in Figure 6.7). Finally, the cameras are moved back to the original position and the real experiment is performed and the standard self-calibration procedure can be applied to correct the mapping function onto the light sheet. With an accurate mechanical setup the accuracy of this approach is the same as if both the calibration and the recording were done inside the measurement volume.

A scan in z-direction through the measurement volume can be done by moving the laser light sheet to a new z-position and computing the self-calibration separately for each z-position. If the travel distance is larger than the depth-of-focus it is necessary to move the cameras and the light sheet simultaneously. In this case it is required to perform a calibration outside in the water basin for each z-scan position separately by adjusting the distance between cameras and front side of the water basin accordingly.

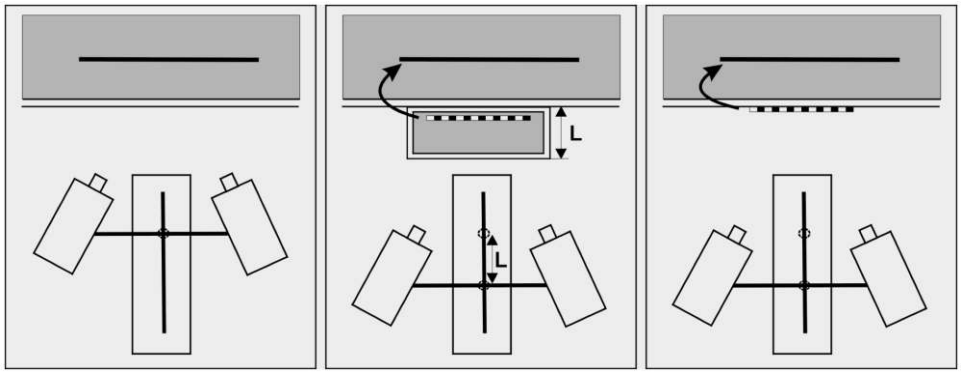

Figure 6.7. Left: recording position. Middle: calibration procedure outside in similar optical setup. Right: calibration outside in air and self-calibration onto recording using 3-media model.

Table 6.6. Measured displacements for calibration in air and self-calibration to recording in water. Displacements given in mm, 1mm = 21.1 pixel. Distance between glass plate and light sheet $dZ_{g\text{-}l}$ is 40 mm.

Translation stage moved by:		dz = 1 mm	dz = 2 mm	dz = 3 mm	dz = 4 mm	dz = 5 mm
Standard Model	Triangulation	0.737	1.491	2.228	2.978	3.720
	Stereo-PIV	0.743 ± 0.004	1.486 ± 0.003	2.217 ± 0.006	2.957 ± 0.007	3.688 ± 0.006
3-Media Model	Triangulation $dZ_{g\text{-}l}$ = 40	0.996	2.005	3.003	4.014	5.016
	Stereo-PIV $dZ_{g\text{-}l}$ = 40	1.006 ± 0.004	2.012 ± 0.004	3.001 ± 0.006	4.001 ± 0.006	4.989 ± 0.015
	Stereo-PIV $dZ_{g\text{-}l}$ = 30	1.006 ± 0.003	2.009 ± 0.004	2.996 ± 0.005	3.994 ± 0.006	4.981 ± 0.007
	Stereo-PIV $dZ_{g\text{-}l}$ = 20	1.003 ± 0.003	2.007 ± 0.004	2.994 ± 0.005	3.991 ± 0.006	4.976 ± 0.007
	Stereo-PIV $dZ_{g\text{-}l}$ = 0	0.972 ± 0.003	1.944 ± 0.005	2.899 ± 0.006	3.865 ± 0.007	4.819 ± 0.009
	Stereo-PIV dZg-l = 40, $\alpha x = 10°$	1.021 ± 0.007	2.041 ± 0.013	3.045 ± 0.018	4.059 ± 0.025	5.061 ± 0.032
	Stereo-PIV dZg-l = 40, $\alpha y = 10°$	1.000 ± 0.001	2.001 ± 0.003	2.995 ± 0.005	3.978 ± 0.006	4.960 ± 0.008

6.2.4.2 Calibration outside in air

Of course, it would easier to perform the calibration outside in air without a water basin and to self-calibrate onto the recorded light sheet in water (Figure 6.7 right). The results are shown in Table 6.6.

This approach leads to large errors for the standard pinhole model. The z-displacement is shortened by about the index-of-refraction of water. During self-calibration it is not possible to refit all parameters of the pinhole model to the distorted water case. Especially the internal camera parameter, like s_x and f, are not changed during the standard self-calibration procedure. In principle, the disparity map, as defined by the 3x3 fundamental matrix equation, has 8 degrees of freedom and only the three plane parameter need to be refitted by the standard self-calibration method. Hence one has the extra degrees of freedom to fit parameters like s_x or the relative camera orientation. But there are too many parameters to be fitted, so one must be restricted to a subset given by the particular experimental setup.

A better approach is to modify the camera pinhole model to accommodate the air-glass-water interface. This method allows an accurate physically motivated model. A three media model (e.g. air-glass-water) has been implemented according to Maas (1992). Using Snell's law and an iterative approach the bending of light rays through glass and water is calculated. The thickness and refractive index of each medium can be specified. The thickness $dZ_{g\text{-}l}$ of the last medium (water) is defined by the distance between the light sheet plane and the previous medium (glass). Currently, this value must still be measured together with the two angles between the light sheet and the glass plate. The distance between light sheet and glass plate can be measured, for example, by focussing on the light sheet with large aperture (small depth of focus) and then traversing the cameras backwards until a target mounted on the front side of the water channel is in focus.

The initial calibration in air is done without the 3-media model which is switched on for self-calibration (triangulation step) and the subsequent Stereo-PIV vector computation.

The results are shown in Table 6.6. With the 3-media model the movement of the random pattern plate is accurately computed both by the triangulation method and the Stereo-PIV evaluation. For larger displacements, again some deviations are visible showing the limits for the 3-media model, both for the triangulation and the Stereo-PIV method. This is not relevant for typical PIV experiments since dz=5 mm corresponds to an extremely large displacement of 100 pixel. The only drawback is that one has to know the distance $dZ_{g\text{-}l}$ between the light sheet and the glass plate. In the current experiment $dZ_{g\text{-}l}$ is 40 mm which was measured conventionally. Ideally one could also fit this from the disparity map, but initial tests indicate that the fit algorithm then becomes unstable and is not able to fit the particle plane and the glass plate at the same time. Further work is needed to explore this possibility.

In Table 6.6 are also shown the results of the self-calibration procedure with assumed wrong distances $dZ_{g\text{-}l}$ to determine the sensitivity of inaccurate

measurements of the position of the laser sheet with respect to the glass plate. The computed Stereo-PIV displacements remain accurate within 1% for offsets of $dZ_{g\text{-}l}$ up to 20 mm. The important feature of the 3-media model is that the z-derivatives of the mapping functions which are off by a factor given by the index-of-refraction of water are again accurately calculated. Any remaining in-plane x-disparities are compensated by the self-calibration procedure. Larger errors are visible for wrongly measured tilts of the light sheet. For an assumed tilt around the y-axis of 10 degrees dz and dy (=0) are accurate within 2% but there is a systematic error in dx of 3%. For a tilt around the x-axis there is a systematic error in dy of 8% and a residual y-disparities of a few pixel, which can not be compensated by self-calibration. Of course, the 3-media model is also of advantage when calibrating in-situ in water. It has been verified that the camera pinhole parameter return to physically meaningful values in comparison to the strange ones as in Table 6.4.

6.2.5 Laser Light Sheet Thickness and Relative Position

As an added benefit of the correction scheme the thickness and relative position of the two laser sheets of the double-pulse PIV laser can be deduced from the correlation maps. The correlation peaks are smeared out due to particles contributing throughout the light sheet as shown in Figure 6.8. Consequently, the light sheet thickness can be computed by simple geometric considerations from the correlation peak width. When the cross-correlation is done on dewarped images the correlation peak width is given by:

$$w_c = d \bullet (1/\tan(\alpha_1) + 1/\tan(\alpha_2)) \qquad (6.9)$$

with d = light sheet thickness and α_1 and α_2 are the viewing angle of camera 1 and 2 relative to the x-axis in the case when the cameras are placed horizontally along the x-axis. This is assuming point particles. For real particles the correlation peak is folded with the particle point spread function which could be calculated by auto-correlation. The width of the correlation peak in units of pixel is a function of the ratio of the thickness of the light sheet in relation to the distance between camera and light sheet. For a typical Stereo-PIV experiment with measured xy-displacements of 5 to 10 pixel one needs a light sheet thickness at least twice as thick to measure z-components of the same order. Therefore, typical correlation peak widths are of the order of 10-20 pixels.

If this analysis is done for both laser light sheets separately, the relative position of the two planes can be calculated by comparing the position of the two correlation peaks/streaks to determine the overlap of the two light sheets and the flatness of each sheet. Another method often used for determining the overlap of the two laser sheet – besides visual inspection - is by setting the dt between the two laser shots as short as possible. Then the two images of each camera show almost the same particle pattern (if the light sheets are well aligned) and a cross correlation gives a high correlation coefficient indicative of good light sheet overlap, decreasing strongly for reduced overlap between the two light sheets. The above method based

on cross correlation of camera 1 and 2 is computationally more intensive, but offers the advantage of showing the real position in space of each laser beam with a clear indication which screw in the laser head to be adjusted.

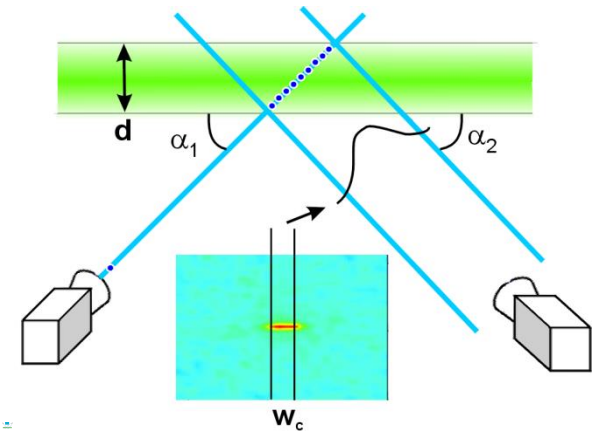

Figure 6.8. Particles throughout the light sheet contribute to the correlation peak. From the peak width the light sheet thickness can be computed.

6.2.6 Summary

A self-calibration correction scheme has been developed to compensate for misalignment between the calibration plate and the light sheet. After fitting a camera pinhole model to a 3D calibration plate a disparity vector map is calculated by cross-correlating the dewarped particle images of camera 1 and 2 taken at the same time. For higher stability and accuracy, the correlation maps of e.g. 5-50 image pairs are summed up. The disparity vectors are used to calculate world points on the real measurement plane by triangulation. A plane is fitted through these points.

Finally, the mapping functions are transformed to the new plane. It is shown that this calibration scheme provides highly accurate mapping functions with final displacement errors smaller than is expected from the other error sources like the basic PIV correlation algorithm for real images. This has been confirmed for different experimental setups. It has been shown that with such a correction the z=0 plane of the mapping function lies within 0.1 pixel of the middle of the light sheet.

The self-calibration scheme is advisable in any case to check the calibration and to improve the accuracy. Since it works well even for very large misalignments, it eliminates the need for an alignment of the calibration plate with the light sheet which is often difficult and time-consuming.

A modified 3-media camera pinhole model has been implemented to account for index-of-refraction changes along the optical path. It is then possible to calibrate outside e.g. a closed water channel and self-calibrate onto the recordings inside the channel. This

method allows Stereo-PIV measurements inside closed measurement volumes not previously possible.

As a side benefit the correlation maps can be analysed to yield the position and thickness of the two laser sheets and therefore the degree of overlap and flatness of each sheet.

6.3 Current Status of Stereo-PIV Self-Calibration

The Stereo-PIV self-calibration procedure has been successfully and widely used for more than a decade, in particular due to its inclusion (with slight modifications) in popular commercial PIV software packages like Davis. It is based on correcting the mapping function itself by coordinate transformation once before starting PIV processing. No further modification of the Stereo-PIV vector computation and 3C-reconstruction procedure is needed. This is considered easier and more elegant than implementing rather complicated modifications to correct for vector location differences, size of interrogation window / magnification and tilted vectors (Willert 1997; Coudert and Schon 2001; Scarano et al. 2005).

The need for Stereo-PIV misalignment correction has been confirmed by Giordano and Astarita (2008) observing strong modulation and dephasing of displacement wavelengths without such a correction.

For self-calibration within the Davis-software, an extension to more than two cameras has been included to facilitate the alignment of thick-sheets / thin-volumes processed by multi-camera Tomographic PIV/PTV. Also, while disparities along the epipolar line (which is e.g. the x-axis when both cameras are aligned along the x-axis) indicate the 3D-position of the light sheet, remaining disparities perpendicular to the epipolar line relate to calibration mapping function errors, which can easily be removed by changing the mapping function parameter. Errors in the mapping function along the epipolar line are swallowed by virtual z-displacements of the light sheet. Light sheet misalignment correction together with correction of disparities perpendicular to the epipolar line ensure that Stereo-PIV can process vectors at the correct locations.

Stereo-PIV self-calibration works less well, when the light sheet becomes thicker, because the correlation peaks to be detected are actually extended streaks with a length proportional to the thickness of the light sheet. At the same time, the background correlation level increases as well. A larger number of images is needed for summation into sufficiently smooth correlation maps, and even after that, depending on laser profile quality, the light sheet might exhibit two distinct peaks along the correlation streak. Or the position of or the highest correlation value changes from front to back of the streak e.g. along the x-axis introducing a tilt in the coordinate system. A possible improvement could be the measurement of the center-of-mass of the correlation streak instead of the peak, which is somewhat more complicated.

Furthermore, when applying Stereo-PIV self-calibration, a spatial offset in the coordinate system might occur (Beresh and Smith 2014) since the newly computed

coordinate origin and in-plane rotation around the z-axis is subject to free choice. A xy-coordinate system defined in the original calibration is independent from the light sheet plane located in space at a different location. The new coordinate origin can be defined in different ways relative to the old one: nearest point on plane, along z-axis, or e.g. along viewing direction of one camera. The same applies to the x- and y-axis direction. A sensible choice would be e.g. to keep the direction of the x-axis similar. Nevertheless, if an accurate coordinate system is required, it either requires placing the calibration plate initially exactly along the light sheet plane and at the correct xy-position, or, if possible, realigning the coordinate system after self-calibration using visible markers in the recorded images.

Recently, Beresh et al. (2016) investigated the performance of Stereo-PIV self-calibration in more detail. While generally confirming the usefulness of the technique, they noticed complications with thicker light sheets as well as larger camera angles, small particle image sizes and high seeding density to gain a readily detectable smooth correlation streak/peak. Especially in crossflow setups requiring thicker light sheets, the self-calibration might converge to different final mapping functions depending on the self-calibration settings. The authors found that image preprocessing with background subtraction and intensity normalization provided the best results.

Some work has been done to eliminate the need of (self-)calibration for special setups. Fouras et al. (2008) propose to use a third camera looking perpendicular to the light sheet defining an accurate coordinate system and at the same time improving the Stereo-PIV accuracy. Grizzi et al. (2010) utilize a uniform reference flow to correct for misalignments and possible calibration plate dot position errors, which is particularly useful for underwater towing tank applications. Schosser et al. (2016) use a cw-laser and record the reflections at different locations to eliminate the need for a calibration plate all together, in particular, for cases where it is difficult to place a calibration plate inside the measurement volume.

6.4 Volume Self-Calibration

6.4.1 Introduction

Volume calibration provides a mapping function M(X,Y,Z) from space to camera pixel coordinates (x,y):

$$(x_i,y_i) = M_i(X,Y,Z) \tag{6.10}$$

for all cameras i.

For 3D-PTV and especially for tomographic PIV with extended volumes errors relating to inaccurate mapping functions are highly relevant. The tomographic reconstruction step requires that each voxel position in space is mapped to a camera pixel position with an error less than about 0.3-0.4 pixel (Elsinga et al. 2006), preferably less than 0.1 pixel.

Back in 2004/05, when Tomographic PIV was developed, it soon became obvious that something has to be done about the calibration accuracy. Luckily, the first experiments by Elsinga et al. to confirm the validity of the Tomographic PIV technique were done with a very sturdy mechanical setup with high calibration accuracy. Processing data from subsequent experiments turned out to be less accurate, where particle images from the 4 cameras dewarped to a certain z-plane showed that the line of sights of the four cameras did not intersect in one point, deviating by 1 pixel and more. Such a check was quite tedious as one has to find first some prominent particle (maybe in sparsely seeded flows) and guess some rough z-position, and to produce a movie of the sum of dewarped images over a range of z-positions. With a perfect calibration, the 3 or 4 particle images would overlap perfectly at the true z-position, and move apart for higher or lower z-positions. Calibration errors become visible by the particle images (at least one) just missing each other at the best z location.

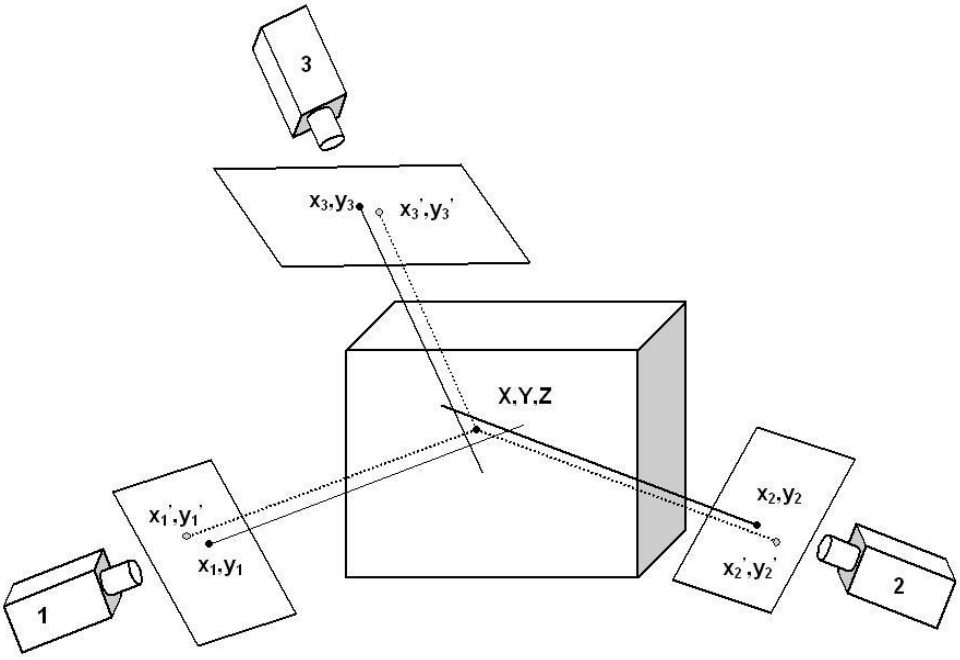

Figure 6.9. Residual triangulation disparities $d_i(X,Y,Z) = (x_i,y_i) - (x_i',y_i')$ due to calibration errors.

At that time, a far from optimal remedy to such calibration errors was to smooth the images by some 3x3 or 5x5 Gaussian filter so that at least part of the particle image of one camera would overlap in the volume with the particle images from the other cameras, so that reconstruction would provide at least some correct voxel intensities for the subsequent 3D-cross-correlation to work. Obviously, it only

worked for small calibration errors, the degree of ghost particles/intensities was very high and the velocity field was quite noisy.

Therefore, a volumetric self-calibration technique was urgently needed, which is capable of correcting the mapping function throughout the volume. Such a technique is described in next section, followed by an experimental verification using tomographic PIV showing significant improvement of the vector field quality.

6.4.2 Method

The basic principle of correcting mapping function errors in a volume using the actual recorded particle images is summarized first, followed by a detailed explanation of each step.

The first step is localizing 2D-particle positions in the image of each camera and finding corresponding 3D particle positions by matching and triangulation which is essentially the first part of the 3D-PTV algorithm as shown in Figure 6.9 for 3 cameras. The procedure is illustrated in the following for 4 cameras, but can be easily extended to other number of cameras, even including 2 (with less accuracy).

The 2D-particle positions (x_i,y_i) of camera i of a single particle in space are triangulated into a best fit world position (X,Y,Z). The optimization criterion is usually done by minimizing the sum of the distances $|(x_i',y_i') - (x_i,y_i)|$ where (x_i',y_i') is the projection of (X,Y,Z) back to image of camera i (Hartley and Sturm 1994). For a perfect mapping function the line of sights of all cameras intersect in a single world point resulting in a zero disparity d_i of

$$d_i = (d_{ix}, d_{iy}) = (x_i',y_i') - (x_i,y_i) \tag{6.11}$$

Collecting disparities d_i for all particles throughout the volume is then used to correct the mapping functions M to M':

$$M_i'(X,Y,Z) = M_i(X,Y,Z) - d_i(X,Y,Z) \tag{6.12}$$

with an appropriate validation and interpolation of the sparse disparities d_i for each particle into a continuous field or a similar method described below in more detail.

This basic principle works well with sparsely seeded 3D-PTV images with e.g. 1000 to 5000 particles in each image, where the matching of corresponding particle images is done with a high confidence level (>95%) (Maas 1996). But it does not work without further refinement for densely seeded images from tomographic PIV. Here the particle seeding density is much higher with typically >50,000 particles in each image equivalent to particle densities per pixel in the images of up to 0.1 ppp similar to standard planar PIV. Ideally one would record first a number of images with less seeding density, but this is often inconvenient or impossible.

Figure 6.10 shows the procedure to match particle images corresponding to the same particle in space. For each particle in the image of camera 1 one finds particles located within a stripe defined by the uncertainty ε_{max} along the length L_z which is the projection of the line of sight of camera 1 through the illuminated

volume from z_1 to z_2 viewed by camera 2 ('epipolar line'). For the combination of particle images for camera 1 and 2 a 3D particle position (X,Y,Z) is computed by triangulation. Then for each particle in the stripe it is checked if in the image of camera 3 and 4 there is a corresponding particle within $\pm\varepsilon_{max}$ around the projection of (X,Y,Z) onto camera 3 and 4 image.

The allowed uncertainty ε_{max} must be larger than the largest expected calibration error. For 3D-PTV with low seeding density and 4 cameras one rarely detects any incorrect ghost particles. The ratio R of ghost particles to true particles is a strong function of the seeding density n_{ppp} and allowed error ε_{max}:

$$R = 32 \bullet L_z \bullet \varepsilon_{max}^5 \bullet n_{ppp}^3 \qquad (6.13)$$

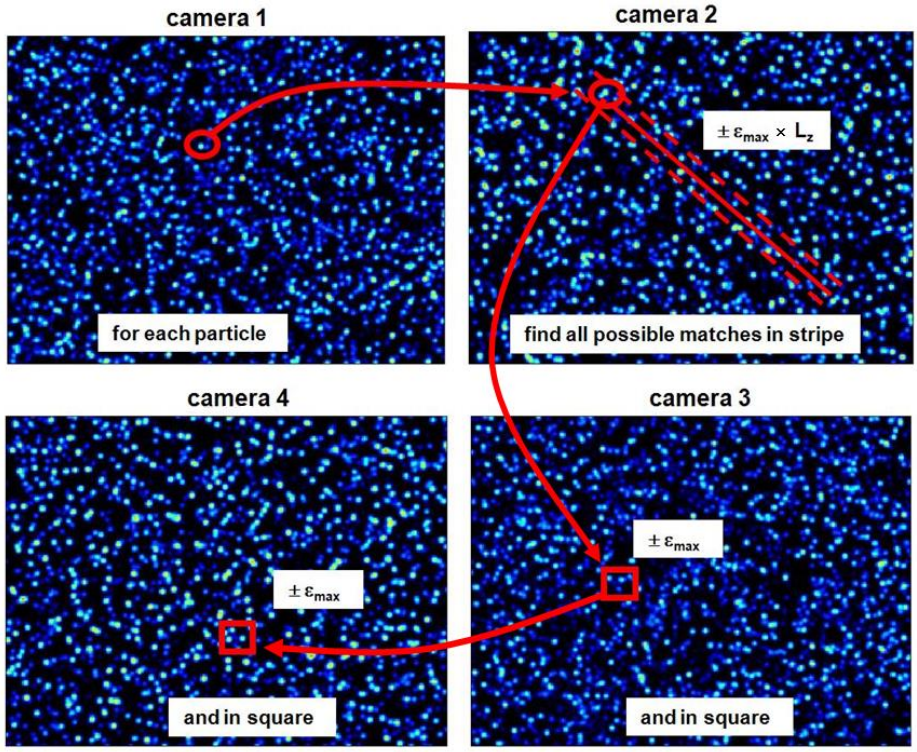

Figure 6.10. Particle triangulation procedure.

Typical conditions with e.g. L_z = 200 pixel, n_{ppp} = 0.05 ppp and allowed error ε_{max} = 4 pixel lead to R = 819 times more ghost particles than true ones. Obviously, it is then very difficult to identify the true particles and their disparity to be used for the mapping function correction. In addition, given such high densities the probability of overlapping particles is high which leads to erroneous 2D and 3D particle positions and noisy disparities.

The solution is to apply an appropriate clustering technique and using not all particles but only the brightest e.g. 10%. Immediately the number of ghost particles

is reduced by nearly several orders of magnitude with the added advantage that even in case of overlapping particles the bright particles are much less influenced by another overlapping weak particle. Usually image preprocessing including global and local intensity renormalization is applied to the 4 camera images to subtract background intensities and to correct particle intensity differences due to e.g. forward-backward laser scattering differences. A single threshold for all camera images can then be used so that the group of particles above a certain threshold is about the same in all camera images.

The complete self-calibration procedure can be divided into the following steps:

a. Measuring 2D particle positions in all camera images.
b. Determining possible 3D particle positions by triangulation.
c. Subdividing the complete illuminated volume into $n_x \bullet n_y \bullet n_z$ sub-volumes.
d. Plotting the disparities of all particles in a sub-volume as a 2D disparity map.
e. For each sub-volume and all cameras, summing of disparity maps over many recordings to get better statistics.
f. For each disparity map detecting highest disparity peak which is the most probable disparity vector $d_i(X,Y,Z)$.
g. Validating and optionally smoothing of the 3D2C disparity vector field d_i.
h. Correcting mapping functions M_i according to eqn. (6.12) for all cameras i.
i. Repeating the complete procedure as a check and for further improvement.

Step a: As described above a suitable threshold is selected to only use the brightest e.g. 10% of all 2D particle images. Particle fitting itself is done in a standard way with a 5x5 2D Gauss fit, reduced to a 3x3 Gauss fit, if neighboring particles gets too close, i.e. if an outer rim pixel is brighter than the inner 3x3 core, falling back to a dual x- and y-1D-Gauss fit which always work. For isolated particles, the position accuracy is typically below 0.1 pixel depending on optical conditions and particle size etc.

Step b: The triangulation procedure computes all possible particles in space with a triangulation uncertainty d_i (eqn. (6.11)) smaller than ε_{max} as shown in Figure 6.10.

Step c: The complete illuminated volume is subdivided into $n_x \bullet n_y \bullet n_z$ sub-volumes (e.g. 5x5x5) in order to collect sufficient 3D-particles in each sub-volume.

Step d: For each sub-volume and all 3D particles within the sub-volume a small 2D Gauss blob is plotted at the disparity position (dix, diy) in a square of e.g. 50x50 pixels corresponding to the allowed maximum error $\pm\varepsilon$max. For each camera i a separate disparity map is generated.

The computation of the disparity d_i can be done in slightly different ways. The first step is always to use the particle positions (x_i,y_i) in the images of camera i to compute a best-fit world position (X,Y,Z) by triangulation (Hartley and Sturm 1994) as in step b together with the residual triangulation error d_i as the difference between $(x_i',y_i') = M_i(X,Y,Z)$ and (x_i,y_i) (eqn. (6.11)). One has an extra degree of

freedom which allows one to use one camera as a reference assuming that the mapping function for this camera is perfect thus correcting only the other mapping functions. This is done by taking Z from the original triangulation and computing an X_{ref} and Y_{ref} by inverting the mapping function for the reference camera:

$$(X_{ref},Y_{ref}) = M_{ref}^{-1}(x_{ref},y_{ref},Z) \quad (6.14)$$

and using X_{ref} and Y_{ref} for computing (x_i',y_i') for the other cameras:

$$(x_i',y_i') = M_i(X_{ref},Y_{ref},Z) \quad (6.15)$$

which is then used in eqn. (6.12). Of course, for the reference camera the disparity is zero. Whether one should use a reference camera deserves further investigation. Tomographic experiments so far have been mostly indifferent, with a few working better with one or the other method.

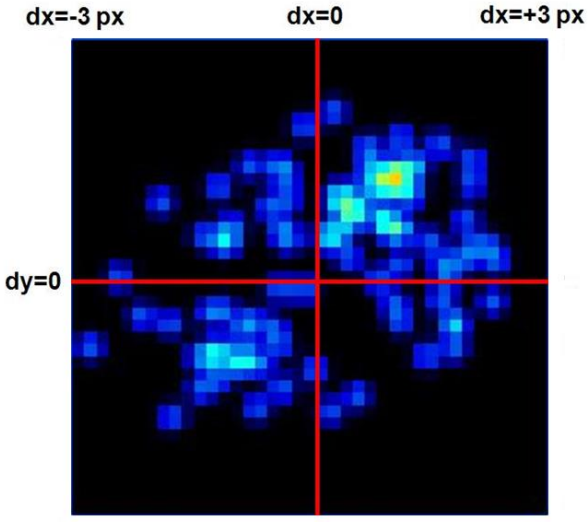

Figure 6.11. Disparity map for a single sub-volume.

Having collected possible 3D particles in space, one now needs to separate disparities of true accurate 2D/3D particle positions from ghost particles and inaccurate ones due to overlapping particles. There are many suitable clustering techniques available. The one used here is based on displaying the disparities for each sub-volume in a 2D disparity map as a histogram with each measurement point plotted as a small 2D Gauss blob. For example, the disparity map might be of size of e.g. ±30 pixel corresponding to a maximum allowed disparity ε_{max} of ±3 pixel, and each disparity d_i is plotted at position (d_{ix}, d_{iy}) as a 2D Gauss blob with a constant width of 2 pixel (0.2 pixel in units of disparity error).

The width of the Gauss curves provides sub-pixel accuracy for the position of the highest disparity peak (step f) similar to correlation peaks in standard PIV. It

should be made larger in case of few detected particles. The height of the Gauss curve is set to 1 for all particles. Alternatively, one could use the particle intensity of the 2D-peak finder to account for the light intensity variations across the volume. Such a display of the disparity allows a good visual inspection of the data quality. This is shown in Figure 6.11 for a real tomographic PIV experiment. One can guess that the true disparity peak is at the top-right, but there are not yet enough particles for good statistics.

Step e: Disparity maps from multiple recordings are summed for better statistics. Most often a single image does not contain sufficient particles to add-up to a sharp unfragmented disparity peak, especially when choosing a large number of sub-volumes. Figure 6.12 shows the emerging disparity peak when adding disparity maps from up to 16 images. The final outcome is one disparity map for each sub-volume in each z-plane for all cameras. Figure 6.13 shows the disparity maps for a single camera for a series of four z-planes on one side of the illuminated volume spaced 1 mm apart. The off-center disparity peaks in the fully illuminated bottom z-plane correspond to a calibration error of up to 2 pixel.

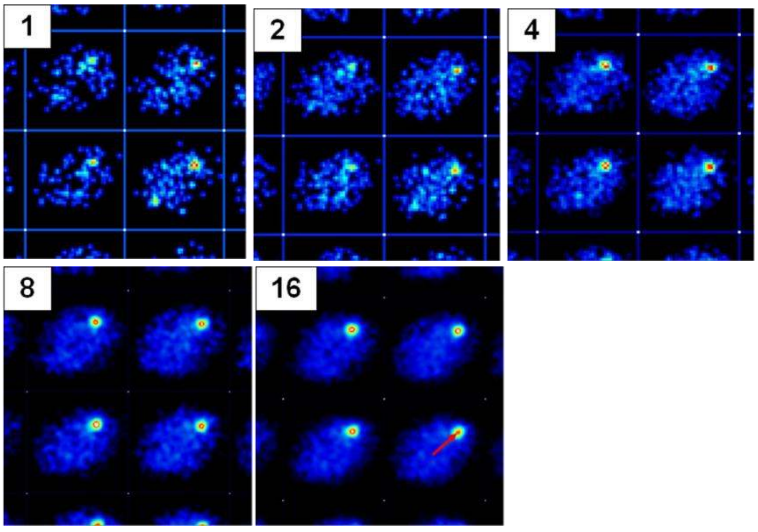

Figure 6.12. Summing disparity maps over 1 to 16 recordings. Color scaling is always from minimum to maximum intensity.

Step f: The sub-pixel disparity peak location is determined e.g. by a 2D or dual 1D-Gauss fit and corresponds to the most likely disparity vector d_i. The disparity peak width is a good indication of the accuracy of the 2D peak finder. For the experiment in Figure 6.12 it is only slightly larger than the selected Gauss width of 0.2 pixel, suggesting that the 2D peak finder accuracy is around 0.1 pixel. In rare cases it has been observed that the disparity peak is smeared due to error gradients within a single (large) sub-volume. Usually the calibration errors are highly uniform across the complete volume.

Step g: The outcome is a 3D2C-disparity vector field for each camera, one vector for each sub-volume. This vector field is validated using a three-dimensional universal outlier median filter (Westerweel and Scarano 2005) over a region of e.g. 3x3x3 or 5x5x5 vectors. One can store secondary disparity peaks in step f for possible selection by the median filter in case the highest peak is eliminated. If the selected volume is larger e.g. in z-direction than the actual illumination, then complete z-planes of sub-volumes might show random outlier vectors.

The median filter with a kernel of 5x5x5 is robust enough to throw out even complete z-planes of random vectors. Note that a 3D median filter is considerably more robust than a 2D filter due to the increased number of neighbour vectors within some spatial domain. Most often it is indicated to apply some additional 3x3x3 vector smoothing to reduce the error inherent in the whole process (Figure 6.14). The true disparity field usually varies little across the image, so it is possible to smooth the estimated disparity field heavily to prevent errors propagating into an erroneous new mapping function.

Choosing an initial volume larger than the illuminated volume is a good method to actually measure the size of the illuminated volume or, respectively, the common area viewed by all cameras. Figure 6.13 shows the disparity maps for consecutive z-planes on one side of the volume indicating at what z-plane the illumination starts. The volume is also slightly tilted with respect to the coordinate system as evidence by the left to right decrease in the disparity peak visibility.

Step h: The mapping functions M_i are corrected for each camera separately according to eqn. (6.12). Since the disparity vector fields are given only on grid positions defined by the center of possibly very few sub-volumes one needs to interpolate the vector field to intermediate positions. We choose to calculate new mapping functions M' on the z-planes defined by the sub-volumes. For each z-plane an array of 20x20 points is taken for which the difference between the original mapping function and the disparity field is computed and a new M' is fitted using third-order polynomial functions in x and y (similar to Soloff et al. 1997).

Step i: The sequence of steps a to h can be repeated after the first self-calibration to check whether the disparity peaks are finally positioned at the center position (0,0). One can choose in subsequent iterations a smaller maximum allowed disparity ε_{max} and a lower threshold for more true particles and at the same time less ghost particles. Usually two or three iterations are sufficient to reduce the mapping function errors down to below 0.1 pixel.

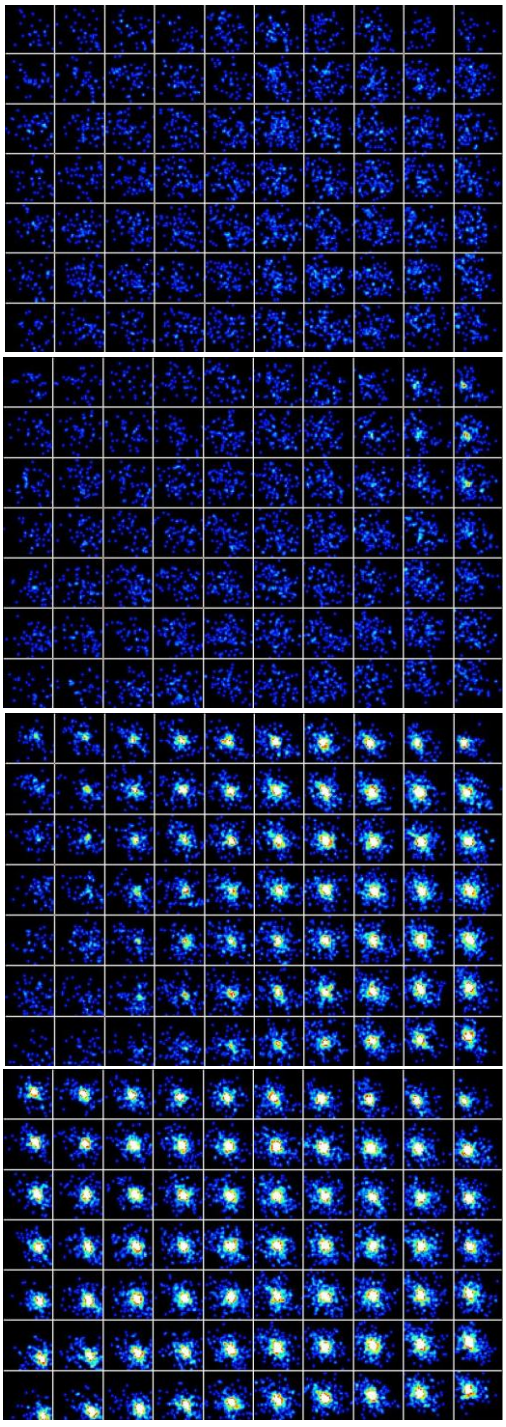

Figure 6.13. Disparity maps for decreasing depth z from top (not illuminated) to bottom (fully illuminated). Sub-volume size in xyz is about 8x8x1 mm.

At the same time the number of sub-volumes and the selected volume can be adjusted. Often it is advantageous to start with e.g. 2x2x2 sub-volumes to first correct roughly the mapping functions and use finer divisions (e.g. 10x10x10) later for a detailed local analysis of the 3D calibration errors.

6.4.3 Application to Tomographic PIV Experiments

This procedure is tested for a tomographic PIV experiment in water observing a transitional wake behind a finite length, circular cylinder with three-dimensional instabilities at Re = 540 (Michaelis et al. 2006) with a volume of 73 x 46 x 16 mm and a final 3D3C vector field with 141 x 89 x 29 vectors. It turns out that the initial mapping function had errors of up to 2-3 pixels close to the cylinder. After self-calibration, the errors are reduced to below 0.1 to 0.2 pixel.

The volume self-calibration procedure improves significantly the contrast of the reconstructed volume and the quality of the vector field in terms of higher correlation values and improved S/N ratios. Shown in Figure 6.15 is the raw vector field without any vector validation (top). Self-calibration eliminates most outliers (bottom). The signal-to-noise ratio of the (3D) vector correlation maps is almost twice as large as before. Figure 6.16 shows the complete volume vector field before and after the calibration procedure after vector post-processing.

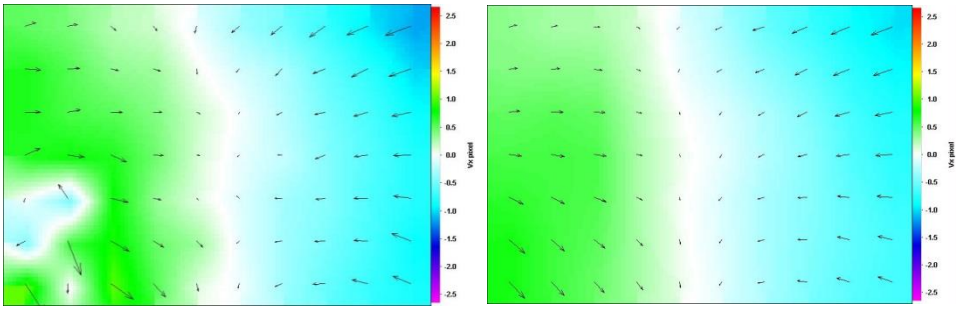

Figure 6.14. Original disparity vector field (left) and after vector validation and smoothing (right).

An important aspect is that without such a volumetric self-calibration procedure one is not even aware of how large the calibration errors actually are. As it turned out, even with great care during the calibration procedure there was hardly any experiment where the calibration errors did not exceed 1 or 2 pixels in some corner of the volume.

In an experiment viewing with cameras from opposite side of the volume it was possible to correct calibration errors in the range of 7 pixels arising due to a double-sided calibration plate tilted slightly relative to the z-direction in which it was moved. This resulted in the two cameras on the back side being shifted relative to the front side cameras.

Not knowing how large the error actually was, one started out with ε_{max} = 3 pixel, not finding any peaks in the disparity maps. Then one had to gradually increase ε_{max} and carefully adjusts the particle detection threshold to minimize the ghost particles and processing time. With ε_{max} = 10 (400 times as many ghost particles as for ε_{max} = 3) and only using 2x2x2 sub-volumes it was finally possible to see a faint disparity peak among the vast amount of ghost particles. Once this large error had been corrected in a first step, it was then easy to further reduce the calibration errors down to 0.1 pixels with fine local resolution possible due to otherwise high-contrast, low-noise images with particle densities less than 0.05 ppp.

Table 6.7. Relevance of calibration errors for different techniques (+ strong, - weak).

Technique	Inaccurate Mapping Function	Misalignment between Calibration Plate and Light Sheet
Stereo PIV	-	++
Thick-Sheet Tomographic PIV	++	++
Full-Volume Tomographic PIV	++	-
3D-PTV	+	-

6.4.4 Relevance for Other PIV Techniques

For standard Stereo-PIV and scanning light-sheet Stereo-PIV (Brücker 1996, Hori and Sakakibara 2004) the planar stereo PIV self-calibration method is usually sufficient to measure and correct the position and rotation of the light sheets which typically lead to disparities of 5-20 pixel. Remaining calibration errors of the order of a few pixels are only relevant in case of very strong local velocity gradients. But especially for thick light sheets required e.g. for cross-flow measurements the volumetric self-calibration technique is recommended. Here standard planar self-calibration often fails if the light sheet profile is not nicely Gaussian, but e.g. shows multiple intensity peaks within the long correlation streak.

Thick light sheet PIV images can be processed with the tomographic PIV algorithm usually adding a third or fourth camera (Wieneke and Taylor 2006). Volumetric self-calibration is then required to reduce the calibration errors to acceptable levels.

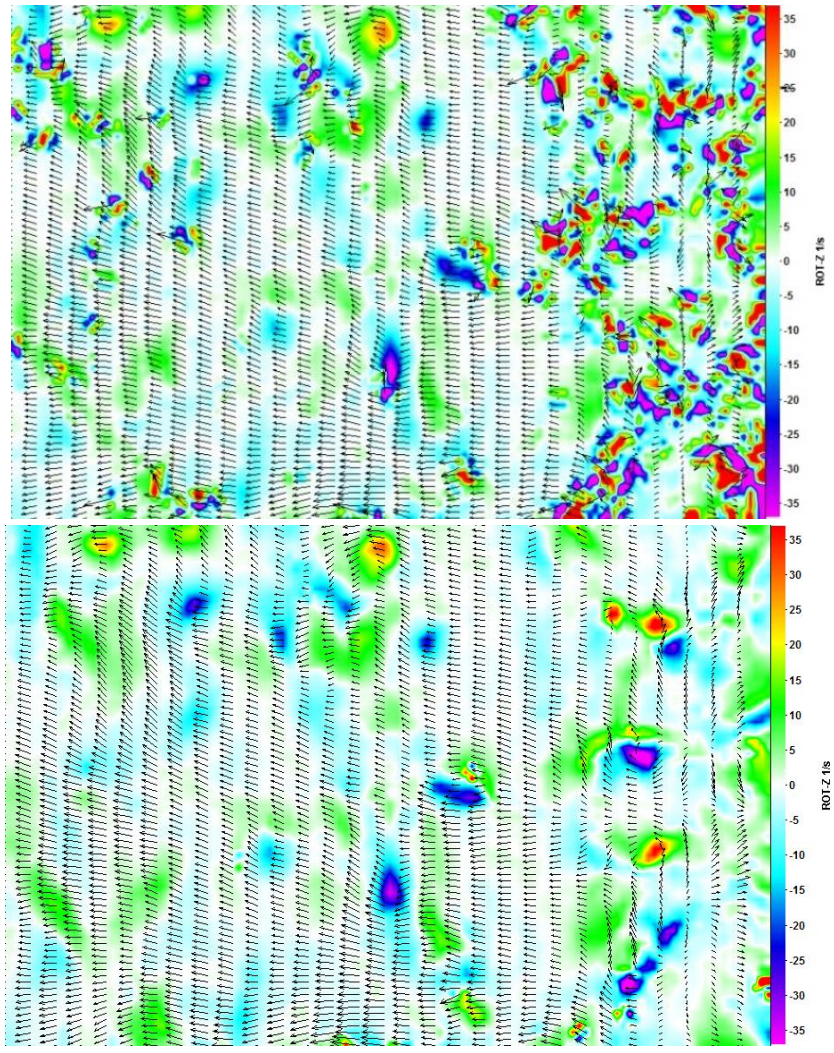

Figure 6.15. Z-plane of volume vector field without (top) and with (bottom) volume self-calibration. Shown is the raw vector field without vector validation with the 3D-vorticity magnitude as background color and every 4th vector in x-direction.

Finally, volumetric self-calibration is also recommended for standard 3D-PTV. For low seeding densities and unique conversion of 2D particle positions into a 3D particle position, a high systematic triangulation error is not critical. But for higher seeding densities the correction of calibration errors by volumetric self-calibration makes it possible to choose a very small threshold for the maximum allowed triangulation error. This significantly reduces the number of ghost particles and can provide some rejection criteria for overlapping particles which otherwise lead to inaccurate 3D particle positions.

Table 6.7 summarizes the importance of the two self-calibration algorithms for correcting laser sheet misalignments and mapping function errors, respectively, for the different planar and volumetric particle image velocimetry techniques.

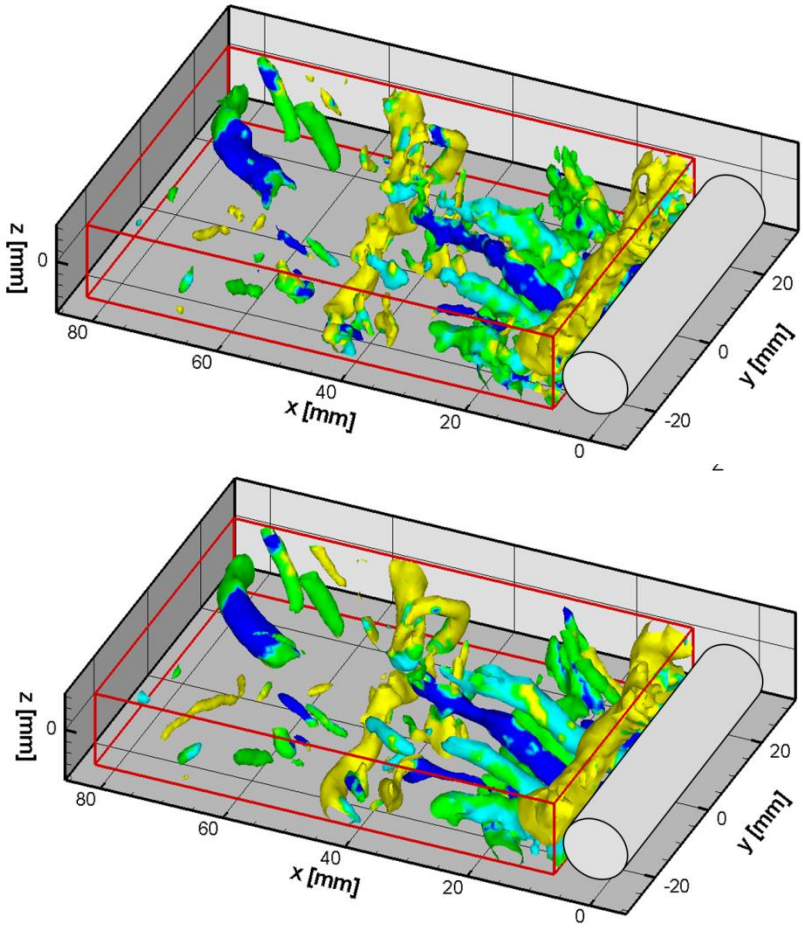

Figure 6.16. Complete 3D flow field without (top) and after self-calibration (bottom) with 3D-vorticity magnitude colored according to dominant sense of rotation (Michaelis et al. 2006).

6.4.5 Summary

A volumetric self-calibration technique (VSC) has been developed to correct mapping function errors using the actual recordings of the particle images. This is especially relevant for tomographic PIV where the mapping errors should be below 0.3 pixel. The method is based on detection of 2D-particle images and triangulation of the 3D-particle position in space. Particle images are usually intensity-normalized across the image and between cameras to account for Mie-scattering differences, and a threshold is used to select only the e.g. 10% brightest particles. Back-

projecting the 3D position toward the camera images and comparing to the original position provides a disparity error for each particle.

In collecting disparities for all particles throughout the volume and a suitable clustering method to eliminate false 3D-particles, one obtains a 3D2C disparity vector field for each camera. Sufficient statistics is obtained by summing the disparities from many recordings. After vector field validation and smoothing this disparity field is then used to correct the original mapping function. It is also possible to measure the actual extent and rotation of the illuminated volume from the disparity maps.

The technique has been applied successfully to a number of tomographic PIV experiments improving significantly the quality of the volumetric vector field. It was found that in most experiments even with a careful calibration procedure calibration errors of 1 – 2 pixel were found somewhere in the volume. After self-calibration this has been reduced to 0.1 – 0.2 pixel. The method is also useful for stereo PIV especially with thicker light sheets since here the standard planar self-calibration technique often fails due to multiple intensity peaks within the light sheet. For 3D-PTV the method can reduce the number of ghost particles allowing higher seeding densities.

6.5 Current Status of Volume Self-Calibration

Since VSC has been efficiently implemented around 2007, this has provided a major improvement for Tomographic PIV processing. Not only was it then possible to correct calibration errors, but even more important, one could measure and visualize the calibration errors by looking at and analyzing the disparity maps. Indeed, a successful VSC analysis and correction is usually taken as a prerequisite for Tomographic PIV to work at all. When one does not see clear disparity peaks (as shown in Figure 6.4), it is most often useless to try (S)MART-reconstruction and 3D-cross-correlation.

VSC is to our knowledge the only volumetric self-calibration procedure for Tomographic PIV and recently for volumetric particle tracking methods like the newly developed time-resolved Shake-the-Box method (STB, Schanz et al. 2016) based on iterative particle reconstruction (IPR, see chapter 7).

Other research groups, concentrating on possible margins of improvement in the reconstruction method itself and on other processing details of Tomographic PIV, implemented the existing VSC method in a similar way. VSC has established itself as the de-facto standard for correcting calibration errors in Tomographic PIV and recently STB as is evident by the large number of researchers using it successfully.

Below are shown the reported performance of VSC which is in agreement with in-house experience. In 79% of all experiments the initial calibrations had disparities above 0.3 pixel, above the limit for accurate (S)MART-reconstruction. Interestingly, quite a few experiments had to cope with calibration errors above 5

pixel. After applying VSC, except in one case, where initial disparities above 10 pixel were reduced to ‚less than 1-2 pixel', all disparities were reduced to acceptable levels, on average even below 0.1 pixel. Of course, the histogram is somewhat biased, since only successful Tomographic PIV/PTV experiments were reported. There were probably a few experiments with very large calibration errors, too high seeding densities, or other problems, which could not be processed at all.

Some work has been done validating the performance of VSC. While more cameras are beneficial for the MART-reconstruction, Discetti and Astarita (2014) report on the detrimental effect on VSC when increasing the number of cameras. With more cameras and given a required large search area for possible misalignments (e.g. > 3-5 pixel), the number of erroneous possible particle triangulations increases dramatically so that in some cases it becomes difficult or even impossible to find the barely visible true disparity peak.

On the other hand, Lynch and Scarano (2014) reported successful VSC correction on a 12-camera Tomographic PIV experiment. Obviously, VSC gets more complicated and time-consuming for more cameras. For all experiments, it is recommended to redo the calibration after the experiment to accomodate cases of cameras having drifted substantially e.g. due to weak mechanical mounting or somebody bumping into a camera just before or during recording. Even better, after recording a few images, a quick check with VSC to confirm the calibration accuracy might be advantageous.

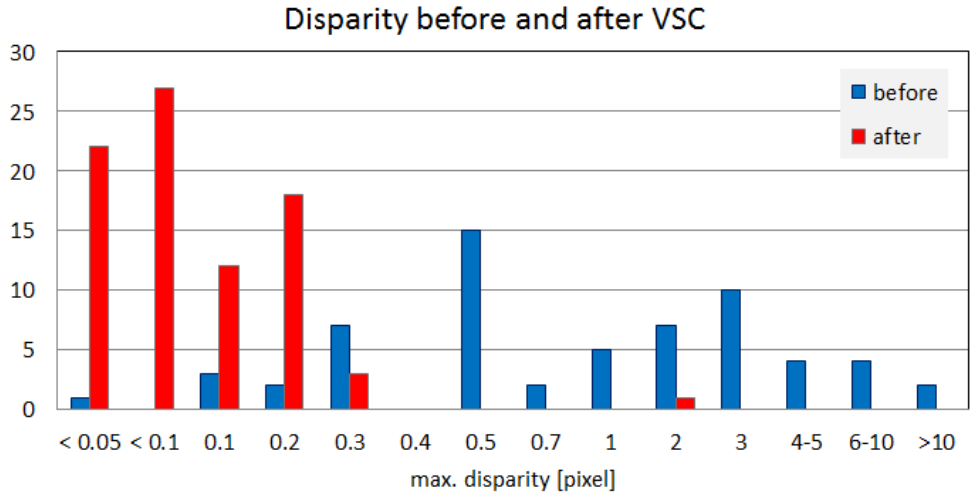

Figure 6.17: Histogram of disparities reported for the initial calibration (62 samples) and after applying VSC (83 samples), data collected by Joke Henne, LaVision GmbH.

One circumstance, where VSC has proven very useful, is in the case of vibrations of wind tunnel, model, cameras or all together. Vibrations can easily amount to disparities of up to 5-10 pixels changing from image to image. Michaelis and Wolf (2011) implemented a single-image VSC. First the complete volume is used for particle triangulation with a search area larger than the expected maximum disparity, possibly only using the brightest few percent of particles, to compute some initial rough translation for all cameras. This is followed by more detailed passes with multiple sub-volumes to correct remaining locally changing calibration errors, once the large shift has been corrected. Michaelis and Wolf (2011) report initial disparities as large as 12 pixel being reduced to remaining 0.02 pixel after several passes of VSC. Luckily, vibrations usually consist of a global translation, while rotations would be more difficult to detect requiring again dissection into sub-volumes. It is certainly tedious and time-consuming to compute a new calibration function for every image processed, but under such conditions this is the only way to process data using Tomographic PIV.

Earl et al. (2015) also investigated the effect of vibrations on tomographic reconstruction, which are especially noticeable in derived turbulent statistics quantities. The authors suggest checking for vibrations using single-image VSC even in case where the apparent reconstruction quality seems to be good. Small-scale vibrations smaller than the diameter of the particle images may be hidden by a global volume self-calibration using many images of the data set, while single-image corrections can potentially improve the vector field accuracy considerably.

Recently, Cornic et al. (2016) investigated VSC in more detail and proposed some improvements. They implemented a volumetric pinhole calibration model with Scheimpflug angles which is more appropriate to the standard setup in Tomographic PIV with Scheimpflug adapters between camera and lens so that all cameras view the same tilted volume in focus. While the basic VSC technique works with all calibration models, the choice of mapping function is mostly a matter of enough free parameter to accommodate all optical distortions. In air a pinhole model preferably with Scheimpflug angles (up to 16 parameters per camera) is often sufficient, but it may not be appropriate e.g. in water or looking through curved optical surfaces or changing index of refraction e.g. in flames. On the other hand, Weinkauff et al. (2013) report only 0.2 pixel remaining disparity for a turbulent lifted jet flame with strongly changing index of refraction.

Higher order (polynomial) models (e.g. 50-100 parameters per camera) may be required to achieve necessary accuracies for Tomographic PIV in difficult optical setups. Cornic et al. (2016) point to the possibility of easily refitting only the external pinhole parameters in case of camera drifts. They also mention the often overlooked fact that VSC actually changes the origin of the coordinate system when disparities are corrected. In practice, small shifts in the coordinate origin of e.g. 1-2 voxel are rarely critical. It is anyway difficult to accurately place the calibration plate at a specific location and orientation within a few pixel during the initial calibration.

Ideally some reference marks should be visible in the recorded images to (re)set the coordinate system. Zunino et al. (2015) fixed a transparent dual-plane calibration target just outside the test section for calibration and to account for possible relative motion between the imaging system and the experiment. This is especially useful when access to the measurement volume is difficult.

7

Iterative Particle Reconstruction

This chapter has been published in Wieneke (2013) Iterative reconstruction of volumetric particle distribution, Meas Sci Technol 24:024008. The introduction has been updated to reflect the current status on IPR and STB.

Both Tomographic PIV and standard particle tracking velocimetry (3D-PTV; Maas et al. 1993; among others) measure a flow field in a full volume. Particle tracking methods usually first detect 2D-particle positions in the images recorded by 3-4 cameras, followed by a triangulation procedure to locate the 3D-particle positions and subsequent tracking of particle positions using some nearest neighbor approach or more advanced schemes requiring smoothness of the velocities field among neighbor particles. 3D-PTV can only be applied to rather low seeding densities below about 0.01 ppp (typically up to 3-10k particles per megapixel sensor), because high seeding densities and resulting overlapping particles decrease the accuracy of 3D-particle positions and produce too many ghost particles.

Tomographic PIV, on the other hand, based on (S)MART as the most popular reconstruction method, tries to iteratively fit an intensity distribution of voxels in the volume such that the re-projected images of this volume fit the recorded images as closely as possible. It is able to reconstruct higher seeding densities up to about 0.05 ppp (more when using the time information e.g. using SMTE, Lynch and Scarano 2015) still producing some ghost intensities/particles. But the subsequent 3D-cross-correlation computing vectors on a regular grid is quite robust. Obviously, the (S)MART reconstruction has to cope with an under-defined system of equations trying to reconstruct $O(10^9)$ voxels from $O(10^6)$ pixels of the images. This only works by applying the sparseness constraint of relatively low seeding density with sufficient number of zero-intensity pixels in the images forcing most voxels in the volume to zero intensity.

The idea now is to combine the sparseness constraint of a rather small number of particles in a stricter sense together with an iterative approach reconstructing the particle distribution in the volume such that the re-projected images of this particle distribution fit the recorded images as close as possible. Instead of a huge number of voxel intensities, only a rather small number of discrete 3D-particle positions need to be determined. This is then again followed by a tracking step like in standard 3D-PTV.

This volumetric iterative particle reconstruction (IPR) method, described in detail in the next section, was initially developed to improve Tomographic PIV regarding possibly higher seeding density increasing the final spatial resolution as well as improving on the accuracy. As it turned out, this goal was not really achieved for standard double-frame Tomographic PIV with a seeding density for IPR still limited to about 0.05 ppp. At least, for lower seeding densities, IPR is not only much faster than Tomographic PIV, but also more accurate than both Tomographic PIV and 3D-PTV, because due to the iterative process it correctly assigns overlapping particles to the right z-locations and eliminates ghost particles. Beyond 0.05 ppp, the process does not converge any more to a unique solution. Different possible particle distributions can produce re-projected images similar to the recorded images.

Luckily, Schanz et al. (2016) put IPR into practical use developing the so called *Shake-the-Box* (STB) method for time-resolved volumetric measurements, where

the additional time information provides an extra dimension of constraint to remove ghost particles. STB provides highly accurate volumetric particle track data for seeding densities up to 0.1-0.2 ppp. In the recent PIV-Challenge (Kähler et al. 2016) synthetic volumetric images have been provided and STB immediately outperformed all other Tomographic PIV contributors, who had optimized their algorithms for many years.

Shake-the-Box works by providing a close predictor particle field from the previous time-step translated by the previously computed velocities. This particle distribution is already very close to the true one and is 'shaken' by the some IPR-iterations to true particle locations. New particles entering the volume are detected from the residual images, ghost particles with false particle tracks should die out after a few time steps. The process converges quickly after 5-20 time-steps to the true solution with almost no ghost particles at all. It still needs to be verified how the method works for noisy experimental data, where 3D-cross-correlation of Tomographic PIV (e.g. together with SMTE) might be more robust. But already a number of experiments have been done successfully, in particular on large scales with Helium-filled soap bubbles. In principle, STB offers the most complete approach to compute time-resolved 3D flow fields recovering all possible information provided by the seeding particles as the ultimate information carriers.

Meanwhile, as part of the NIOPLEX EU-research project, it has been shown that the particle tracks from STB provide better pressure fields than derived from Tomographic PIV vector fields due to the higher possible spatial resolution and using accurate acceleration data at the correct location not averaged over some interrogation volume (Blinde et al. 2016).

Recently, Cornic et al. (2015; based on their earlier work in Champagnat et al. 2014) developed a similar iterative sparse particle reconstruction algorithm named *LocM-CoSaMP* computing particles distributions on a regular volumetric grid with a voxel-to-pixel ratio of 0.5 – i.e. the particle location is still inaccurate up to ±0.25 pixel – to be followed by a subsequent, not yet specified sub-voxel refinement step, which actually could be IPR again. The authors report possible seeding densities up to 0.12 ppp for non-time-resolved double-frame images with a higher Q-ratio quality factor than standard MLOS-SMART (Atkinson and Soria 2009).

Some work has been done to improve Tomographic PIV by enforcing the intensity distribution of voxels to fit closer to the expected Gaussian blob shape of particles (Castrillo et al. 2016; Discetti et al. 2013). Significant improvement in reconstruction accuracy has been reported compared to standard (S)MART, thus enabling higher seeding densities.

Clearly, using the information of a finite number of particles improves Tomographic PIV by reducing the degrees of freedom. With the additional use of the time information as in Shake-the-Box or voxel-based fluid-trajectory-correlation (FTC, Lynch and Scarano 2013; FTEE, Jeon et al. 2014; SMTE, Lynch and Scarano 2015) these methods enable the measurement of time-resolved volumetric flow

fields with low noise and high spatial resolution and with the possibility to extract instantaneous pressure fields (van Oudheusden 2013; Blinde et al. 2016).

7.1 Iterative Particle Reconstruction Method

3D particle tracking involves the measurement of the 2D particle image positions in the recording images, followed by a triangulation process to determine 3D particle locations, which are then tracked in time. Various tracking algorithms have been proposed (e.g. neural network, fuzzy, string force) using either the *spatial coherence* of neighboring particles having similar displacements and/or the even more stringent *time coherence* over 3 or more time steps requiring that individual particles do not exhibit an abrupt change of their velocity, but stay within an upper limit given by some acceleration threshold.

An accurate positioning of the particle images relies on the small probability of overlapping particle images. Moreover, the robustness of the triangulation requires a modest seeding density because the number of possible matches among particle images grows strongly with the seeding density as shown later. As a result, most experiments performed with 3D-PTV report rather low seeding densities of less than 0.001 particles per pixel (ppp) in the recorded images corresponding to a few 100 to 1000 particles with 1 megapixel format sensors. For higher seeding densities the overlapping particles lead to inaccurate 2D- and 3D-particle positions, and the matching ambiguity in the triangulation procedure will produce more and more ghost particles. For this reason, 3D-PTV has been mostly employed to produce detailed studies of rather sparse Lagrangian particle statistics over relatively long trajectories.

The evaluation of a dense velocity field that enables to compute the local velocity gradient tensor components requires a dense 3D3C-measurement preferably on a regular grid. This can only be obtained increasing the seeding density above e.g. 0.01 ppp and in turn achieve the quantitative visualization of vortical structures by detection criteria such as Q, based on the local properties of the velocity gradient tensor (Hunt et al. 1988) For this purpose Holographic PIV (Herrmann and Hinsch 2004), scanning 2D- or Stereo-PIV (Brücker 1997, Hori and Sakakibara 2004), and more recently Tomographic PIV (Elsinga et al. 2006) have been applied.

Tomographic PIV ('Tomo-PIV') using the same experimental setup and hardware as 3D-PTV reconstruct the 3D volume with particles discretized into voxels using a tomographic reconstruction algorithm. Tomographic reconstruction methods update the intensity of each voxel in the measurement volume by comparing the original recorded images with the projected images from the intensity distribution in the volume. Voxel intensities are updated using the difference (ART) or ratio (MART) between recorded images and the reprojected images. In simple terms this corresponds to the way how the cameras would see a specific voxel intensity distribution. Typically, 4-10 iterations are needed for convergence, somewhat more for SMART.

A fast one-pass multiplication along the line of sight (Multiplicative First Guess (MFG), Worth and Nickels 2008; MLOS, Atkinson and Soria 2009) has been proposed to compute an initial intensity distribution followed by further (x)ART. Essentially MLOS with slight implementation differences is almost identical to a single pass of SMART operating on a volume with a constant value. In the same way one can take the minimum along the line of sight (MinLOS) which has been shown to perform better than MLOS as long as the camera images have the same intensity (Michaelis et al. 2010). A comparison between stand-alone MLOS, MinLOS and fully iterative Tomo-PIV shows that any single pass analysis such as M(in)LOS returns a less accurate result than iterative MART analysis. Reconstruction of acceptable accuracy is limited to seeding density of about 0.01-0.03 ppp (Michaelis et al. 2010). The processing time of the MART reconstruction can be decreased up to a factor of 5-10 by updating only non-zero voxels e.g. identified by an initial MLOS step (Worth and Nickels 2008, Atkinson and Soria 2009). Recently, other approaches to speed-up the reconstruction process have been investigated by Discetti and Astarita (2011).

Tomo-PIV employs a weighting function between voxels and pixels describing how e.g. a voxel sphere is imaged onto the relevant camera pixels or, conversely, how a pixel represented e.g. by a cylinder intersects with a voxel along the line of sight. In real experiments there are a number of imaging artifacts like defocusing, astigmatism or intensity differences between cameras in forward-/backward-configuration, which demand a more accurate and locally varying description of the optical transfer function (OTF) between volume points and pixels. Schanz et al. (2010) implemented a locally varying OTF in the MART formalism and demonstrated the high potential of this approach to improve the accuracy of the tomographic reconstruction in case of non-uniform OTF.

In general, MART tries to solve an underdetermined system with e.g. 10^9 parameters corresponding to the intensity of each voxel. Given only $O(10^6)$ pixels in the recorded images, a unique solution relying strongly on the positive-definiteness of volume intensities can only be calculated for sufficiently low seeding densities of typically less than 0.05 ppp corresponding to a 'source density' (number of particle times particle image area) of less than 1 with typically less than 1-10% of all voxels with non-zero intensities. Each particle is then represented by a blob of e.g. 3x3x3 non-zero voxels, e.g. for 100k particles this leads to about 3 Mio non-zero voxels. This reduces the number of free parameters drastically provided one knows already the possible particle positions e.g. by an initial MLOS-pass identifying zero voxels to be excluded in further sparse MART-iterations.

The particle blobs created by MART are in fact somehow artificial because in most experiments with diffraction limited optics the true particle size is much smaller than a single voxel. The spread over a few voxel – determined by the pixel-voxel weighting coefficients and the arbitrary pixel-to-voxel size ratio (usually 1) – is, however, beneficial, in that it allows to accurately evaluate the sub-pixel position of a particle avoiding 'peak locking' effects in the subsequent correlation-based displacement calculation.

Obviously representing particles as points in the volume with a position XYZ, intensity I and a radius R takes only 5 parameter (4 in diffraction limited optics without R) compared to e.g. 3^3=27 voxel parameter, leading to e.g. only 500k free parameter to be fitted for 100k particles.

The idea presented here is to use a similar iterative reconstruction algorithm like MART, but not to represent particles as blobs of non-zero voxels, rather to represent particles as points with position *X*, *Y*, *Z*, intensity *I* and radius *R* where this set of parameter is iteratively updated by comparing the reprojections of the particle distribution with the original images.

Basically, all the methods calculating volumetric particle distributions can be characterized by the final representation of the volume as voxel intensities (MLOS, MART, …) or as a list of 3D-particle positions (3D-PTV). In addition, a method is either a direct computation method computing the result in a non-iterative straight way (MLOS, 3D-PTV) or using an iterative reconstruction approach comparing the volume representation with the originally recorded images (MART) trying to find the exact solution to the inverse propagation problem (Table 7.1).

Table 7.1. Particle and voxel reconstruction methods.

	Particle Representation	Voxel Representation
Direct computation	2D-peak detection + triangulation (3D-PTV)	MFG, MLOS, MinLOS
Iterative reconstruction	Iterative particle reconstruction	xMART, SPG, L_1, … (Tomographic PIV)

3D-PTV computes 2D-particle location and possible 3D-locations by photogrammetric triangulation, but does not compare the projection of the final particle distribution to the original images. MLOS and MinLOS directly compute the voxel intensities in the volume, again without a comparison. Tomo-PIV iteratively adjusts the reconstructed voxel intensities to match the recorded images as close as possible. The method proposed here corresponds to the remaining category of iterative particle reconstruction ('IPR').

Once the particle distribution in the volume has been computed for 2 or more time steps, voxel-based volumes are further processed by 3D-cross-correlation to compute dense regular-grid 3D3C-flow fields, while sparse Lagrangian particle trajectories are derived from the 3D-particle locations. It is also possible to switch representations by converting 3D-particle locations to artificial voxel blobs and continue with cross-correlation (Schimpf et al. 2003), or by detecting 3D-particle locations in the voxel-based volume (Schröder et al. 2008) to be able to do high density particle tracking and statistics.

For both MART and IPR an accurate spatial calibration is mandatory with remaining calibration errors preferable below 0.1 px. This can be achieved with a volumetric self-calibration procedure using the actual recorded particle images (section 6.4).

The new iterative particle reconstruction method (IPR) is described in the next section and compared in section 7.3 to MART, MLOS and standard 3D-particle triangulation from 3D-PTV (same as single-pass IPR, referred to as '3D-PTV' in the following) using synthetic data with constant and varying OTF. The focus will be on the quality of the reconstructed volume, not on subsequent tracking or correlation methods. Finally, the method is tested with experimental data in section 7.4.

7.2 Algorithm

IPR starts out with an initial particle distribution computed by 2D-particle detection and 3D-triangulation to find possible 3D-particle location (Figure 7.1). Then in every iteration the method computes from the 3D particle distribution the projected images and compares them to the original camera images in order to correct the particle parameter as specified in more detail later. While MART updates only voxel intensities, IPR requires an adjustment in the (X,Y,Z)-particle position as well as the particle intensity I.

In the following, it is assumed that the optics is diffraction limited without the need to fit particle sizes which are supposed to be much smaller than a voxel. The optical transfer function is represented as a Gaussian ellipse, which covers most experimental optical distortion effects like blurring and astigmatism. A particle p with coordinates X_p, Y_p, Z_p and intensity I_p is projected into the image of camera i=1-n as:

$$I^i_{part}(\mathrm{xi}, \mathrm{yi}, \mathrm{p}) = \mathrm{I_p}\ \mathrm{a}\ e^{-\left(b\,x'^2 + c\,y'^2\right)} \tag{7.1}$$

with rotation

$$\begin{aligned} x' &= (x_i - x_{ip})\cos\alpha + (y_i - y_{ip})\sin\alpha, \\ y' &= -(x_i - x_{ip})\sin\alpha + (y_i - y_{ip})\cos\alpha \end{aligned} \tag{7.2}$$

and particle image center

$$(x_{ip}, y_{ip}) = M_i\,(X_p, Y_p, Z_p) \tag{7.3}$$

mapped from world coordinates to pixel position by the spatial mapping functions M_i. The OTF-parameter a, b, c, α may be different for each camera and locally varying in space (X,Y,Z).

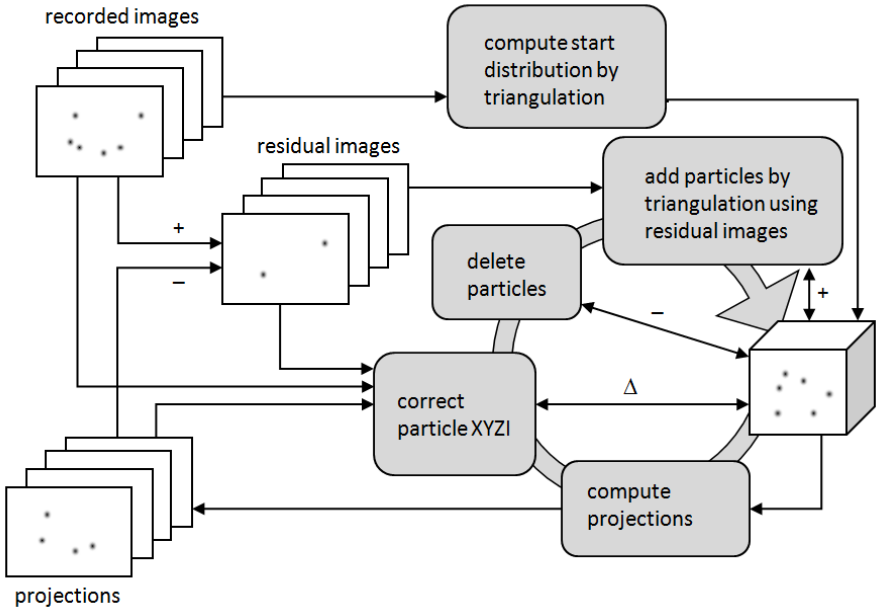

Figure 7.1. Flow chart of iterative particle reconstruction method.

Given a certain particle distribution in the measurement volume the reprojected images I^i_{proj} of camera i are calculated by

$$I^i_{proj}(x_i, y_i) = \sum_p I^i_{part}(x_i, y_i, p). \quad (7.4)$$

The residual image I^i_{res} is given by the original image I^i_{orig} subtracting the reprojected image I^i_{proj}:

$$I^i_{res}(x_i, y_i) = I^i_{orig}(x_i, y_i) - I^i_{proj}(x_i, y_i) \quad (7.5)$$

The method for updating of coordinates X_p, Y_p, Z_p and intensity I_p parameter of a single particle p, done for all particles consecutively, is based on analysing the particle-augmented residual image:

$$I^i_{res+p}(x_i, y_i) = I^i_{res}(x_i, y_i) + I^i_{part}(x_i, y_i, p) \quad (7.6)$$

Non-zero residuals added to the current particle shape will provide information of a better position and intensity of particle *p*. The task at hand is to find a new parameter set (X'_p, Y'_p, Z'_p, I'_p) minimizing the residual R:

$$R = \sum_{i,x_i,y_i} \left(I^i_{res+p}(x_i, y_i) - I^i_{part}(x_i, y_i, X'_p, Y'_p, Z'_p, I'_p) \right)^2 \quad (7.7)$$

summing over all cameras and a neighbourhood of e.g. twice the particle radius around (x_{ip}, y_{ip}) covering the complete particle shape. This is shown schematically in Figure 7.2 where adding the particle to the residual lead to a new location in camera pixel position x_i and hence in world position X. Note that a particle shift d*X*,d*Y*,d*Z* in

the volume leads to interdependent shifts dx_i,dy_i in the camera images depending on the geometric arrangement of the cameras. The simultaneous fit of *XYZI* can be done by a Powell minimizer of the residual (Powell 1964) which turned out to be quite accurate but very time consuming. Within a few Powell iterations the fit converges but this typically requires about 80-120 calculations of particle shapes I^i_{part} with different parameter sets.

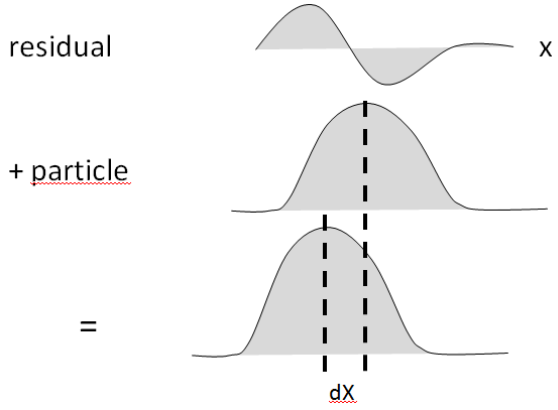

Figure 7.2. Adding particle image shape to residual image and fitting a new particle position.

Therefore a simpler method ('Pos') has been used which as well computes for each particle the particle-supplemented image I^i_{res+p} but then only varies the particle world position X'_p by -0.1,0,+0.1 voxel and computes a new X'_p location by taking the position with the minimum residual R fitting a quadratic polynomial function on the 3 residual values. This is repeated for the particle *Y* and *Z* position. The particle shape needs to be computed only 7 times in total (times n cameras) allowing displacement corrections of up to ±0.1 voxel for each pass.

The particle intensity correction (method 'Int') is done in two steps. First the intensity of each particle is adjusted requiring that I^i_{res+p} stays strictly just below the recorded image intensity I^i_{orig}:

$$I'_p = I_p \min_{i,x_i,y_i}\left(\frac{I^i_{orig}(x_i,y_i)}{I^i_{part}(x_i,y_i,p)}\right) \tag{7.8}$$

using all pixels within center peak location ± particle image radius. A larger area could lead to instabilities due to low values of I^i_{part} in the tail of the Gaussian curve. This is followed by a fast MART-like correction multiplying the particle intensity with the ratio of the summed intensity of I^i_{res+p} relative to the sum of intensity of the computed particle shape I^i_{part}:

$$I'_p = I_p \sum_{i,x_i,y_i} I^i_{res+p}(x_i,y_i) \,/\, \sum_{i,x_i,y_i} I^i_{part}(x_i,y_i,p) \tag{7.9}$$

again, summing over center peak location ± particle image radius.

A particle is removed (method 'R') when its intensity after correction falls below a specified threshold, e.g. $1/10^{th}$ of the average particle intensity. In addition a particle is removed when its position is within 1 pixel of another particle. Otherwise a true particle might be reconstructed as a sum of a few particles within a small region which should be avoided. The probability that two real particles lie within 1 voxel distance in the volume is very low for the levels of seeding density discussed here.

The standard 3D-PTV triangulation algorithm to locate 3D-particle positions is executed to compute the initial particle distribution using the original recordings as well as later using the residual images. The most important parameter determining the number of detected 3D-particles is the allowed triangulation error ε. After 2D-particle detection, the triangulation procedure tries to find all possible 3D-particle locations where the sum of the differences of the projected 2D-particle locations in the images with the measured 2D-particle location stays below the specified triangulation error (Hartley and Sturm 1994). For overlapping particles, the fitted 2D-particle locations deviate from the true position, so the allowed triangulation error ε when set to small values (e.g. <0.5-1.0 px) effectively eliminates noisy 3D-particles originating from overlapping particles. In addition, small ε greatly reduce the possibility of detecting ghost particles which number scales with ε^5 for 4 cameras. Conversely, larger ε (e.g. >2 px) allow most overlapping particles to appear in the volume but with the disadvantage of much higher ghost particle level especially at higher seeding density scaling with N_{ppp}^3.

In the standard triangulation procedure all 4 images must have particle peaks which are then triangulated to a 3D-position. This has been extended to allow only 3 cameras to have a peak, from which a 3D-position is calculated, while the fourth camera is only required to have sufficient intensity at the corresponding 2D-position but the intensity peak may be strongly shifted due overlapping particles. This is a more tolerant way to find possible particles in the volume. The two 3D-PTV methods relating to 3 and 4 peaks are named 'P3' and 'P4' in the following.

The above building blocks can be assembled in many different ways. For the analysis of the synthetic images in the next section the following scheme has been selected which converges well even for higher seeding densities:

n_1 (P4 + R + m (Pos + Int + R + Proj)) + n_2 (P3 + R + m (Pos + Int + R + Proj))

where n_1 and n_2 are the number of outer loops with adding particles by 4/3-peak triangulation followed by m times adjustment of particle position and intensity, each time computing new projected and residual images ('Proj'). At the beginning P4 is quite conservative to detect only safe particles. After a few iterations the computed particle distribution is close enough to the true solution to allow more possible particles to enter using P3 in order to resolve complicated combinations of overlapping particles. The synthetic images in the next section have been analysed with $n_1 = n_2 = 8$, m = 6, and ε = 1.0 for all seeding densities.

7.3 Results using synthetic data

A range of synthetic images have been generated with particles within a volume size of 1000 x 1000 x 300 voxel. Particles have a constant image diameter of 2 pixels and the imaged seeding density varies from 0.0004 to 0.2 ppp. The 4 cameras have been positioned at a square at angles of ±30 degrees. The camera images have size 1300 x 1300 pixel to record the full volume by all cameras. The data has been processed using 3D-PTV with ε=0.5/1.0/2.0, MLOS, MART and IPR with the DaVis 8 software (LaVision GmbH). Particle positions in voxel-based MLOS and MART volumes have been computed by a Gaussian 3D-particle fit to allow statistical comparison to true particle locations.

A particle in 3D space is considered 'true' if it is within 1 voxel distance of a true particle location, while ghosts have no true particles within 1 px distance. The number and fraction of detected true particles as well as the fraction of ghost particles relative to the number of true particles is shown in Figure 7.3 to Figure 7.7 together with the average positional error of true particles and the summed intensity of the ghost particles relative to the total sum of true intensities. Defining true and ghost particles with 2 px distance instead of 1 px threshold does not change the curves significantly.

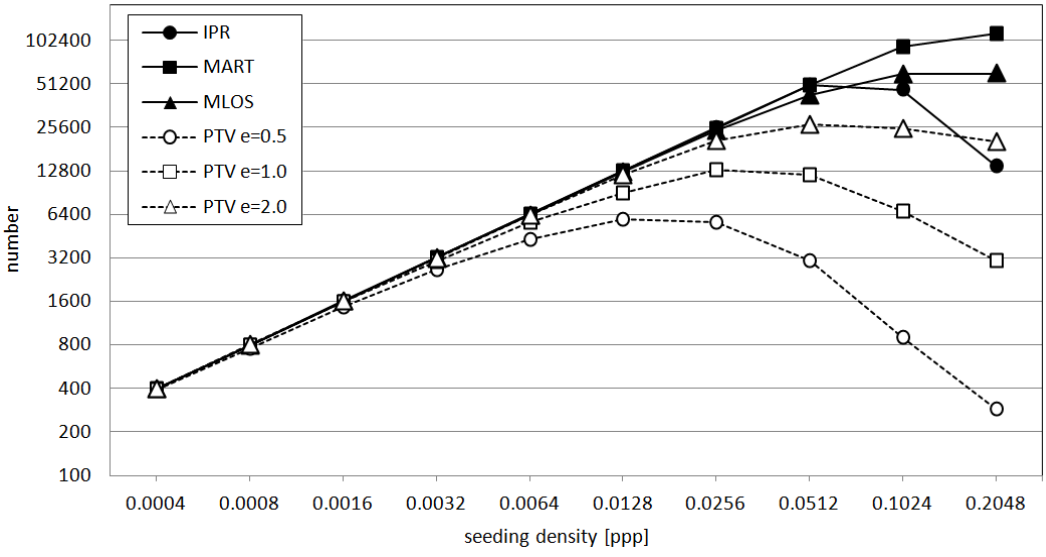

Figure 7.3. Number of detected true particles.

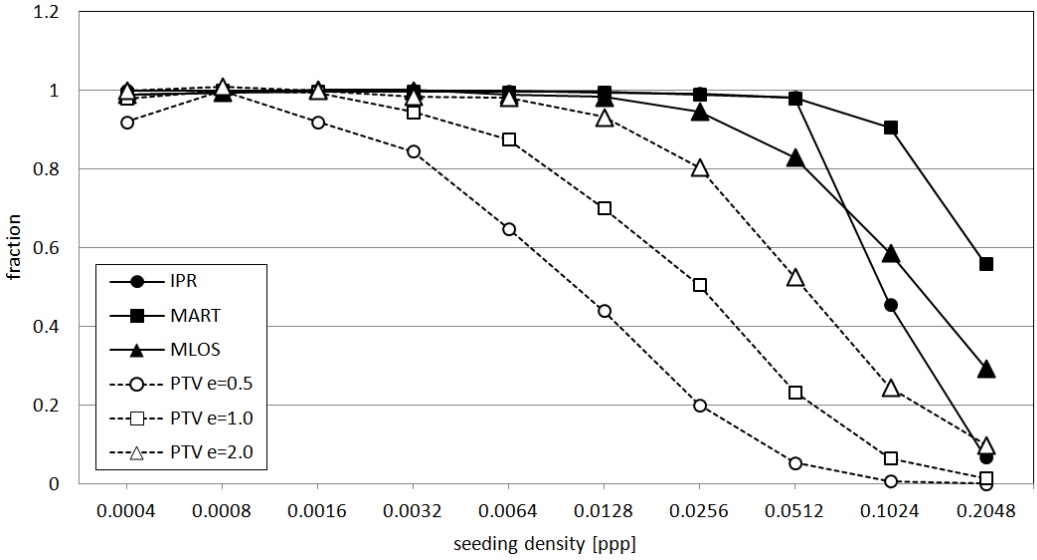

Figure 7.4. Fraction of detected true particles.

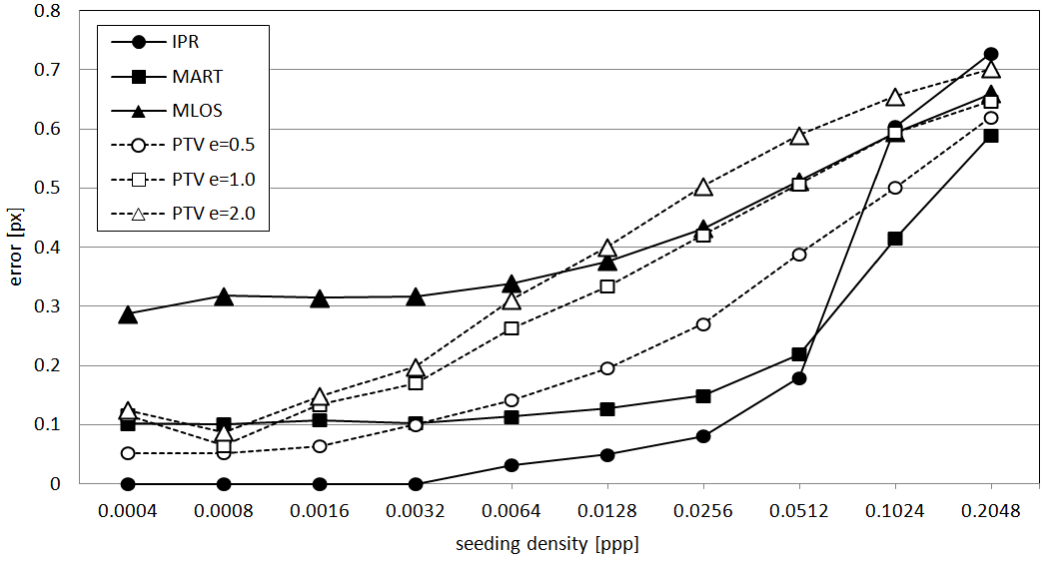

Figure 7.5. Positional error of detected true particles.

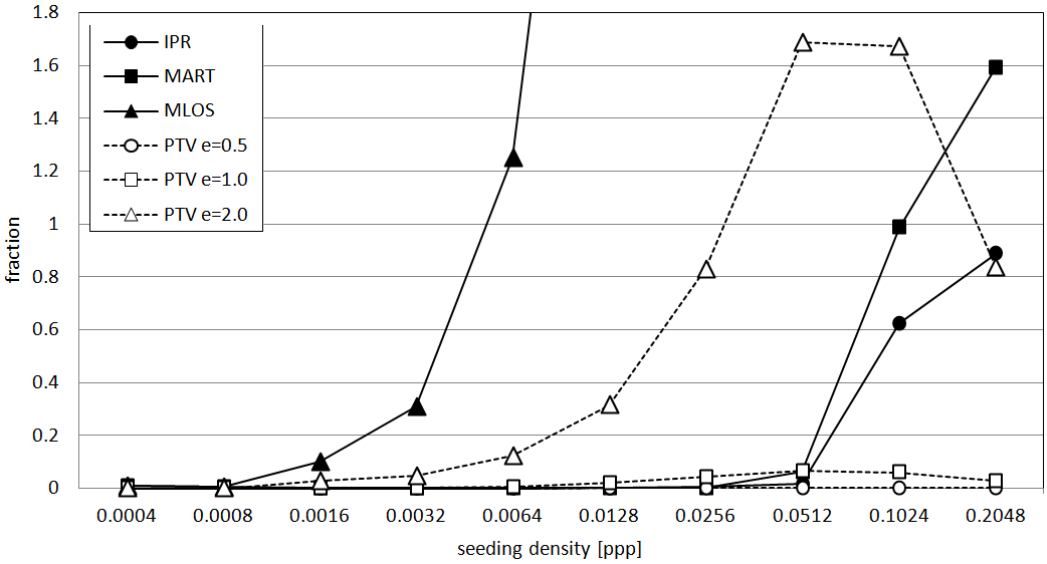

Figure 7.6. Fraction of ghost particles.

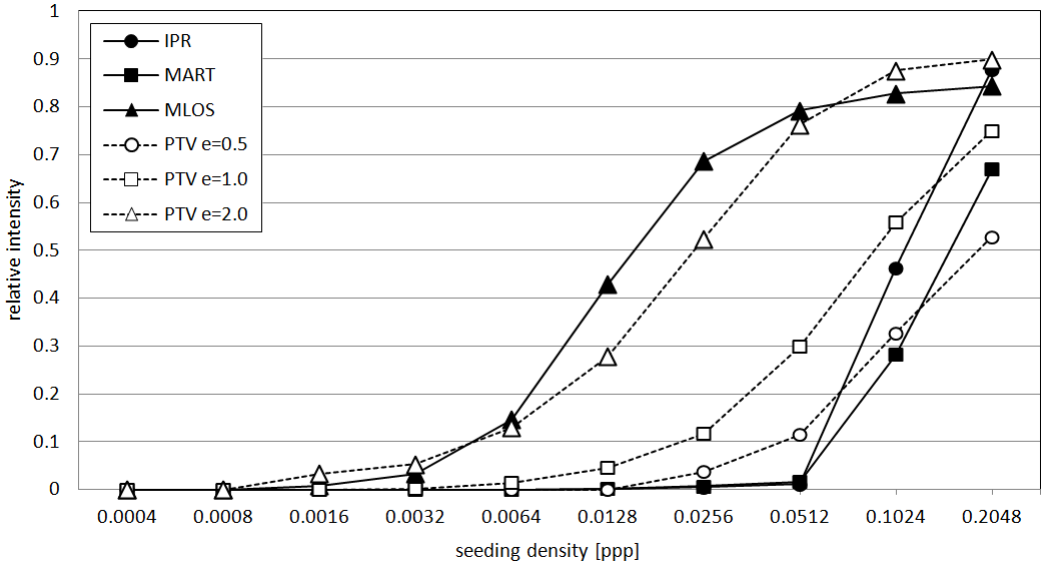

Figure 7.7. Relative intensity of ghost particles.

As expected the number of detected true particles for 3D-PTV depends strongly on the allowed triangulation error ε. For ε = 0.5 already at N = 0.01 ppp the number of detected particles becomes less than 50%. This is shifted for ε = 1.0/2.0, but for ε = 2.0 at N = 0.025 ppp the high level of ghosts prevents a reliable tracking of 3D-particles. Even before at N = 0.01 ppp the error in the position of particles

reaching 0.4 px is significant. This agrees with reported maximum seeding densities for 3D-PTV of about 5k particles @ 1kx1k (0.005 ppp). At low seeding densities the error is only due to overlapping particles. Well imaged non-overlapping particles may be detected within a positional error smaller than 0.01px.

MLOS on the other hand already starts with high particle position errors of 0.3 px at low seeding densities, detecting most true particles even for higher seeding densities, but produces a significant number of ghost particles above 0.005 ppp, which will add to displacement errors. Michaelis et al. (2010) quote for MLOS the lowest errors (0.2-0.4 px) in the displacement field for seeding density of 0.01-0.03 ppp.

Tomo-PIV with 5-pass iterative MART produces reliable results up to 0.05 ppp with almost 100% detection of true particles and still low level of ghost intensities. The positional error for a single particle never gets below 0.1 px, but, of course, averaging over a number of particles in the interrogation volume can reduce the error in the velocity field e.g. down to 0.05 px for 32^3 volumes. MART starts to fail above 0.05 ppp, unless more than 4 cameras or advanced multi-frame reconstruction techniques like MTE (Novara and Scarano 2011) or even better SMTE (Lynch and Scarano 2015) are used.

IPR performs similar to MART up to N = 0.05 ppp concerning the number of detected particles and ghost level, but with a significantly smaller positional error for lower seeding densities. This is attributed to the ability of IPR to detect single particles in the volume as points with known OTF-properties, requiring only 4-5 parameter (*XYZIR*) to specify a particle instead of e.g. 3x3x3 voxels in the case of MART. At $N_{ppp} = 0.05$ IPR has 200k free parameters compared to $1kx1kx300 = 3x10^8$ for non-sparse MART. The transition to the unreliable operating range is much steeper for IPR above 0.05 ppp. MART appears to maintain some more robustness in the range between 0.05 and 0.2 ppp (see section 7.3.1).

Comparing the original images with the images projected back from the computed particle / voxel distribution in the reconstructed volume at N = 0.0064 and 0.05 ppp (Figure 7.8), one can see that MART and IPR accurately model the recorded images. 3D-PTV at N = 0.0064 ppp can detect all non-overlapping particles, slightly more for $\varepsilon = 2.0$, but at 0.05 ppp hardly any particles are detected ($\varepsilon = 0.5$) or the distribution of detected particles contains too many ghost particles ($\varepsilon = 2.0$). MLOS calculates similar images as MART and IPR but more smeared out with larger position errors.

7.3.1 Convergence

For seeding densities below 0.01 ppp the algorithm converges quickly and in a robust way to the true solution within 5-20 iterations quite independently of the parameter settings, e.g. controlling how restrictive particles are added or deleted and the type of particle position and intensity correction. Only when the fraction of overlapping particle images becomes significant and the triangulation procedure creates ghost particles on levels higher than 10-30% one has to optimize the

strategy to achieve an acceptable convergence rate. At the beginning, it is advantageous to be very restrictive in adding particles, only adding reliable ones with low triangulation errors in order to keep the number of ghost particles low, e.g. less than 20-50% of the true ones. Later one can relax on the restrictions in order to find remaining true particles and successively reducing the intensity of the ghost particles which do not fit perfectly. Eventually most ghost particles will be deleted when their intensity falls below the specified removal threshold.

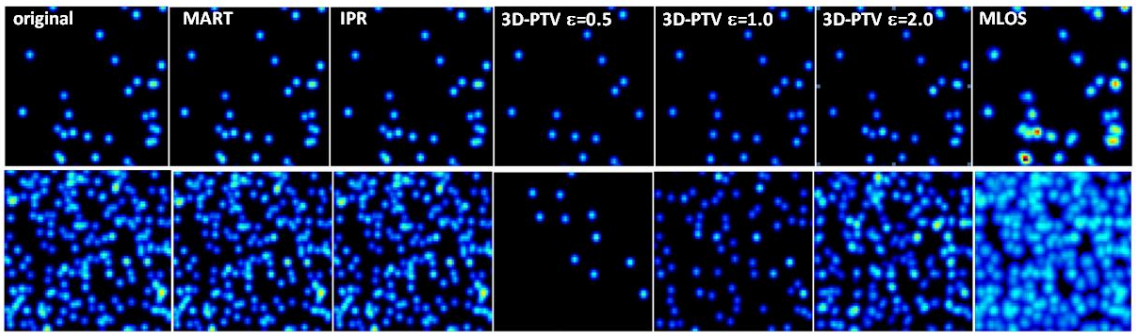

Figure 7.8. Original and reprojected images, top: N = 0.0064 ppp, bottom: N = 0.0512 ppp.

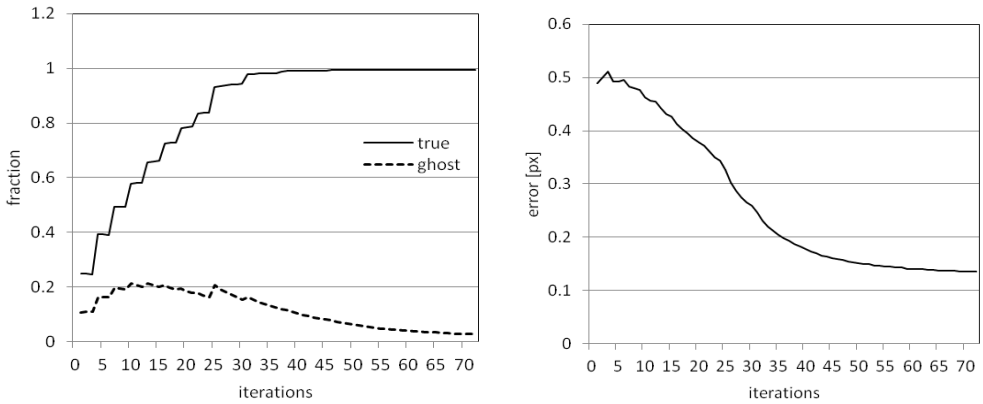

Figure 7.9. Left: fraction of true and ghost particles, right: error of true particles.

Above is shown the convergence behaviour for N_{ppp} = 0.05 where the ghost level intensity stays sufficiently low to allow the true particles to emerge.

Convergence starts to fail above 0.05 ppp when the solution is no longer unique, i.e. many possible particle distributions in the volume lead to projected images close enough to the recorded images. More accurately the true solution might still be unique, but the procedure may be trapped in a superposition of many local minima which account well for a specific group of particles.

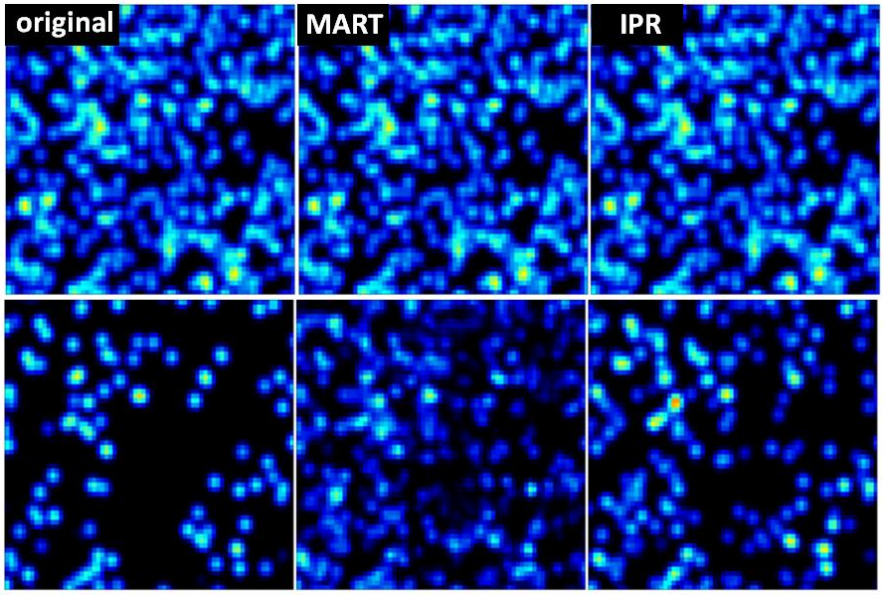

Figure 7.10. N = 0.1 ppp, top: orginal image / projected image, bottom: part of volume adding planes z = 150-200.

As shown in Figure 7.10 for N_{ppp} = 0.1 the projected images almost perfectly agree with the recorded images (top), but looking at the particle distribution in the volume (bottom) it is clear that IPR deviates strongly from the true particle distribution, while MART seems to be closer to the true solution but with more low intensity ghosts. Apparently, there exist many solutions to the reconstruction problem, where IPR seems to pick out a single solution with fewer particles and higher intensity due to its discrete particle nature, while MART seems to converge more to some weighted superposition of all possible solutions. When the projected images agree so well with the recordings, there is no information available for finding the true solution. One expects this to be even more pronounced for real experimental data with higher noise level where slight intensity differences potentially distinguishing between true and ghost particles are drowned in noise. It is also evident that non-iterative procedures like standard 3D-PTV or MLOS, which are not using the information gained from comparing projections and recordings, are much less able to deal with high seeding densities failing at much lower seeding densities compared to MART and IPR.

7.3.2 Synthetic data with non-uniform imaging conditions

The potential of the current approach is better described when dealing with tomographic systems that operate under conditions where astigmatism or defocusing effects are present. This circumstance should not be regarded as an experimental imperfection, since often experiments are performed at the limits of

the illumination intensity budget and the imaging system is set to collect as much light as possible, compromising the particle image sharpness in some regions of the domain.

In view of the above, synthetic data has been generated with strongly non-uniform OTFs incorporating locally varying astigmatism and defocusing (Figure 7.11). The results (Figure 7.12 to Figure 7.14) confirm the ability of IPR to deal with such cases with a stable convergence provided one is able to determine the OTF experimentally. The curves are similar to Figure 7.4 to Figure 7.6 but shifted to the left toward lower seeding densities, mainly due to the particle sizes being a factor of 2-4 larger so that the limiting level of unity source density is reached at lower seeding density around 0.025 ppp. IPR performs much better than MART (and 3D-PTV), but for a fair comparison the varying OTF should also be incorporated into MART as done by Schanz et al. (2010).

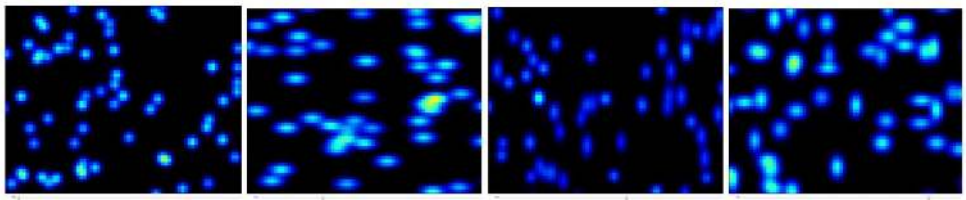

Figure 7.11. Left to right camera 1-4: constant particle size of 2 px, elongated, sharp – defocused, astigmatism.

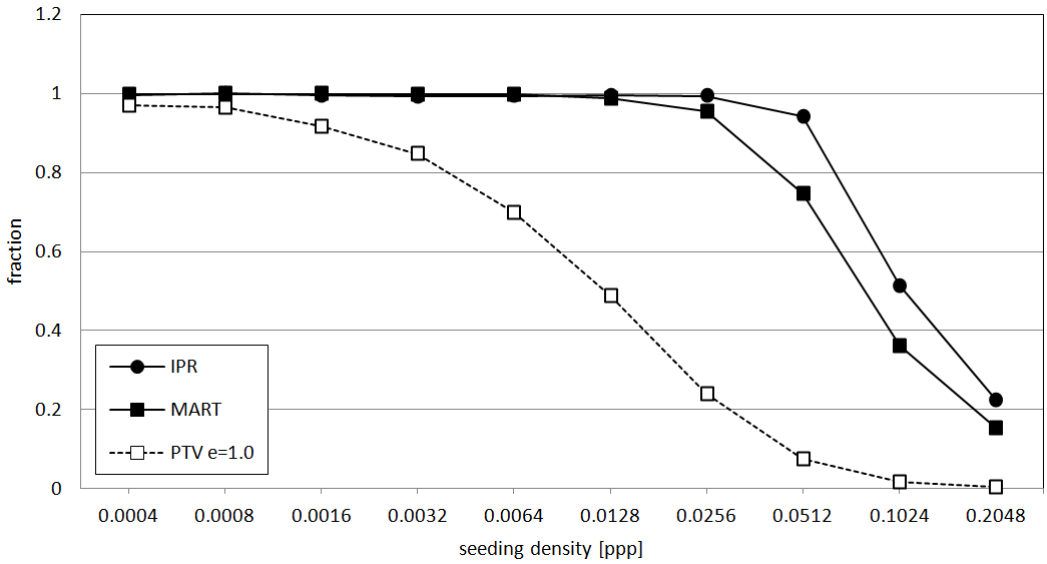

Figure 7.12. Fraction of detected true particles.

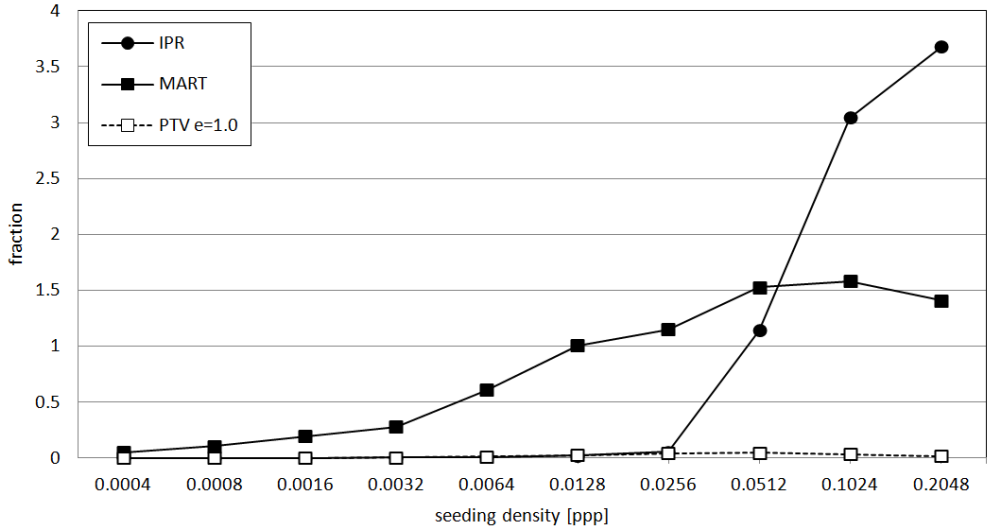

Figure 7.13. Fraction of ghost particles.

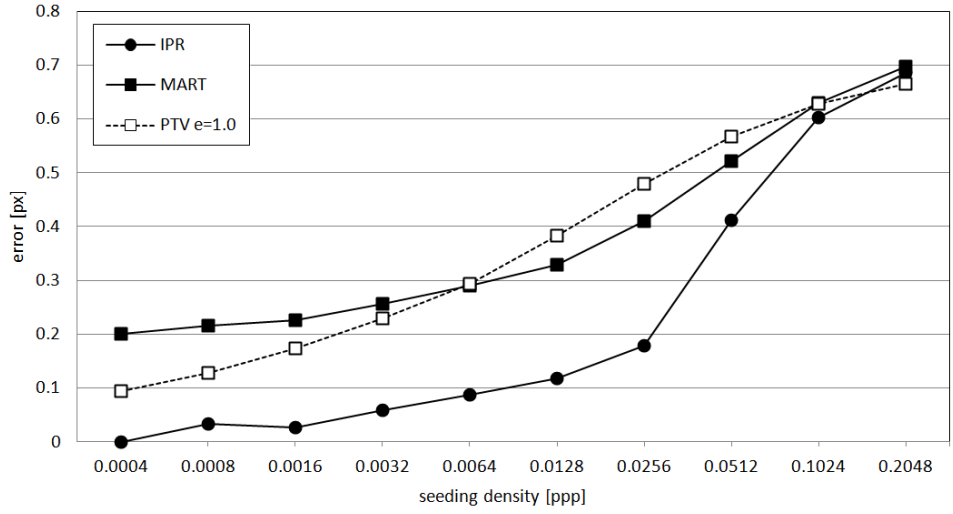

Figure 7.14. Error of detected true particles.

7.3.3 Requirements for Dense Flow Fields

Analyzing small scale flow structures and computing spatial derivatives requires dense 3D3C flow fields with sufficient spatial resolution. Also for sparse 3D-PTV vector fields high seeding densities are advantageous for analyzing turbulent transport and multi-particle statistics in detail (Lüthi et al. 2007).

Nevertheless, it is quite challenging to compute very dense vector fields. For 1k x 1k x 300 voxel volumes, a seeding density of 0.01 ppp yields only 1 particle in a 32^3 voxels sub-volume. Therefore, the data is typically processed by 48^3 or 64^3 voxels boxes and 50/75% overlap with 3 to 8 particles per sub-volume. With a depth of 1000 voxel the seeding density must be even 3x higher with even higher ghost level. This leaves quite a narrow range of allowed seeding densities for full-field dense measurements of 0.01 to 0.05 ppp narrowed further if particle images are larger than 2-3 pixel in diameter.

Several directions can be envisaged that could achieve higher particle densities in the measurement volume. One is to make the aspect ratio of depth to width smaller down e.g. to 1:10 which still provides enough z-vector planes for computing the complete 3x3 strain tensor but limiting the visualization of extended 3D flow features (fat-sheet or thin-volume Tomo PIV). Note that the relative amount of ghost intensity reduces for thin volumes improving the vector quality further.

Another approach is to use higher resolution cameras. With four 4k x 4k cameras one can increase the number of computed vectors above 1 Mio observing very small flow structures (Schröder et al. 2011). Also increasing the number of cameras to e.g. 6-8 one can cope with higher seeding densities probably beyond 0.1 ppp as it is being recently investigated. Belden et al. (2010) used 8-12 cameras with additive-LOS-type processing. The above IPR method has also been tested with only 3 or 2 cameras and as expected the maximum possible seeding density drops rapidly by a factor of 2-4, which excludes any utilization of such method for dense vector calculation.

Finally, when time-resolved data is available from high-speed cameras with sufficient temporal oversampling the time-coherence constraint can be used very efficiently to remove ghost particles and to enhance the signal from the true particles. An example has been given with the motion tracking enhancement method (MTE-MART) introduced by Novara and Scarano (2011) further improved by SMTE (Lynch and Scarano 2015). Of course, time-series particle tracking has been used extensively for 3D-PTV data, but especially for IPR with already higher possible seeding densities it offers to improve the reconstruction quality even further suitable for computation of dense vector fields with high spatial resolution (as meanwhile shown by STB).

7.4 Experimental results

High-quality experimental data of a jet in water produced by Violato and Scarano (2011) has been processed by IPR, MART, 3D-PTV and MLOS. Images of 1k x1k @ 1 kHz from 4 cameras at f#=32 are used to reconstruct volumes of 600 x 600 x 1000 voxel. For IPR-reconstruction, still lacking a procedure to determine the OTF experimentally, a constant particle diameter of 1.8 px is assumed, which is optimal in minimizing the difference between the original recordings and the reprojected images. The seeding density is on average 0.03 ppp with denser regions in the middle of the image since the jet is illuminated cylindrically.

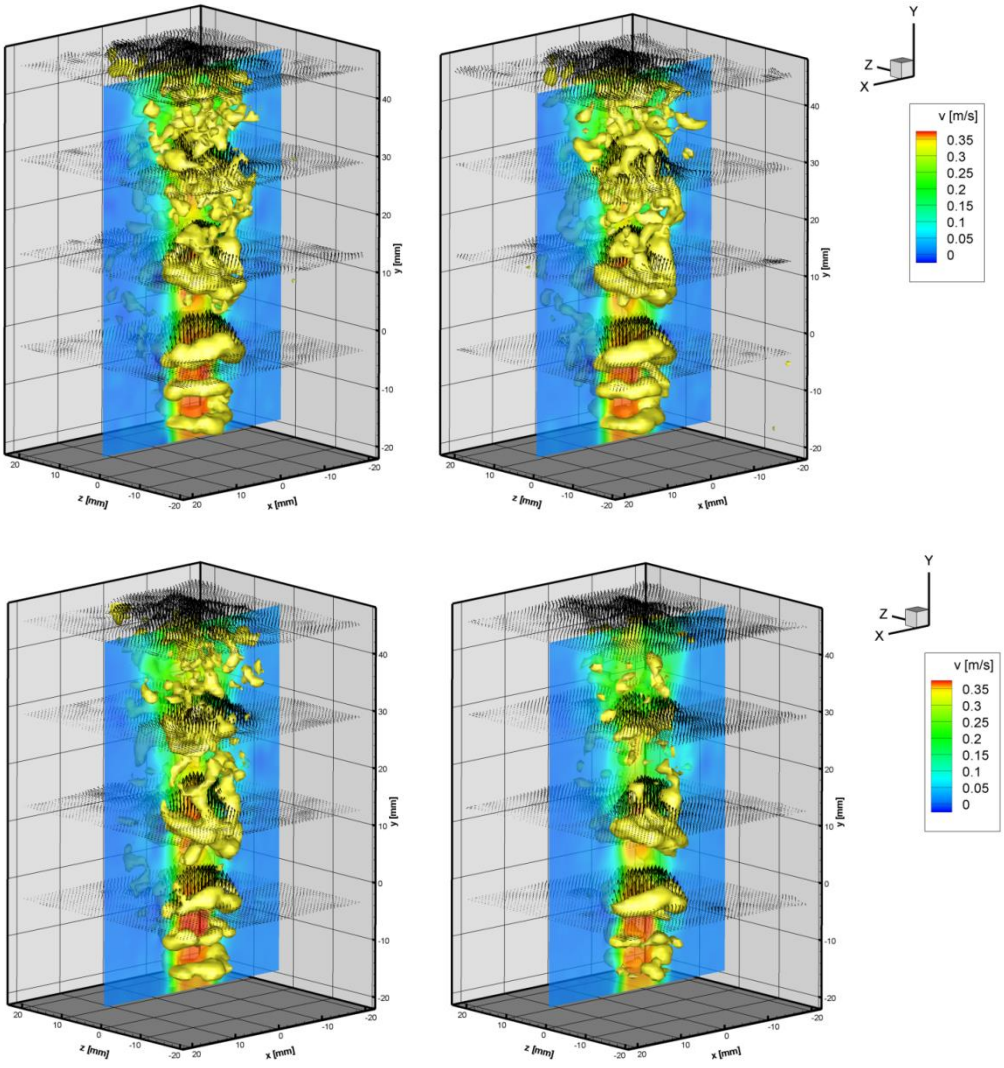

Figure 7.15. Top-left: IPR, right: MART, bottom-left: 3D-PTV, right: MLOS.

IPR and 3D-PTV particle data is converted to volume voxels and cross-correlated (Schimpf et al. 2003) in order to compare with the dense vector fields from MART and MLOS. 3D cross-correlation analysis is performed with 48^3 sub-volumes and 75% overlap. One could apply particle tracking on IPR/3D-PTV data and subsequently convert the sparse vector field to a regular grid, but at least within a single pair of objects the resulting vector field without using time-regression filters turns out to be less accurate.

The resulting flow fields from IPR and MART are quite similar (Figure 7.15), with IPR visually slightly noisier. Single-pass 3D-PTV exhibit distorted flow features and seems to be even noisier especially at the top. The MLOS analysis exhibit a clear spatial modulation in agreement with the findings of Elsinga et al. (2009). As a result most fine-scale details are absent.

7.5 Summary

An iterative particle reconstruction technique (IPR) has been developed which computes the distribution of particles in a measurement volume recorded by e.g. 3-4 cameras. Instead of single-pass 2D-particle detection and 3D-triangulation (3D-PTV) the method compares iteratively original and reprojected images to update and correct the particle distribution in the volume.

The method is compared to MART, MLOS, and single-pass triangulation (3D-PTV). IPR shows much better results for all seeding densities compared to 3D-PTV and MLOS and similar to MART for seeding densities up to 0.05 ppp, but with lower particle position error. With 4 cameras the convergence of IPR as well as MART starts to fail above 0.05 ppp when multiple possible 3D-distributions of particles are consistent with the recorded images.

For locally varying particle shapes due to e.g. defocusing or astigmatism IPR can incorporate non-uniform optical transfer functions (OTF) improving the result considerably compared to IPR or MART without OTF.

For low seeding densities the results can be computed within seconds, for 0.05 ppp and about 100 iterations it takes about 14 min per volume compared to optimized non-sparse 5x MART with 10-20 min.

A particle representation instead of voxel intensities is more favourable for advanced time-series analysis with Lagrangian particle tracking, where it is possible to use the time-coherence of particle tracks to feed back for improved particle reconstruction, similar to MTE for MART (Novara and Scarano 2011).

8

Conclusions and Outlook

Particle Image Velocimetry (PIV) is a powerful flow measurement technique to gain insight into fluid dynamics. The availability of well-integrated commercial systems and advances in optics, camera and laser performance have established PIV as the preferred technique for instantaneous planar and volumetric flow measurements. Compared to point-wise techniques, PIV enables direct visual insight into the distribution and evolution of spatially coherent structures. High-repetition rate lasers and high-speed cameras with above 1-20 kHz frame rate provide time-resolved data with further insight into transient phenomena, fluid-structure interaction or turbulent analysis. PIV has been applied to a wide range of applications from micro-scales to large meter-sized experiments and even larger natural flow phenomena.

Despite the significant advances in hardware and PIV processing schemes, only in the last few years a quantitative analysis of the associated uncertainties of experimental velocity fields has become a prominent subject of attention. The work here addresses a few aspects related to this.

In chapter 2, the fundamental properties of computed velocity fields have been investigated, viewing PIV processing as a kind of black box without going into algorithmic details. The discussion is limited to planar fields in double-frame 2D-PIV and Stereo-PIV, but can be easily extended to time-resolved and volumetric data.

First of all, the computed velocity field should be viewed as a *continuous* displacement field. For data provided as vectors on a regular grid, a *recipe* should be provided to interpolate the velocity to any position in space e.g. by spline interpolation. A sparse representation on a grid provides practical advantages of reduced storage requirement and facilitating binary neighborhood vector validation schemes more easily. Most PIV processing schemes assume – at least implicitely – a smooth velocity transition e.g. using advanced iterative predictor-corrector schemes with image deformation. The spacing between vectors as a function of overlap factor and size of interrogation window should not be confused with the actual effective spatial resolution to be determined quantitatively as discussed further in chapter 2.

The basic velocity field information u(x,y), v(x,y) and w(x,y) is augmented by additional properties, which are important to judge the quality and accuracy of the data:

- Local uncertainty of the velocity field components
- Autocorrelation coefficients of noise: spatial, inter-component and temporal (for time-resolved PIV)
- Response function to displacement wavelengths

The uncertainty of each velocity vector and associated spatial (temporal) autocorrelation values are required for uncertainty quantification and propagation. The wavelength response function (MTF) indicates the ability of a PIV processing scheme to detect small displacement wavelengths, which is related to the effective spatial resolution.

PIV processing can be analyzed using a linear filter model, i.e. assuming that the computed displacement field is the result of some spatial filtering of the underlying true flow field given a particular shape of the filter function. Using this mathematical framework, relationships are derived between the underlying filter function, wavelength response function and response to a step function, power spectral density, and spatial autocorrelation of the filter function and noise.

A definition of a *spatial resolution* is provided as the sum of the autocorrelation coefficients, similar to the integral length/time scale used for turbulence characterization. For example, a simple single-pass processing with a square interrogation window of nxn pixel leads to a filter length – as the inverse of the spatial resolution – of n pixel as expected. Such a definition of a spatial resolution is independent of some arbitrary threshold e.g of the wavelength response function (MTF) and provides the user with a single number to appropriately set the parameters of the PIV algorithm required for detecting small velocity fluctuations. Still, assessing the complete performance of the PIV algorithm requires the knowledge of the full functional form of the autocorrelation and wavelength response function.

PIV processing in the DaVis software is taken as an example for computing the above functions and spatial resolution as a function of interrogation window size, overlap and other parameters. It is shown that PIV in Davis can indeed be well approximated by a linear filter model with some Gaussian/Mexican-hat shape, but there is one function and value for the spatial resolution for the wavelength response and another one for the noise autocorrelation. The reason for this has not been investigated further. It is probably due to the non-linear effect of the predictor-corrector scheme.

In chapter 3, following an overview of the most important error sources in PIV, the current status of work related to the estimation of uncertainty bounds of computed velocity components is reviewed. An uncertainty quantification (UQ) method based on correlation statistics is presented, which has been compared to other available UQ-methods in two recent publications (Sciacchitano et al. 2015; Boomsma et al. 2016) showing good sensitivity to a variety of error sources, at least the ones visible in the image.

Uncertainty quantification of mostly systematic error sources due to experimental deficiencies is difficult to quantify, which remains an active area of research. Additionally, work is in progress for accurate UQ-methods for volumetric Tomographic PIV as well as for 3D-PTV/STB data (Sciacchitano and Lynch 2015). Also, more advanced PIV processing schemes like multi-frame time-resolved PIV (e.g. pyramid correlation, Sciacchitano et al. 2012), FTC and others still require appropriate UQ-schemes.

Chapter 4 discusses the topic of uncertainty propagation for derived instantaneous and statistical quantities like vorticity, averages, Reynolds stresses and others. Stereo-PIV requires propagating the uncertainties of the 2C-velocity fields of the two cameras into uncertainties of the computed final 3C-velocity field.

A new denoising scheme is presented which uses the uncertainties comparing to the local flow gradients in order to devise an optimal filter kernel for reducing the noise but keeping the true flow fluctuations (chapter 5). This is an alternative to *adaptive PIV* approaches locally varying the interrogation window size and shape according to e.g. image quality and flow gradients (e.g. Theunissen et al. 2007, 2008, and 2010).

For Stereo-PIV and volumetric PIV/PTV, an accurate perspective calibration is mandatory. One of the main error sources for Stereo-PIV is the misalignment between the actual position of the light sheet and where it is supposed to be according to the initial calibration procedure. The Stereo-PIV self-calibration technique is reviewed in section 6.2 together with the current status on this topic. For volumetric PIV/PTV, a volumetric self-calibration (VSC) procedure is presented in section 6.4 again reviewing of the current status on this subject.

Nowadays, both techniques are applied routinely. In particular, for MART reconstruction in Tomographic PIV it is required to achieve calibration accuracies better than 0.3 pixel. Volume self-calibration is considered a necessary initial check and pre-requisite for Tomographic PIV. If the procedure doesn't provide clearly visible disparity peaks close to the origin, then Tomographic PIV will also most likely fail. VSC has meanwhile been adapted to the challenging case of large vibrations requiring single-image self-calibration.

Finally, in chapter 7 an iterative method for reconstructing particles (IPR) in a volume is presented. This is the basis for the recently introduced Shake-the-Box (STB) technique (Schanz et al. 2016), which performed very well compared to contributors using Tomographic PIV in the recent PIV Challenge (Kähler et al. 2016). IPR/STB allows for an order of magnitude higher seeding densities compared to traditional 3D particle tracking velocimetry (Maas et al. 1993) suffering from problems with overlapping particles.

Shake-the-Box has recently been applied to large-scale volumes seeded with Helium-filled soap bubbles (HSFB) with a size of about 0.3 mm (Figure 8-1). Such neutrally buoyant bubbles scatter more than 1000 times more light than 1 µm oil droplets (Kühn et al. 2011; Caridi et al. 2015; Scarano et al. 2015; Schanz et al. 2016). As a light source, even pulsed LED-illumination is sufficient, possibly replacing expensive high-repetition rate lasers at least for lower flow velocities.

The combination of HSFB and STB or Tomographic PIV/PTV opens up the possibility of large-scale time-resolved volumetric flow measurements in air with volumes even larger than one m^3. In comparison, the largest air volume so far measured using Tomographic PIV and oil droplets has been orders of magnitude smaller in the range of around 100 cm^3.

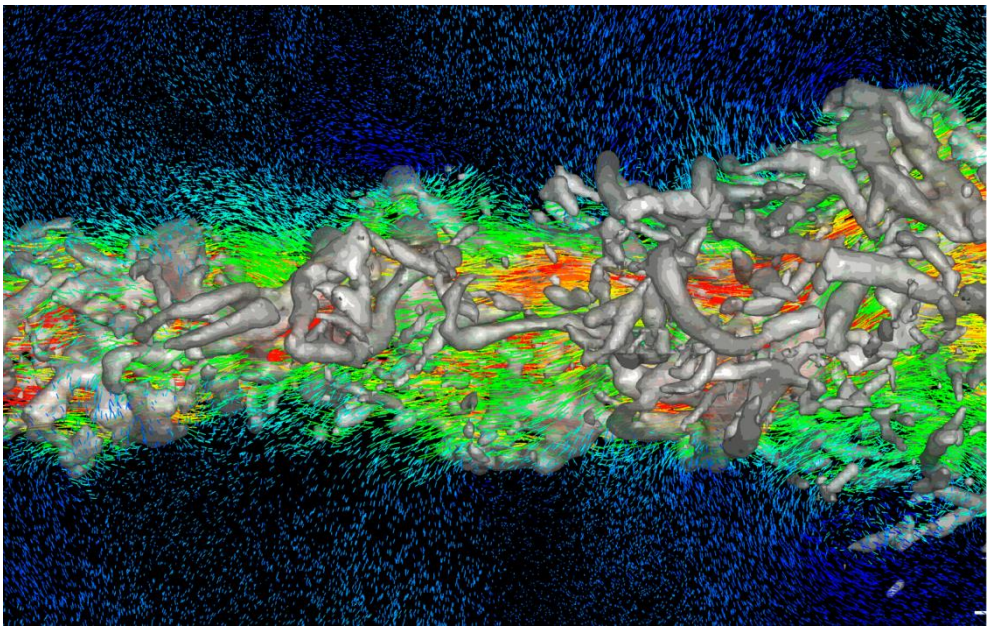

Figure 8.1. Thermal plume (image rotated), seeding: HSFB, field-of-view: 0.8 x 0.5 x 0.5 m, iso-surfaces of Q-value together with particles tracks, courtesy of Schröder and Schanz, DLR Göttingen.

Another promising development concerns the use of *data assimilation* techniques to improve the accuracy of the flow measurements or to extract pressure data (see review about pressure from PIV by van Oudheusden 2013). A full Navier-Stokes formulation or a simplified vortex-in-cell (VIC) description based on the vorticity transport equation can be applied as a regularization to volumetric, typically time-resolved, velocity field data.

Schneiders et al. (2014, 2016b, 2016c, Figure 8-2) have applied VIC/VIC+ in various ways increasing the temporal or spatial resolution of regular-grid Tomographic PIV and sparse particle tracking data, in particular converting sparse data to a regular grid. A similar technique named *flow fit* has been developed by Gesemann et al. (2016).

At the same time, the associated pressure field can be extracted even from a single snap-shot (Schneiders et al. 2016a) but more accurately from time-resolved particle tracking or Tomographic PIV data including acceleration data. In a recent comparison, it has been shown that pressure computation methods using particle tracks from STB-data worked better than from Tomographic-PIV data on a regular grid (Blinde et al. 2016),

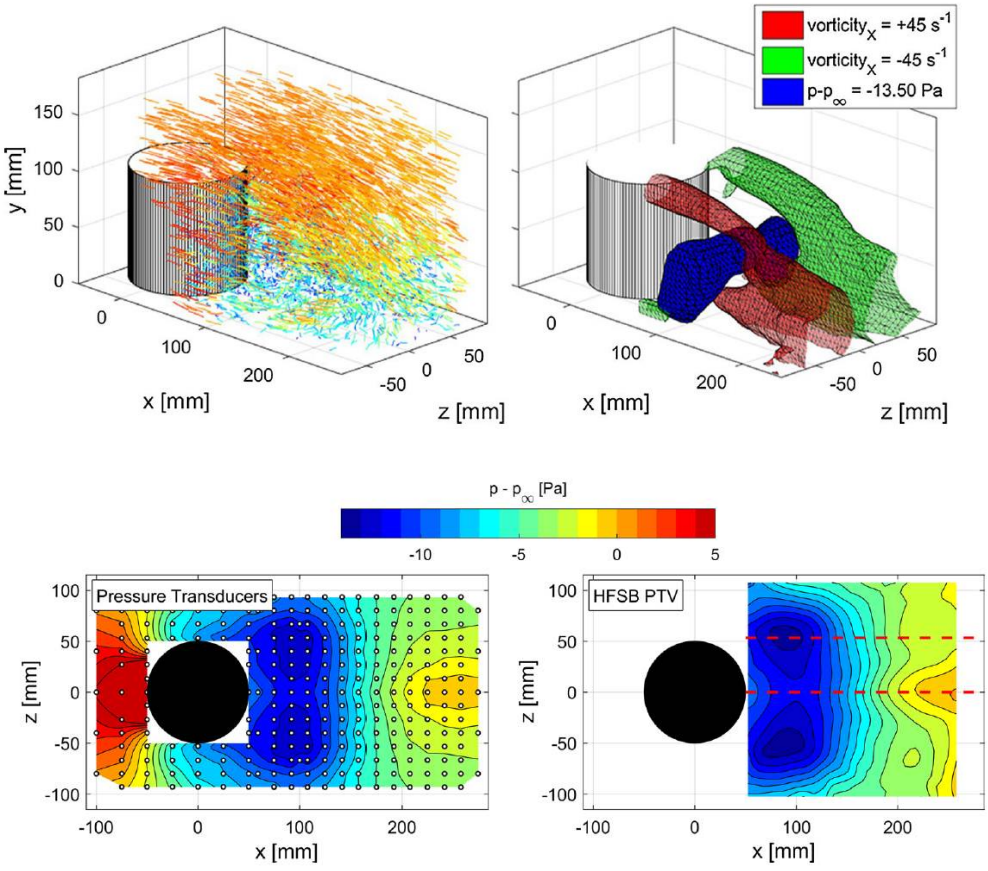

Figure 8.2. Pressure computation from Tomographic PTV data using HSFB. Particle tracks, vorticity and pressure (top) and comparison of surface pressure to pressure transducer values (bottom). From Schneiders et al. (2016c).

This reinforces the renewed interest in volumetric particle tracking, which as a technique has been developed already about 30 years ago. But only recently, with more advanced processing (IPR/STB) and data assimilation techniques like VIC+/flow-fit in combination with high performance hardware and novel seeding particles (HSFB), this method has come closer to its full potential extracting velocity, acceleration and even pressure for every seeding particle. This is the most complete information to be extracted from PIV/PTV using seeding tracers as indicator of local fluid element trajectories.

References

Ackermann F (1984) Digital Image Correlation: Performance and Application. In Photogrammetry, Thomsen Symposium, Birmingham, UK

Adrian RJ (1984) Scattering particle characteristics and their effect on pulsed laser measurements of fluid flow: speckle velocimetry vs. particle image velocimetry. Appl Opt 23:1690–1691

Adrian RJ (2005) Twenty years of particle image velocimetry. Exp Fluids 39:159–69

Adrian RJ and Westerweel J (2011) Particle Image Velocimetry. Cambridge University Press

Ahn S and Fessler JA (2003) Standard errors of mean. variance and standard deviation estimators, http://web.eecs.umich.edu/~fessler/papers/files/tr/stderr.pdf

Arroyo M and Greated C (1991) Stereoscopic particle image velocimetry. Meas Sci Technol 2: 1181–6

Astarita T and Cardone G (2005) Analysis of interpolation schemes for image deformation methods in PIV, Exp Fluids 38:233–243

Astarita T (2006) Analysis of interpolation schemes for image deformation methods in PIV: effect of noise on the accuracy and spatial resolution. Exp Fluids 40:977–987

Astarita T (2007) Analysis of weighting windows for image deformation methods in PIV. Exp Fluids 43:859–872

Astarita T (2008) Analysis of velocity interpolation schemes for image deformation methods in PIV, Exp Fluids 45:257

Astarita T (2009) Adaptive space resolution for PIV, Exp Fluids 46:1115:1123

Astarita T (2012) A Scheimpflug camera model for stereoscopic and tomographic PIV, 16th Int Symp on Applications of Laser Techniques to Fluid Mechanics, Lisbon, Portugal

Atkinson C, Buchmann N, Amili O and Soria J (2014) On the appropriate filtering of PIV measurements of turbulent shear flows. Exp Fluids 55(1):1-15

Atkinson C and Soria J (2009) An efficient simultaneous reconstruction technique for tomographic PIV. Exp Fluids 47:553–568

Azijli I and Dwight RP (2015) Solenoidal filtering of volumetric velocity measurements using Gaussian process regression. Exp Fluids 56:198

Bardet PM, Andre MA and Neal DR (2013) Systematic timing errors in laser-based transit-time velocimetry. 10th Int Symp on Particle Image Velocimetry, Delft, The Netherlands

Belden J (2013) Calibration of multi-camera systems with refractive interfaces. Exp Fluids 54(2):1–18

Belden J, Truscott T T, Axiak M C and Techet A H (2010) Three-dimensional synthetic aperture particle image velocimetry. Meas Sci Technol 21:125403

Bendat JS and Piersol AG (2010) Random data – Analysis and measurement procedures, 4th edition, John Wiley & Sons Inc., Hoboken, New Jersey

Benedict LH and Gould RD (1996) Towards better uncertainty estimates for turbulence statistics, Exp Fluids 22:129-136

Blinde B, Michaelis D, van Oudheusden B, Weiss PE, de Kat R, Laskari A, Jin Jeon Y, David L, Schanz D, Huhn F, Gesemann S, Novara M, McPhaden C, Neeteson N, Rival D, Schneiders J and Schrijer F (2016) Comparative assessment of PIV-based pressure evaluation techniques applied to a transonic base flow. 18th Int Symp on Applications of Laser Techniques to Fluid Mechanics, Lisbon, Portugal

Beresh SJ and Smith BL (2014) Effects of spatial realignment in stereo PIV calibration. AIAA Paper 2014-1101

Beresh SJ, Wagner JL and Smith BL (2016) Self-Calibration Performance in Stereoscopic PIV Acquired in a Transonic Wind Tunnel. Exp Fluids 57:48

Bhattacharya S, Charonko J and Vlachos P (2016) Stereo-particle image velocimetry uncertainty quantification. Meas Sci Technol 28:015301

Bomphrey RJ, Henningsson P, Michaelis D and Hollis D (2012) Journal of The Royal Society Interface 9(77):3378-86

Boomsma A, Bhattacharya S, Troolin D, Pothos S and Vlachos P (2016) A comparative experimental evaluation of uncertainty estimation methods for two-component PIV. Meas Sci Technol 27:094006

Browne M, Mayer N, Cutmore TRH (2007) A multiscale polynomial filter for adaptive smoothing. Dig Sig Proc 17:69–75

Brücker Ch (1996) 3-D scanning-particle-image-velocimetry: Technique and application to a spherical cap wake flow. Exp Fluids 56:157-179

Brücker C (1997) 3-D Scanning PIV applied to an air flow in a motored engine using digital high-speed video. Meas Sci Technol 8:1480-1492

Calluaud D, David L (2004) Stereoscopic particle image velocimetry measurements of a flow around a surface-mounted block, Exp Fluids 36:33-61

Caridi GCA, Ragni D, Sciacchitano A and Scarano F (2015) A seeding system for large-scale Tomographic PIV in aerodynamics. In: 11th international symposium on particle image velocimetry, Santa Barbara, USA

Castrillo C, Cafiero G, Discetti S and Astarita T (2016) Blob-enhanced reconstruction technique. Meas Sci Technol 27:094011

Champagnat F, Cornic P, Cheminet A, Leclaire B, Le Besnerais G and Plyer A (2014) Tomographic PIV: particles versus blobs. Meas Sci Technol 25:084002

Champagnat F, Plyer A, Le Besnerais G, Leclaire B, Davoust S and Le Sant Y (2011) Fast and accurate PIV computation using highly parallel iterative correlation maximization. Exp Fluids 50:1169-1182

Charonko JJ and Prestridge K (2016) Error and uncertainty for dissipation estimates using particle image velocimetry. 18th Int Symp on Applications of Laser Techniques to Fluid Mechanics, Lisbon, Portugal

Charonko JJ and Vlachos PP (2013) Estimation of uncertainty bounds for individual particle image velocimetry measurements from cross-correlation peak ratio. Meas Sci Technol 24:1-16

Chen J and Katz J (2005) Elimination of peak-locking error in PIV analysis using the correlation mapping method. Meas Sci Technol, 16:1605–18

Christensen KT (2004) On the influence of peak-locking errors on turbulence statistics compared from PIV ensembles. Exp Fluids 36(3):484–497

Cholemari MR (2007) Modeling and correction of peak-locking in digital PIV. Exp Fluids 42(6):913-922

Coleman HW and Steele WG (2009) Experimentation, validation, and uncertainty analysis for engineers. 3rd edition, John Wiley & Sons Inc., Hoboken, New Jersey

Cornic P, Champagnat F, Cheminet A, Leclaire B and Le Besnerais G (2015) Fast and efficient particle reconstruction on a 3D grid using sparsity. Exp Fluids 56:62

Cornic P, Illoul C, Cheminet A, Le Besnerais G, Champagnat F, Le Sant Y and Leclaire B (2016) Another look at volume self-calibration: calibration and self-calibration within a pinhole model of Scheimpflug cameras. Meas Sci Technol 27:9, Special Section on PIV 2015

Coudert S and Schon JP (2001) Back-projection algorithm with misalignment corrections for 2D3C stereoscopic PIV. Meas Sci Technol 12:1371–1381

de Silva CM, Philip J, Marusic I (2013) Minimization of divergence error in volumetric velocity measurements and implications for turbulence statistics. Exp Fluids 54:1557

Discetti S and Astarita T (2014) The detrimental effect of increasing the number of cameras on self-calibration for tomographic PIV, Meas Sci Technol, 25:8

Discetti S and Astarita T (2011) A fast multi-resolution approach to tomographic PIV. Exp Fluids 52:765-777

Discetti D, Natale A and Astarita T (2013) Spatial filtering improved tomographic PIV. Exp Fluids 54:1505

Earl TA, Cochard S, Thomas L, Tremblais B and L David L (2015) Implementation of vibration correction schemes to the evaluation of a turbulent flow in an open channel by tomographic particle image velocimetry. Meas Sci Technol 26 015303

Eckstein A, Charonko J and Vlachos P (2008) Phase correlation processing for DPIV measurements. Exp Fluids 45(3):485–500

Elsinga GE, Scarano F, Wieneke B and van Oudheusden BW (2006) Tomographic particle image velocimetry. Exp Fluids 41:933– 947

Elsinga GE and Westerweel J (2011) The point-spread-function and the spatial resolution of PIV cross-correlation methods. 9th Int Symp on Particle Image Velocimetry, Kobe, Japan

Elsinga GE, Westerweel J, Scarano F and Novara M (2009) On the velocity of ghost particles. 8th Int. Symp. PIV, Melbourne, AU

Fouras A, Jacono DL and Kerry Hourigan K (2008) Target-free Stereo PIV: a novel technique with inherent error estimation and improved accuracy, Exp Fluids 44(2):317-329

Fournel T, Coudert S, Lavest JM, Collange F, Schon JP (2003) Self-calibration of telecentric lenses: application to bubbly flow using moving stereoscopic camera, 4th Pacific Symposium on Flow Visualization and Image Processing, Chamonix (France)

Fournel T, Lavest JM, Coudert S and Collange F (2004) Self-calibration of PIV video cameras in Scheimpflug condition. In: Stanislas M, Westerweel J, Kompenhans J (eds) Particle image velocimetry: recent improvements, Proceedings of the EUROPIV 2 Workshop, Zaragoza (Spain), March/April 2003. Springer, Berlin Heidelberg New York, 391–405

George WK, Beuther PD and Lumley JL (1978) Processing of Random Signals, Proceedings of the Dynamic Flow Conference 1978 on Dynamic Measurements in Unsteady Flows. Springer Netherlands

Gesemann S, Huhn F, Schanz D and Schröder (2016) From noisy particle tracks to velocity, acceleration and pressure fields using B-splines and penalties. 18th Int Symp on Applications of Laser Techniques to Fluid Mechanics, Lisbon, Portugal

Gesemann S, Schanz D, Schröder A, Petra S, Schnörr C (2010) Recasting Tomo-PIV reconstruction as constrained and L1-regularized non-linear least squares problem. 15th Int. Symp. Appl. Laser Tech. Fluid Mech., Lisbon, Portugal

Giordano R and Astarita T (2009) Spatial resolution of the Stereo PIV technique, Exp Fluids 46(4):643

Grizzi S, Francisco Pereira F and Di Felice F (2010) A simplified, flow-based calibration method for stereoscopic PIV. Exp Fluids 48(3):473-486

Grayson K, de Silva CM, Hutchins N and Marusic I (2016) Laser light sheet profile and alignment effects on PIV performance, 18th Int Symp on Applications of Laser Techniques to Fluid Mechanics, Lisbon, Portugal

Hain R and Kähler C (2007) Fundamentals of multi-frame particle image velocimetry (PIV). Exp Fluids 42:575–587

Hartley R and Sturm P (1994) Triangulation, ARPA Image Understanding Workshop, Monterey, Ca 957-966

Hartley R and Zissermann A (2000) Multiple view geometry in computer vision, Cambridge University Press, UK

Harris FJ (1978) On the use of windows for harmonic analysis with the discrete Fourier transform. Proc IEEE 66:51-83

Hearst RJ and Ganapathisubramani B (2015) Quantification and adjustment of pixel-locking in particle image velocimetry. Exp Fluids 56(10):1-5

Herman GT and Lent A (1976) Iterative reconstruction algorithms. Comput Biol Med 6:273–294

Herrmann SF, Hinsch KD (2004) Light-in-flight holographic particle image velocimetry for wind-tunnel applications. Meas Sci Technol 15:613-62

Hild F and Roux S (2006) Digital Image Correlation: from Displacement Measurement to Identification of Elastic Properties – a Review. Strain 42:69–80

Hinze JO (1975) Turbulence. McGraw–Hill

Hori T and Sakakibara J (2004) High Speed Scanning Stereoscopic PIV for 3D Vorticity Measurement in Liquids, Meas Sci Technol, 15:1067-1078

Horn BK and Schunck BG (1981) Determining optical flow, Artificial Intelligence, vol 17, pp 185-203

Huang HT, Fielder HE and Wang JJ (1993) Limitation and improvement of PIV, Part II: Particle image distortion, a novel technique. Exp Fluids 15:263-73

Hunt JCR, Wray A and Moin P (1988) Eddies, stream, and convergence zones in turbulent flows. Center for Turbulence Research Report CTR-S88

Iannetta F, Sciacchitano A, Arpino F and Scarano F (2016) Numerical and experimental comparison of velocity derived quantities in rectangular cavity flows, Fourth International Conference on Computational Methods for Thermal Problems THERMACOMP2016, Georgia Tech, Atlanta, USA

Jeon JY, Chatellier L and David L (2014) Fluid trajectory evaluation based on an ensemble-averaged cross-correlation in time-resolved PIV. Exp Fluids 55:1766

Kähler C, Astarita T, Vlachos P, Sakakibara J, Hain R, Discetti S, La Foy R and Cierpka C (2016) Main results of the 4th International PIV Challenge. Exp Fluids 57:97

Kähler C, Scharnowski S and Cierpka C (2012) On the resolution limit of digital particle image velocimetry. Exp Fluids 52:1629–1639

Katkovnik V (2005) Multiresolution local polynomial regression: A new approach to pointwise spatial adaptation. Dig Sig Proc 15:73–116

Khintchine A (1934) Korrelationstheorie der stationären stochastischen Prozesse. Mathematische Annalen 109(1):604–615

Kühn M, Ehrenfried K, Bosbach J and Wagner C (2011) Large-scale tomographic particle image velocimetry using helium-filled soap bubbles. Exp Fluids 50:929

Louhichi H, Fournel T, Lavest JM, and Aissia HB (2007) Self-calibration of Scheimpflug cameras: an easy protocol. Meas Sci Technol 18(8):2616

Lecordier B and Trinité M (2003) Advanced PIV algorithms with image distortion—validation and comparison from synthetic images of turbulent flow. 5th Int Symp on Particle Image Velocimetry, Busan, Korea

Legrand M, Nogueira J, Ventas R and Lecuona A (2012) Simultaneous assessment of peak-locking and CCD readout errors through a multiple Δt strategy. Exp Fluids 53:121–135

Liao Q and Cowen EA (2005) An efficient anti-aliasing spectral continuous window shifting technique for PIV. Exp. Fluids, 38(2), 197-208.

Lindken R, Poelma C and Westerweel J (2003) Compensation for spatial effects for non-uniform seeding in PIV interrogation by signal relocation. 5th Int Symp on Particle Image Velocimetry, Busan, Korea

Lucas BD and Kanade T (1981) An iterative image registration technique with an application to stereo vision, Image Understanding workshop, pp 121-130, DARPA

Lüthi B, Ott S, Berg J and Mann J (2007) Lagrangian multi-particle statistics. J Turbulence 8 45

Lukin A (2007) Tips and Tricks: Fast Image Filtering Algorithms, Proceedings of GraphiCon'2007, Moscow, Russia, pp 186-189

Lynch K and Scarano F (2013) A high-order time-accurate interrogation method for time-resolved PIV. Meas Sci Technol 24:035305

Lynch K and Scarano F (2014) Experimental determination of tomographic PIV accuracy by a 12-camera system. Meas Sci Technol 25:084003

Lynch K and Scarano F (2015) An efficient and accurate approach to MTE-MART for time-resolved tomographic PIV. Exp Fluids 56:66

Maas HG, Gruen A and Papantoniou D (1993) Particle tracking velocimetry in 3-dimensional flows, Exp Fluids 15:133–146

Maas HG (1992) Digitale Photogrammetrie in der dreidimensionalen Strömungs-messtechnik. ETH Zürich - Dissertation Nr. 9665

Maas HG (1996) Contributions of digital photogrammetry to 3D PTV. In: Three-Dimensional Velocity and Vorticity Measuring and Image Analysis Techniques. (ed Dracos T). pp 191-208, Kluwer, NL

Medan Y, Yair E and Chazan D (1981) Super Resolution Pitch Determination of Speech Signals, IEEE Transaction on Signal Processing, Vol 39, No1

Melling A (1997) Tracer particles and seeding for particle image velocimetry. Meas Sci Technol 8:1406

Meinhart CD, Wereley ST, Santiago JG (1999) A PIV algorithm for estimating time-averaged velocity fields, Proceedings of Optical Methods and Image Processing in Fluid Flow, 3rd ASME/JSME Fluids Engineering Conference, San Francisco

Meynart R (1982a) Convective flow field measurement by speckle velocimetry. Rev Phys Appl 17:301–305

Michaelis D, Neal D and Wieneke B (2016) Peak-locking reduction for particle image velocimetry. Meas Sci Technol 27(10)

Michaelis D, Novara M, Scarano F and Wieneke B (2010) Comparison of volume reconstruction techniques at different particle densities. 15th Int. Symp. Appl. Laser Techniques Fluid Mech., Lisbon, Portugal

Michaelis D, Poelma C, Scarano F, Westerweel J and Wieneke B (2006) A 3D time-resolved cylinder wake survey by Tomographic PIV, 12th International Symposium on Flow Visualization, Göttingen, Germany, Sept 10-14

Michaelis D and Wolf CC (2011) Vibration compensation for tomographic PIV using single image, volume self-calibration. 9th Int Symp on Particle Image Velocimetry, Kobe, Japan

Neal DR, Sciacchitano A, Smith BL and Scarano F (2015) Collaborative framework for PIV uncertainty quantification: the experimental database. Meas Sci Technol 26(7):074003

Nobach H (2011) Influence of individual variations of particle image intensities on high-resolution PIV. Exp Fluids 50(4):919

Nobach H and Bodenschatz E (2009) Limitations of accuracy in PIV due to individual variations of particle image intensities. Exp Fluids 47:27

Nogueira J, Lecuona A and Rodriguez PA (1999) Local field correction PIV: on the increase of accuracy of digital PIV systems. Exp Fluids 27:107–116

Nogueira J, Lecuona A and Rodriguez PA (2001) Local field correction PIV, implemented by means of simple algorithms, and multigrid versions. Meas Sci Technol 12:1911–1921

Nogueira J, Lecuona A and Rodriguez PA (2005a) Limits on the resolution of correlation PIV iterative methods. Fundamentals. Exp Fluids 39:305–313

Nogueira J, Lecuona A and Rodriguez PA (2005b) Limits on the resolution of correlation PIV iterative methods. Practical implementation and design of weighting functions. Exp Fluids 39:314-321

Novara M and Scarano F (2011) Performances of motion tracking enhanced Tomo-PIV on turbulent shear flows. Exp Fluids 50:1027-1041

O'Neill PL, Nicolaides D, Honnery D and J. Soria J (2004) Autocorrelation Functions and the Determination of Integral Length with Reference to Experimental and Numerical Data. 15th Australasian Fluid Mechanics Conference, The University of Sydney, Sydney, Australia

Overmars EFJ, Warncke NGW, Poelma C and Westerweel J (2010) Bias errors in PIV: the pixel locking effect revisited. 15th Int Symp on Applications of Laser Techniques to Fluid Mechanics, Lisbon, Portugal

Oxlade AR, Valente PC, Ganapathisubramani B and Morrison JF (2012) Denoising of time-resolved PIV for accurate measurement of turbulence spectra and reduced error in derivatives. Exp Fluids 53(5):1561-1575

Pereira F, Stüer H, Graff E C, Gharib M (2006) Two-frame 3D particle tracking. Meas Sci Technol 17:1680-1692

Persoons T (2014) Time-Resolved High-Dynamic-Range Particle Image Velocimetry Using Local Uncertainty Estimation. AIAA Journal, DOI: 10.2514/1.J053651

Peters WH and Ranson WE (1982) Digital Imaging Techniques in Experimental Stress Analysis. Opt Eng 21:427-432

Petra S, Schröder A and Schnörr C (2009) 3D tomography from few projections in experimental fluid. Dynamics, imaging measurement methods for flow analysis. Book Series: Notes on numerical fluid mechanics and multidisciplinary design 106, 63-72

Pickering CJD and Halliwell N (1984) LSP and PIV: photographic film noise. Appl Opt 23:2961–2969

Powell MJD (1964) An efficient method for finding the minimum of a function of several variables without calculating derivatives. Computer Journal, 7:155–162

Prasad AK (2000) Stereoscopic particle image velocimetry. Exp Fluids 29:103–16

Prasad AK, Adrian RJ, Landreth CC and Offutt PW (1992) Effect of resolution on the speed and accuracy of particle image velocimetry interrogation. Exp Fluids 13(2-3):105-116

Prasad AK and Adrain RJ (1993) Stereoscopic particle image velocimetry applied to liquid flows. Exp Fluids 15:49-60

Raffel M, Willert CE, Wereley ST and Kompenhans J (2007) Particle image velocimetry: A practical guide. Springer Verlag, Berlin, 2nd Ed.

Raiola M, Discetti S and Ianiro A (2014) On the suppression of PIV measurement noise with a POD based filter, 17th Int Symp on Applications of Laser Techniques to Fluid Mechanics, Lisbon, Portugal

Roesgen T (2003) Optimal subpixel interpolation in particle image velocimetry. Exp Fluids 35(3):252–6

Roth G and Katz J (2001) Five techniques for increasing the speed and accuracy of PIV interrogation. Meas Sci Technol 12:238–245

Scarano F (2004a) On the stability of iterative PIV image interrogation methods, 12th Int Symp on Applications of Laser Techniques to Fluid Mechanics, Lisbon, Portugal

Scarano F (2004b) A super-resolution particle image velocimetry interrogation approach by means of velocity second derivatives correlation. Meas Sci Technol 15(2):475

Scarano F (2013) Tomographic PIV: principles and practice. Meas Sci Technol 24:012001

Scarano F, David L, Bsibsi M and Calluaud D (2005) S-PIV comparative assessment: image dewarping + misalignment correction and pinhole + geometric projection. Exp Fluids 39:257–266

Scarano F and Riethmuller ML (1999) Iterative multigrid approach in PIV image processing with discrete window offset. Exp Fluids 26:513-23

Scarano F and Riethmuller ML (2000) Advances in iterative multigrid PIV image processing. Exp Fluids Suppl 29(1):S051-S060

Scarano S, Ghaemi S, Caridi G, Bosbach J, Dierksheide U and Sciacchitano A (2015) On the use of helium-filled soap bubbles for large-scale tomographic PIV in wind tunnel experiments. Exp Fluids 56:42

Schanz D, Gesemann S and Schröder A (2016) Shake-The-Box: Lagrangian particle tracking at high particle image densities. Exp Fluids 57:70

Schanz D, Gesemann S, Schröder A, Wieneke B and Michaelis D (2010) Tomographic reconstruction with non-uniform optical transfer functions (OTF) and an additive SMART approach. 15th Int. Symp. Appl. Laser Techniques to Fluid Mech., Lisbon, Portugal

Scharnowski S and Kähler C (2016a) Estimation and optimization of loss- of- pair uncertainties based on PIV correlation functions. Exp Fluids 57:23

Scharnowski S and Kähler C (2016b) On the loss- of- correlation due to PIV image noise. Exp Fluids 57:119

Schiavazzi D, Coletti F, Iaccarino, G and Eaton JK (2014) A matching pursuit approach to solenoidal filtering of three-dimensional velocity measurements. J of Comp Physics 263:206-221

Schimpf A, Kallweit S and Richon JB (2003) Photogrammetric particle image velocimetry. 5th Int. Symp. Particle Image Velocimetry, Busan, Korea

Schosser C, Fuchs T, Hain R and Kähler C (2016) Non- intrusive calibration for three-dimensional particle imaging. Exp Fluids 57:69

Schneiders JFG, Dwight RP and Scarano F (2014) Time-supersampling of 3D-PIV measurements with vortex-in-cell simulation. Exp Fluids 55:1692

Schneiders JFG, Dwight RP and Scarano F (2015) Tomographic PIV noise reduction by simulating repeated measurements. 11th Int Symp on Particle Image Velocimetry, Santa Barbara, CA, USA

Schneiders JFG, Pröbsting S, Dwight RP, van Oudheusden BW and Scarano F (2016a) Pressure estimation from single-snapshot tomographic PIV in a turbulent boundary layer. Exp Fluids 57:53

Schneiders JFG and Scarano F (2016b) Dense velocity reconstruction from tomographic PTV with material derivatives. Exp Fluids 57:139

Schneiders JFG, Caridi GCA., Sciacchitano A and Scarano F (2016c) Large-scale volumetric pressure from tomographic PTV with HFSB tracers. Exp Fluids 57:164

Schrijer F and Scarano F (2008) Effect of predictor–corrector filtering on the stability and spatial resolution of iterative PIV interrogation. Exp Fluids 45:927–941

Schröder A, Geisler R, Staack K, Wieneke B, Elsinga G E, Scarano F and Henning A (2008) Lagrangian and Eulerian views into a turbulent boundary layer flow using time-resolved tomographic PIV. 14th Int. Symp. Appl. Laser Techniques to Fluid Mech., Lisbon, Portugal

Schröder A, Schanz D, Heine B and Dierksheide U (2011) Transitional flow structures downstream of a backwardfacing-step – An investigation using high resolution tomo PIV. 9th Int. Symp. PIV, Kobe, JP

Schröder A and Willert C (Eds.) (2008) Particle Image Velocimetry: New Developments and Recent Applications. Springer Berlin Heidelberg, ISBN 978-3-540-73527-4, DOI 10.1007/978-3-540-73528-1

Sciacchitano A, Wieneke B and Scarano F (2013) PIV uncertainty quantification by image matching. Meas Sci Technol 24:1-16

Sciacchitano A and Lynch K (2015) A posteriori uncertainty quantification for tomographic PIV data. 11th Int Symp on Particle Image Velocimetry, Santa Barbara, CA, USA

Sciacchitano A, Neal DR, Smith BL, Warner SO, Vlachos PP, Wieneke B and Scarano F (2015) Collaborative framework for PIV uncertainty quantification: comparative assessment of methods. Meas Sci Technol, 26(7):074004

Sciacchitano A, Scarano F and Wieneke B (2012) Multi-frame pyramid correlation for time-resolved PIV, Exp Fluids 53:1087–1105

Sciacchitano A and Wieneke B (2016) PIV uncertainty propagation, Meas Sci Technol 27(8):084006

Soloff SM, Adrian RJ and Liu ZC (1997) Distortion compensation for generalized stereoscopic particle image velocimetry. Meas Sci Technol 8:1441

Stanislas M, Okamoto K and Kähler C (2003) Main results of the First International PIV Challenge. Meas Sci Technol 14:R63–R89

Stanislas M, Okamoto K, Kähler C and Westerweel J (2005) Main results of the Second International PIV Challenge. Exp Fluids 39: 170–191

Stanislas M, Okamoto K, Kähler C, Westerweel J and Scarano F (2008) Main results of the Third International PIV Challenge. Exp Fluids 45: 27

Sutton MA, Wolters WJ, Peters WH, Ranson WE and McNeil SR (1983) Determination of Displacements Using an Improved Digital Image Correlation Method. Image Vision Computing l(3):133-139

Sutton MA, Cheng M, Peters WH, Chao YJ, and McNeil SR (1986) Application of an Optimized Digital Image Correlation Method to Planar Deformation Analysis. Image Vision Computing 4(3):143-150

Sutton MA and Hild F (2015) Recent Advances and Perspectives in Digital Image Correlation. Exp Mech 55:1–8

Sutton MA, Orteu JJ and Schreier H (2009) Image Correlation for Shape, Motion and Deformation Measurements. Springer, ISBN 978-0387787466

Swamy NVC and Gowda BHL (1979) Auto-correlation measurements and integral time scales in three-dimensional turbulent boundary layers. Applied Scientific Research 35:265-316

Taylor JR (1997) An Introduction to Error Analysis: The Study of Uncertainties in Physical Measurements, Sausalito, CA: University Science Books

Tennekes H and Lumley JL (1972) A first course in turbulence, The MIT Press, Cambridge, Massachusetts, and London, England

Theunissen R, Scarano F and Riethmuller ML (2007) An adaptive sampling and windowing interrogation method in PIV, Meas Sci Technol 18(1):275-287

Theunissen R, Scarano F, Riethmuller ML (2008) On improvement of PIV interrogation near stationary interfaces. Exp Fluids 45:557-572

Theunissen R, Scarano, F and Riethmuller ML (2010) Spatially adaptive PIV interrogation based on data ensemble. Exp Fluids 48(5):875-887

Timmins BH, Wilson BW, Smith BL and Vlachos PP (2012) A method for automatic estimation of instantaneous local uncertainty in particle image velocimetry measurements. Exp Fluids 53:1133–1147

Tokgoz S, Elsinga GE, Delfos R and Westerweel J (2012) Spatial resolution and dissipation rate estimation in Taylor--Couette flow for tomographic PIV. Exp Fluids 53:561

Tsai RY (1987) A versatile camera calibration technique for high- accuracy 3D machine vision metrology using off-the-shelf TV cameras and lenses. IEEE J Robot Autom RA-3:323–344

van Doorne CWH and Westerweel J (2007) Measurement of laminar, transitional and turbulent pipe flow using stereoscopic-PIV. Exp. Fluids 42:259–79

van Oudheusden BW (2013) PIV-based pressure measurement, Meas Sci Technol 24:032001

Vétel J, Garon A and Pelletier D (2011) Denoising methods for time-resolved PIV measurements. Exp Fluids 51(4):893-916

Violato D and Scarano F (2011) Three-dimensional evolution of flow structures in transitional circular and chevron jets. Phys. Fluids 23 124104

Vollmers H (2001) Detection of vortices and quantitative evaluation of their main parameters from experimental velocity data, Meas Sci Technol 12 1199-1207

Wang C, Gao Q, Wang H, Wei R, Li T and Wang J (2016) Divergence-free smoothing for volumetric data. Exp Fluids 57:15

Webber WF (1973) Techniques for image registration. Conference on Machine Processing of Remotely Sensed Data, LARS Symposia

Weinkauff J, Michaelis D, Dreizler A and Böhm B (2013) Tomographic PIV measurements in a turbulent lifted jet flame. Exp Fluids 54:1624

Westerweel J and Scarano F (2005) Universal outlier detection for PIV data. Exp Fluids 39:1096–1100

Wieneke B (2005) Stereo-PIV using self-calibration on particle images. Exp Fluids 39:267

Wieneke B (2008) Volume self-calibration for 3D particle image velocimetry. Exp Fluids 45: 549

Wieneke B (2013) Iterative reconstruction of volumetric particle distribution. Meas Sci Technol 24:024008

Wieneke B (2015) PIV uncertainty quantification from correlation statistics. Meas Sci Technol 26(7): 074002

Wieneke B (2017) PIV anisotropic denoising using uncertainty quantification, Exp in Fluids 58:94

Wieneke B and Pfeiffer K (2010) Adaptive PIV with variable interrogation window size and shape. 15th Int Symp on Applications of Laser Techniques to Fluid Mechanics, Lisbon, Portugal

Wieneke B and Taylor S (2006) Fat-sheet PIV with Computation of Full 3D-Strain Tensor using Tomographic Reconstruction. 13th Int Symp on Applications of Laser Techniques to Fluid Mechanics, Lisbon, Portugal

Wiener N (1930) Generalized Harmonic Analysis. Acta Mathematica 55: 117–258, doi:10.1007/bf02546511

Willert C (1997) Stereoscopic digital particle image velocimetry for application in wind tunnel flows. Meas Sci Technol 8:1465–1479

Willert C (2006) Assessment of camera models for use in planar velocimetry calibration, Exp Fluids 41:135-143

Willert C and Gharib M (1991) Digital particle image velocimetry. Exp Fluids 10:181–93

Wilson BM and Smith BL (2013a) Taylor-series and Monte-Carlo-method uncertainty estimation of the width of a probability distribution based on varying bias and random error. Meas Sci Technol 24(3):035301

Wilson BM and Smith BL (2013b) Uncertainty on PIV mean and fluctuating velocity due to bias and random errors. Meas Sci Technol 24(3):035302

Worth N A and Nickels T B (2007) Acceleration of Tomo-PIV by Estimating the Initial Volume Intensity Distribution. Exp Fluids 45 847-856

Wrobel B and Ehlers M (1980) Digitale Bildkorrelation von Fernerkundungsaufnahmen aus Wattgebieten. Bildmessung und Luftbildwesen 3:67-79

Xue Z, Charonko JJ and Vlachos PP (2014) Particle image velocimetry correlation signal-to-noise ratio metrics and measurement uncertainty quantification, Meas Sci Technol, 25(11) 115301

Zhang Z (2000) A flexible new technique for camera calibration. IEEE Trans Pattern Anal Mach Intell 22(11):1330–1334

Zitova B and Flusser J (2003) Image registration methods: a survey. Image and Vision Computing 21:977–1000

Zunino H, Adrian R and Ding L (2015) Non-intrusive calibration technique. 11th Int Symp on Particle Image Velocimetry, Santa Barbara, California

Appendix A

Assumption:

The autocorrelation function $AF_F(\Delta x)$ of filter F(x) is the same as the autocorrelation $AF_{\delta u}(\Delta x)$ of the random noise $\delta u(x)$ of neighboring vectors separated by Δx:

$$AF_F(\Delta x) \equiv AF_{\delta u}(\Delta x)$$

with

$$AF_{\delta u}(\Delta x) = \frac{\int \delta u(x)\,\delta u(x+\Delta x)\,dx}{\int \delta u(x)\,\delta u(x)\,dx}$$

Proof:

Let's for simplification assume that each pixel carries displacement information $u(x) = u_{true}(x) + \delta u(x)$ with error $\delta u(x)$ independent for each pixel with constant standard deviation σ_{u_px}. The measured displacement is given by eqn. (2.1):

$$\begin{aligned} u_F(x) &= \sum_{x'} F(x')u(x+x') = \sum_{x'} F(x')\left(u_{true}(x+x') + \delta u(x+x')\right) \\ &= u_{F\_true}(x) + \sum_{x'} F(x')\delta u(x+x') \end{aligned}$$

where the last term is the expected random error δu_F of u_F. The covariance between the random errors of two computed vectors separated by Δx is given by:

$$\begin{aligned} \operatorname{cov}(\delta u_F(x), \delta u_F(x+\Delta x)) &= E\left[\left(\delta u_F(x) - E\left[\delta u_F(x)\right]\right)\cdot\left(\delta u_F(x+\Delta x) - E\left[\delta u_F(x+\Delta x)\right]\right)\right] \\ &= E\left[\delta u_F(x)\cdot\delta u_F(x+\Delta x)\right] \\ &= E\left[\sum_{x'} F(x')\delta u(x+x')\sum_{x''} F(x'')\delta u(x+\Delta x+x'')\right] \\ &= E\left[\sum_{x'}\sum_{x''} F(x')F(x'')\delta u(x+x')\delta u(x+\Delta x+x'')\right] \end{aligned}$$

using $E\left[\delta u_F(x)\right] = 0.$ The errors are assumed to be pixel-wise independent with the expectation function $E\left[\delta u(x_1)\cdot\delta u(x_2)\right] = \delta_{x_1,x_2}\sigma^2_{u\_px}$ with $\delta_{i,j} = 1$ for i=j and zero otherwise. Therefore:

$$\operatorname{cov}(\delta u_F(x), \delta u_F(x+\Delta x)) = \sum_{x'} \sum_{x''} F(x')F(x'')\delta_{x',\Delta x+x''}\sigma^2_{u\_px}$$
$$= \sigma^2_{u\_px} \sum_{x'} F(x')F(x'+\Delta x)$$

Thus, the normalized autocorrelation coefficient $AF_{\delta u}(\Delta x)$ given by:

$$AF_{\delta u}(\Delta x) = \frac{\operatorname{cov}_{\delta u}(\Delta x)}{\operatorname{cov}_{\delta u}(0)} = \frac{\sum_x F(x)F(x+\Delta x)}{\sum_x F(x)^2} = AF_F(\Delta x) \qquad \text{q.e.d.}$$

This is also valid when switching back to particles as displacement carriers – effectively replacing pixel positions and pixel errors with particles and particle position errors – provided there is sufficient statistics with enough particles in each interrogation window. One should note that knowledge of the actual value of the pixel or particle displacement errors is not needed.

Appendix B

Assumption:

The sum of the autocorrelation coefficients given by

$$L_{sr} = \int_{-\infty}^{+\infty} AF_{\delta x}(\Delta x)\ d(\Delta x)$$

is equal to the inverse of the sum of the filter coefficients squared:

$$L_{sr} = 1 / \int_{-\infty}^{+\infty} F(x)^2\, dx$$

Proof:

$$L_{sr} = \int_{-\infty}^{+\infty} AF_{\delta x}(\Delta x)\ d(\Delta x) = \int_{-\infty}^{+\infty} AF_{F}(\Delta x)\ d(\Delta x)$$

since $AF_{\delta u} \equiv AF_{F}$ (eqn. (2.4)). Thus, according to eqn. (2.3):

$$L_{sr} = \int_{-\infty}^{+\infty} \frac{\int_{-\infty}^{+\infty} F(x)F(x+\Delta x)\,dx}{\int_{-\infty}^{+\infty} F(x)F(x)\,dx}\ d(\Delta x)$$

$$= \frac{1}{\int_{-\infty}^{+\infty} F(x)^2\,dx} \iint_{\pm\infty} F(x)F(x+\Delta x)\,dx\,d(\Delta x)$$

$$= \frac{1}{\int_{-\infty}^{+\infty} F(x)^2\,dx} \int_{-\infty}^{+\infty} F(x) \left[\int_{-\infty}^{+\infty} F(x+\Delta x)\,d(\Delta x) \right]^{=1} dx$$

$$= \frac{1}{\int_{-\infty}^{+\infty} F(x)^2\,dx} \int_{-\infty}^{+\infty} F(x)\,dx = \frac{1}{\int_{-\infty}^{+\infty} F(x)^2\,dx} \qquad \text{q.e.d.}$$

Appendix C

Assumption:

If a PIV algorithm based on a linear spatial filter has a 2D spatial resolution of L_{sr} x L_{sr} it reduces the noise of pixel-wise contribution of displacement information by a factor of L_{sr} with:

$$L_{sr} = 1 / \sum_i F(x_i)^2$$

Proof:

Again, let's for simplification assume that each pixel carries displacement information $u(x) = u_{true}(x) + \delta u(x)$ with error $\delta u(x)$ independent for each pixel with constant standard deviation σ_{u_px}. The measured displacement is given by eqn. (2.1) . Simple error propagation leads to the standard deviation σ_{u_F} of:

$$\sigma_{u_F}^2 = \sum_{i=-\infty}^{\infty} \left(\frac{\partial u_F}{\partial x_i} \right)^2 \sigma_{u\_px}^2 = \sum_x F(x)^2 \sigma_{u\_px}^2 = \frac{\sigma_{u\_px}^2}{L_{sr}}$$

So the random error is reduced by a factor of $\sqrt{L_{sr}}$ in 1D and by L_{sr} in 2D. Here, as in appendix A, one ignores that the information and error of neighboring pixels is not independent. Typically, it is correlated over the particle image size, but this can be neglected provided the correlation length is sufficiently smaller than L_{sr}.

Appendix D

Assumption:

Wiener–Khinchin theorem (1930/1934):

$$\mathrm{FFT}\left(\mathrm{AF}(\Delta x)\right) = \mathrm{PSD}(f)$$

Simplified proof:

The Fourier transform of the unnormalized autocorrelation function is given by:

$$\begin{aligned}
\mathrm{FFT}(\mathrm{AF}) &= \int_{-\infty}^{+\infty}\left[\int_{-\infty}^{+\infty} F(x')F(x'+x)dx'\right] e^{-i2\pi fx}dx \\
&= \int_{-\infty}^{+\infty}\int_{-\infty}^{+\infty} F(x')F(x'+x)\, e^{-i2\pi fx}dx'dx \\
&= \int_{-\infty}^{+\infty} F(x')\left[\int_{-\infty}^{+\infty} F(x'+x)\, e^{-i2\pi fx}dx\right]dx'
\end{aligned}$$

Substituting $x'' = x + x'$:

$$\begin{aligned}
\mathrm{FFT}(\mathrm{AF}) &= \int_{-\infty}^{+\infty} F(x')\left[\int_{-\infty}^{+\infty} F(x'')e^{-i2\pi fx''}e^{+i2\pi fx'}dx''\right]dx' \\
&= \int_{-\infty}^{+\infty} F(x')\, e^{+i2\pi fx'}\underbrace{\left[\int_{-\infty}^{+\infty} F(x'')e^{-i2\pi fx''}dx''\right]}_{=R_A} dx' \\
&= R_A(f)\int_{-\infty}^{+\infty} F(x')e^{+i2\pi fx'}dx' \\
&= R_A^2(f) = \mathrm{PSD}(f) \qquad \text{q.e.d.}
\end{aligned}$$

Publication List

Most relevant:

Wieneke B (2017) PIV anisotropic denoising using uncertainty quantification. Exp Fluids, 58:94

Sciacchitano A and Wieneke B (2016) PIV uncertainty propagation. Meas Sci Technol 27(8):084006

Wieneke B (2015) PIV uncertainty quantification from correlation statistics. Meas Sci Technol 26(7):074002

Wieneke B (2013) Iterative reconstruction of volumetric particle distribution. Meas Sci Technol 24:024008

Wieneke B and Pfeiffer K (2010) Adaptive PIV with variable interrogation window size and shape. 15th Int Symp on Applications of Laser Techniques to Fluid Mechanics, Lisbon, Portugal

Wieneke B (2008) Volume self-calibration for 3D particle image velocimetry. Exp Fluids 45:549

Wieneke B and Taylor S (2006) Fat-sheet PIV with Computation of Full 3D-Strain Tensor using Tomographic Reconstruction. 13th Int Symp on Applications of Laser Techniques to Fluid Mechanics Lisbon, Portugal

Elsinga GE, Scarano F, Wieneke B and van Oudheusden BW (2006) Tomographic particle image velocimetry. Exp Fluids 41:933– 947

Wieneke B (2005) Stereo-PIV using self-calibration on particle images. Exp Fluids 39:267

Others:

Michaelis D, Neal D and Wieneke B (2016) Peak-locking reduction for particle image velocimetry. Meas Sci Technol 27(10)

Sciacchitano A, Neal DR, Smith BL, Warner SO, Vlachos PP, Wieneke B and Scarano F (2015) Collaborative framework for PIV uncertainty quantification: comparative assessment of methods. Meas Sci Technol 26(7):074004

Hein M, Wieneke B and Seemann R (2014) Calculation of the weighting function and determination of the depth of correlation in micro-PIV from experimental particle images. Meas Sci Technol 25 (8):084008

Sciacchitano A, Wieneke B and Scarano F (2013) PIV uncertainty quantification by image matching. Meas Sci Technol 24:1-16

Adam J, Klinkmüller M, Schreurs G and Wieneke B (2013) Quantitative 3D strain analysis in analogue experiments simulating tectonic deformation: Integration of X-ray computed tomography and digital volume correlation techniques. Journal of Structural Geology 55, 127-149

Sciacchitano A, Scarano F and Wieneke B (2012) Multi-frame pyramid correlation for time-resolved PIV. Exp Fluids 53:1087–1105

Schanz D, Gesemann S, Schröder A, Wieneke B and Novara M (2012) Non-uniform optical transfer functions in particle imaging: calibration and application to tomographic reconstruction. Meas Sci Technol 24(2):024009

Becker F, Wieneke B, Petra S, Schroder A and Schnörr C (2012) Variational adaptive correlation method for flow estimation. IEEE Transactions on Image Processing 21(6):3053-3065

Tokgoz S, Geisler R, van Bokhoven LJA and Wieneke B (2012) Temperature and velocity measurements in a fluid layer using background-oriented schlieren and PIV methods. Meas Sci Technol 23(11):115302

Schröder A, Geisler R, Staack K, Elsinga GE, Scarano F, Wieneke B, Henning A, Poelma C and Westerweel J (2011) Eulerian and Lagrangian views of a turbulent boundary layer flow using time-resolved tomographic PIV. Exp Fluids 50:1071

Petra S, Schröder A, Wieneke B and Schnörr C (2008) On sparsity maximization in tomographic particle image reconstruction. Joint Pattern Recognition Symposium 294-303

Becker F, Wieneke B, Yuan J and Schnörr C (2008) A variational approach to adaptive correlation for motion estimation in particle image velocimetry. Joint Pattern Recognition Symposium, 335-344

Van Doorne CWH, Hof B, Nieuwstadt FTM, Westerweel J and Wieneke B (2007) Investigation of turbulent puffs in pipe flow with time-resolved stereoscopic PIV. Exp Fluids 42:259-279

Michaelis D, Poelma C, Scarano F, Westerweel J and Wieneke B (2006) A 3D time-resolved cylinder wake survey by Tomographic PIV, 12th International Symposium on Flow Visualization, Göttingen, Germany, Sept 10-14

Lindken R, Westerweel J and Wieneke B (2006) Stereoscopic micro particle image velocimetry. Exp Fluids 41(2):161-171

Foeth EJ, van Doorne CWH, van Terwisga T and Wieneke B (2006) Time resolved PIV and flow visualization of 3D sheet cavitation. Exp Fluids 40(4):503-513

Adam J, Urai JL, Wieneke B, Oncken O, Pfeiffer K, Kukowski N, Lohrmann J, Hoth S, van Der Zee W and Schmatz J (2005) Shear localisation and strain distribution during tectonic faulting—new insights from granular-flow experiments and high-resolution optical image correlation techniques. Journal of Structural Geology 27(2):283-301

Nobes DS, Wieneke B and Tatam RP (2004) Determination of view vectors from image warping mapping functions. Optical Engineering 43(2):407-414

Wieneke B and Clayton DD (1983) Aggregation of grains in a turbulent pre-solar disk. Chondrules and their Origins 284-295

Selection of Patents

2003, EP 1 460 433 (Stereo-PIV Self-Calibration)

2003, EP 1 517 150 (Tomographic PIV)

2006, EP 1 926 049 (Volume Self-Calibration)

2009, EP 2 494 522 (OTF for Tomographic PIV/PTV)

2013, EP 2 344 898 (IPR, Iterative Particle Reconstruction)

2015, DE 10201305648 Schröder A, Schanz D, Wieneke B (Shake-the-Box)

Research and Professional Experience:

Bernhard Wieneke received his M.Sc. in Physics at Rice University in 1983. He joined LaVision GmbH in 1989, when LaVision was founded as a spin-off of the Laser-Laboratory Göttingen and the Max-Planck-Institute in Göttingen. He has been developing software and hardware for optical measurement systems, in particular for flow diagnostics (PIV) and surface deformation measurement systems (DIC). Since 2010 he holds the position of the managing director of LaVision GmbH together with Dr. Heinrich Voges.

He has participated in many German and European research projects and co-supervised several Bachelor, Master and PhD-students in cooperation with European research institutes.

Acknowledgement

Given the long time it took to complete this thesis, there are numerous people who directly or indirectly contributed to its success, too many to mention them all. First of all, my collegues and superiors at LaVision (Karsten, Heiner, Dirk, among others) supported me generously and gave me lots of freedom to persue my efforts to improve our PIV systems. If they had known how many months it actually takes to work on a paper, they might have kicked me out, but once published everybody was happy about it. Furthermore, I'm very grateful about the long-time fruitful cooperation with the guys at TU-Delft (Fulvio, Gerrit, Andrea, Jan, Jerry), DLR Göttingen (Andreas, Daniel, Matteo, Sebastian, Markus) and many others like Ralf, Jürgen, Michael, Bart and Christian. Fulvio encouraged me to put together my already existing work into a PhD-thesis, just like Iris, who regretted it somewhat once she found out, that I partly spend our vacations working on it.